

MOVPE of GaSb-based materials and solar cell structures

DISSERTATION

zur

Erlangung des Doktorgrades
der Naturwissenschaften
(Dr. rer. nat.)

dem Fachbereich Physik
der Philipps-Universität Marburg
vorgelegt von

Carsten Agert

aus Ziegenhain

Marburg/Lahn 2001

Vom Fachbereich Physik der Philipps-Universität angenommen am 30.10.2001.

Erstgutachter: Dr. habil. W. Stolz

Zweitgutachter: Prof. Dr. W. Rühle

Tag der mündlichen Prüfung: 15.11.2001

Most of the experiments (including all crystal growth and the device fabrication) were performed at the Fraunhofer Institute for Solar Energy Systems in Freiburg, Germany.

The photoluminescence study was carried out in close co-operation with Dr. Peter Gladkov, Academy of Sciences, Prague, Czech Republic.

SPA- , AFM-, and most of the Hall-data were measured during an external research project with Dr. Nigel Mason, Clarendon Laboratory, University of Oxford, UK.

Contents

Zusammenfassung (deutsch)	7
1. Technologische Motivation	7
2. Wissenschaftliche Ergebnisse und Ausblick	8
1 Motivation and introduction	11
2 Fundamentals	13
2.1 III-V semiconductors	13
2.1.1 Introduction	13
2.1.2 Crystal growth	15
2.1.3 Materials and devices based on GaSb	16
2.2 Solar cells	17
2.2.1 The ideal device	17
2.2.2 The real device	20
2.2.3 The multijunction device	22
3 Experiment	26
3.1 Growth: Metalorganic Vapour Phase Epitaxy (MOVPE)	26
3.2 Characterisation	29
3.2.1 HR-XRD: Structural properties	29
3.2.2 Photoluminescence: Optical properties	29
3.2.3 Hall effect: Electrical properties	30
3.2.4 SPA: Surface properties	31
3.2.5 SIMS	32
4 Results - MOVPE of III-antimonides	33
4.1 Introduction	33
4.2 MOVPE of GaSb	34
4.2.1 Substrate preparation / Oxide desorption	34

4.2.2 Morphology of homoepitaxial GaSb	40
4.2.3 GaSb growth rate.....	41
4.2.4 Electrical properties: Undoped and Te-doped GaSb	42
4.2.5 Optical properties versus growth parameters	47
4.3 MOVPE of (AlGa)(AsSb)	50
4.3.1 Introduction	50
4.3.2 Influence of growth temperature	53
4.3.3 Aluminium incorporation.....	55
4.3.4 Arsenic incorporation	59
4.3.5 Parasitic pre-reactions: Influence of TMSb- and TBAs-partial pressure	61
4.3.6 Parasitic pre-reactions: DMEAA and TEGa	63
4.3.7 Carbon contamination	67
4.3.8 Oxygen contamination	69
4.3.9 p-type background doping	71
4.3.10 Tellurium as n-dopant	73
4.3.11 DMEAA at interfaces: Stabilisation and carry-over	74
4.4 Summary	77
5 Results - Silicon as novel acceptor dopant in GaSb.....	79
5.1 Incorporation behaviour	79
5.2 Carrier mobility / compensation	80
5.2.1 Introduction	80
5.2.2 Results	82
5.2.3 Summary	85
5.3 Optical properties	86
5.3.1 Introduction	86
5.3.2 Experiment.....	88
5.3.3 PL-results: Undoped GaSb	89
5.3.4 PL-results: Si-doped GaSb.....	90
5.3.5 Discussion of PL-results: Heavily doped GaSb	92
5.3.6 Discussion of PL-results: Lightly doped GaSb.....	95
5.3.6.1 Introduction	95
5.3.6.2 D-line	98
5.3.6.3 BE4-line.....	98
5.3.6.4 E- and A-lines	98
5.3.6.5 N-line	101
5.3.6.6 Comments on the limitations of the model	101
5.3.6.7 Summary	102

6	Results - Solar cells	103
6.1	Introduction	103
6.1.1	Band structure in real space	103
6.1.2	Fabrication technology	105
6.2	GaSb homojunction solar cells	107
6.2.1	Fundamental aspects of cell structure design	107
6.2.2	Emitter doping level	111
6.2.3	Base doping level	113
6.3	(AlGa)(AsSb) homojunction solar cells	114
6.4	Heterojunction solar cells	116
6.5	Tandem solar cells	121
6.6	Summary	125
7	Summary and outlook	126
	Abbreviations	128
	References	129
	Appendix: Substrates	137
	Substrate morphology	137
	Epi-layer morphology versus substrate miscut angle	139
	Publications	142
	Curriculum Vitae	144
	Acknowledgements	145

Zusammenfassung (deutsch)

1. Technologische Motivation

Der Begriff „Photovoltaik“ bezeichnet die direkte Umwandlung von Licht in Elektrizität. Die verbreitetste technologische Umsetzung ist der beleuchtete pn-Übergang in Halbleitermaterialien, die sogenannte Solarzelle. Entsprechende Bauelemente auf Basis von III-V Halbleitern können deutlich höhere Wirkungsgrade erreichen als die weitverbreiteten Silizium-Solarzellen, kommen aber wegen des höheren Materialpreises derzeit nur im Weltraum zur Anwendung. Dies könnte sich in Zukunft durch die Weiterentwicklung konzentrierender Systeme ändern, in denen eine kostengünstige Optik das Sonnenlicht auf eine vergleichsweise kleine Solarzelle fokussiert. Dadurch wird die benötigte Zellfläche pro elektrischer Leistung des Systems deutlich verringert. Der Schwerpunkt der Kosten des Systems wird von den teuren Solarzellen auf die kostengünstige Optik und die Nachführung der Sonnenbewegung verlagert. Im Rahmen dieses Ansatzes können hocheffiziente Solarzellen auf Basis von III-V Halbleitern wirtschaftlich betrachtet im Vorteil gegenüber Bauelementen aus Silizium sein.

Einer der Hauptverlustmechanismen bei der photovoltaischen Energieumwandlung ist die Thermalisierung angeregter Ladungsträger an die Bandkanten des Halbleiters. In sogenannten Kaskaden-Solarzellen können die entsprechenden Verluste verringert und deutlich erhöhte Wirkungsgrade erreicht werden: Hierbei werden hochenergetische Photonen in einem Halbleitermaterial mit großer Bandlücke absorbiert, während Licht mit Energien unterhalb der Bandlücke transmittiert wird. Diese niederenergetischen Photonen werden von einer Solarzelle auf Basis eines Halbleiters mit kleinerer Bandlücke genutzt, die hinter der ersten Solarzelle angeordnet ist. Das entsprechende System wird als „Tandemzelle“ bezeichnet. Hierbei können die beiden Zellen in einem einzigen Halbleiterkristall als seriell verschaltete Bauelemente aufeinander aufgewachsen werden („monolithische Tandemzelle“, Beispiel: (GaIn)P/GaAs) oder als getrennte Bauelemente ausgeführt sein („mechanisch gestapelte Tandemzelle“, Beispiel: GaAs/GaSb). Die Effizienz solcher Systeme kann weiter erhöht werden, indem man das Licht auf eine größere Anzahl aufeinander abgestimmter Bauelemente aufteilt. Ein sinnvoller Kompromiß zwischen zusätzlichem technologischem Aufwand und Wirkungsgrad-Gewinn ist für ein System gegeben, das auf vier verschiedenen Bandlücken basiert. Eine mögliche Umsetzung wäre eine monolithische (GaIn)P/GaAs-Tandemzelle, die mechanisch über eine zweite monolithische Tandemzelle gestapelt wird. Die optimale Bandlückenkombination für diese zweite Tandemzelle ergibt sich aus Simulationen zu 1 eV / 0.7 eV. Damit ist die gitterangepasste Materialkombination (AlGa)(AsSb)/GaSb auf GaSb-Substrat ein vielversprechender Kandidat für dieses Bauelement, dessen Realisierung jedoch noch aussteht.

Für die Produktion moderner Bauelement-Strukturen auf Basis von III-V Halbleitern (z. B. Solarzellen) wird der Einsatz industrierelevanter Multiwafer-MOVPE-Reaktoren (metalorganic vapour phase epitaxy) angestrebt, da sie eine großflächige Abscheidung der Materialien erlauben. Das Verfahren der MOVPE ist für die Abscheidung von (AlGa)(AsSb) und GaSb jedoch noch vergleichsweise wenig entwickelt. Insbesondere

wegen des geringen Dampfdruckes von Antimonspezies bei typischen Wachstumstemperaturen und der Instabilität von Stibin ist ein entsprechender Prozeß sehr viel komplexer als die analoge Abscheidung von Arseniden und Phosphiden. Beispielsweise wurde über eine erste mit MOVPE hergestellte, antimonbasierende Laser-Struktur nicht vor dem Jahr 1991 berichtet. In diesem Zusammenhang bedeuten die komplexen Wachstumsbedingungen beim Einsatz eines modernen Multiwafer-Reaktors eine besondere Schwierigkeit für die MOVPE der Antimonide. Die erfolgreiche Abscheidung einer monolithischen (AlGa)(AsSb)/GaSb-Tandemzellen-Struktur wird hierdurch zusätzlich erschwert.

Vor diesem technologischen Hintergrund sollten im Rahmen dieser Doktorarbeit zahlreiche Aspekte von sowohl grundlegender als auch angewandter Natur bearbeitet werden. Das Spektrum wissenschaftlicher Fragestellungen reicht hierbei von grundlegenden Fragen des Antimonid-Kristallwachstums über die elektronischen und optischen Eigenschaften von Dotierstoffen bis hin zu teils neuartigen Bauelement-Strukturen wie der oben erwähnten monolithischen (AlGa)(AsSb)/GaSb-Tandemzelle.

2. Wissenschaftliche Ergebnisse und Ausblick

Die vorliegende Doktorarbeit präsentiert Ergebnisse zu einem breitgefächerten Spektrum grundlegender und angewandter Aspekte des MOVPE-Wachstums antimonhaltiger Materialien und photovoltaischer Bauelement-Strukturen. Die entsprechenden Ergebnisse lassen sich in drei Bereiche gliedern: Zunächst wurden grundlegende Fragen des komplexen Kristallwachstums-Prozesses untersucht (Kapitel 4). Weiterhin wurden die elektronischen und optischen Eigenschaften des Silizium-Akzeptors in GaSb gemessen und analysiert (Kapitel 5). Auf Basis der somit erarbeiteten physikalischen und materialwissenschaftlichen Grundlagen konnten teils neuartige Bauelement-Strukturen abgeschieden und untersucht werden (Kapitel 6). Die Eigenschaften der entsprechenden Solarzellen wurden mit den Resultaten zu Materialeigenschaften und Kristallwachstum korreliert. Im folgenden wird ein Überblick über die erzielten Ergebnisse gegeben.

Es wurden zahlreiche für den Epitaxie-Prozeß wichtige Fragen hinsichtlich der GaSb-Wirtskristalle ("Substrate") untersucht. Da die Qualität kommerziell erhältlicher GaSb-Substrate infolge eines natürlichen Oxids und schlechter Polier-Techniken noch vergleichsweise mangelhaft ist, sind Verfahren der Oberflächen-Präparation innerhalb des MOVPE-Reaktors (sogenannte „in-situ Verfahren“) von großem Interesse. In diesem Zusammenhang wurde die Desorption natürlicher Oxide mittels der SPA-Technologie (Surface Photo Absorption) analysiert, wobei eine Aktivierungsenergie von 3 eV für den beobachteten Prozeß bestimmt werden konnte. Zudem konnte erstmalig die in-situ Ätzung von GaSb durch Tertiärbutylchlorid in einem MOVPE-Reaktor demonstriert werden. Auf naßchemisch präparierten Substraten wurde homoepitaktisches GaSb im Multiwafer-MOVPE-Reaktor abgeschieden und erfolgreich p- und n-dotiert. Das Material zeigte mit den besten Literaturdaten vergleichbare elektrische und optische Eigenschaften. Die größte Herausforderung im Bereich der MOVPE von Antimoniden stellt jedoch die Abscheidung aluminiumhaltigen Materials dar. Da die Standard-Aluminiumquelle Trimethylaluminium hierzu nicht geeignet ist, wurden zwei mögliche Alternativstoffe eingesetzt und miteinander verglichen: Tritertiärbutylaluminium (TTBAI)

und Dimethylethylaminalan (DMEAA). Während TTBAI eine sehr hohe Sauerstoff-Verunreinigung des Materials verursachte, konnte mit DMEAA erstmalig sowohl p- als auch n-leitendes (AlGa)(AsSb) in vergleichsweise guter Qualität in einem Multiwafer-Reaktor abgeschieden werden. Dieser Erfolg wird jedoch erkauft durch schwierige Epitaxie-Bedingungen beim Einsatz des hochreaktiven DMEAA. Verfrühte Zerlegung und heterogene Vorreaktionen manifestierten sich durch folgende Wachstumseigenschaften: ein nicht-lineares Einbauverhalten des Aluminiums, Abscheidung von Vorreaktionsprodukten im Einlaßbereich des Reaktors, eine starke Abhängigkeit des Aluminiumgehaltes von der Wachstumstemperatur und Trägergasgeschwindigkeit sowie ein unscharfes Schaltverhalten an Grenzflächen. Die beobachteten ungewöhnlichen Eigenschaften müssen bei der Planung von Epitaxie-Strukturen und Bauelementen unbedingt berücksichtigt werden. Die weiteren Arbeiten auf diesem Gebiet müssen sich auf zwei Bereiche konzentrieren: Einerseits muß die Reinheit der metallorganischen Aluminiumquellen seitens der Hersteller weiter verbessert werden. Außerdem ist eine noch weitergehende Untersuchung und Verbesserung des MOVPE-Wachstumsprozesses notwendig, um die Materialqualität noch zu erhöhen. Die Untersuchungen sollten zudem auf Zusammensetzungen ausgedehnt werden, die gitterangepaßt zu Indiumphosphid sind, da hier ein großes Potential für neuartige Heterostrukturen und diesbezügliche Anwendungen vorhanden ist.

Ein Schwerpunkt der materialwissenschaftlichen Untersuchungen war der Einsatz von Silizium als Akzeptordotant in GaSb. Der erfolgreiche Einsatz dieses Elementes als p-Dotant in der GaSb-MOVPE konnte erst von einer einzigen Gruppe berichtet werden [37] und bezüglich der physikalischen Eigenschaften des Akzeptors ist noch sehr wenig bekannt. Im Rahmen dieser Doktorarbeit wurde daher eine umfassende Untersuchung des Einbauverhaltens bei Einsatz von Silan als Quellensubstanz durchgeführt. Die elektrischen Eigenschaften und das Kompensationsverhältnis wurden über einen weiten Dotierbereich untersucht. Auf Grundlage der vielversprechenden Ergebnisse wurde eine genaue Photolumineszenz-Untersuchung Silizium-dotierten Galliumantimonids durchgeführt. Eine bislang kontroverse PL-Linie bei 800 meV konnte erklärt werden als ($e \text{ Si}_{\text{sb}}^0$)-Übergang, der aufgrund von Silizium-Verunreinigungen der metallorganischen Ausgangsstoffe auch in nominell undotiertem Material auftreten kann. Daher ist die Identifizierung des beobachteten Übergangs auch für die PL-Charakterisierung der Materialreinheit von GaSb wichtig. Für die Analyse war die Berücksichtigung der Potentialfluktuationen notwendig, die aus der inhomogenen Ladungsdichte-Verteilung in hochdotierten teilkompensierten Halbleitern folgen. Auf dieser Basis war es zudem möglich, alle PL-Linien im hochenergetischen Teil des Spektrums zu erklären. Die Aktivierungsenergie des Silizium-Akzeptors konnte zu $E_A = 8.8 \pm 0.4$ meV abgeschätzt werden. Die Dotierung mit Silizium resultierte im Vergleich zu nominell undotierten Schichten in verbesserten Mobilitäten, verringerten Kompensationsverhältnissen und deutlich höheren Photolumineszenz-Intensitäten. Zukünftige Untersuchungen zu den physikalischen Eigenschaften des Silizium-Akzeptors sollten sich auf den Einbaumechanismus konzentrieren: Die Natur des auf einem strukturellen Defekt basierenden natürlichen Akzeptors in GaSb legt nahe, daß eine extrinsische Dotierung mit einem Gruppe IV-Akzeptor die Bildung des natürlichen Akzeptors unterdrücken kann. Damit ergäbe sich eine Möglichkeit, durch Wasserstoff-Passivierung des Silizium-Akzeptors erstmals insgesamt sehr niedrig dotiertes GaSb herzustellen und zu untersuchen.

Auf dem Fundament der Grundlagenuntersuchungen zum MOVPE-Wachstum der Antimonide und zum Silizium-Akzeptor wurden anschließend photovoltaische

Bauelemente entwickelt. Eine grundlegende Zellstruktur wurde auf Basis der Materialdaten entworfen und abgeschieden. Eine gute Oberflächenpassivierung des Materials erwies sich als unerlässlich und konnte durch eine (AlGa)(AsSb)-"Fensterschicht" erreicht werden. Infolge der vielversprechenden grundlegenden Ergebnisse zum Silizium-Akzeptor wurde dieses Element auch in den Solarzellen-Strukturen als Dotierstoff eingesetzt. Die internen Quanteneffizienzen der Bauelemente, die zu teils sehr guten Werten von mehr als 90% über einen großen Spektralbereich abgeschätzt werden können, belegen die hohe Materialqualität Si-dotierten Galliumantimonids über weite Dotierbereiche. Auf der Grundlage der umfassenden materialwissenschaftlichen Untersuchungen zum Wachstum aluminiumhaltiger Kristalle konnte auch eine (AlGa)(AsSb)-Solarzelle ($E_{\text{gap}} \sim 0.9$ eV) realisiert werden. Diese Solarzelle ist das erste MOVPE-gewachsene Minoritäten-Bauelement mit (AlGa)(AsSb) im aktiven Bereich. Darauf aufbauend konnte auch erstmalig eine GaSb-basierende monolithische (AlGa)(AsSb)/GaSb-Tandemzelle mittels der MOVPE abgeschieden werden, die jedoch noch weiter verbessert werden muß. Hier sollte sich die zukünftige Arbeit in erster Linie auf die in der Struktur enthaltene Tunneldiode konzentrieren, für die der Typ IIB-Übergang zwischen InAs und GaSb von Interesse ist. Schließlich wurde eine neue Klasse GaSb-basierender Solarzellen abgeschieden und untersucht, die auf einem pn-Heteroübergang basieren. Bei erhöhter Leerlaufspannung lieferte eine p:GaSb/n:(AlGa)(AsSb)-Struktur die gleiche Quanteneffizienz wie eine analoge Solarzelle, die auf einem konventionellen homoepitaktischen pn-Übergang in GaSb beruht. Die verbesserte Spannung wird einem verringerten Sättigungsstrom zugeschrieben. Die weitere Entwicklung von Solarzellen mit 0.72 eV-Absorbermaterialien sollte sich daher auf diesen Strukturtyp konzentrieren, der auch in zukünftige Tandemzellen eingebaut werden kann.

Insgesamt konnten die auf den Gebieten des Kristallwachstums (Kapitel 4) und der Photolumineszenz-Charakterisierung von Si-dotiertem GaSb (Kapitel 5) gewonnenen grundlegenden wissenschaftlichen Erkenntnisse erfolgreich für die Entwicklung photovoltaischer Bauelemente (Kapitel 6) eingesetzt werden. Weitergehende Aspekte für anknüpfende Arbeiten auf sowohl grundlegenden als auch angewandten Gebieten wurden aufgezeigt.

1 Motivation and introduction

Photovoltaic cells based on III-V semiconductors can achieve much higher efficiencies than their silicon based counterparts. Due to the high costs of III-V substrates economically competitive terrestrial applications of III-V based solar cells include concentrating systems where the area of cell required for a given power output is notably reduced. Here, the costs of the whole system are displaced from the cells to the concentrating elements (including tracking systems) so that sophisticated III-V cells with maximised efficiencies can be employed.

One of the main loss mechanisms in solar cells is the thermalisation of hot photoexcited carriers to the band edges. Higher efficiencies can be achieved with multi-band gap systems. Here, high-energy photons are absorbed in a wide-band gap solar cell while low-energy photons are transmitted through the material. A second cell based on a lower-band gap material is placed behind the first one. This second cell converts the lower-energy photons into electricity. Such a photovoltaic system is called a "tandem cell". A corresponding device (the monolithic (GaIn)P/GaAs-tandem cell) is already in commercial use. The efficiency of such a system can be enhanced even more by further increasing the number of cells based on different band gaps. The efficiency gain per additional cell is reduced with every added device. A reasonable trade-off between efficiency and technological effort is given for a system based on four cells. A possible realisation could be a (GaIn)P/GaAs-tandem cell which is mechanically stacked on top of a second monolithic tandem cell. Modelling shows that the latter device should be based on the band gaps 1 eV and 0.7 eV. These values suggest the material combination (AlGa)(AsSb)/GaSb as promising candidate. However, a monolithic (AlGa)(AsSb)/GaSb-tandem cell still remains to be shown.

The production of sophisticated large area III-V devices (e. g. photovoltaic cells) makes the employment of industrial size multiwafer MOVPE (metalorganic vapour phase epitaxy) reactors desirable. However, the MOVPE growth of antimonides is a rather recent field. Due to the low volatility of elemental antimony and the instability of stibine, the growth of Sb-containing III-V semiconductors is notably different and much less studied compared to arsenides and phosphides. As a result, a GaSb-based MOVPE-grown laser structure was not reported until 1991. In addition, the complex growth processes in industrial size multiwafer MOVPE reactors represent an additional challenge for the deposition of high-quality Sb-containing III-V compounds and device structures.

Based on the above considerations, this thesis covers a wide range of both fundamental and applied aspects. These include the complex MOVPE growth of various III-antimonides as well as the electronic and optical properties of silicon-doped GaSb. The corresponding results made the development of novel photovoltaic device structures possible (e. g. monolithic (AlGa)(AsSb)/GaSb-tandem cells). The properties of the related solar cells are analysed with regard to the results on growth and material properties.

Chapter 2 gives a brief summary of fundamental aspects of III-V semiconductors, related crystal growth techniques and the peculiarities of the antimonide material system. Moreover, the basic device properties of solar cells are described. A simplified model for pn-junctions with an incident light spectrum is derived. Subsequently, the key properties

of real photovoltaic devices are introduced and characteristic I/V-curve parameters are presented. Eventually, multijunction devices are described and the results of a related band gap versus efficiency modelling are demonstrated.

Chapter 3 presents the main experimental techniques that have been used for this thesis. It starts with a section on the fundamentals of MOVPE. The employed reactor is described and a first overview is given concerning the peculiarities of the MOVPE of antimonides. Subsequently, the main characterisation methods are introduced: High-resolution X-ray diffraction (HR-XRD), photoluminescence (PL), Hall effect, surface photo absorption (SPA), and secondary ion mass spectroscopy (SIMS).

Chapters 4 to 6 are dedicated to the results of this thesis. While chapter 4 deals with the actual crystal growth, chapter 5 describes the results concerning silicon as novel acceptor dopant in the MOVPE of antimonides, and chapter 6 focuses on photovoltaic devices.

Chapter 4 begins with a general introduction related to the MOVPE of antimonides. In section 4.2 current points at issue concerning the MOVPE of Al-free antimonides are discussed, such as substrate preparation and substrate orientation. The electrical and optical data of the related material are shown to be well in line with the best values in the literature. Section 4.3 deals with the MOVPE of aluminium containing materials. As this field is still one of the most demanding challenges for MOVPE growth nowadays, a comprehensive introduction is given first. Subsequently, the successful growth of high-quality p- and n-type (AlGa)(AsSb) in a multiwafer MOVPE reactor is reported for the first time. Two promising novel Al-precursors (tertiarybutylaluminium and dimethyl-ethylamine alane adduct) are compared to each other. Various aspects of the growth process and the related properties of the crystals are discussed in detail. Finally, a summary of the growth of antimonides in an industrial scale multiwafer planetary MOVPE reactor is given.

Chapter 5 deals with silicon as novel acceptor dopant in the MOVPE of GaSb. The chapter presents the incorporation behaviour and the electrical properties. The compensation ratio is determined for various doping levels. The PL properties of non-intentionally doped and silicon doped GaSb are studied. All PL peaks in the high-energy part of the spectrum can be explained within the concept of potential fluctuations due to the charged impurity distribution. The observed properties make the silicon acceptor an interesting novel candidate for GaSb-based device applications.

Chapter 6 presents device related results. The fabrication technology is described in detail. Several device structures are presented, namely pn-homojunctions for both GaSb and (AlGa)(AsSb), pn-heterojunctions and tandem cells. The importance of surface passivation by high band gap window layers is demonstrated. The silicon acceptor proves to be beneficial for the device performance.

Chapter 7 gives an overall summary and a related outlook. In addition, a collection of AFM pictures is given in the annex concerning substrates and epilayer morphologies.

Parts of this work have already been published elsewhere. Corresponding references are given in the publication list at the end of this work.

2 Fundamentals

2.1 III-V semiconductors

2.1.1 Introduction

III-V semiconductors are crystalline materials with the ZnS-structure (figure 2.1). This structure consists of two inter-penetrating face centred cubic (sub-)lattices which are displaced from each other by a translation along $(\frac{1}{4}, \frac{1}{4}, \frac{1}{4})$.

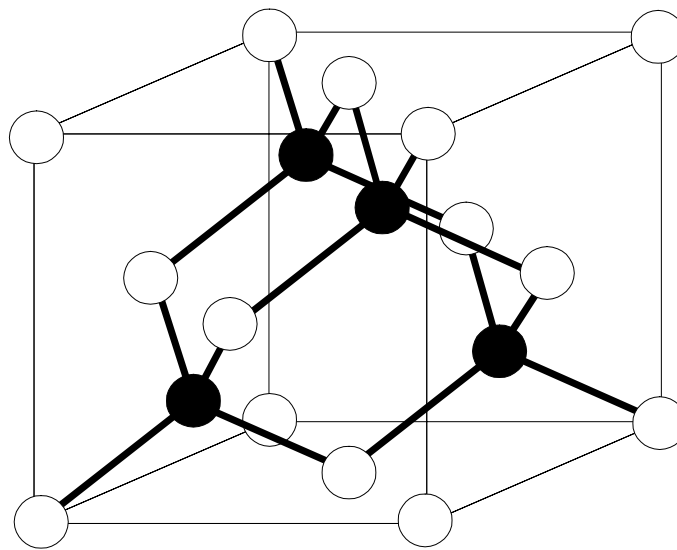


Figure 2.1: ZnS-crystal structure. Two inter-penetrating fcc lattices are displaced from each other by a translation along $(\frac{1}{4}, \frac{1}{4}, \frac{1}{4})$. One lattice consists of group III-, the other of group V-elements.

One lattice consists of group III-, the other of group V-elements. In contrast to their elemental group IV-counterparts, these so-called “compound semiconductors” have partly ionic bonds due to transfer of electronic charge from the group III atom to the group V atom. They can be binary crystals (such as galliumarsenide) or mixtures on the respective sublattices (such as gallium-indium-phosphide-arsenide). As they will always consist of 50% group III- and 50% group V-atoms, the usual notation gives only the composition with regard to the respective sublattice (e.g. $(\text{Al}_{0.6}\text{Ga}_{0.4})\text{As}$). The band structure of III-V semiconductors can be “engineered” by changing the composition of the crystal. For example, adding aluminium to GaSb leads to an increase of the direct band gap, while a transition to an indirect band gap occurs at around $(\text{Al}_{0.2}\text{Ga}_{0.8})\text{Sb}$. The band gaps of binary III-V semiconductors and their ternary mixtures are shown as a function of the composition in figure 2.2. While the lattice constant is a linear function of the composition (“Vegard’s law”), this does not hold for the band gap energy.

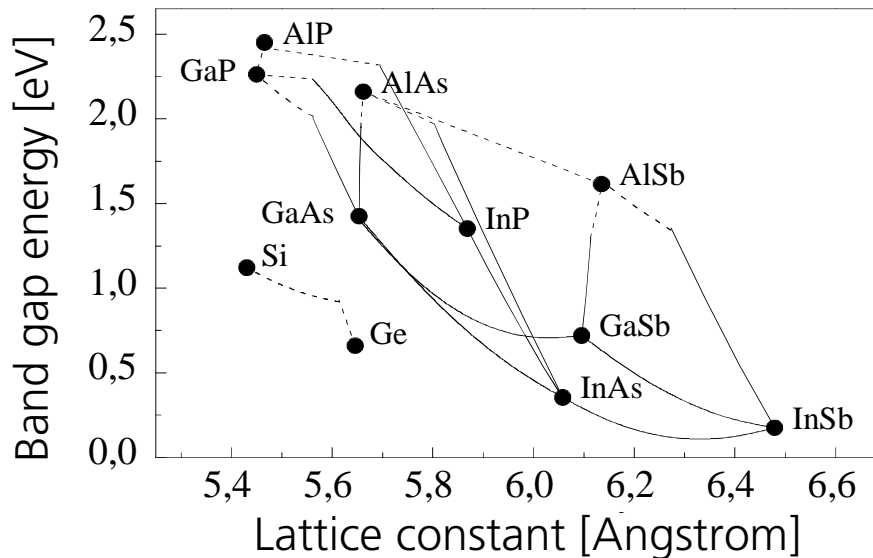


Figure 2.2: Band gaps of binary III-V semiconductors and their ternary mixtures as a function of the composition. Direct materials are represented by solid, indirect materials by dotted lines.

Most devices based on III-V semiconductors consist of epitaxial structures grown on binary substrate crystals (see as well section 2.1.2). The most common substrate materials are GaAs and InP. For some applications more exotic substrates are used such as Ge, GaP, GaSb, InAs or InSb. As lattice-matched growth is important in order to avoid structural defects, only crystal compositions with identical lattice-constants are usually grown onto each other. While ternary crystals are limited to one particular lattice-matched composition (e. g. $(\text{Ga}_{0.47}\text{In}_{0.53})\text{As}/\text{InP}$), quaternary mixtures provide an extra degree of freedom (e. g. $(\text{GaIn})(\text{PAs})/\text{InP}$). Here, a whole range of different band gaps can be realised for a fixed lattice constant. An exception is the material system AlAs/GaAs where the lattice constants are so similar to each other that all ternary compositions of $(\text{AlGa})\text{As}$ can be grown on GaAs as substrate material.

Modern device structures consist of many different lattice-matched materials grown onto each other. Their particular properties can vary in many respects, e. g. band gap and doping. In addition, intentional strain can be used to alter the band structure in the valence band, the band alignment for heterostructures can vary considerably and very thin films can be grown that even show quantum effects. These features form the basis of all modern opto-electronic devices. For further information, there are various excellent textbooks on this subject such as [54, 92, 126].

With respect to the opto-electronic device “solar cell”, the major difference between elemental group IV-semiconductors (e. g. silicon) and III-V semiconductors is that the first are indirect while the latter are often direct materials. Hence, the absorption depth for light is notably different. III-V devices have the extra advantage that complex high-efficiency multijunction structures can be realised (see section 2.2.3). On the other hand silicon has a much lower price and better availability. The present thesis will focus on Sb-containing III-V semiconductors for solar cell applications.

2.1.2 Crystal growth

The crystal growth of III-V compound semiconductors can be categorised into “bulk crystal growth”- and “epitaxial crystal growth”-techniques. Very good summaries on this subject can be found in [92] and [126]. A corresponding overview will be given in the following:

The aim of the bulk growth is to produce large ingots which can then be sliced and processed into substrates. The two main bulk growth techniques are the “Czochralski method” and the “Bridgman method”. The Czochralski method involves melting the raw material in a crucible and then placing a seed crystal in contact with the melt. While the seed is slowly rotated, the melt surface cools and additional material is solidified from the melt onto the seed. As arsenic and phosphorus have very high vapour pressures at the melting temperatures of the compounds, they tend to leave the melt and condense on the sidewalls. Therefore the Czochralski method is usually modified for III-V growth by isolating the melt from the air by a layer of molten boron oxide. This material floats on the surface and prevents the volatile elements from escaping. This modification of the Czochralski method is called “LEC method” (Liquid-Encapsulated Czochralski method). In the Bridgman method a temperature gradient is created along the length of a stationary boat which contains the molten material. The temperature around the seed crystal is held below the melting point to form the crystal. All these bulk crystal growth techniques are reasonably matured for GaAs and InP while it is still difficult to obtain high-quality material for most other compound semiconductors. Here, especially the surface treatment for subsequent epitaxial processes is problematic. Recent efforts also include the growth of ternary materials for substrate purposes [101].

In epitaxial techniques, an epitaxial layer (or “epilayer”) is subsequently grown onto the substrate. The word “epitaxy” comes from the Greek words “epi” (= upon) and “taxis” (= ordered) and describes the ordered continuation of the underlying substrate crystal structure. The main epitaxial techniques are “Liquid Phase Epitaxy (LPE)”, “Molecular Beam Epitaxy (MBE)” and “Vapour Phase Epitaxy (VPE)”. In LPE, usually a group III metal is used as solvent for the group V element. When a substrate is brought into contact with the liquid phase and the solvent gets supersaturated with the group V element by cooling, the nucleation of the crystal starts on the substrate surface. Consequently, this is a technique close to equilibrium where it is difficult to grow heterostructures with abrupt interfaces. As it is quite inexpensive, many relatively uncomplicated devices such as (AlGa)As double heterostructure lasers and LEDs are still grown with LPE. In MBE, crucibles containing elemental charges are heated in an ultra high vacuum environment (UHV, $\sim 10^{-11}$ torr). This creates a molecular or atomic beam of the elements from the crucibles to the heated substrate surface where epitaxial growth takes place. Since the molecules can travel for meters without collision and no chemical reactions occur, this method is conceptually simple and very powerful with regard to heterostructure physics. However, there are still problems with certain materials (e. g. phosphides and nitrides). In VPE techniques the pressures are much higher. Here, gases that contain the necessary chemical elements are delivered from a gaseous environment and made to react chemically in the vicinity of the substrate. A typical example for this technique is the growth of silicon according to $SiH_4 \rightarrow Si + 2H_2$. While this technique is mainly used for homoepitaxial growth of high purity materials, a related but much more sophisticated method is used for III-V heterostructures: the “Metalorganic Vapour Phase Epitaxy

(MOVPE)". Here, the VPE-process is based on gaseous metalorganic compounds. As this technique was employed for the growth of III-antimonides in the present thesis, a detailed description will be given in section 3.1.

2.1.3 Materials and devices based on GaSb

III-antimonides have larger lattice constants and smaller band gaps than their arsenic- and phosphorus-based counterparts (figure 2.2). Apart from these obvious differences they also have many more interesting peculiarities. For example, the L-valley in the conduction band of GaSb is only approximately 0.07 eV above the Γ -valley [83], not-intentionally doped GaSb is always highly p-type due to a native structural defect, AlSb is *not* lattice-matched to GaSb in contrast to the GaAs/AlAs-system, mixtures on the group-V sublattice have large miscibility gaps, and Auger recombination is significant. Compared to arsenides and phosphides, growth and device processing technology is in its infancy. At present, the only antimonide-based devices in large-scale commercial use are Hall- and magnetoresistive sensors based on InSb [119, 121] with its extraordinarily high electron mobility.

The growth of antimonides is difficult due to the low vapour pressure of antimony species. This is illustrated by the following considerations: If the arsenic pressure during the growth of GaAs gets very high, a second condensed phase ($GaAs(s) + As(s)$) can in theory be formed ([96], fig. 3.11). The corresponding arsenic pressure for the formation of the second phase is approximately equal to the arsenic pressure over pure elemental arsenic and clearly exceeds 1 bar at typical growth temperatures. Due to this high value the $GaAs(s) + As(s)$ -phase will never occur in typical conditions of epitaxial growth techniques. In contrast, for GaSb the corresponding pressure of the less volatile antimony over pure elemental antimony will be below 0.1 mbar ([33], fig. 1) and a $GaSb(s) + Sb(s)$ -phase may well be experimentally observed. The range of suitable growth parameters for stoichiometric growth of antimonides is therefore rather narrow.

Despite the above difficulties the antimonides are subject to renewed interest due to their many potential applications in novel devices. These include low-band gap photovoltaic cells as well as infrared emitters and detectors (see section 4.3.1). While a wide variety of direct and indirect materials can be grown on GaSb and InAs as substrates, the most promising suggestions with respect to commercial application are based on InP. As both Ga(AsSb) and Al(AsSb) can be grown lattice-matched to InP, the large difference between their refractive indices (~ 0.7 for GaSb/AlSb, ref. 8 & 9 in [62]) can be used for the growth of high reflectivity Bragg mirrors with a reduced number of periods compared to the (GaIn)(PAs)-system. Moreover, (AsSb)-compounds have been suggested for very fast transistors. However, the corresponding As/Sb-ratios are in the centre of related miscibility gaps for the materials. Consequently, they can only be grown with epitaxial techniques that work far from thermodynamical equilibrium (e. g. MBE, MOVPE). Even here, phase separation effects must be expected and the range of suitable growth parameters is narrow (e. g. [82]).

For further reading very good review articles exist in the literature, such as [35] on the physics of GaSb, [73] on device related properties of GaSb, and [1] on the MOVPE-growth of antimonides.

2.2 Solar cells

2.2.1 The ideal device

A photovoltaic cell is basically a large area pn-junction. In order to understand the internal operation of such a device, the spatial distribution of the important electrical quantities must be described by a set of five equations [46]:

- Poisson's equation, one of Maxwell's equations, is the differentiated form of Gauss's law and relates the divergence of the electric field to the space charge density.
- Two current density equations, one for electrons and one for holes, describe the total current density related to electric fields (i.e. drift currents) and concentration gradients (i. e. diffusion currents). Under certain conditions ([54], p. 359) mobilities and diffusion constants are related through the Einstein relationships.
- The two continuity equations are "bookkeeping" equations that consider the generation and recombination of electrons and holes.

These expressions form a coupled set of nonlinear differential equations. It is not possible to find a related general analytical solution. However, reasonable approximations can give valuable solutions. In this context, a widely used model to describe pn-junctions is the Schottky model which will be described in the following.

When a p-type semiconductor is in direct contact with a corresponding n-type material, the constant Fermi-level throughout the whole structure in thermodynamic equilibrium means that there must be a potential change in the transition region near the junction. Poisson's equation says that this potential change is related to a space charge. This space charge arises from a diffusion of majority carriers into their minority regions. There, they recombine with the other carrier type and the resulting concentrations of mobile carriers are negligible: the region around the junction becomes a so-called "depletion region". The main contribution to the space charge density comes from the ionized dopants. The electric field associated with the space charge counteracts the diffusion and a stable situation arises. The potential change is usually called "diffusion voltage V_D " and is determined directly through the position of the Fermi level in the quasi-neutral regions far from the junction.

The usual approximation to describe a pn-junction is the so-called "depletion approximation" or "Schottky model", where

- a constant space charge is assumed within the depletion region,
- the corresponding space charge is given by the density of ionized impurities, and
- the transition between the depletion region and the quasi-neutral regions is abrupt.

The electric field and the potential distribution across the junction can now be calculated [40]. Important results are the magnitude of the built-in potential V_D and the width of the depletion region W_D :

$$e \cdot V_D = kT \cdot \ln \left(\frac{N_A N_D}{n_i^2} \right) \quad W_D = \left(\frac{2\epsilon\epsilon_0}{e} \cdot \frac{N_A + N_D}{N_A \cdot N_D} \cdot V_D \right)^{1/2}$$

It is now important to derive the I/V -curve of the biased junction. A qualitative overview can provide a first insight: At all times, there will be a thermal generation of minority

carriers. If these diffuse to the junction they will be swept into the other region by the electric field. This is the so-called “generation current” or “drift current”. In thermal equilibrium, this current will be compensated by a “recombination current” (or “diffusion current”) of high-energetic majority carriers that can overcome the potential barrier and recombine as minority carriers with majority carriers in the other region. While the generation current will not be influenced by an applied external voltage ([92] p. 299), the recombination current depends strongly on the magnitude of the potential barrier and will be an exponential function of the applied voltage.

An applied voltage is defined as positive when the positive contact of the source is connected to the p-region of the diode. Such a positive voltage (“forward bias”) will lower the potential barrier and allow a corresponding increase of the recombination current. The related carriers will recombine with majority carriers in the other region. The minority currents have their maximum values at the edges of the depletion region but can spread widely into the quasi-neutral regions; this is an important design issue for example for LEDs (see p. 447 and fig. 6.5 in [92]). If a negative voltage is applied (“reverse bias”) the potential barrier increases and eventually the total current will be determined by the generation current. As the generation current is the maximum possible current in reverse bias, it is frequently as well denoted as saturation current.

The above qualitative description can be expressed mathematically by the Shockley equation. Here, an ideal situation is described which neglects generation and recombination effects in the depletion region. In photovoltaics, the Shockley equation is often referred to as the one-diode-model:

$$I_d(V) = I_0 \cdot \left[\exp\left(\frac{e \cdot V}{kT}\right) - 1 \right]$$

The index “d” stands for “dark” because no photogenerated current has been considered up to this point. The constant I_0 is the saturation (<=> generation <=> drift) current mentioned above which is often as well termed “dark” current. Naturally, both carrier types have to be considered for a complete analysis ([54], p. 362):

$$I_0 = (I_n^{gen} + I_p^{gen})$$

The minority carrier concentrations at the edges of the depletion region and the resulting minority carrier diffusion currents can be calculated. As diffusion (<=> recombination) currents determine all current flow associated with an applied external voltage, the I/V -curve of the pn-junction can as well be expressed in terms of the diffusion currents. A comparison of the resulting expression with the above equation gives the saturation (<=> generation <=> drift) current in terms of material parameters ([54], p. 366)¹

$$I_0 = (I_n^{gen} + I_p^{gen}) = A \cdot e \cdot n_i^2 \left(\frac{D_e}{N_A L_e} + \frac{D_h}{N_D L_h} \right)$$

¹ Note that $n_i^2 = N_A \cdot n_p = N_D \cdot p_n$, $(D/\tau)^{1/2} = D/L = L/\tau$, $D = kT \cdot \mu/q$.

where A is cross-sectional area of the diode, D_e and D_h are the diffusion coefficients of the minority carriers, L_e and L_h are the diffusion lengths of the minority carriers, N_A and N_D are the acceptor and donor concentrations, and n_i is the intrinsic carrier concentration. The factor n_i^2 means that the saturation current will increase exponentially with decreasing band gap energy of the material.

Without proof, the I/V -curve of a pn-diode when *illuminated* can be written as:

$$I(V) = I_0 \cdot \left[\exp\left(\frac{e \cdot V}{kT}\right) - 1 \right] - I_L$$

Here, I_0 is again the above saturation current. The photogenerated current I_L is given by

$$I_L = e \cdot A \cdot G \cdot (L_e + L_h + W_D)$$

where G is the rate of generation of electron-hole pairs by light and W_D is the width of the depletion region ([46], equ. 4.44). The equation shows that basically all the carriers generated by light in the depletion region and within a minority carrier diffusion length on either side contribute to the photocurrent. Note that the photocurrent is in the direction of a reverse current. As the photocurrent is linearly superimposed on the usual forward current in the I/V -curve, the illuminated diode has a forward current when an external voltage bigger than the open-circuit voltage V_{oc} (definition of V_{oc} : see section 2.2.2 below) is applied. For voltages *below* V_{oc} the cell acts as a current source in the reverse direction.

When the I/V -curve of a device is known, the maximum power of the cell and the efficiency $\eta = \frac{P_{\max}}{P_{\text{light}}}$ can be calculated. A theoretical maximum for η can be derived with

the following assumptions:

- All incident photons with energies above the band gap are absorbed and contribute to the photocurrent I_L .
- An infinite number of photovoltaic converters with all possible band gaps is assumed to be in thermodynamic equilibrium with the sun. The necessary luminescence of a corresponding converter can be translated into a saturation current I_0 . Details can be found in [25, 28]. For a single pn-junction a thermodynamic "radiative" saturation current minimum is obtained:

$$I_0 = e_0 \frac{2\pi}{h^3 c^2} \cdot (kT \cdot E_g^2 - 2k^2 T^2 - 2k^2 T^2 E_g + 2k^3 T^3) \cdot \exp\left(-\frac{E_g}{kT}\right)$$

With these assumptions all the parameters are known for the calculation of an idealised I/V -curve. For a given incident spectrum the efficiency can therefore be calculated as a function of the band gap of the underlying material. For example, the idealised efficiency of a GaAs solar cell in direct sunlight (AM 1.5d) at a concentration ratio of 100 and a cell temperature of 300K is 34.4% [25]. This value emphasises that even in the idealised case the photovoltaic conversion efficiency is far from 100%. The main loss mechanisms depend directly on the band gap: Photons with energies far above the

band gap create hot carriers whose excess energy is lost in thermalisation to near the band edge. Photons with energies below the band gap are not absorbed and lost for the conversion process. These two effects alone lead to a reduction of the efficiency in the order of 50% ([38], p. 242). The third unavoidable loss mechanism is the thermalisation of carriers over the potential barrier: A diode can never give a voltage output corresponding to the band gap energy, and $e \cdot V < E_g$ will always apply ([38], p. 243).

2.2.2 The real device

In section 2.2.1 an ideal pn-junction was described. For a more realistic model additional points have to be considered. The thermodynamic saturation current minimum must be considered unrealistic as the value based on the Shockley model is generally much higher. Besides, surface recombination can influence the saturation current. If a surface is closer to the depletion region than approximately one minority carrier diffusion length, the surface recombination velocity S must be compared to the ratio D/L in order to determine whether the proximity of the surface will lead to an increase or a decrease of the saturation current I_0 ([38], fig. 5.6):

- If $S \gg D/L$, the minority carrier current flow into the surface will be the dominating effect, transport is controlled by the minority mobility of the layer and I_0 will be much higher than in the infinite layer case.
- If $S \approx D/L$ (within approximately two orders of magnitude), the minority carrier current flow into the surface will be a dominating effect. I_0 will be higher than in the infinite layer case for $S > D/L$ and lower for $S < D/L$.
- If $S \ll D/L$, the minority carrier current flow into the surface will be no dominating effect, very few carriers will be lost at such an excellent surface, transport is no longer controlled by S but by the lifetime of the layer, and I_0 will be much lower than in the infinite layer case.

However, the effect of surface recombination is not only limited to the changes in the "dark" saturation current. Naturally, a high recombination velocity surface will also lead to a loss of photoexcited minority carriers which have been created within a diffusion length from the surface.

Both generation/recombination in the depletion region and Ohmic resistances must as well be considered. These effects are included in the so-called two-diode-model which is beyond the scope of this introduction. Similarly, losses associated with reflection of the material and the metal grid are not discussed.

Examples for measured I/V -curves of a real device under different levels of illumination are shown in figure 2.3. These I/V -curves are usually described by a set of typical parameters which will be presented in the following:

The short-circuit current I_{sc} is defined for $V = 0$ V. At this point the I/V -curve gives

$$I_{sc} = I(0) = -I_L$$

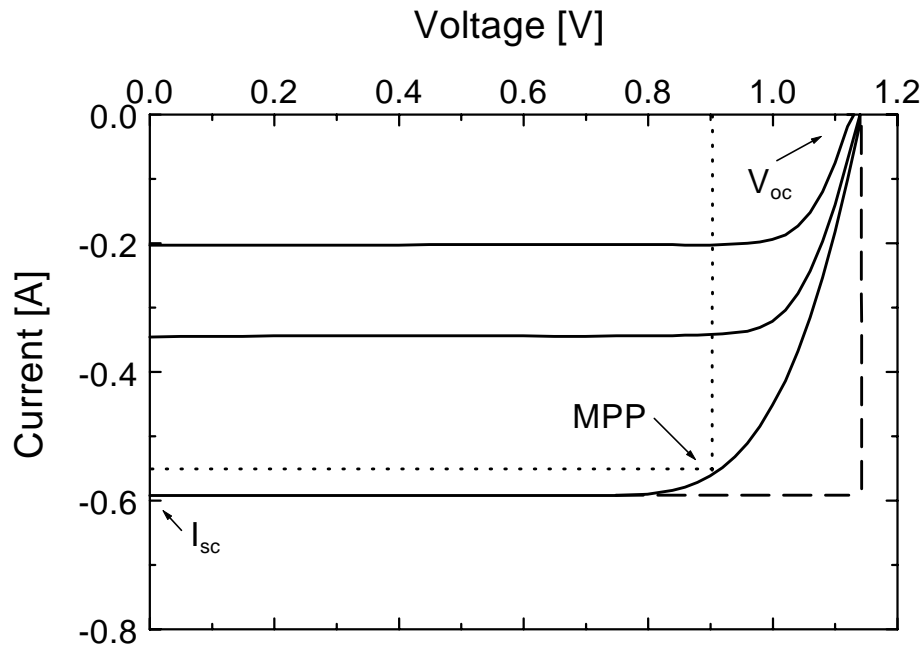


Figure 2.3: *I/V*-curves of an LPE-grown concentrator GaAs-solar cell (diameter: 4mm) under different levels of illumination. Typical parameters for the characterisation of *I/V*-curves are presented: Open circuit voltage V_{oc} , short-circuit current I_{sc} , and maximum power point MPP.

As I_L is proportional to the generation rate G , the short-circuit current of the device is proportional to the intensity of the light. The open-circuit voltage V_{oc} is defined for $I(0)$. At this point the *I/V*-curve gives

$$V_{oc} = \frac{kT}{e} \ln \left(\left| \frac{I_{sc}}{I_0} \right| + 1 \right)$$

The equation shows that V_{oc} increases logarithmically with I_L , i. e. with the intensity of the light. On the other hand, V_{oc} decreases with increasing saturation current I_0 . As I_0 is proportional to n_i^2 (see page 17), V_{oc} is directly related to the band gap of the material.

The device gives the maximum power at the point marked as MPP ("maximum power point") in figure 2.3. By defining the so-called fill-factor FF as the ratio

$$FF := \frac{I_{MPP} \cdot V_{MPP}}{I_{sc} \cdot V_{oc}} = \frac{\text{Area defined by dotted rectangle in fig. 2.3}}{\text{Area defined by dashed rectangle in fig. 2.3}}$$

the efficiency of a cell can be described in terms of V_{oc} and I_{sc} as:

$$\eta = \frac{P_{max}}{P_{light}} = \frac{I_{sc} \cdot V_{oc} \cdot FF}{P_{light}}$$

This expression shows the dependence of the efficiency on the band gap very clearly: On the one hand a higher band gap will reduce both n_i and I_0 so that V_{oc} will be subject to a

corresponding increase. At the same time I_{sc} will decrease due to the reduced absorption in wide-band gap materials. The optimum band gap for a given incident spectrum can be obtained from simulation (e. g. [68]).

Similarly the effect of concentration of the incident light can be seen: While I_{sc} and P_{light} will increase proportional to each other without changing the overall efficiency, V_{oc} will also grow with $\ln(I_{sc})$ and give an increase of the efficiency under concentrated light.

The evaluation of the devices developed in chapter 6 will basically focus on V_{oc} and I_{sc} . Instead of the mere value for I_{sc} , the external spectral quantum efficiency will be given there. This quantity is defined by

$$EQE(\lambda) := (1 - R(\lambda)) \cdot \frac{|I_L(\lambda)|}{e \cdot \Gamma(\lambda)}$$

where R is the reflection, Γ is the photon flux, and I_L is the photogenerated current. The EQE is determined by measuring the short-circuit current using monochromatic light with known photon flux. The EQE is mainly useful in two respects:

- As different wavelengths are absorbed in different parts of the device, the spectral information of the EQE gives guidelines for further optimisation of a device structure.
- When the EQE is known in absolute terms, the total light generated current can be calculated for any desired incident spectrum $d\Gamma(\lambda)/d\lambda$ (e.g. [14], equ. 4.26 in [38]):

$$|I_L| = |I_{sc}| = e \cdot \int_0^{\infty} EQE(\lambda) \cdot \frac{d\Gamma(\lambda)}{d\lambda} d\lambda$$

2.2.3 The multijunction device

At the end of section 2.2.1 the two main loss mechanisms for the photovoltaic energy conversion were identified: Firstly, photons with energies far above the band gap create hot carriers whose excess energy is lost in thermalisation. Secondly, photons with energies below the band gap are not absorbed and lost for the conversion process. Selecting the optimum band gap for the material of a single-junction solar cell can be regarded as a trade-off between these two loss mechanisms.

Higher efficiencies can be achieved with multi-band gap systems. High-energy photons are absorbed in a wide-band gap solar cell, while low-energy photons are transmitted through the material. A second cell based on a lower-band gap material is then placed behind the first one. This second cell can now convert the lower-energy photons into electricity. Such a photovoltaic system is called a "tandem cell". The two cells can either be realised separate from each other and connected independently (four terminal approach) or grown monolithically on top of each other (two terminal approach). The latter approach is difficult with respect to three points:

- The Ohmic connection between the two cells must be realised with a tunnel diode. The deposition of such a structure is difficult because very high doping levels and sharp interfaces must be achieved.
- The two terminal approach means that the same current flows in both cells. For optimum efficiencies, this current must be equal to the current in the maximum power point of *both* cells. Otherwise the cell with the lower current will limit the

performance of the other cell. Usually the employed band gaps in combination with a given spectrum do not automatically fulfil this condition. A partial transparency of the top cell achieved by thinning the absorber layers can often be employed as a solution to this problem.

- Different band gap materials have to be realised that are lattice-matched to each other. The choice of suitable material combinations is very limited.

The efficiency of such a system can be enhanced even more by further increasing the number of cells based on different band gaps. The efficiency gain per additional cell is reduced with every added device (fig. 6.4 in [71]). A reasonable trade-off between efficiency and technological effort is given for a system with four cells. As a successful monolithic four-junction device has not been shown up to now, a mechanical stack of two monolithic tandem cells is a promising alternative approach. Here, the technologically mature monolithic (GaIn)P/GaAs tandem cell could serve as a first tandem cell for the *high*-energy photons. This device will be mechanically stacked on top of a second monolithic tandem cell which absorbs *low*-energy photons. The optimum band gap combination of the second monolithic tandem cell has to be calculated by simulation. In order to design a corresponding simulation software, the following assumptions were made:

- A solar spectrum below a GaAs-wafer is used as incident spectrum.
- The top cell is completely transparent for photons with energies below the band gap.
- The EQE is 100% for all photons above the band gap in both cells.
- Current-matching is achieved by a partially transparent top cell where applicable.
- The saturation current is assumed to be the thermodynamic "radiative" minimum given in section 2.2.1.

The Shockley equation can now be applied in order to develop a model for an "ideal" tandem cell:

$$I_{\text{top cell}}(V) = I_{0, \text{top cell}} \cdot \left[\exp\left(\frac{e \cdot V_{\text{top cell}}}{kT}\right) - 1 \right] - I_{L, \text{top cell}}$$

$$I_{\text{bottom cell}}(V) = I_{0, \text{bottom cell}} \cdot \left[\exp\left(\frac{e \cdot V_{\text{bottom cell}}}{kT}\right) - 1 \right] - I_{L, \text{bottom cell}}$$

$$V_{\text{tandem cell}} = V_{\text{top cell}} + V_{\text{bottom cell}}$$

$$I(V)_{\text{tandem cell}} = I(V)_{\text{top cell}} = I(V)_{\text{bottom cell}}$$

As $eV \gg kT$, the „-1“ can be neglected and the resulting I/V -curve is given by:

$$V_{\text{tandem cell}} = \frac{kT}{e} \left[\ln\left(\frac{I_{\text{top cell}}(V) + I_{L, \text{top cell}}}{I_{0, \text{top cell}}}\right) + \left(\frac{I_{\text{bottom cell}}(V) + I_{L, \text{bottom cell}}}{I_{0, \text{bottom cell}}}\right) \right]$$

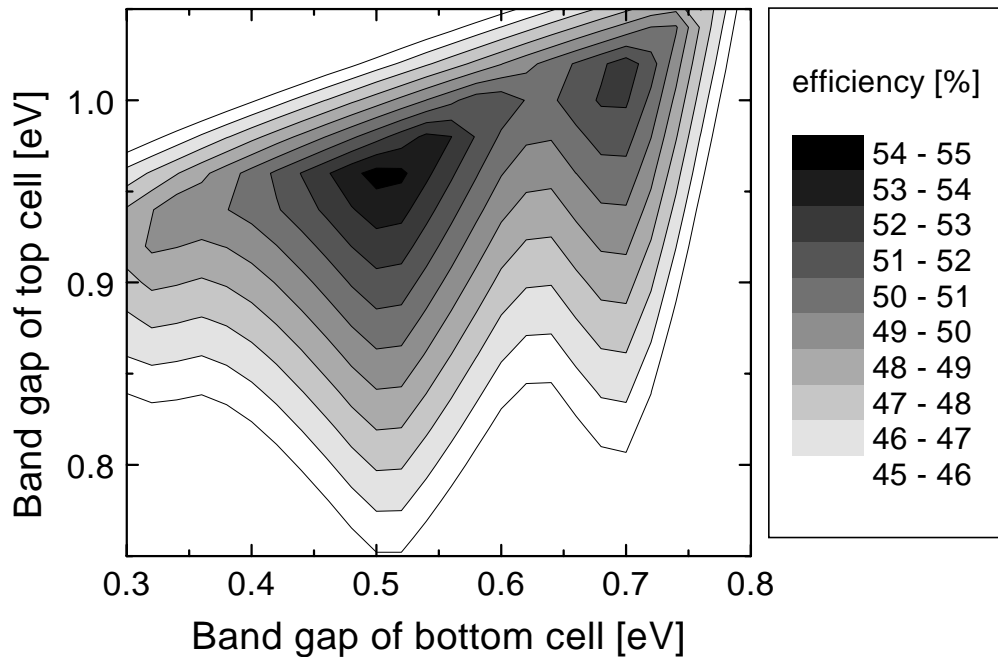


Figure 2.4: *Ideal efficiency of a monolithic tandem cell as function of the underlying band gaps (cell temperature: 333K). The incident spectrum is 500 times AM1.5d (1000 W/m²) under a GaAs-wafer (temperature: 333K). The resulting incident power is 500 times 389 W/m². Two areas with optimised efficiencies can be clearly identified. [Software and calculations: G. Létay, Fraunhofer ISE]*

The I/V-curve can now be calculated for various band gap combinations. The resulting power at the MPP can be translated into an efficiency. This information can be summarised in a matrix of efficiencies as a function of the band gaps (figure 2.4).

Two areas with optimised efficiencies can be identified in the figure. The corresponding band gap combinations are approximately 0.96 eV / 0.5 eV and 1 eV / 0.7 eV. The first combination gives slightly higher values for the efficiency but the only suitable lattice-matched material combination is (AlGa)(AsSb)/(GaIn)(AsSb), i. e. two quaternaries with GaSb or InAs as substrate material (section 2.1.1). On the other hand, there are three possible candidates for a lattice matched band gap combination close to 1 eV / 0.7 eV:

a) (GaIn)(NAs)/Ge

A band gap of 1 eV can be realised in (GaIn)(NAs) which is grown lattice matched to germanium substrates. As the band gap of germanium at 300K is 0.66 eV, a corresponding tandem device seems possible. However, (GaIn)(NAs) has not yet been reported in sufficient quality up to now.

b) (GaIn)(PAs)/(GaIn)As on InP-substrates

This material combination is technologically mature. Both materials are Al-free and can be grown in high qualities on InP as substrate material. However, indium is a rather rare element and InP is quite expensive. These factors might eventually prohibit a large-scale distribution of corresponding photovoltaic devices. While a mechanical stack of a GaAs-(GaIn)As tandem cell [74] and a CBE-grown (GaIn)As-tunnel junction have already been shown, a related tandem device has not been reported yet.

c) (AlGa)(AsSb)/GaSb

With GaSb ($E_{\text{gap}}(300\text{K})=0.72\text{ eV}$) as bottom cell, figure 2.4 suggests a theoretical efficiency of approximately 52% for the tandem cell when a concentrated solar spectrum below a GaAs-wafer is used as reference power (i. e. 500 times 389 W/m^2). A GaSb single junction cell alone gives 44% in equivalent calculations. For a reference power of 1000 W/m^2 (i. e. the complete solar spectrum without the GaAs filter), these values correspond to 20% for the tandem cell and 17% for the single junction cell. Hence, the ideal 4-junction device will give only 3% more than a 3-junction device with regard to the absolute efficiency of the whole system. Consequently, the 1eV-cell (i.e. the 3rd junction in a 4-junction system) must be very good in order to lead to a real gain of efficiency.

As described in chapter 4, the MOVPE of GaSb-based materials is a rather recent and difficult field, and the material quality is often unsatisfactory. Hence, the development of a successful (AlGa)(AsSb)/GaSb tandem cell must be considered an ambitious challenge. However, it was decided to choose the antimonide-based approach for this work due to the considerable potential of these materials with regard to a wide range of interesting physics and novel devices, e.g. 0.5 eV thermophotovoltaic cells.

As solar cells based on III-V semiconductors are significantly more expensive than their silicon based counterparts, an economically competitive terrestrial application can only be in a concentrating system where the area of cell required for a given power output is notably reduced. An example for such a system based on the above 4-junction approach is shown in figure 2.5.

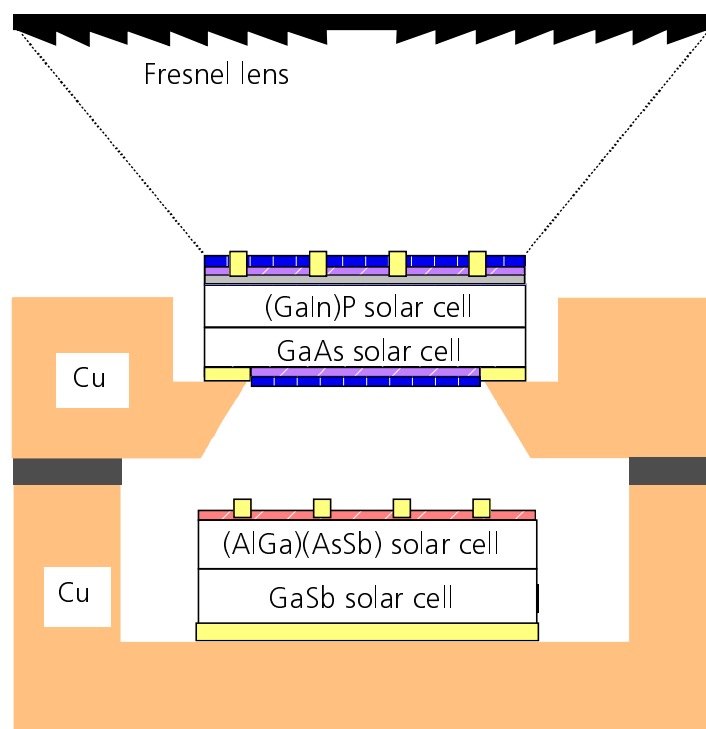


Figure 2.5: Four-junction photovoltaic system in a concentrating application.

The monolithic tandem cell for the high-energy photons consists of the material combination (GaIn)P/GaAs, while the second tandem cell for the low-energy photons is based on the combination (AlGa)(AsSb)/GaSb.

3 Experiment

3.1 Growth: Metalorganic Vapour Phase Epitaxy (MOVPE)

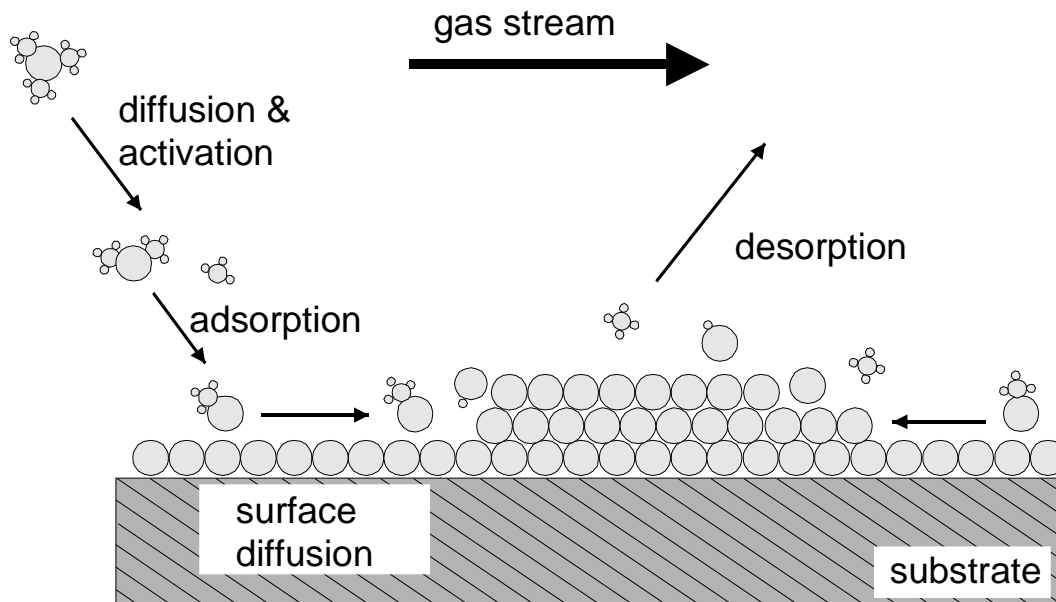


Figure 3.1: Principle of metalorganic vapour phase epitaxy. The source species are carried to the substrate in an H_2 -gas stream. After thermal activation they get adsorbed on the surface where they diffuse to their incorporation sites. Finally, organic rest groups desorb and are carried away with the gas stream.

Metalorganic vapour phase epitaxy (MOVPE) was already introduced in section 2.1.2 as vapour-phase epitaxial process based on gaseous metalorganic compounds. Common synonyms are organometallic vapour phase epitaxy (OMVPE) and metalorganic chemical vapour deposition (MOCVD). They all describe a very powerful technique for the epitaxial growth of III-V semiconductors.

In MOVPE, a combination of liquid or solid metalorganics and hydride gases is usually employed as source materials, the so-called "precursors". The following description of the technique will focus on the growth of GaAs as model system. Hydrogen is bubbled through metalorganic compounds (e. g. trimethylgallium or "TMGa" as group III-source) which are stored in steel cylinders in temperature-stabilised baths. The metalorganic evaporates and a saturated mixture with hydrogen is formed. This mixture is then further diluted with H_2 and transported to the actual growth chamber. Similarly, the gaseous hydride arsine as group V source is transported to the reactor in hydrogen as carrier gas. (An increasing tendency to replace this stable and highly dangerous hydride gas by metalorganic liquids such as tertiarybutylarsine (TBAs) can currently be observed.) As a result, there is a continuous flow of hydrogen carrier gas in the growth chamber with embedded group III- and V-source molecules over a heated susceptor onto which a substrate is placed. Close to the substrate surface a boundary layer is formed where the gas velocity is almost zero. Thermally activated precursor species diffuse through this

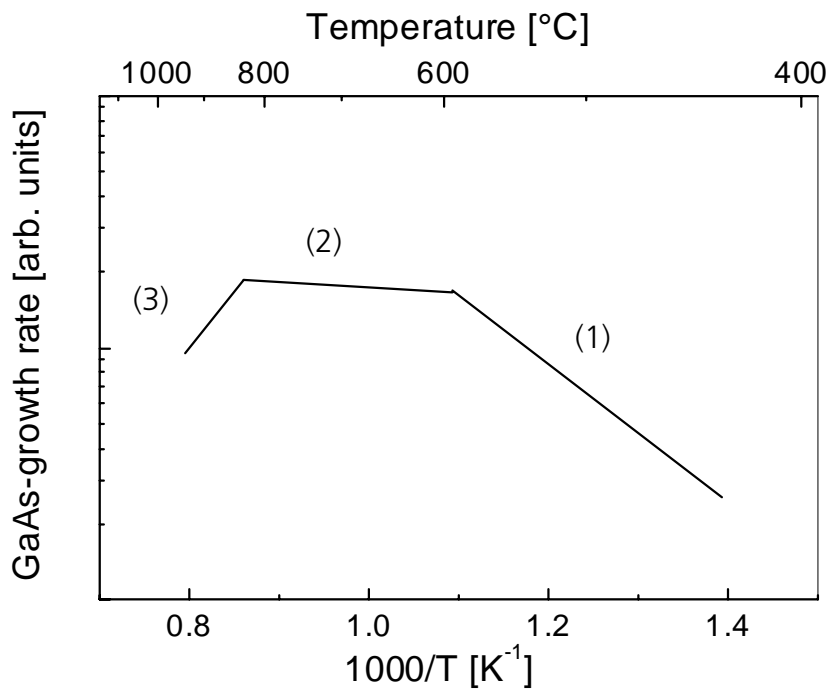
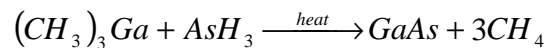


Figure 3.2: Sketch of the GaAs growth rate as a function of the growth temperature for the precursor combination $TMGa/AsH_3$. Three distinct temperature regions can be identified which are discussed in more detail in the text.

barrier and get adsorbed on the growth surface. Here, the species diffuse to energetically favourable incorporation sites where they contribute to the crystal growth. The remaining organic groups desorb and are carried away with the gas stream. The overall growth reaction can be described by a highly simplified expression:



Despite the significant degree of simplification in the above considerations, important features of the process can be derived:

- The atomic hydrogen from the pyrolysis of the V-precursor is important for the saturation of organic radicals that arise from the decomposition of the metalorganic precursors.
- As already described in section 2.1.3, a second condensed phase ($GaAs(s) + As(s)$) can not occur for arsenides and phosphides due to the high vapour pressure of excess arsenic and phosphorus at typical growth temperatures. Therefore, the incongruent evaporation of the components of III-V semiconductors at typical growth temperatures can generally be prevented by a group V overpressure in the MOVPE-reactor without causing nonstoichiometric growth. The related excess hydride gas contributes further to a complete saturation of organic radicals.
- The molar flow rate of group III elements into the reactor determines the overall growth rate of the crystal.

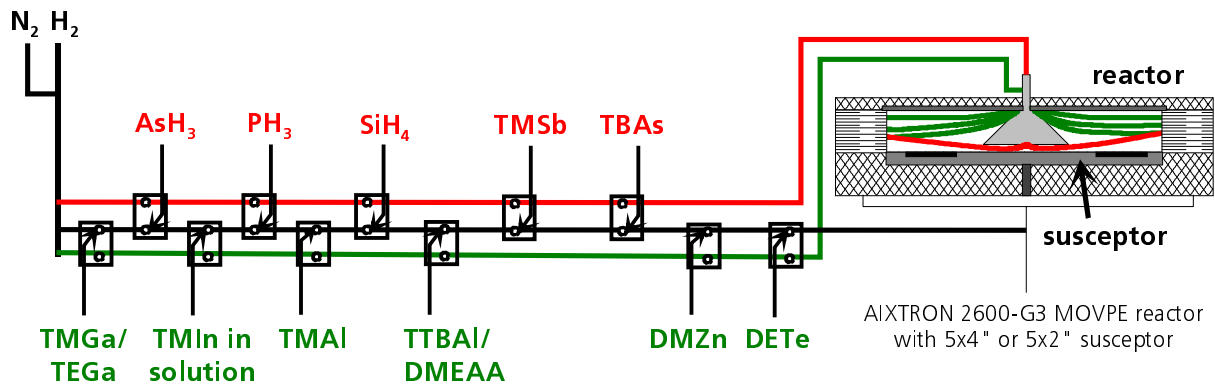


Figure 3.3: Sketch of the MOVPE-equipment that was used for the experiments of this thesis. An industrial scale multiwafer planetary susceptor geometry was combined with a large number of precursor lines in order to develop the growth of GaAs- and GaSb-based materials in the same reactor.

- Apart from the mass transport to the growth area, the rate limiting processes for the growth of the crystal are the thermal activation of the precursor species and the diffusion of the activated species through the stagnant boundary layer. The resulting growth rate of GaAs as a function of temperature is shown in figure 3.2. Three typical regions can be identified in the figure: In a low-temperature region (1) the thermal activation of the precursor species is the dominant rate limiting step. In a mid-temperature region (2) the thermal activation is complete and diffusion through the boundary layer is the dominant process. As this mechanism depends only weakly on temperature, the overall growth rate is almost constant in this region. At higher temperatures (3) the growth rate decreases again due to parasitic processes. Usually the mid-temperature region is chosen for the deposition of high-quality material. Consequently, the decomposition behaviour of the employed precursors must be matched to the optimum growth temperature range of the crystal to be grown.

The above points introduce some of the problems concerning the MOVPE-growth of antimonides: Compared to arsenides and phosphides, the V/III-ratio (i. e. $\sum P_{\text{partial}}(\text{V} - \text{precursor}) / \sum P_{\text{partial}}(\text{III} - \text{precursor})$) for antimonides must be held close to unity due to the less volatile antimony. Otherwise a second condensed phase ($\text{GaSb}(s) + \text{Sb}(s)$) and related nonstoichiometric growth will occur. Consequently, the saturation of organic radicals is rather incomplete in an antimonide process and carbon contamination of the crystals is a problem. Moreover, the growth temperatures for the antimonide crystals must be lower compared to standard materials. As a consequence, the thermal activation behaviour of common group III precursors does not match the growth conditions for antimonides. One of the challenges for the MOVPE of III-antimonides is therefore the search for novel precursors that decompose at lower temperatures. These challenges will be described in more detail in section 4.1 and 4.3.1.

For the experiments related to this thesis an industrial scale multiwafer planetary MOVPE-reactor was equipped with a significant number of precursor lines (figure 3.3) in order to make the development of GaAs- and GaSb-based structures possible in the same machine. Arsine (AsH_3), phosphine (PH_3), silane (SiH_4), trimethylantimony (TMSb), tertiarybutylarsine (TBAs), trimethyl- and triethylgallium (TMGa, TEGa), trimethylindium (TMIIn), trimethylaluminium (TMAI), tritertiarybutylaluminium (TTBAI), dimethylethyl-

amine alane adduct (DMEAA), dimethylzinc (DMZn), and diethyltelluride (DETe) were employed as source molecules in various experiments. The reactor pressure was held at 100 mbar in all experiments, palladium-diffused hydrogen was generally used as carrier gas, and a total flow rate of 1 mol/min was chosen. Further details on experimental parameters will be found at relevant places in the subsequent text.

3.2 Characterisation

3.2.1 HR-XRD: Structural properties

High resolution X-ray diffraction (HR-XRD) can give valuable information on the structural properties of the deposited crystals. In a simplified picture monochromatic X-rays are reflected at the crystal planes and constructive interference will occur if the Bragg-condition is fulfilled:

$$n\lambda = 2d \sin \theta_B$$

Here, λ stands for the employed X-ray wavelength (e. g. Cu - K_α with $\lambda=0.154052$ nm), d is the distance between reflecting planes, n describes the order of the reflex and θ_B is the Bragg angle.

Usually, the distance between the Bragg angles related to the substrate and the epilayer is the quantity of interest: As the substrate lattice constant is known, the distance between these peak positions allows a very accurate determination of the epilayer lattice constant. For the corresponding analysis of strained layers the elastical constants of the crystal must be considered. As the lattice constant of a ternary crystal can be assumed to be a linear function of the composition (Vegard's law), HR-XRD is widely used for the related compositional analysis.

However, the X-ray diffraction patterns contain much more information than mere lattice constants. The reader is referred to a very good book by Bauer and Richter [13] concerning further details such as the X-ray diffraction patterns of superlattice structures and a more sophisticated analysis based on the dynamical theory.

For the X-ray diffraction measurements in this thesis a standard set-up was used consisting of a Cu - K_α X-ray source, a silicon two-crystal monochromator/collimator and a scintillation detector.

3.2.2 Photoluminescence: Optical properties

The principle of photoluminescence is the absorption of photons of energy higher than E_{gap} and the resulting radiative recombination of excited carriers. The corresponding optical properties of a direct III-V semiconductor can provide important information on the band structure of the material and the minority carrier properties.

Photoexcited carriers will thermalise amongst themselves in a time short compared to recombination, so that a quasi-equilibrium distribution of both charge carrier types can be assumed. In this non-equilibrium situation the carriers can recombine both radiatively and non-radiatively. Various radiative channels are possible such as the recombination of two free carriers (band-band luminescence), a free carrier with a second carrier bound to a shallow impurity (free-to-bound transition), two carriers bound to shallow impurities (donor-acceptor pair transition), and excitonic emission (exciton: bound electron-hole pair). Due to the high density of states in the bands and the thermal smearing of the Fermi-function, shallow impurities are ionized at elevated temperatures and carriers are excited into the bands. Consequently, band-band luminescence dominates at room-temperature. Only at very low temperatures carriers are frozen on impurities, so that samples are usually held at liquid helium temperature in order to obtain meaningful information on the energetic structure. Details on the behaviour of various transitions can be found in chapter 5. In addition, the reader is referred to a book by Yu and Cardona [126].

In the case of GaSb, the band gap of the sample is very close to the band gap of germanium detectors which are commonly employed for the detection of luminescence in the near infrared. Still, this kind of detector can be used if the sample is held at liquid helium temperature and a spectral correction of the detector response is considered. The PL spectra in this thesis were obtained with a spectrometer utilising a 1 m Jobin Yvon grating monochromator. The optical cryostat was a closed cycle He-refrigerator KelCool™ UCH130 from Balzers that allows PL measurements in the temperature range 3.6-290 K. The excitation source was a He-Ne laser at 632.8 nm with a maximum power of 15 mW. The beam was focused onto the sample surface in a spot with a diameter of ~350 μm. Neutral density filters were used to vary the excitation density in the range 0.1 - 15 W/cm². The luminescence was detected using an Edinburgh Instruments EL-L high purity germanium system cooled to 77 K.

3.2.3 Hall effect: Electrical properties

Typical electrical properties of a semiconductor which are directly accessible through Hall measurements are the majority carrier concentration and the related mobility. The mobility μ of a charge carrier is defined by $v_D = \mu \cdot E$ (v_D : drift mobility, E : electric field). As the related current density j is given by $j = \sigma \cdot E$ (σ : conductivity), the conductivity of a semiconductor can be shown to be $\sigma = e \cdot (n \cdot \mu_e + p \cdot \mu_h)$. The corresponding electron mobility in a metal can be shown to be $\mu_n = e \cdot \tau / m$ (τ : relaxation time). In a semiconductor the situation is slightly more complicated. Here, the charge carrier distribution in the bands means that carriers with different masses can contribute to the electrical transport. The usual mobilities in a semiconductor must therefore be understood as an average value. In this context, the minority carrier contribution to the electrical transport can usually be neglected due to $np = n_i^2$.

When a sample is placed in a magnetic field B and a current I is passed through it, the Lorentz' force will lead to an electric field perpendicular to both B and I . This will lead to a voltage across the sample according to $U_H = R_H \frac{B \cdot I}{d}$ (d : sample width, R_H : Hall

coefficient), called the Hall-voltage U_H . When both electrons and holes are present in the sample, the Hall coefficient can be shown to be:

$$R_H = \frac{p \cdot \mu_p^2 - n \cdot \mu_n^2}{e(p \cdot \mu_p + n \cdot \mu_n)^2}$$

In a doped sample the minority carriers can again be neglected due to $np = n_i^2$ and the Hall coefficient becomes $R_H = \frac{1}{e \cdot p}$ or $R_H = -\frac{1}{e \cdot n}$ for p- or n-type material, respectively. The majority carrier mobility can now be expressed as $\mu = R_H \cdot \sigma$.

Both the Hall coefficient R_H and the conductivity can now easily be derived from measured parameters. In order to minimise errors that arise from geometric imperfections of the contact arrangement, the so-called van-der Pauw technique is usually applied where the related correction is calculated beforehand based on resistivity measurements between the contacts.

In the case of GaSb, Hall measurements are complicated because a semi-insulating substrate is not available for homoepitaxy. Therefore, semi-insulating GaAs is usually employed as a lattice-*mismatched* substrate for electrical measurements on GaSb. As a result, the density of structural defects in the epilayer is high and might influence the electrical data. In addition, the combination of residual strain at growth temperature and different thermal expansion coefficients between substrate and epilayer will produce a strained Hall sample where a valence-band splitting of a few milli electronvolts can be expected. Any changes in Fermi level or sample temperature will now alter the hole distribution ratio between light and heavy holes and a two-carrier type approach should be chosen for an accurate analysis of Hall-measurements of p-type samples. However, the effect is generally considered to be negligible. In section 4.2.4 a similar effect is shown to occur in temperature-dependent Hall measurements of n-type GaSb due to the proximity of the L- and Γ -valley in the conduction band. Further information on Hall-measurements and processing of GaSb/si-GaAs-samples can be found in [49]. Here it is as well shown that Hall-measurements and CV-measurements on pn-junctions are well in agreement with each other for low p-doping levels.

3.2.4 SPA: Surface properties

Surface photo absorption (SPA) uses p-polarised light which is reflected on a sample surface at a high angle of incidence close to Brewster's angle. For the experiments described in this thesis a 633 nm diode laser was used. At Brewster's angle the bulk contribution to the reflected intensity is minimal with respect to light polarised parallel to the plane of incidence. Any change in surface reflectivity can therefore be expected to reveal itself markedly in a change of the p-polarised reflectance.

During the pre-growth deoxidation of III-V substrates in an MOVPE environment a reproducible change of the SPA optical response has been reported [7]. Consequently, SPA can be of crucial assistance with respect to monitoring the in-situ treatment of substrates. The related literature focuses on the deoxidation of GaAs [6, 9, 10] while

little information on other types of substrates is available. Further information on the interpretation of SPA signals with regard to surface oxides can be found in section 4.2.1.

The measurements for this thesis were performed in a vertical MOVPE-reactor at atmospheric pressure in the Clarendon Laboratory of the University of Oxford. Hydrogen was used as carrier gas in the experiments. The laser beam was focused onto the sample and the photodetector using a geometry that involved reflection on the stainless steel shower head lid of the reactor.

3.2.5 SIMS

Secondary ion mass spectroscopy (SIMS) can be used to analyse the density of impurities in solids. Material from a solid is removed by sputtering. Most of the sputtered species are neutral atoms and cannot be analysed. However, the related ionised atoms can be passed through an energy filter and a mass spectrometer, giving an “ion count rate versus time” information. The time can then easily be translated into a depth by measuring the crater depth and assuming a constant sputter rate. The analysis of the ion count rate is more difficult and involves calibration standards with a known concentration of impurities. Here, the ion count rate for a given concentration in the solid depends strongly on the surrounding matrix. The SIMS measurements analysed in this thesis were performed by external SIMS laboratories², where GaSb- and $(\text{Al}_{0.2}\text{Ga}_{0.8})\text{Sb}$ -calibration standards for silicon, carbon and oxygen had been prepared by ion implantation.

When electrically active dopants are analysed, it must be considered that SIMS measures the *total* impurity density and not the electrically active concentration. The comparison between Hall- and SIMS-measurements can therefore provide valuable information on compensation ratios (section 5.2.2).

A limitation of the method is “tailing”: When sputtering from a highly contaminated region into a very pure region of the sample, the crater walls contain the entire impurity profile and any stray signal will contribute to the desired crater floor signal. Likewise, material from the crater edges can be deposited on the crater floor, thereby leading to an enhanced count rate. Spot focus and ion count rate are two important parameters in this context. The related effect can be observed in the SIMS profile shown in figure 4.33.

² Fraunhofer Institute for Applied Solid State Physics, Freiburg, Germany
RTG Mikroanalyse GmbH, Berlin, Germany

4 Results - MOVPE of III-antimonides

4.1 Introduction

In this section a brief summary of the MOVPE of III-antimonides will be given. Particular attention will be drawn to the additional difficulties that occur in comparison to GaAs- or InP-based materials.

The major difference between arsenides and phosphides on the one hand and antimonides on the other hand is the low vapour pressure of Sb-species over a crystal surface at typical growth temperatures. This small volatility of antimony can easily lead to nonstoichiometric growth, i. e. to the formation of solid Sb on the growth surface [33]. As a consequence, the group V pressure for antimonides has to be accurately controlled in a very narrow range of V/III ratios near unity [1].

The group V hydride (i. e. stibine, SbH_3) is too unstable for a successful use in MOVPE. Therefore alkyl antimony compounds are generally used as group V sources. As the atomic hydrogen from the arsine-/phosphine-decomposition in a standard MOVPE process is very important for the saturation of organic radicals that arise from the decomposition of the group III precursors, the related lack of atomic hydrogen in the Sb-process will obviously lead to problems of carbon incorporation especially for compounds containing aluminium.

Both the lack of a stable hydride and the low vapour pressure of Sb-species lead to a particular problem concerning the desorption of oxides from substrate surfaces during the initial stages of a growth run. This will be discussed in more detail in the following section 4.2.1.

In accordance with their low melting points, the growth temperatures of III-antimonides are much lower than in the case of As- or P-based compounds. Consequently, the standard precursors TMGa and TMAI lead to growth in the kinetically controlled regime, where their incomplete pyrolysis determines the growth rate of the crystal. This can lead to major inhomogeneities of the crystal composition and was shown to prevent the successful deposition of (AlGa)Sb with TMAI (see section 4.3.2). A solution for this problem in the case of gallium is the employment of TEGa instead of TMGa. In the case of aluminium, there is no generally accepted solution for the problem. A more detailed summary will be given in section 4.3 because the search for a suitable aluminium precursor for the growth of (AlGa)Sb is one of the major subjects of this chapter.

Precursors that decompose at lower temperatures than the standard precursors will at the same time have a higher reactivity. Thus, when a precursor is matched to the desired growth temperature regime it will often also give severe problems concerning pre-reactions and pre-deposition. There are a several interesting reports on the choice of the antimony, gallium and aluminium precursors in the literature, e.g. [18, 22, 44, 45, 90, 109, 116, 118]. The most suitable precursor combination is still not clearly identified.

In addition to the above mentioned MOVPE-related points, there are several more unexpected challenges related to the material characterisation and device processing: Not-intentionally doped GaSb is always highly p-type due to a native acceptor defect (see section 4.2.4). Correspondingly, semi-insulating GaSb substrates are not available. Epitaxial structures for Hall characterisation are therefore usually grown on highly lattice-mismatched semi-insulating GaAs. Besides, as the work function of a undoped GaSb surface does not allow a Schottky barrier to be formed [1], CV-measurements can not be performed neither in an electrochemical etch profiler nor by use of metal contacts. Due to the low band gap of GaSb the photoluminescence of the material is difficult to detect. Usually, the high energy peaks of the spectrum can be resolved with a germanium detector at 77K when the sample is held at helium temperature. Mixtures on the group V sublattice show severe miscibility gaps. There is a significant lattice mismatch between GaSb and (AlGa)Sb, so the resulting strain in aluminium containing compounds has to be compensated by the addition of arsenic. The amphoteric group IV elements silicon and germanium can not be used as n-type dopants in antimonides. In this context, only Sn is sometimes applied as donor dopant (see section 4.3.10). Finally, selective etching between GaSb and (AlGa)Sb has never been reported. In summary, a researcher who is experienced with GaAs- or InP-based materials will encounter many unexpected challenges in the field of the antimonides. It is not surprising that an antimonide-based MOVPE-grown laser structure was not reported until 1991 (ref. 14 in [1]).

4.2 MOVPE of GaSb

4.2.1 Substrate preparation / Oxide desorption

The epitaxy of high-quality III-V semiconductors depends on a complete removal of all impurities and oxide layers present on the substrate surface prior to growth. GaAs-substrates are nowadays usually sold as "epiready", i. e. a pre-growth wet-chemical treatment should no longer be necessary in most cases. This is achieved by the preparation of a well-defined thin (~3 nm [7]) layer of oxide by the manufacturer after the surface has been polished and washed. Typical oxides would be As_2O_3 , Ga_2O_3 , and Ga_2O , which can then be desorbed at elevated temperatures in the growth environment. Whilst As_2O_3 and Ga_2O can be desorbed at temperatures around 400°C, Ga_2O_3 is desorbed at higher temperatures around 500°C and above ([6] and references therein). It was shown that the desorption temperatures can be significantly lower when tertiarybutylarsine is present in the MOVPE environment [6]. This is usually attributed to the evolution of reactive atomic hydrogen from the pyrolysis of the group V-hydride. It has been shown that atomically resolved terraces can be found on the surface if the oxide has been reduced under TBAs. On the other hand, merely heating up the substrate in molecular hydrogen and allowing the oxide to desorb does not give such high-quality surfaces (ref. 9 in [7]).

In contrast to GaAs, GaSb substrates are not available as "epiready". The reactive nature of the GaSb surface leads to a rapid formation of a native oxide layer in contact with H_2O or air. Due to the lack of an antimony precursor that would pyrolyse to give atomic hydrogen, the substrate oxide can not be reduced in the growth environment and deoxidation must be evaporative. As a consequence, a wet-chemical oxide removal prior

to growth is usually carried out. Here, it is quite difficult to produce a high-quality GaSb surface for subsequent epitaxial growth and the related recipes are usually laborious [32, 59, 60]. Very good results have been published for a treatment which involves concentrated HCl to remove the native oxide, etching in $\text{Br}_2\text{-HCl-HNO}_3\text{-CH}_3\text{COOH}$ and finally rinsing in 2-propanol [116]. In a widely used simplification of this recipe the $\text{Br}_2\text{-HCl-HNO}_3\text{-CH}_3\text{COOH}$ step is often omitted. It is important to note that the use of water must be avoided after the oxide removal due to the rapid re-oxidation of GaSb in contact with H_2O .

The GaSb substrates used in this work were treated with concentrated HCl for 30s. Afterwards, they were rinsed in a 3-step 2-propanol cascade and then immediately transferred into a nitrogen glovebox atmosphere. Before growth they were annealed for 10 minutes at 600°C under a small flow of TMSb in hydrogen as carrier gas. However, SIMS experiments generally showed very strong oxygen and carbon peaks at the epilayer/substrate-interface. Consequently, the employed preparation method must be improved. Here, in-situ procedures are generally preferred to ex-situ wet-chemical preparations. Therefore the thermal desorption of the native oxide layer on GaSb was analysed in detail by surface photoabsorption (SPA).

The principle of SPA was explained in section 3.2.4. When performed at or close to the Brewster angle, the SPA signal is highly surface sensitive. Consequently, one of the areas where SPA can be of crucial assistance is in-situ monitoring of the deoxidation of substrates. The related literature focuses on the deoxidation of GaAs [6, 9, 10] while little information on other types of substrates is available. For GaAs, the high temperature optical constants have been determined and the measured SPA-signals could well be explained and simulated as a function of temperature and angle of incidence [8]. The data shown in [6] suggest that the p-polarised reflectivity at the optimum angle of incidence (i. e. close to the Brewster angle) is approximately a linear function of the thickness of the oxide on the GaAs substrate surface. The following SPA spectra of GaSb will be interpreted on this basis. Figure 4.1 shows the SPA optical response of two different GaSb surfaces.

The two graphs in figure 4.1 each contain the following experiments: The black solid lines (SPA #640, SPA #660) show the SPA optical response of the respective substrate taken directly from the box into the reactor. The related temperature in the heating and cooling cycles are also shown. It is worth noting that the SPA #660 represents the standard annealing procedure which was employed for the layers of all chapters of this work. It can be seen, that a sharp drop of the SPA intensity occurs at a fixed temperature of 510°C . This temperature was found to be independent of the substrate orientation, the substrate manufacturer and the final value of the temperature ramp. Based on the earlier work on GaAs, this drop is interpreted as a rapid oxide desorption process. The second peak in these spectra is not fully understood: It usually occurred when the T-ramp reached its maximum and a fixed temperature was held constant, independent of the actual value. The change of the rate of the temperature increase seems to induce a change of the SPA optical response. This effect occurred only when thick oxides were being desorbed; otherwise the peak did not appear.

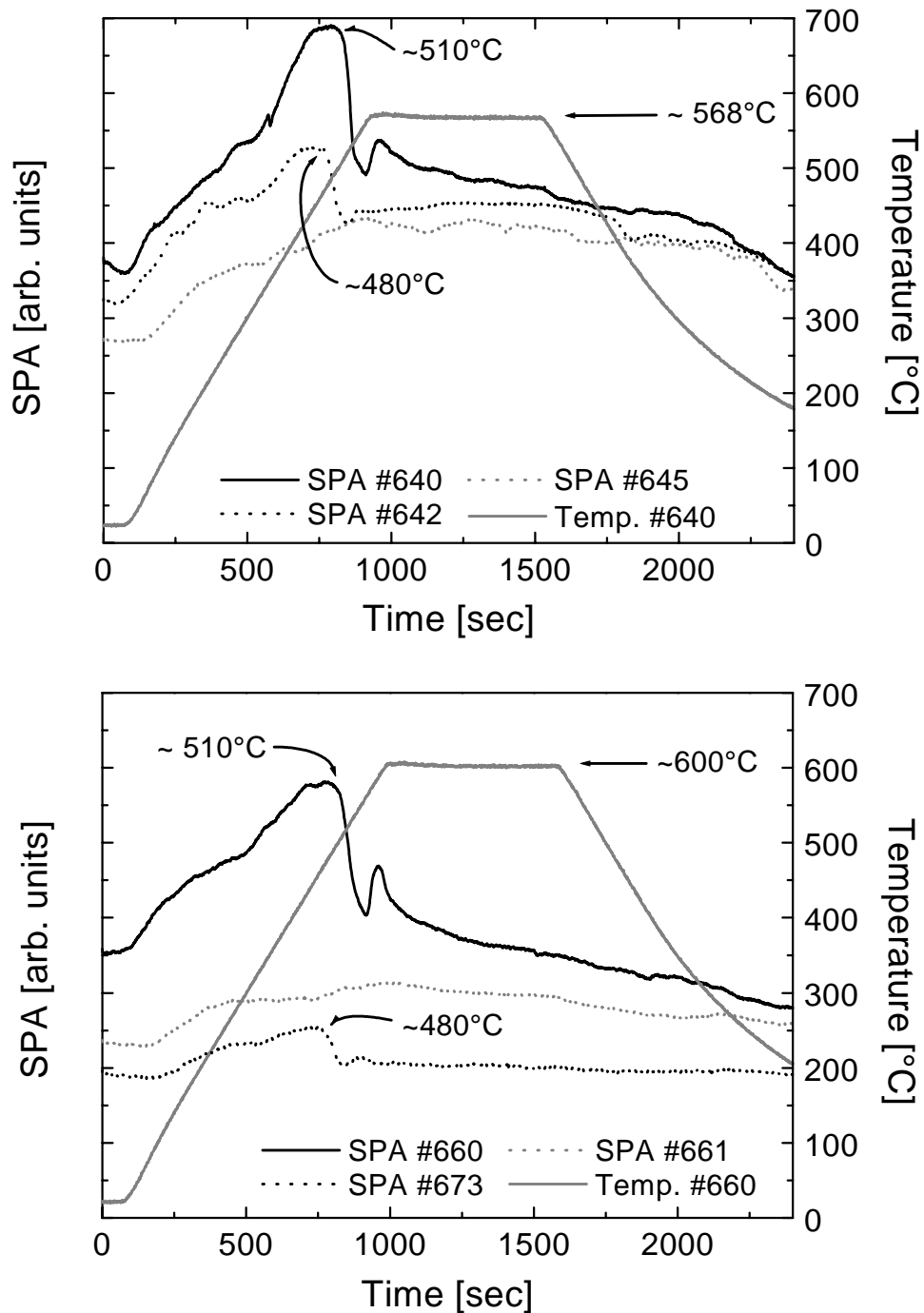


Figure 4.1: SPA optical response of GaSb-substrates in a heating and cooling cycle. While a GaSb substrate with a 2° to (111)A miscut was used in the first measurement, the optical response below was recorded using a 2° to (110) GaSb substrate from a different manufacturer.

The measurements shown in grey dots (SPA #645, SPA #661) represent direct re-runs of the heating cycle without any exposure of the substrates to air. As expected, a deoxidation drop of the SPA-intensity can not be observed.

In order to confirm the above hypothesis, the substrates were then exposed to air for two days and the experiment was repeated (SPA #642, SPA #673). The related formation of an oxide layer was confirmed by the re-occurrence of the deoxidation-drop

in both SPA optical responses. The drop now occurred at a lower temperature of about 480°C, possibly indicating a different chemical composition of the fresh (and thin) oxide compared to older (and thicker) oxide layers. The same effect has been reported for GaAs [10]. Here it should also be noted that (due to a limited reproducibility of the SPA setting over a period of several days) the measurement should not be compared in absolute terms with the measurements that had been performed two days before.

Given the above results, it can be concluded that the observed drop of the SPA optical response can indeed be related to a desorption of an oxide layer on the substrate surface. The intensity continues to drop slowly when the temperature is held at a constant value. This behaviour suggests that the deoxidation process continues for many minutes. Due to the lack of a stable antimony hydride precursor this result had to be expected because the substrate oxide can not be rapidly reduced with atomic hydrogen and deoxidation must take place merely evaporative instead.

In the following, the deoxidation process was analysed as a function of temperature. GaSb substrates were heated up to temperatures *below* the point of rapid deoxidation (~510°C) and the resulting slow decrease of the SPA optical response was measured. The following figure 4.2 presents the SPA data, where the spectra were normalised to have the same intensity at 400°C.

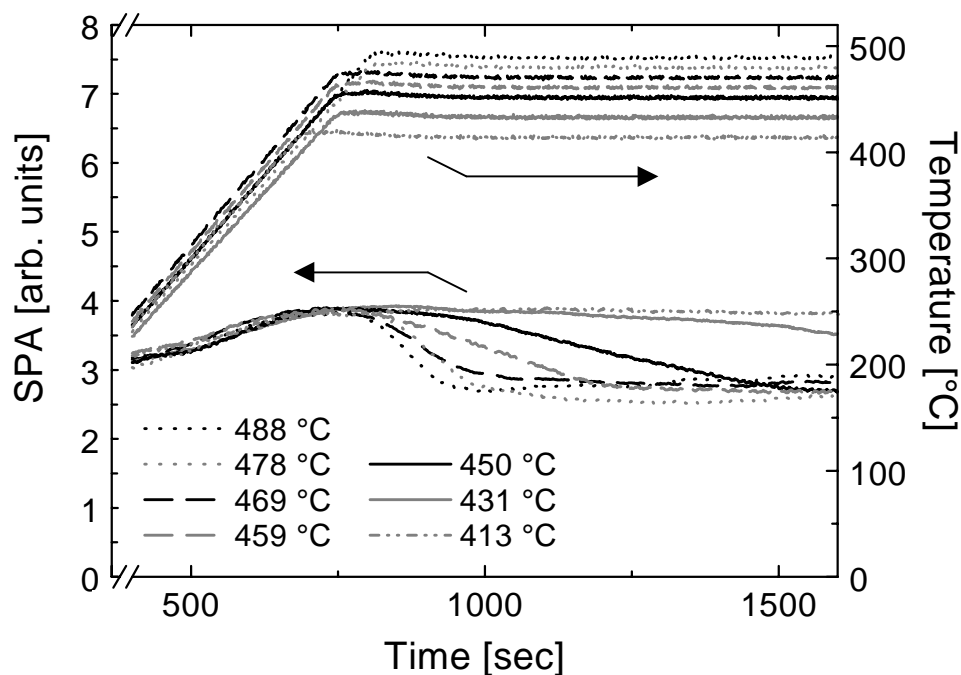


Figure 4.2: SPA optical response of GaSb-substrates (misorientation: 2° off (100) to (111)A) recorded at different temperatures well below 510°C.

A slow deoxidation process is observed and the decrease of the SPA signal is a reasonably linear function of time. The reduction rate of the SPA signal can therefore be analysed in an Arrhenius plot (figure 4.3). Apart from the two highest temperatures, an activated behaviour with constant activation energy is confirmed. The slope of the curve corresponds to an activation energy of 3 eV. The corresponding experiment for GaAs has been reported to give a value of 2 eV [6]. A possible explanation for the higher value

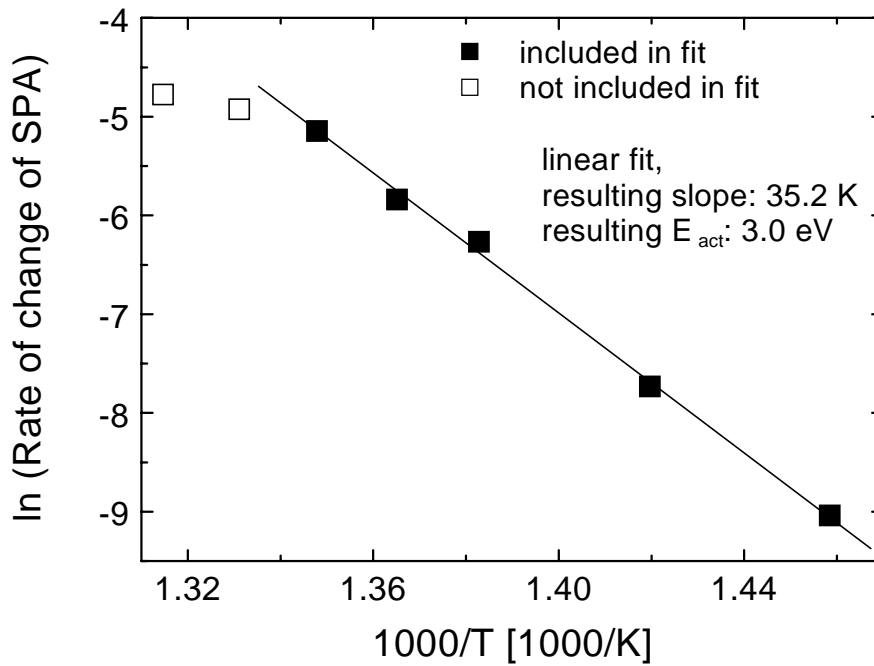
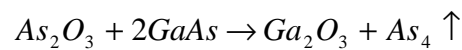
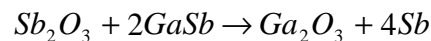


Figure 4.3: Arrhenius plot of the reduction rates of the SPA optical response as shown in figure 4.2.

in the case of GaSb is based on the different vapour pressures of arsenic and antimony at elevated temperatures: As already mentioned above, in the case of GaAs the As^{III}-oxide As₂O₃ desorbs at comparably low temperatures. Here, the following mechanism is believed to take place:



Accordingly, the activation energy of 2eV reported in [6] is believed to represent the desorption of the gallium oxide Ga₂O₃. Assuming the presence of the analogous oxides on GaSb (i. e. Sb₂O₃ and Ga₂O₃) and a corresponding reaction



the resulting elemental antimony will *not* desorb readily from the surface due to its low vapour pressure. Therefore the desorption of Ga₂O₃ from GaSb will be hindered by the presence of elemental antimony, leading to a higher activation energy of the overall reaction. Another interpretation of a GaSb-reflectance drop in the same temperature range is given in [105], where the desorption of elemental antimony is suggested to be responsible. While such a rapid desorption of elemental Sb would be surprising, nevertheless a necessity for further research on in-situ GaSb-preparation is underlined.

The above results can be summarized as follows:

- The SPA optical response of a GaSb substrate shows a characteristic drop between 480°C and 510°C which can be attributed to the desorption of a native oxide layer.
- The SPA signal suggests that the desorption process continues at small rates over many minutes.
- The observed activation energy is even higher than in the case of GaAs.
- The difficult GaSb deoxidation is believed to be based on

- a) the lack of stable antimony hydride precursor (which would be able to reduce the oxide with atomic hydrogen), and
- b) the low vapour pressure of antimony at typical growth temperatures (which is believed to hinder the overall desorption process).

As already mentioned above, SIMS experiments showed a very strong oxygen peak at the epilayer/substrate-interface for the layers grown in this work despite a very thorough wet-chemical oxide removal and a subsequent in-situ oxide desorption procedure. These oxygen impurities act as deep recombination centres for minority carriers. This is underlined by the fact that the photoluminescence intensity of GaSb layers could be highly improved by a high-bandgap buffer layer which keeps optically generated minority carriers away from the epilayer/substrate interface.

Obviously novel methods should be developed for an improved GaSb substrate preparation. One possible approach is the in-situ generation of atomic hydrogen, for example by a simple thermal cracker. Promising results have been reported in [19]. Apart from this, an in-situ etching technique would be another very interesting candidate. Particularly tertiarybutylchloride (TBCl) is of high interest because the substance should not be corrosive before chlorine radicals are produced by thermal cracking. It is a liquid at room-temperature (vapour pressure constants: $A=1413K$, $B=7.365$ [Merck, technical data sheet]) and can be employed in a usual bubbler configuration. Corresponding reports can be found in the literature on in-situ etching of GaAs (CBE,[64]) and InP (MOVPE, [122]).

In preliminary experiments TBCl was tested for GaSb in-situ etching purposes. GaSb substrates were covered with SiO_2 mesa masks, and TBCl was added to the gas phase for several minutes at typical growth temperatures. Afterwards, the SiO_2 was removed in HF and the etch edge was analysed with an AFM. The desired etching could indeed be achieved in preliminary experiments (see figure 4.4). However, a corrosion of the bubbler walls was observed after some days. This set-back was most likely caused by impurities in the employed TBCl batch: In the presence of acidic or alkaline impurities hydrolysis can produce HCl in solution which will then be corrosive. As a conclusion, these promising preliminary experiments should be repeated with a high-purity batch of TBCl. If conditions for etched surfaces with excellent morphologies can be established, this would mark a major step forward for the in-situ preparation of GaSb substrates.

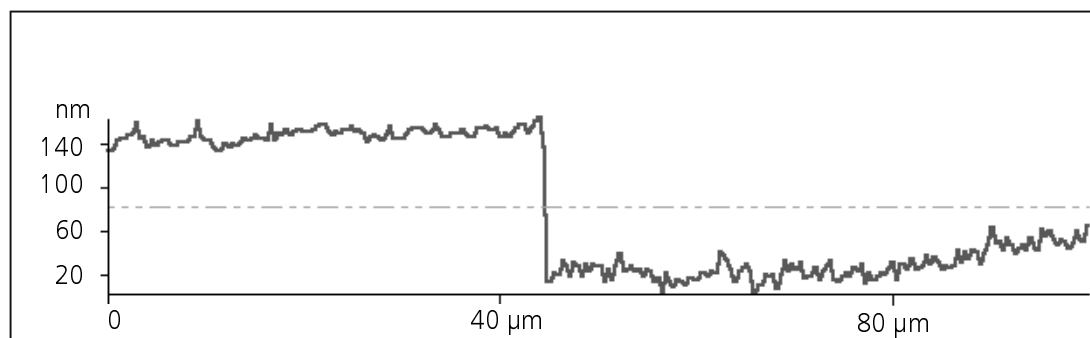


Figure 4.4: Etch edge of a GaSb mesa which was prepared in-situ with TBCl.

4.2.2 Morphology of homoepitaxial GaSb

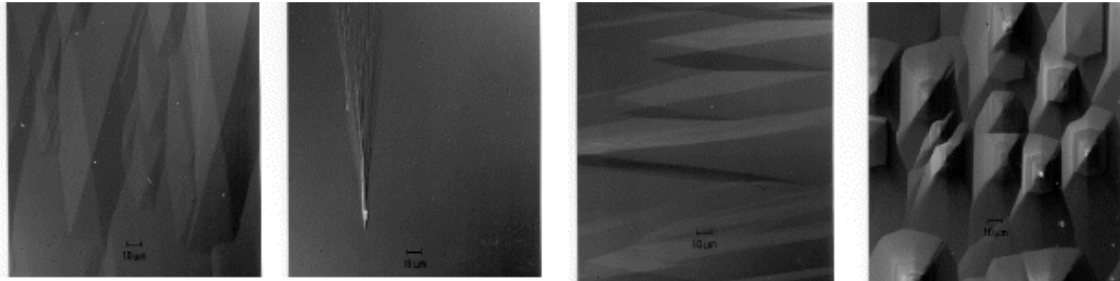


Figure 4.5: *Morphology of GaSb grown on (100) exact substrates as a function of the V/III-ratio (shown: 170 μ m x 170 μ m). V/III-ratios from left to right: 1.1, 2.1, 2.7, 4*

In order to obtain good surface morphologies for homoepitaxially grown GaSb many different growth parameters have to be carefully optimised. Apart from the substrate preparation the following factors were found to have a significant influence on the film morphology: V/III-ratio, substrate orientation and growth temperature.

As illustrated by the micrographs in the substrate-section of the annex, exact (100) oriented substrates gave very bad morphologies for most V/III-ratios. A significant improvement could be achieved with misoriented substrates, of which the 2° to (110)-orientation was the most favourable.

The influence of the V/III-ratio is illustrated in figure 4.5. Various GaSb layers were grown at different V/III-ratios on (100) exact oriented substrates. The layer grown at a V/III-ratio of 2.1 showed a very good morphology. (The defect depicted in the figure was only used for focussing.) All other V/III-ratios led to a deterioration of the surface morphology. The corresponding V/III-ratio range for good morphologies was very narrow and hardly reproducible. This effect was less pronounced on misoriented substrates, but similarly even here the best morphologies were obtained at V/III-ratios around 2.

The influence of the growth temperature has to be analysed together with the substrate misorientation: While substrates with a 2° to (111)A miscut gave good morphologies in the range 550°C ... 575°C and very bad surfaces at higher temperatures, their counterparts with a 2° to (111)B orientation gave good morphologies at 625°C but higher defect densities at the lower temperatures. In order to draw experimental conclusions from these results, other factors must as well be considered: On the one hand a tendency for better electrical data (measured on semi-insulating GaAs substrates) was observed at lower temperatures around 550°C, while on the other hand the optical properties of GaSb and the growth rates of (AlGa)Sb were much improved at higher temperatures. Thus, the desired properties of a final device structure have to be considered when a particular combination of growth temperature and substrate misorientation is chosen.

4.2.3 GaSb growth rate

The growth rate of GaSb was determined at different growth temperatures and V/III ratios. As no etch solutions are known that would etch GaSb and stop on a lattice-matched etch-stop layer, the only way to get accurate information on the growth rate is the deposition of structural superlattices which can then be analysed by HR-XRD. The design of these structures is particularly difficult in the case of GaSb as substrate material because there are no lattice matched ternary materials such as in the GaAs/(AlGa)As- or GaAs/(GaIn)P-system. All materials that are reasonably lattice matched to GaSb are quaternaries which involve mixing on both sublattices. Besides, due to pre-reactions between different precursors (see for example section 4.3.6) a mixing on the group III-lattice can not be used for the corresponding superlattice structures (see section 4.3.6). Thus, GaSb/Ga(AsSb)-superlattices were chosen as an alternative. However, the lattice constant of Ga(AsSb) is highly mismatched to GaSb even for very small As-concentrations. Therefore, the thickness of the single Ga(AsSb) layers and the number of superlattice periods are very limited in order to prevent relaxation. A suitable structure was developed which finally contained 20 periods of 24 nm GaSb and 6 nm Ga(As_{0.03}Sb_{0.97}). This structure was then used to analyse the growth rate of GaSb as a function of temperature and V/III ratio. At the same time, the structure could be used to measure the arsenic incorporation behaviour. A typical XRD measurement is shown in the following figure 4.6.

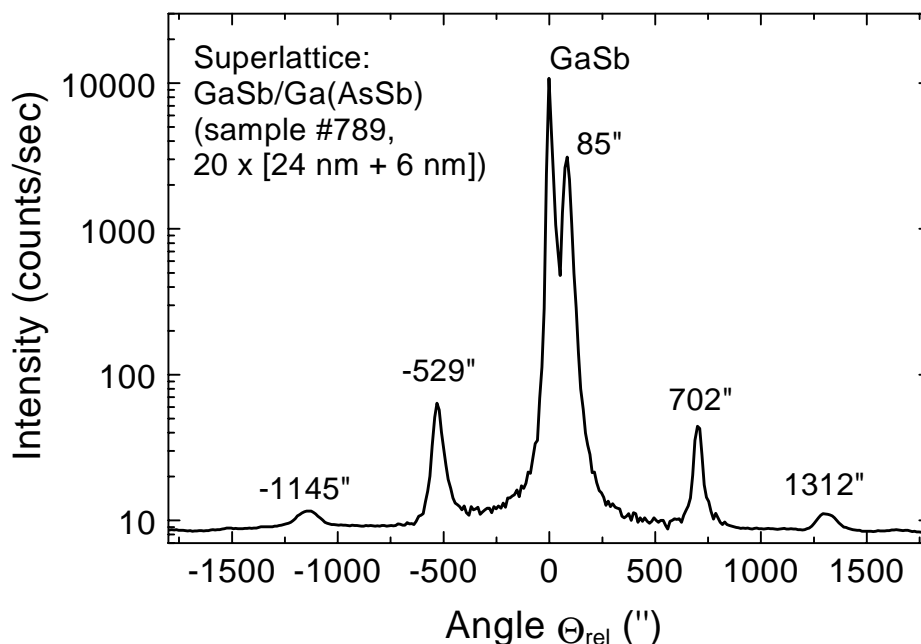


Figure 4.6: High resolution x-ray diffraction of GaSb/Ga(AsSb) superlattice. The structure consists of 20 periods. Each period has about 24 nm of GaSb and 6 nm of Ga(As_{0.03}Sb_{0.97}). The measurements show nearly theoretical FWHM's.

The corresponding values of the superlattice period lengths for GaSb/Ga(AsSb) superlattices grown at different temperatures but otherwise identical conditions are shown in figure 4.7, indicating a constant growth rate within an average error of 3.2%.

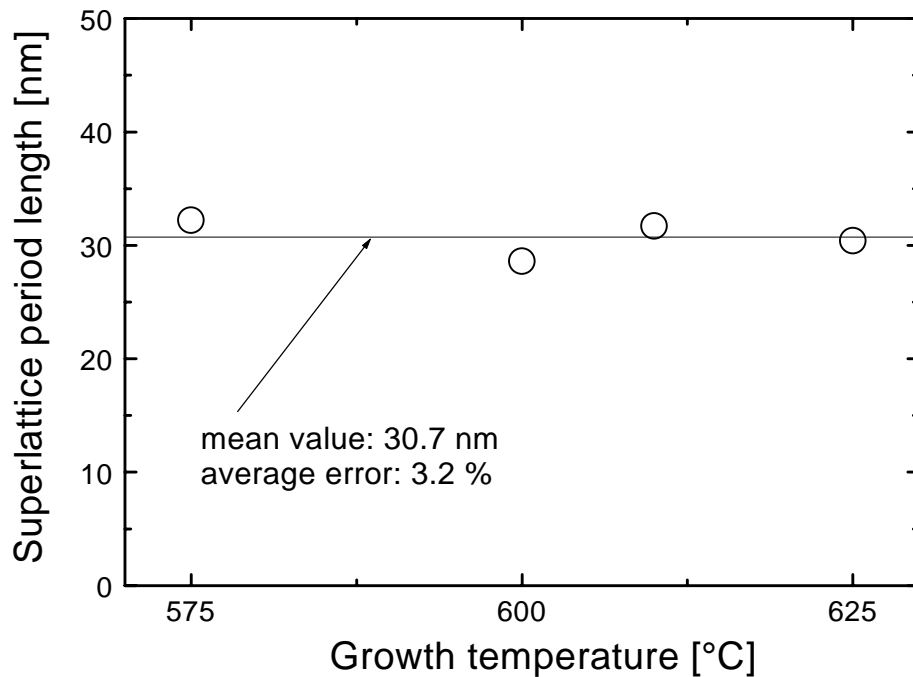


Figure 4.7: Superlattice periods of GaSb/Ga(AsSb) superlattices grown at different temperatures but otherwise identical conditions. The results indicate at constant efficiency of TEGa in the temperature range 575°C ... 625°C.

It can therefore be assumed that the TEGa-efficiency is constant over the range of employed temperatures (575°C ... 625°C). For GaSb layers grown at 1.8 $\mu\text{m/h}$, 575°C and a V/III ratio of 2 the resulting reactor efficiency for TEGa was approximately 250 nm/mmol. The corresponding value for GaAs grown with TMGa and arsine in the same reactor was approximately 300 nm/mmol. As it must be expected to be very difficult to adjust a suitable decomposition profile for the precursor combination TEGa/TMSb at 575°C in a reactor which was originally designed for the combination TMGa/AsH₃ at much higher temperatures, the above value of 250 nm/mmol is a very satisfying result.

A variation of the V/III-ratio between 2 and 3 did not influence the measured growth rates. As a result, significant pre-reactions between TEGa and TMSb are very unlikely. In addition, the reactor efficiency has proven to be reliably stable over several months.

4.2.4 Electrical properties: Undoped and Te-doped GaSb

The transport properties of GaSb are rather unusual compared to most other III-V semiconductors: Firstly, as-grown crystals contain very high concentrations of a native acceptor defect. Secondly, L minima in the conduction band lie energetically very near the Γ minimum and contribute significantly to the transport behaviour at elevated temperatures. As intentionally p-doped layers will be analysed in detail in chapter 5, this section 4.2.4 will focus on the electrical data of not intentionally doped and tellurium doped GaSb.

The native acceptors (NA's) which dominate not intentionally doped GaSb are believed to be based on a gallium vacancy-gallium antisite complex ($V_{\text{Ga}}, \text{Ga}_{\text{Sb}}$). The formation of

this defect can be expected to be enhanced by a deficiency of antimony during growth. This assumption was confirmed in growth experiments from nonstoichiometric melts. A brief summary of related papers can be found in [120]. The native acceptor defect has been established to be a doubly ionizable acceptor with ionization energies of about 34 and 102 meV ([77], [76] and references therein). The ionized state can be observed in PL-experiments at higher temperatures: At low temperatures, the Fermi level is below the acceptor level, no thermal release of holes occurs, the NA's are neutral, and only this neutral state can be seen in the PL. If the temperature is increased, the Fermi level moves upwards and the native acceptors get ionised to NA^- . However, as the native acceptor has the ability to bind *two* holes, a DAP (= donor acceptor pair) transition involving the NA^- -state can now be observed [76]. In transport (i. e. majority carrier) experiments of undoped samples this deep lying second acceptor level is not observed at room temperature because it is not appreciably ionised. However, due to the position of the Fermi level in n-type material, the deep acceptor level will be completely ionised in n-type samples even at low temperatures. Thus, the compensating p-type background resulting from native acceptors in n-type GaSb will be at least twice as high as the NA concentration [35].

Electrical data of not intentionally doped GaSb grown by MOVPE using various different antimony precursors are reported for example in [1, 18, 30, 37, 45, 90, 118]. The typical transport data of GaSb grown for this work are $p_{300K} \sim 2 \cdot 10^{16} \text{ cm}^{-3}$, $\mu_{300K} \sim 7.5 \cdot 10^2 \text{ cm}^2/\text{Vs}$, $p_{77K} \sim 5 \cdot 10^{15} \text{ cm}^{-3}$, $\mu_{77K} \sim 3.4 \cdot 10^3 \text{ cm}^2/\text{Vs}$ (growth parameters: 575°C, V/III=2, 1.8 $\mu\text{m}/\text{h}$, growth time: 1 hour). These data are among the best values reported in the above-mentioned literature. While the electrical data showed the tendency to improve slightly (= lower p-type background, higher mobility) when the growth temperature was lowered to 550°C, this lower temperature made the optical properties of GaSb slightly worse and was not advantageous for the growth of Al-containing materials (see sections 4.2.6 and 4.3). Consequently, 575°C was established as standard growth temperature for the binary layers in this work.

In order to achieve n-type conductivity for GaSb, two difficulties have to be overcome:

- The native acceptor concentration will act as compensating p-type background.
- Since silicon and germanium can not be used as donor dopants in GaSb, the choice for n-type doping is mainly limited to group VI elements (sulphur, selenium and tellurium). Apart from this, there are very few reports on successful n-type doping of Al(AsSb) with tin [20, 22].

While doping with H_2S lead to p-type GaSb [78, 106], n-type conductivity has been achieved with both H_2Se [75, 98] and metalorganic tellurium compounds (dimethyltelluride [DMTe], diethyltelluride [DETe]) [75, 81, 106]. Here, DETe can either be used as a metalorganic liquid in a bubbler configuration or as diluted mixture with H_2 in a pressurised gas cylinder. For the present work it was decided to employ DETe in a bubbler configuration due to the following reasons:

- Gaseous mixtures of group VI-metalorganics with H_2 in pressurised cylinders are known to be unstable with respect to the yield of the dopant molecule per withdrawn gaseous volume.
- H_2Se is a highly toxic gas.
- While the Te donor can be described satisfactorily by the hydrogenic model, the binding energies of Se are reported to be significantly higher [35].

- The maximum electron concentrations in the literature for Te-doped GaSb are higher than for Se-doped layers. The following maximum electron concentrations are reported for DETe: $2 \cdot 10^{18} \text{ cm}^{-3}$ [106] and $1 \cdot 10^{18} \text{ cm}^{-3}$ [75].
- For MOVPE-grown aluminium-containing antimonides tellurium has been reported as successful n-dopant [44, 109].

Te-doped GaSb was grown at various different DETe molar flow rates. The layers were analysed using SIMS and temperature-dependent Hall-measurements. The results are summarised in the following figure 4.8:

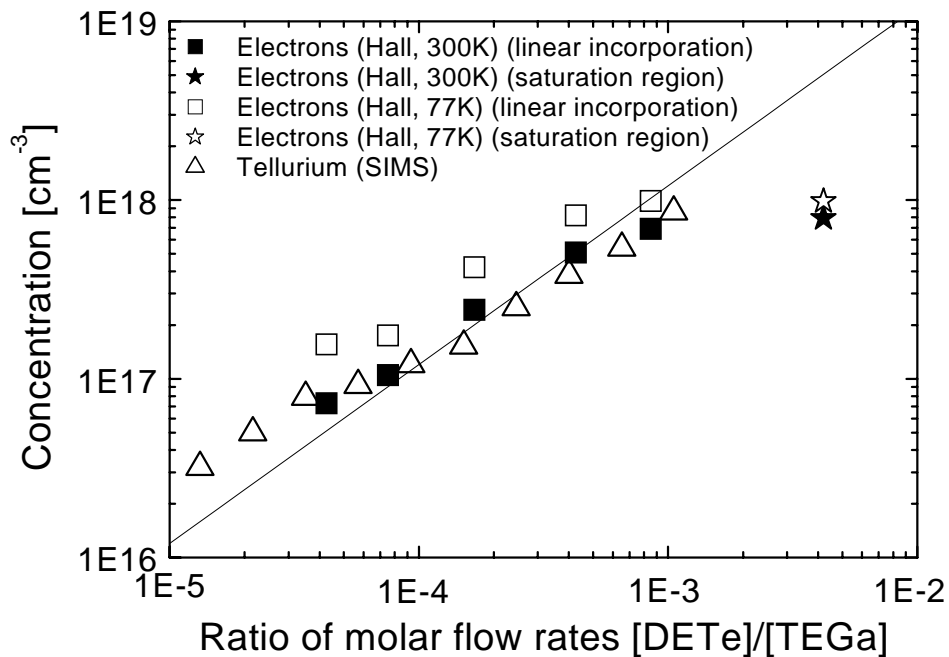


Figure 4.8: Hall- and SIMS-measurements on tellurium-doped GaSb. The line graph („unity line”) represents a linear relation between gas phase and solid composition.

In the examined range for tellurium concentrations between $\langle \text{Te} \rangle = 2 \cdot 10^{16} \text{ cm}^{-3}$ and $\langle \text{Te} \rangle = 1 \cdot 10^{18} \text{ cm}^{-3}$ the SIMS analysis shows an approximately linear incorporation behaviour. The electron concentrations as measured by Hall at 300K agree well with the SIMS data within the measured range (i. e. up to molar flow rate ratios of $\frac{[\text{DETe}]}{[\text{TEGa}]} = 1 \cdot 10^{-3}$). Three surprising features of the data deserve further attention:

- 1) For molar flow rate ratios above $\frac{[\text{DETe}]}{[\text{TEGa}]} = 1 \cdot 10^{-3}$ the electron concentration does no longer increase when the DETe molar flow rate is increased. A possible explanation for this behaviour is found in the literature: Nakamura et al. [75] report a critical concentration for both Se and Te in MOVPE-grown GaSb above which the linear behaviour of both dopants breaks down. Above this critical point (which lies significantly higher for Te than for Se) the concentration of dopant atoms increases

superlinearly with increasing molar flow rate, while the electron concentration gets *reduced* by increasing dopant flows. The superlinear incorporation behaviour is suggested to be due to the formation of complexes between gallium and the dopant on the growth surface. This model is also suggested elsewhere (ref. 154 in [35]) where the critical point is reported as $1.5 \cdot 10^{18} \text{ cm}^{-3}$. The stagnant or even declining electron concentration is suggested to be due to the formation of an additional deep donor. Related evidence was found by Nakamura et al. [75] in temperature dependent Hall measurements of samples with dopant concentrations above the critical point. The concentration of the shallow donor was shown to decrease with the onset of the formation of the deep donor. However, it remained unclear whether the deep donor formation is related to the formation of the complexes.

Unfortunately the SIMS data in figure 4.8 have not been measured beyond the critical point so that a superlinear incorporation behaviour can not be confirmed here. However, the observed behaviour of the electron concentration confirms the corresponding results of Nakamura and co-workers. The competition between Sb and Te for free Sb sites recommends lower V/III ratios for higher doping levels. However, even a reduced V/III-ratio of 1.5 did not lead to an increase of the electron concentration. Based on data on Te-doped (GaIn)(AsSb) published by Wang [110] it seems likely that the miscut angle of the substrate will slightly influence the upper limit for the tellurium incorporation as well in the case of GaSb. Still, a significant increase of the electron concentration in Te-doped GaSb can not be expected and a corresponding maximum electron concentration of $1 \dots 2 \cdot 10^{18} \text{ cm}^{-3}$ for MOVPE-grown Te-doped GaSb must be accepted. As Sn-doped $\text{Al}(\text{As}_{0.16}\text{Sb}_{0.84})$ with an electron concentration of $5 \cdot 10^{18} \text{ cm}^{-3}$ is reported in [20], tetraethyltin might also be an alternative dopant to achieve higher doping levels in GaSb.

- 2) In figure 4.8, the measurement of the electron concentration at 77K shows a higher carrier density than the measurements at 300K. In order to examine this result in

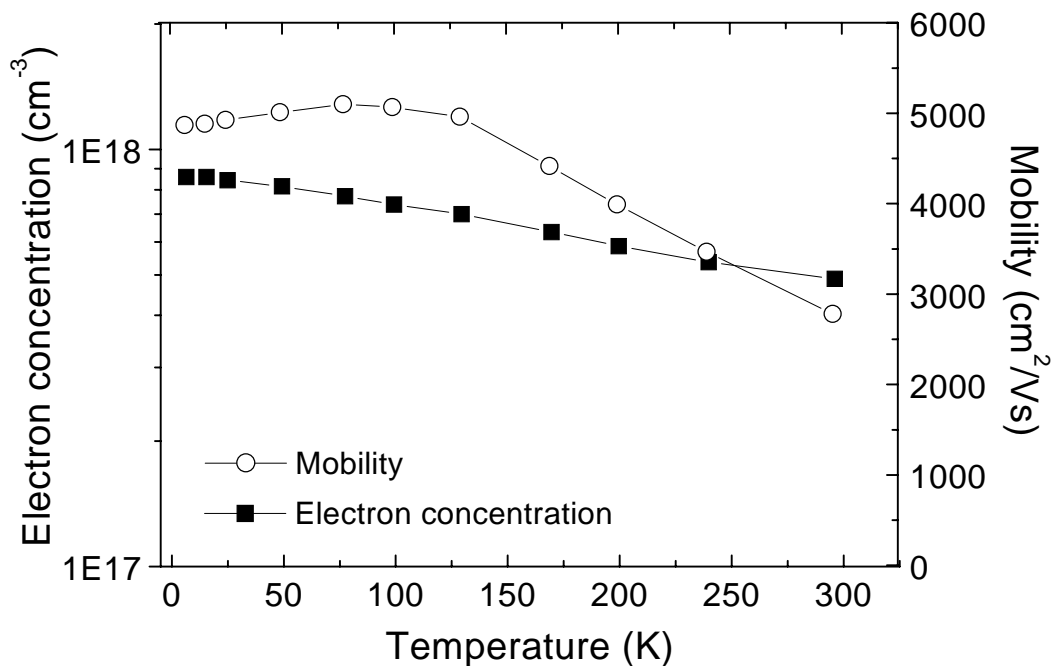


Figure 4.9: Temperature dependent Hall measurement of tellurium-doped GaSb.

more detail, one sample was analysed by a temperature dependent Hall measurement in the range between Helium temperature and 300K (figure 4.9).

At first sight one might attribute the surprising result to a high concentration of a compensating background acceptor with a high activation energy or to the temperature dependence of the surface and interface depletion widths (e. g. [67]). However, the principal explanation for the observed behaviour is the small energy gap between the Γ minimum and the lowest L minimum (~ 0.07 eV [83]): The data shown in figure 4.9 were analysed in the one-carrier-type approximation, i. e.

$R_H = -\frac{1}{e \cdot n}$. At elevated temperatures this assumption is not valid because L valleys will be populated and contribute to the conduction. As the related mobility is much lower for electrons in an L valley than for electrons in the Γ valley, the Hall coefficient must be written as $R_H = -\frac{n_\Gamma \cdot \mu_\Gamma^2 + n_L \cdot \mu_L^2}{e(n_\Gamma \cdot \mu_\Gamma + n_L \cdot \mu_L)^2}$. Consequently, even for a

constant total number of electrons the Hall coefficient will increase when $\frac{n_L}{n_\Gamma}$ increases and the single-carrier-type approximation will pretend lower carrier concentrations at higher temperatures.

Besides, the experimentally confirmed condition for the transition between activated and metallic conduction is $N \cdot a_B^3 \approx 0.02$ ([91], p. 253) where N is the carrier concentration and a_B is the Bohr radius of the impurity. As $N \cdot a_B^3 \approx 4$ for the sample in figure 4.9, metallic conduction must clearly be expected. This explains the high carrier concentrations as well at very low temperatures.

- 3) In figure 4.8 the 300K Hall measurements are well in agreement with the SIMS measurement of the atomic tellurium concentration. Taking into account the above

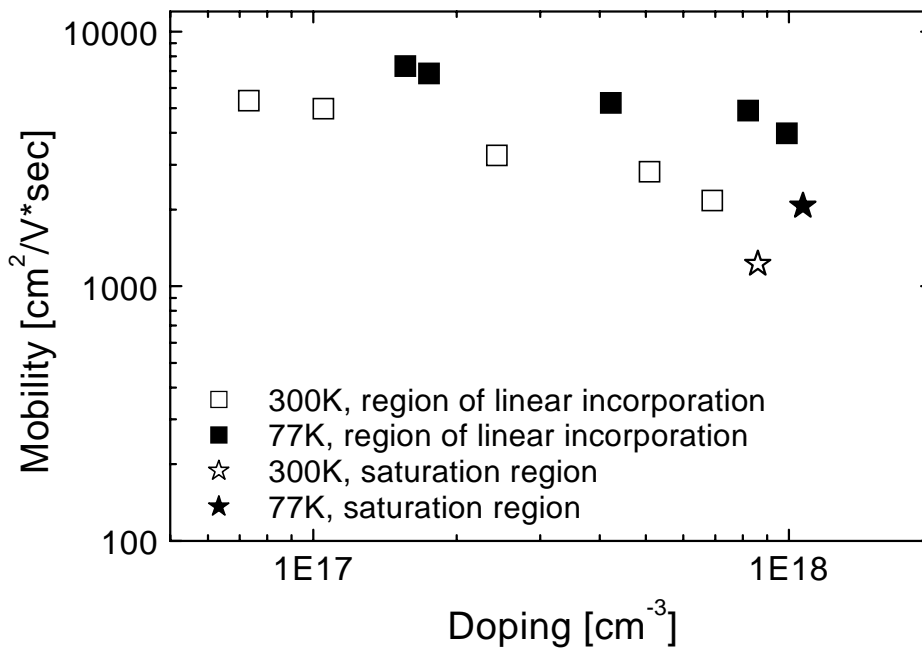


Figure 4.10: Mobility versus electron concentration for tellurium doped GaSb.

remarks, it should be more appropriate to accept the 77K Hall data as the “true” electron concentration. Consequently, the electron concentration would be higher than the atomic concentration of donor atoms. This apparent contradiction found a simple answer: The SIMS laboratory had used a 300K Hall measurement of a tellurium doped GaSb-sample for calibration purposes.

In addition, the carrier mobilities were measured for various different doping levels. The results are shown in figure 4.10. The comparably low mobility of the “saturation region”-sample can be explained by the formation of Ga-Te-complexes which was described above. A comparison with the electrical data of other groups (e. g. [31, 81]) shows that the values of figure 4.10 represent very high quality material.

4.2.5 Optical properties versus growth parameters

A detailed discussion and literature summary concerning the photoluminescence of homoepitaxial GaSb is included in chapter 5. However, a brief description of the PL properties of GaSb-samples as a function of the growth parameters will be given in the present section 4.2.5.

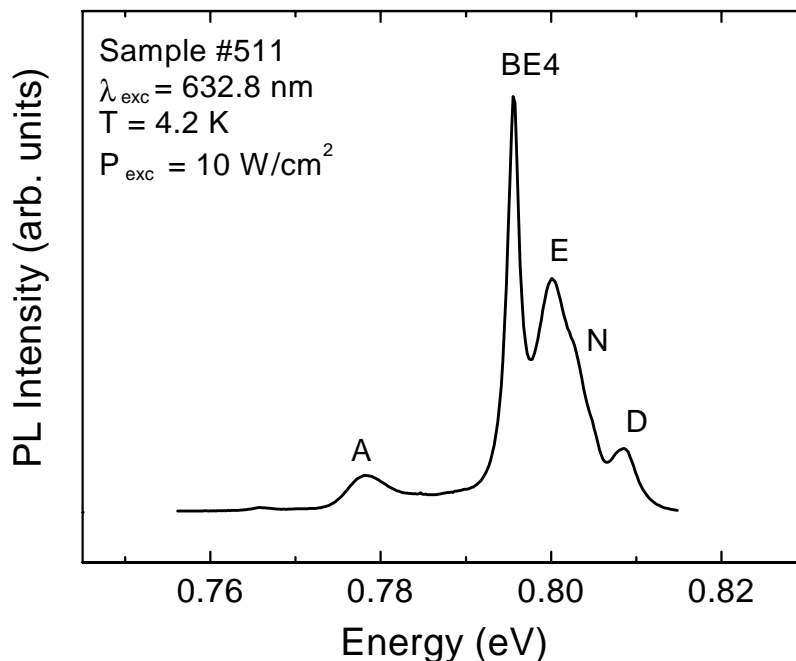


Figure 4.11: Typical photoluminescence spectrum for homoepitaxially grown undoped GaSb in this work.

As demonstrated in figure 4.11, the PL of the GaSb samples grown in this work shows mainly the following peaks:

- A-line: The transition related to this line involves the native acceptor defect. The line is interpreted as donor acceptor pair transition or (e, NA^0) transition in the literature.
- BE4-line: The line is generally interpreted as PL recombination of an exciton bound to an unidentified neutral acceptor. In high quality material an LO-phonon replica of this

peak can be observed at 0.767 eV, corresponding to a related wavenumber of $\bar{\nu}_{LO}(\Gamma) = 232.6 \text{ cm}^{-1}$ [66].

- E-line: For MBE- and MOVPE-grown layers this line has been ascribed to a donor acceptor pair transition or to an (e, A^0) transition involving a previously unidentified acceptor. The related acceptor impurity will be identified as silicon in chapter 5.
- N-line, D-line: In chapter 5 these lines will be identified as bound exciton recombination and band-band luminescence, respectively.

As the native acceptor (NA) is believed to be a gallium vacancy-gallium antisite complex, the blocking of Sb-sites with antimony at higher V/III ratios can be expected to decrease

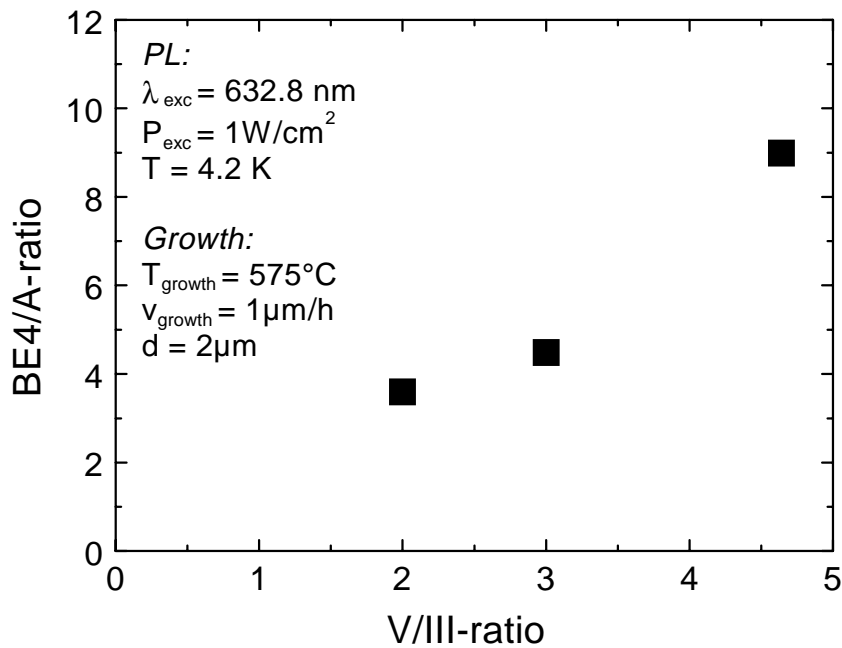


Figure 4.12: Photoluminescence: BE4/A- versus V/III-ratio for nominally undoped GaSb

the NA concentration. This assumption was confirmed in growth experiments from nonstoichiometric melts where increased Sb concentrations produced significant reductions in the level of background acceptors [120]. As the A-line transition involves the native acceptor defect, Chidley et al. [30] suggested the relative strengths of the A- and BE4-lines as a guide to material quality. Correspondingly, they report that electrically higher quality material shows a higher BE4/A-ratio. In contrast, Wang et al. report in [118] that the PL of their layers with the best electrical properties have very strong A-lines, suggesting that a strong acceptor transition is *not* necessarily associated with a high hole concentration. The BE4/A-ratios as a function of the V/III-ratio for otherwise comparable layers grown in the present work are shown in the figure 4.12.

An increase of the BE4/A-line intensity with increasing V/III-ratio was observed. This result is in line with the above assumption of lower NA concentrations in Sb-rich growth environments. However, a related decrease of the hole concentration in Hall measurements could not be observed. This confirms the results of Wang mentioned above, but contradicts Chidley et al. [30].

In addition, it is of interested to examine the BE4/A-ratio and the integrated PL intensity as a function of the growth temperature (figure 4.13). Both quantities show the same behaviour and have a maximum at around 600°C. It is interesting to note that the hole concentration as measured by Hall showed the tendency to decrease when the growth temperature was lowered in the investigated range between 625 and 550°C. Again, as already stated by Wang et al. [118] and mentioned above, the interpretation of the optical data is not in agreement with the majority carrier concentration as measured by Hall. Besides, there might as well be a link to the V/III-results shown in the above figure 4.12: While TEGa was shown to have a constant activation in the investigated temperature range (see section 4.2.3), TMSb is in the kinetically controlled regime and the effective V/III-ratio will increase with increasing temperature up to approximately 600°C. The observed increase of the BE4/A-ratio with increasing temperature might therefore well be due to an increase of the effective V/III-ratio as seen in figure 4.12.

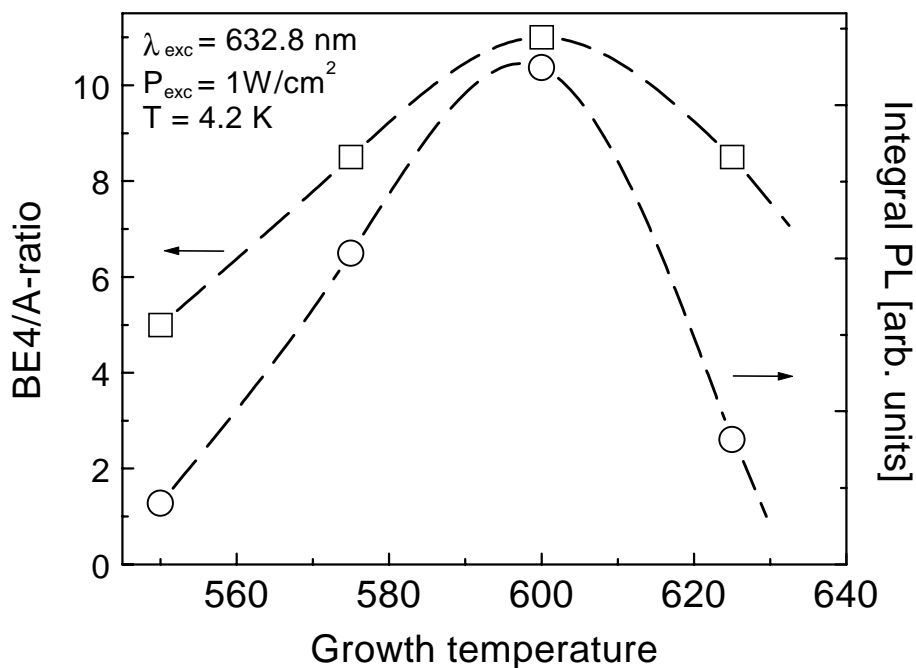


Figure 4.13: Photoluminescence: BE4/A-ratio versus growth temperature for nominally undoped GaSb.

4.3 MOVPE of (AlGa)(AsSb)

4.3.1 Introduction

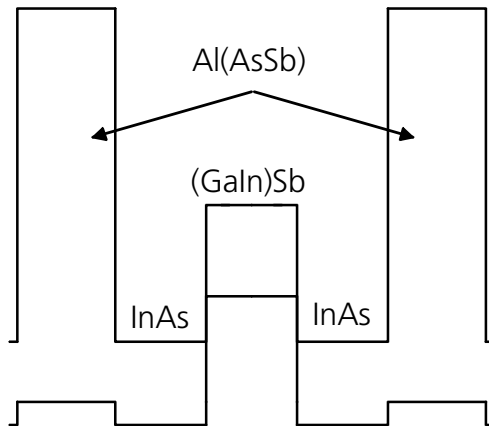


figure 4.14:

Band structure of a „W“-laser [107]. In this type II-interband laser structure the GaSb hole quantum well is bounded by two InAs electron quantum wells. Due to the second electron quantum well there is a significant wavefunction overlap in spite of the type II-alignment.

Al-containing antimonides are of interest not only for multijunction photovoltaic devices (see chapter 2) but as well for example as confinement layers in near- and mid-infrared emitters. As many chemicals in gas phase have characteristic absorption lines in the mid-IR, related lasers are of interest for chemical sensing. Besides, there is a wide range of possible military applications including IR countermeasures and IR illumination. Both type-I and type-II interband lasers are being developed. A very interesting type-II design is the so-called “W”-laser: As the GaSb/InAs junction is a crossed gap type-II system with the conduction band of InAs lying below the valence band of GaSb, in Al(AsSb)/InAs/(GaIn)Sb/InAs/Al(AsSb)-structures there is a hole quantum-well (i. e. the (GaIn)Sb) surrounded by two electron quantum-wells (i. e. the InAs) again surrounded by Al(AsSb) layers which confine only electrons and have almost no valence band offset to InAs. Hence, the conduction band alignment in real space

looks like a “W”. The advantages of this structure include a significant wavefunction overlap despite the type II-alignment, very good carrier confinement, and the suppression of Auger recombination. A brief review on this subject can be found in [107]. In addition to those mid-IR applications (i. e. $\sim 3 - 5 \mu\text{m}$), the Al-containing antimonides are as well of great interest for telecommunication wavelengths ($\sim 1.55 \mu\text{m}$): Due to the large difference in the refractive indices of Ga(As)Sb and Al(As)Sb, high reflectivity mirrors for $1.55 \mu\text{m}$ -vertical cavities can be deposited on InP, InAs, and GaSb, and related lasers are being developed [11, 42, 61, 62, 104]. Additionally, the band alignment of InAs/GaSb can as well be used for tunnel diodes [56, 57, 100].

Up to now, the growth of (AlGa)Sb is dominated by MBE and reports on successful MOVPE-grown devices are very rare [111-113, 117] due to the extremely difficult MOVPE-deposition of these materials. In order to illustrate the specific problems, some typical features of the MOVPE of Al-containing *arsenides* will be summarised before the actual growth of Al-containing *antimonides* will be described.

As already mentioned in section 4.1, the atomic hydrogen from the arsine decomposition is very important for the saturation of organic radicals that arise from the decomposition of the group III precursors. Consequently, a reduced carbon

incorporation is usually found in (AlGa)As at elevated V/III-ratios, no matter if AsH₃ or TBAs are used [69]. As the aluminium concentration x_{Al} of (Al_xGa_{1-x})As does usually not depend on the V/III ratio or the employed As-precursor [128], the group V overpressure can easily be used as a free parameter to optimise the material quality. In order to verify this behaviour, (Al_{0.8}Ga_{0.2})As-layers were deposited at various temperatures and V/III-ratios, and the carbon contamination levels were measured by SIMS. The results are shown in figure 4.15a. As expected, the carbon level in (Al_{0.8}Ga_{0.2})As was found to decrease significantly when the V/III ratio was increased, while a temperature increase led to higher carbon contaminations.

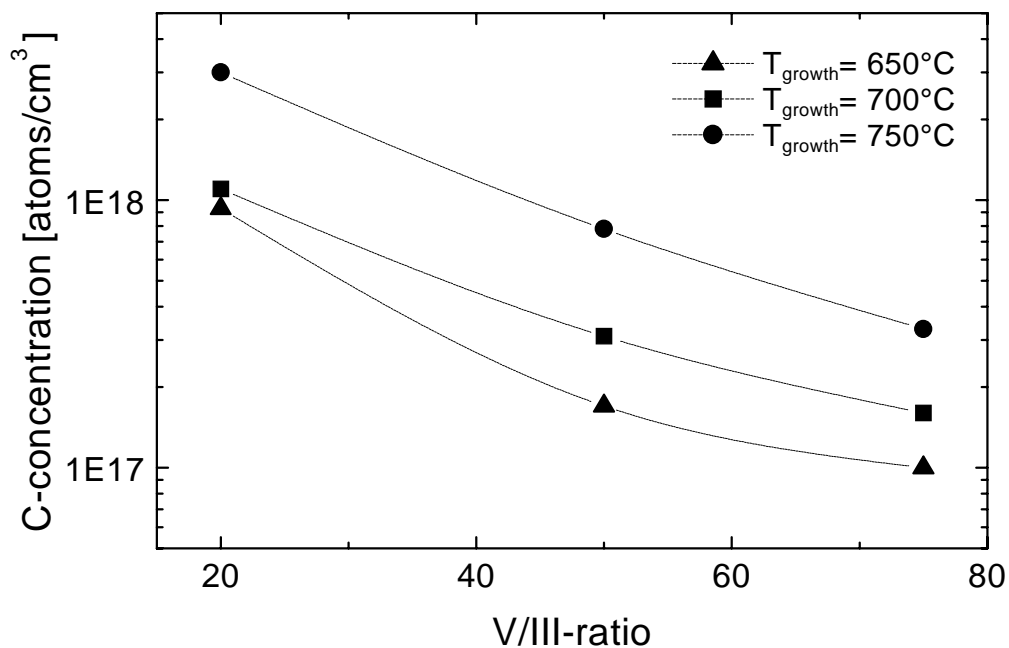


Figure 4.15a: Carbon contamination level in (Al_{0.8}Ga_{0.2})As grown using TMGa, TMAI and AsH₃ at different growth temperatures and V/III-ratios.

Similarly, when arsine is used as group V source, reduced oxygen concentrations are found in (Al_{0.8}Ga_{0.2})As when higher V/III-ratios and growth temperatures are employed. Related SIMS-measurements are shown in figure 4.15b. As oxygen forms a deep level, the material quality is much improved at reduced O-concentrations.

It was already described in section 4.1 that antimonides have to be grown in a very narrow range of V/III ratios close to unity. It was as well pointed out that no group V hydride can be used as antimony source. As a consequence, a saturation of organic radicals or oxygen impurities can not take place when (AlGa)Sb is grown. The above methods to improve the quality of (AlGa)As can not be employed for (AlGa)Sb. Thus, oxygen and carbon impurities are the major problem for this material.

Another major challenge is based on the low growth temperature of the antimonides: Here, the standard Al-precursor TMAI results in growth in the kinetically controlled regime (or even no growth at all, see section 4.3.2), where its incomplete pyrolysis

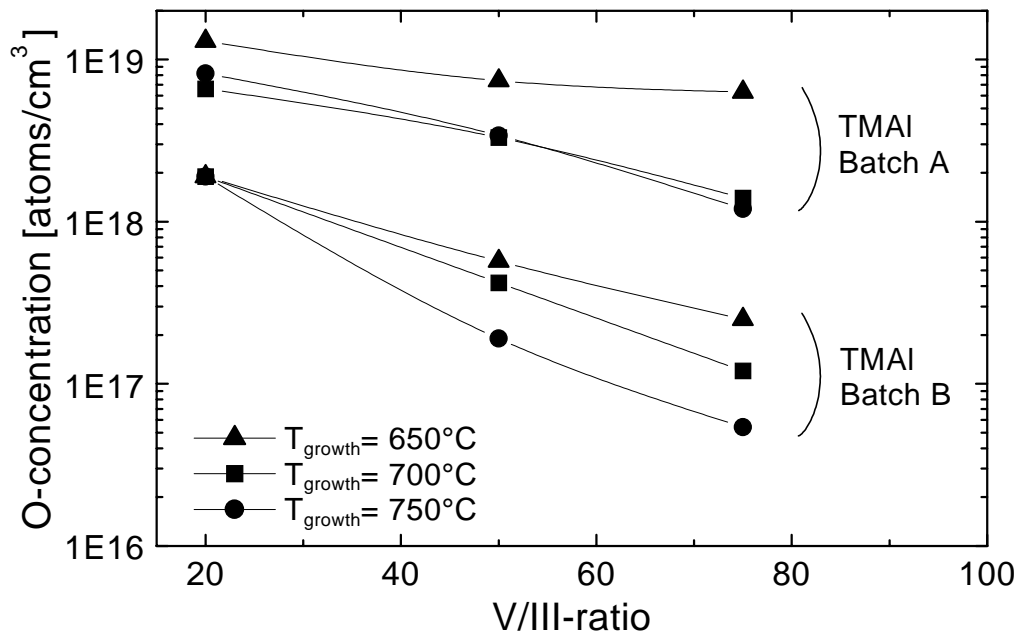


Figure 4.15b: Oxygen contamination level in $(\text{Al}_{0.8}\text{Ga}_{0.2})\text{As}$ grown using TMGa, TMAI and AsH_3 at different growth temperatures and V/III-ratios.

determines the growth rate and composition of the crystal. Therefore, novel Al-precursors are being developed and tested for the MOVPE-growth of $(\text{AlGa})\text{Sb}$. This work mainly focuses on tritertiarybutylaluminium [44, 109, 111-113, 116, 117] and amine alane adducts [4, 5, 20-22, 65]. A few reports can as well be found on TMAI [63] and an “all-ethyl” (i. e. TEGa, TEAl, TESb) approach [17]. These novel precursors have to be employed in extremely high purity grades because the quality of $(\text{AlGa})\text{Sb}$ can not be improved by varying the growth temperature or the V/III ratio, as mentioned above. Besides, as the low decomposition temperatures come along with a high chemical reactivity, the novel low-temperature precursors lead to severe problems concerning pre-reactions (e.g. alkyl exchange reactions) and pre-deposition.

In addition, one has to consider that the lattice mismatch between GaSb and $(\text{AlGa})\text{Sb}$ is much more significant than between GaAs and $(\text{AlGa})\text{As}$. Therefore, for thick bulk layers arsenic has to be added to the crystal in order to adjust the correct lattice constant. As the decomposition temperature of arsine is quite high, the thermal decomposition behaviour of TBAs is much better suited for this purpose [95]. Due to the nowadays very good quality of this precursor, it can be employed without any additional problems in a standard bubbler configuration.

4.3.2 Influence of growth temperature

As already described in the preceding sections, typical growth temperatures for Al-containing antimonides are lower than for analogous arsenides and phosphides. This can lead to incomplete pyrolysis of precursors, resulting in growth in the kinetically controlled regime. As a consequence, the thermal activation behaviour of novel aluminium precursors in a given reactor environment is of particular interest. The two most promising precursors TTBAI and DMEAA (plus TMAI for comparison) were chosen to be tested for the growth of (AlGa)Sb at various different growth temperatures.

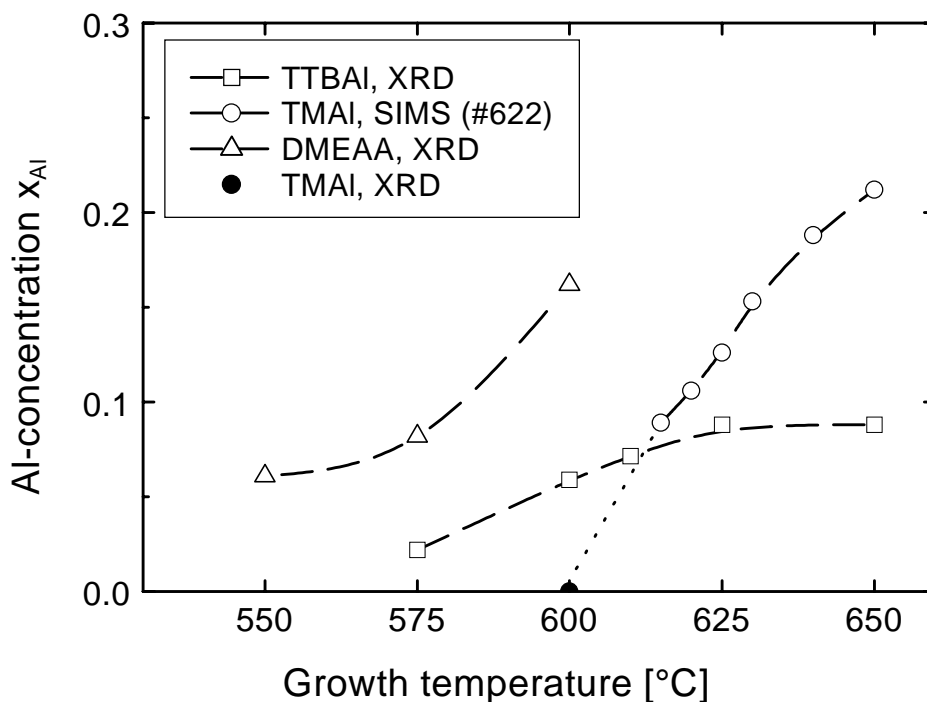


Figure 4.16: Al-concentration in (AlGa)Sb as a function of growth temperature. The given lines are a guide to the eye. Gas phase concentration ratios of the aluminium precursors: TTBAI 0.18, TMAI 0.56, DMEAA 0.53. The SIMS data of layer #622 were calibrated with an HR-XRD measurement of a corresponding (AlGa)Sb-bulk sample (#617). No aluminium was found in (AlGa)Sb grown with TMAI at $T_{\text{growth}} < 615^{\circ}\text{C}$.

As the growth rate of GaSb grown from TEGa and TMSb was found not to depend on the growth temperature between 575°C and 625°C (see section 4.2.3), the Al-content x_{Al} in the layers as measured by HR-XRD and SIMS could be expected to be a direct indicator for the efficiency of the Al-precursors. Here, the SIMS count rates for AlSb were calibrated using the results of HR-XRD measurements on related bulk layers. A linear relation was found. However, the SIMS sputter conditions for (AlGa)Sb had not been fully optimised by the SIMS laboratory, leading to a blurred depth resolution deeper in the layers. If blurred peaks occurred, the maximum count rates were used throughout this work. The results on the temperature behaviour are shown in fig. 4.16.

TMAI shows a steep increase of x_{Al} between 615°C and 650°C. A similar result is reported in [55] for the temperature range 640°C to 680°C. In experiments below 615°C, HR-XRD did not give a peak related to (AlGa)Sb, suggesting that no significant amounts of aluminum were present in the layers. This result did not depend on the concentration of TMAI in the gas phase.

TTBAL was employed at growth temperatures between 575°C and 650°C. At first sight, the observed behaviour of the precursor seems to represent the typical pyrolysis behaviour of metalorganics in the kinetically controlled regime. However, TTBAL is known to decompose already between 100°C and 200°C [108]. Consequently, the observed temperature dependence must be due to a different effect. At high temperatures the Al-concentration saturates at a value that represents approximately 50% of the gas phase concentration defined by the molar flow rates as $X_{Al} = \frac{[TTBAL]}{([TTBAL] + [TEGa])}$. The poor efficiency in combination with the low vapour pressure of TTBAL (see section 4.3.3) led to extremely low growth rates in the multiwafer reactor in the order of a few hundred nanometers per hour. This overall behaviour clearly limits the usefulness of TTBAL for the MOVPE of Al-containing Sb-compounds in multiwafer reactors.

In contrast, DMEAA allowed reasonable growth rates for (AlGa)Sb even at the lowest employed temperature of 550°C. However, this is merely due to its higher vapour pressure because the overall efficiency is as poor as for TTBAL. Just like TTBAL, DMEAA is known to decompose readily at very low temperatures and the observed temperature dependence of the Al-concentration is again believed not to reflect the thermal activation behaviour of the precursor. Increasing the total carrier gas flow rate led to a higher efficiency of DMEAA, indicating that the related activation profile shows a very steep decrease just after the inlet nozzle of the reactor. This result stands for severe pre-deposition and was confirmed by the deposition pattern visible on the susceptor.

In sections 4.3.5 and 4.3.6 it will be proven that DMEAA and TTBAL are subject to pre-reactions involving both TMSb and TEGa. The poor efficiencies of TTBAL and DMEAA measured above can therefore be attributed to a combination of pre-reactions and (at least in the case of DMEAA) as well pre-deposition. The observed temperature dependence of the aluminium incorporation can possibly be attributed to the thermal decomposition of a pre-reaction product over the hot susceptor. Whether the observed temperature dependence of the TMAI efficiency is due to its decomposition behaviour or as well to pre-reactions must remain unclear. The above findings could not be compared to results from other groups because no temperature dependent efficiency data for TTBAL or DMEAA are available in the literature.

In summary, the thermal activation behaviour of TMAI is not suited to the growth of (AlGa)Sb in the multiwafer reactor. The low-temperature sources DMEAA and TTBAL suffer from pre-reactions and pre-deposition. Both precursors show a poor overall efficiency which is as well temperature dependent. While the high-vapour pressure source DMEAA can still give reasonable growth rates in spite of its poor efficiency, TTBAL can not be recommended from this point of view.

4.3.3 Aluminium incorporation

Accurate control of the crystal composition is a very important point for the growth of ternaries and quaternaries. Hence, the Al-concentration in the crystal was measured for various different gas phase compositions. The situation gets further complicated in the case of TTBAI and DMEAA because the group V partial pressure in the reactor will influence the group III composition of the crystal (see section 4.3.5). The data in this section must therefore be interpreted cautiously. However, the main phenomena get clear even by a merely qualitative discussion.

The analysis for TTBAI is particularly difficult because the literature data on the vapour pressure are contradictory [44, 116]. Therefore it was decided to start the analysis by growing and analysing some structures of the well-known (AlGa)As system. Thereby, a minimum value for the vapour pressure of the aluminium precursor can be estimated.

The functional dependence between the group III partial pressures in the gas phase and the aluminium concentration in the solid can be described with the following expression that defines a "well-behaved" precursor:

$$\frac{f_{TTBAI}(\dots) \cdot P_{\text{partial}}(TTBAI)}{f_{TEGa}(\dots) \cdot P_{\text{partial}}(TEGa) + f_{TTBAI}(\dots) \cdot P_{\text{partial}}(TTBAI)} = x_{Al} = (1 - x_{Ga})$$

Here, $P_{\text{partial}}(\dots)$ stands for the nominal partial pressures of the precursors in the growth atmosphere and x_{Al} stands for the aluminium concentration in the solid. The functions

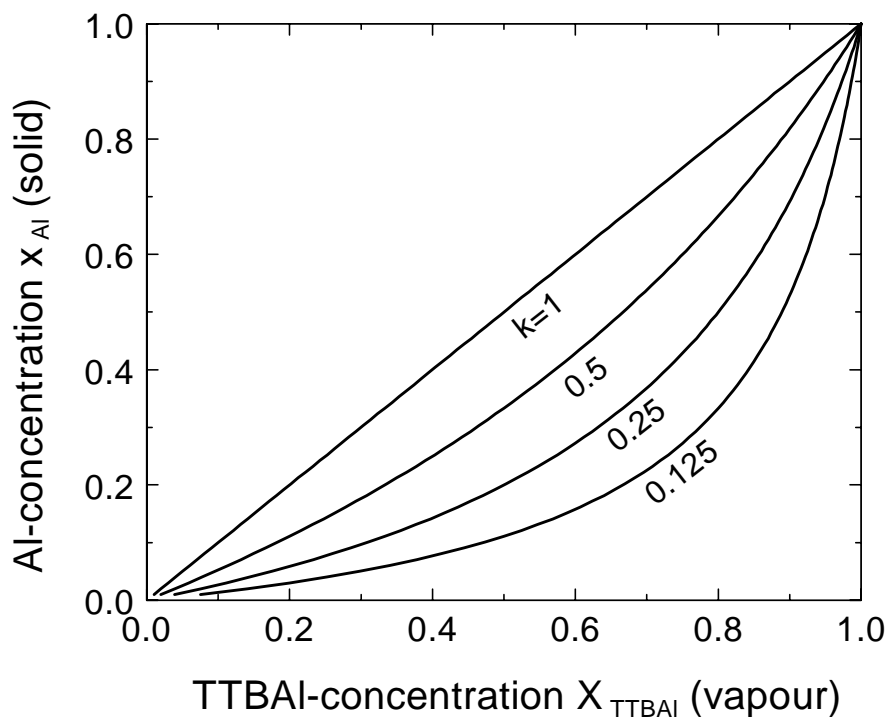


Figure 4.17: Standard model for the incorporation behaviour of well-behaved precursors. (AlGa)As was chosen as an example where different values of the distribution coefficient k are shown.

f_{TTBAI} and f_{TEGa} describe all deviations of the real conditions from the nominal values. These functions will usually not vanish, and so the relation can be summarized with the definition $f^{III}(\dots) := f_{TEGa}(\dots)/f_{TTBAI}(\dots)$:

$$\frac{f^{III}(\dots) \cdot P_{partial}(TTBAI)}{P_{partial}(TEGa) + f^{III}(\dots) \cdot P_{partial}(TTBAI)} = x_{Al}$$

This expression can be shown to be equivalent to the widely used description using a „distribution coefficient k “ with $k := f^{III}$:

$$\frac{x_{Al}}{x_{Ga}} = k \cdot \frac{P_{partial}(TTBAI)}{P_{partial}(TEGa)}$$

This function can as well be written as:

$$X_{TTBAI}^{vapour} := \frac{P_{partial}(TTBAI)}{P_{partial}(TTBAI) + P_{partial}(TEGa)} = \frac{1}{1 + k \cdot \frac{1 - x_{Al}^{solid}}{x_{Al}^{solid}}}$$

This is an important expression because it contains only the usual quantities X^{vapour} and x^{solid} which are easy to handle. The function is shown in figure 4.17 for different values of k . As it contains only one fitting parameter, very few data points are usually sufficient in order to obtain the full incorporation model for all ternary crystal compositions.

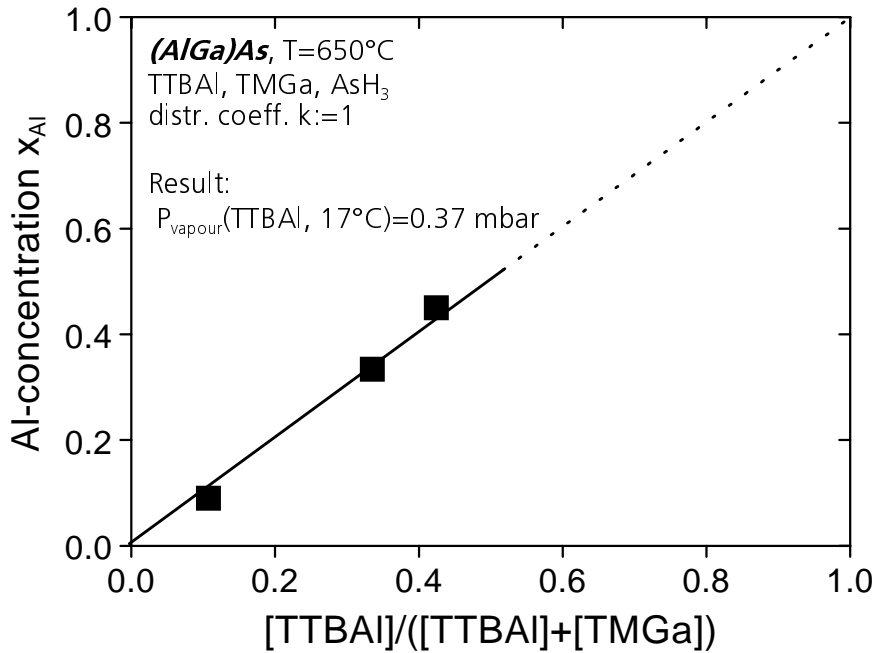


Figure 4.18: *TTBAI-incorporation behaviour in (AlGa)As. In order to obtain a minimum value for the unknown vapour pressure of TTBAI, the distribution coefficient k is assumed as one and $P_{vapour}(TTBAI)$ is fitted to the data.*

As mentioned above, the situation is further complicated for TTBAI because the vapour pressure must be treated as unknown. An estimate for a minimum value can be obtained by assuming $k=1$ and treating the TTBAI vapour pressure as fitting parameter. The result is shown in figure 4.18: The (AlGa)As-incorporation behaviour of TTBAI can be described within the above mentioned standard model for well-behaved precursors. The corresponding fitting procedure gives a value of 0.37 mbar at 17°C for TTBAI. This result can now be used for the analysis of the incorporation behaviour in the antimonides, i. e. in (AlGa)Sb.

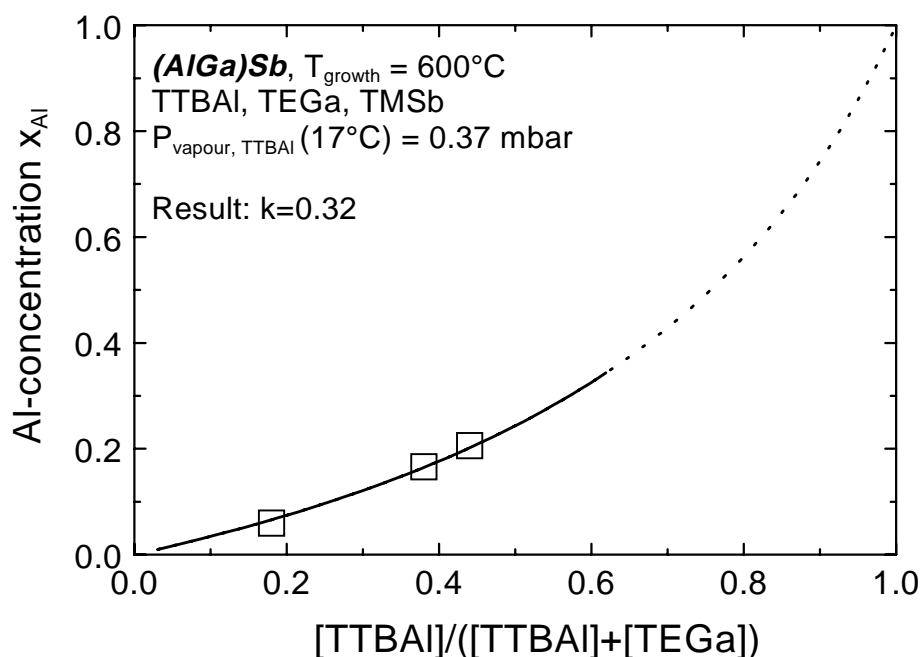


Figure 4.19: TTBAI-incorporation behaviour in (AlGa)Sb. The vapour pressure estimate of 0.37 mbar at 17°C for TTBAI gives a distribution coefficient of 0.32, i. e. a significantly reduced efficiency compared to (AlGa)As.

Three (AlGa)Sb layers with different Al-concentrations but otherwise identical growth conditions were deposited with TTBAI. The results are shown in figure 4.19. Again, the data can be described within the standard model for well-behaved precursors. However, a reduced efficiency of the TTBAI is found: A distribution coefficient of 0.32 results from the fitting procedure. This can partly be attributed to the employed temperature of 600°C (see figure 4.16), where TTBAI has not yet reached its maximum efficiency. However, the lack of efficiency can not be fully explained by the temperature argument. Further loss mechanism must be assumed (e.g. pre-deposition and pre-reactions, see previous section). A corresponding literature report [109] is discussed on page 58.

Similar experiments were performed with the DMEAA. As reliable data on the vapour pressure of this source are available from the manufacturers, no (AlGa)As-layers were grown in advance. DMEAA was widely used throughout this work for reasons derived in the following section. As a consequence, plenty of data points are available for the analysis of the incorporation behaviour. Here, both SIMS and HR-XRD measurements were used to determine the Al-concentration in the solid. The results are shown in figure 4.20. The SIMS data point marked as "normalization layer" was used for

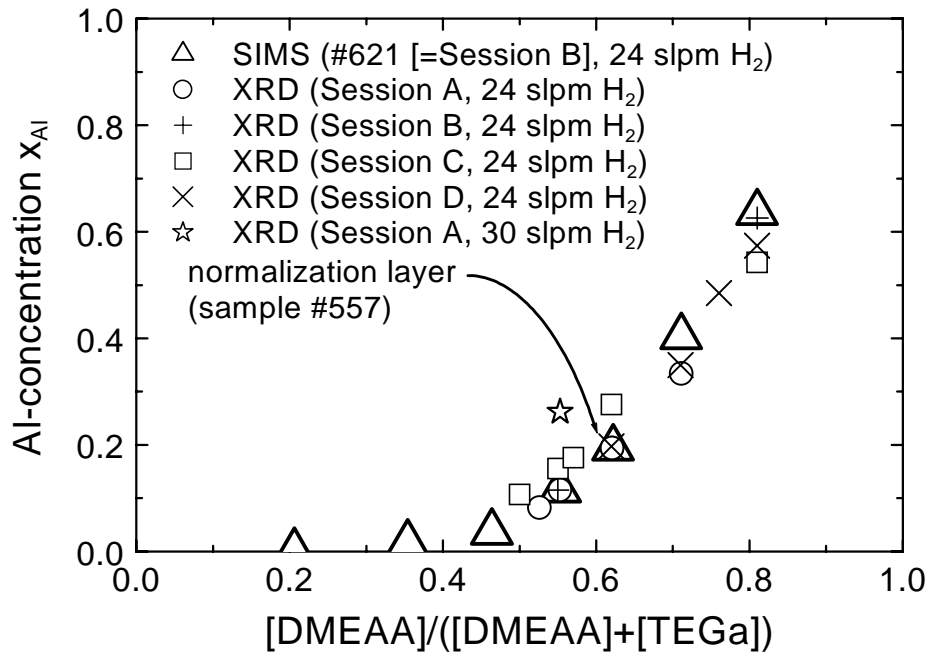


Figure 4.20: *DMEAA-incorporation behaviour in (AlGa)Sb. As no aluminium is found in the crystal for DMEAA-gas phase concentrations below approx. 0.35, the incorporation behaviour can not be described with the usual model.*

calibration of the SIMS count rate on the basis of a HR-XRD measurement of a corresponding bulk layer. The following results can be drawn from the data:

- 1) There is absolutely no aluminium incorporation for gas phase concentrations below approximately 0.35. Consequently, DMEAA can not be described by the above standard model. It is no "well-behaved" precursor with respect to the incorporation behaviour.
- 2) The SIMS data are well in agreement with the HR-XRD results for layers grown at identical conditions. There are three regions where deviations occur:
 - For DMEAA concentrations above 0.7 the SIMS data are higher than the HR-XRD results. This can be explained by the onset of relaxation in those layers: For a given Al-concentration, the XRD-peak lies closer to the substrate peak in partly relaxed layers compared to fully strained layers. As all measurements were interpreted based on the assumption of fully strained crystals, the XRD-results of partly relaxed layers underestimate the true Al-concentrations. This becomes particularly evident for the layers with the highest Al-concentration. Here, a very thin (i. e. almost fully strained, ~165 nm) bulk sample gave the same result in HR-XRD and SIMS, while the two other samples suggested decreasing Al-concentrations with increasing thickness (i. e. increasing relaxation, ~250nm and ~375 nm).
 - For DMEAA concentrations in the range 0.5 ... 0.7 the XRD-data from session C lie systematically above all other points. Here, a new DMEAA-bubbler had been connected to the system. This bubbler not only gave increased Al-concentrations but as well significantly higher oxygen levels. These two findings may well have the same underlying reason: The corresponding alane diethyletherate adduct has a higher vapour pressure than the dimethylethylamine alane adduct, leading to both a higher oxygen *and* a higher aluminium concentration.

- The XRD-data point for a bulk sample grown at an increased H₂-carrier gas flow rate of 30 l/min lies well above all other data points. Clearly, the efficiency of DMEAA is increased at higher gas velocities. This is an indirect confirmation for the occurrence of parasitic pre-reactions and pre-deposition.

Unfortunately, no reports on the incorporation behaviour of DMEAA in (AlGa)Sb could be found in the literature. There is only one corresponding report on the behaviour of TTBAI [109] where the results are very similar to the above observations for DMEAA: Aluminium could only be found in the solid if a certain gas phase concentration was exceeded. Consequently the distribution coefficient was not well-defined. However, the TTBAI-efficiency was smaller than 1 everywhere. Just like in section 4.3.5, increasing the V/III-ratio led to a reduced Al-concentration in the solid. Based on these findings, Wang [109] as well suggests pre-reactions between TTBAI and TMSb, so that Al-containing species are depleted from the gas phase.

In summary, both precursors have been shown to be subject to a reduced efficiency. This is most likely due to pre-deposition and pre-reactions, so that Al-containing species are depleted from the gas phase. While TTBAI still has a “well-behaved” incorporation which can be analytically described with the standard distribution coefficient, the data points for DMEAA do not fit into the regular model.

4.3.4 Arsenic incorporation

As already said above, the lattice mismatch between GaSb and (AlGa)Sb is much more significant than between GaAs and (AlGa)As for comparable aluminium concentrations. Therefore, for thick bulk layers arsenic has to be added to the crystal in order to adjust the correct lattice constant. It was decided to use TBAs instead of arsine because the thermal decomposition behaviour of TBAs is much better suited for this purpose [95].

In order to analyse the mixing behaviour on the group V sublattice one would normally start with the expression derived above, adapted to the group V elements:

$$\frac{x_{As}}{x_{Sb}} = k \cdot \frac{P_{partial}(TBAs)}{P_{partial}(TMSb)}$$

However, Cao et al. [27] have pointed out that for alloys containing arsenic and antimony, arsenic is much more likely to be incorporated into the solid because the bond between arsenic and gallium is much stronger than between antimony and gallium. As both TMSb and TBAs will be completely pyrolysed at typical growth temperatures, thermodynamics controls the incorporation behaviour [27] and a very high distribution coefficient will result due to the different bond strengths. In this context, Chen et al. [29] have shown that the antimony concentration in Al(AsSb) saturates rapidly with increasing [TMSb]/[TMAI]-ratio (when [TBAs]/[TMAI] is held constant), and the arsenic concentration in Al(AsSb) is a linear function of the [TBAs]/[TMAI]-ratio (when [TMSb]/[TMAI] is held constant). In conclusion, excess antimony in the gas phase did not lead to its further incorporation into the Al(AsSb) solid, while arsenic behaved very much like a group III element in standard material systems such as

(AlGa)As. These results can be well understood on the basis of the different bond strengths mentioned above.

Consequently, an analysis according to the above expression for the group V distribution coefficient does not make much sense. It can rather be expected that in the case of Ga(AsSb) the arsenic incorporation is better described by:

$$\frac{x_{As}}{x_{Ga}} = k \cdot \frac{P_{partial}(TBAs)}{P_{partial}(TEGa)}$$

For small arsenic concentrations this expression can be approximated as

$$x_{As} = c \cdot \frac{P_{partial}(TBAs)}{P_{partial}(TEGa)}$$

where c is a free fitting parameter. This linear approximation should be suitable to describe the arsenic incorporation in those concentration ranges which are of interest for the lattice matching of (AlGa)(AsSb). In order to verify this assumption, GaSb/Ga(AsSb)-superlattices were chosen as test structures. This has two advantages over the deposition of simple ternary bulk layers: Firstly, the growth rate can be determined very accurately from the superlattice satellite peaks in the HR-XRD. Secondly, it has to be considered that the lattice constant of Ga(AsSb) is highly mismatched to GaSb even for very small As-concentrations. Therefore a thick bulk layer for XRD-analysis could only contain extremely small amounts of arsenic before relaxation would occur. In a suitably designed GaSb/Ga(AsSb)-superlattice there can be much more arsenic in the Ga(AsSb) layers because their total thickness is reduced. Still, the thickness of the single Ga(AsSb) layers and the number of superlattice periods are very limited in

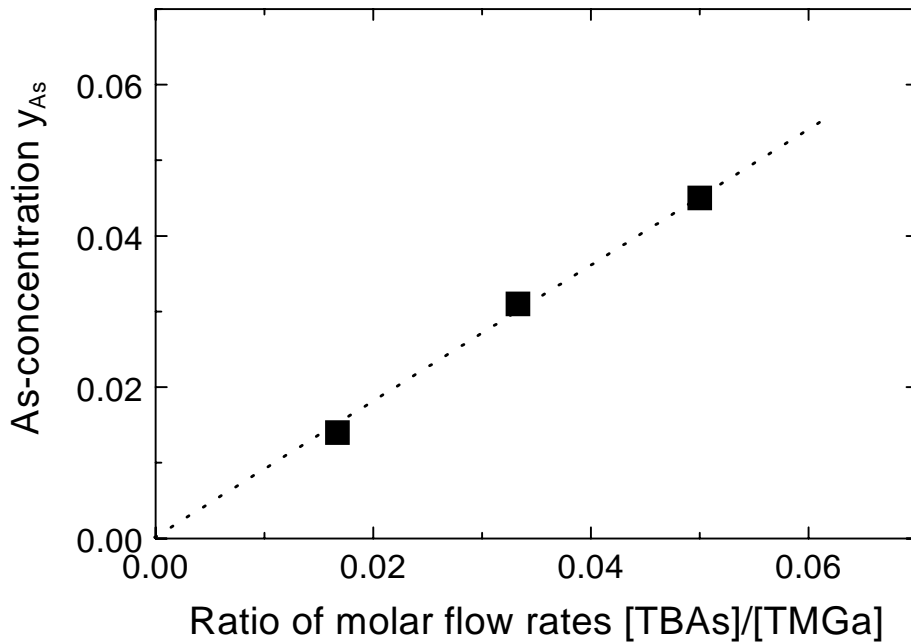


Figure 4.21: As-incorporation into Ga(AsSb). As expected, the arsenic concentration is found to be a linear function of the molar flow rate ratio [TBAs]/[TMGa].

order to prevent relaxation. A suitable structure was developed which finally contained 20 periods of 24 nm GaSb and 6 nm Ga(As_{0.03}Sb_{0.97}) (compare section 4.2.3). An example for an HR-XRD rocking measurement can be found in figure 4.6. The results for small arsenic concentrations are shown in figure 4.21. The experiments illustrated in the figure were performed with TMGa, but the same behaviour was in principle found as well for TEGa. The above assumption of a linear incorporation behaviour according to

$$x_{As} = c \cdot \frac{P_{\text{partial}}(\text{TBA}s)}{P_{\text{partial}}(\text{TEGa})}$$

is clearly confirmed with a fitting constant c close to unity. Consequently, the arsenic concentration in quaternary antimonides can easily be controlled. The observed incorporation behaviour should even make the group V mixing for lattice matching of Ga(AsSb) and Al(AsSb) to InP substrates a relatively straightforward task.

Eventually it should be noted that the necessary partial pressures for TBAs are extremely small. Only a double-diluted circuit can be expected to be a reliable source.

4.3.5 Parasitic pre-reactions: Influence of TMSb- and TBAs-partial pressure

When (AlGa)As is grown in a standard MOVPE process using TMGa/TMAI/AsH₃, the excess arsine in the growth atmosphere does generally not influence the group III distribution coefficient. In other words: As no parasitic pre-reactions occur in the gas phase, the employed V/III ratio has no influence on the crystal composition. On the

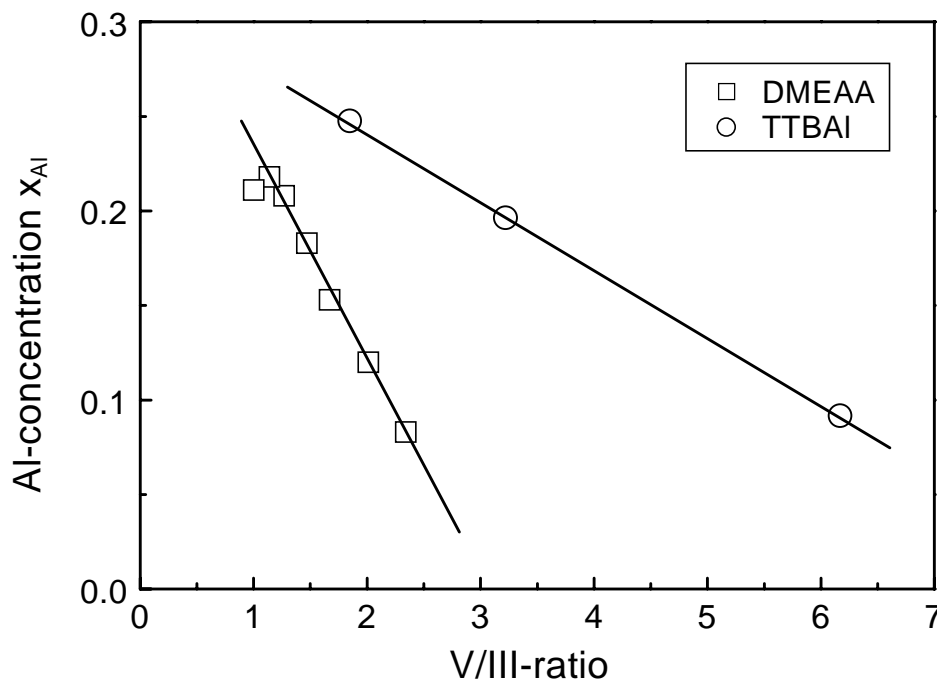


Figure 4.22: Al-concentration in (AlGa)Sb as a function of the V/III-ratio. The observed behaviour suggests parasitic pre-reactions between TMSb and TTBAI/DMEAA.

contrary, for $(\text{AlGa})\text{Sb}$ it was shown in the preceding sections that both TTBAI and DMEAA are highly likely to be subject to parasitic pre-reactions involving the other precursors. However, so far it is unclear which of the other precursors undergoes pre-reactions with the aluminium sources, and to which extent.

In order to analyse the related behaviour with respect to the group V source, $(\text{AlGa})\text{Sb}$ was grown using DMEAA and TTBAI. While all other growth parameters were held constant, the V/III ratio was varied. The results are shown in figure 4.22. An increased V/III ratio led to a significantly reduced aluminium concentration in the solid for both aluminium sources. The effect is more dramatic in the case of DMEAA than for TTBAI. The observed behaviour can be attributed to severe pre-reactions between both Al-precursors and TMSb . The steeper decrease of the DMEAA-curve compared to the TTBAI is in line with the well-known high reactivity of amine alane adducts [97].

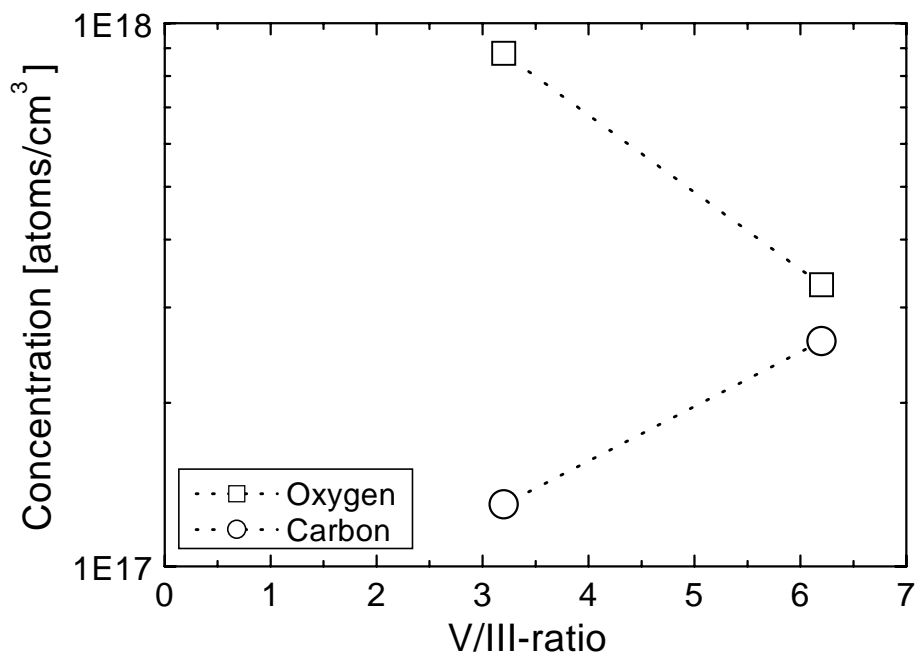


Figure 4.23: Oxygen and carbon concentration in $(\text{AlGa})\text{Sb}$ grown using TTBAI/TEGa/TMSb as a function of the nominal V/III ratio for fixed x_{Al} .

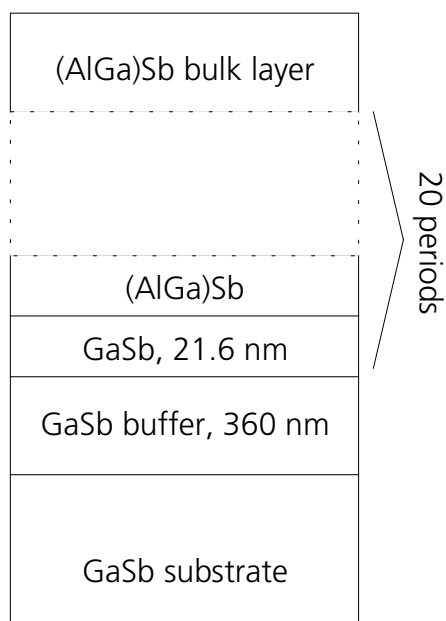
This result has important consequences: Firstly, the V/III ratio has to be adjusted as small as possible in order to maximise the group III efficiency. Secondly, the effective V/III ratio over the growth surface for different x_{Al} is difficult to determine due to the parasitic pre-reactions involving both group III- and group V-precursors. Thirdly, the incorporation studies of the preceding section have to be interpreted carefully because they depend on the various V/III ratios. Fourthly, the observed extent of the pre-reactions makes alkyl exchange reactions likely, which might eventually lead to an increased carbon incorporation into the layers (see section 4.3.7). Fifthly, it will be very difficult to compare the material quality of $(\text{AlGa})\text{Sb}$ grown at different V/III-ratios because the Al-concentration will always vary with the TMSb variation. However, in one of the many SIMS structures examined in this work two layers could be identified with an effectively identical aluminium concentration grown at different V/III ratios. The results for these layers grown using TTBAI is shown in figure 4.23. While the carbon concentration increases with increasing V/III ratio, the oxygen contamination decreases. This result

suggests that the origin of the carbon contamination is the group V source, while oxygen is present in the group III sources or the reactor environment. Consequently, high-purity Al-precursors should be employed at low V/III ratios in order to optimise the material quality.

Similarly, the oxygen and carbon concentrations were compared for lattice-mismatched (AlGa)Sb and lattice-matched (AlGa)(AsSb), both deposited with TTBAI. No beneficial influence of the additional TBAs in the gas phase could be observed. The amount of atomic hydrogen added to the process by the addition of a few percent of TBAs is probably not sufficient to lead to a significant effect.

4.3.6 Parasitic pre-reactions: DMEAA and TEGa

In the preceding section it was shown that the aluminium precursors TTBAI and DMEAA undergo parasitic pre-reactions involving the group V precursor TMSb. However, so far it remained unclear whether the gallium precursor TEGa is as well subject to pre-reactions with the aluminium precursors. This was analysed in detail for the precursor combination TEGa/DMEAA/TMSb.



The principal question can be expressed as „Is the efficiency of TEGa for the growth of GaSb the same as for the growth of (AlGa)Sb?“. In order to find an answer to this problem, 4 GaSb/(AlGa)Sb-superlattices with different Al-concentrations were grown and analysed by HR-XRD. The structure is presented in figure 4.24. The periodicity of the superlattice and the average aluminium concentration can be obtained from the related rocking curves. Besides, it can be assumed that the efficiency of TEGa in the aluminium-free layers of the superlattice is known from the results in section 4.2.3. The thick (AlGa)Sb bulk layer on top of the structures will not be analysed in this section. However, in section 4.3.11 this layer will be considered with respect to Al-carry over at interfaces. A thin GaSb cap layer is not included in figure 4.24.

Figure 4.24:

(AlGa)Sb superlattice structure. The film thicknesses of (AlGa)Sb are not specified and have to be treated as unknown.

Firstly the superlattices will be briefly analysed assuming that there are no pre-reactions between DMEAA and TEGa. This assumption will be shown to be wrong. In a different, *second* approach the extent of the pre-reactions will be estimated.

If no pre-reactions between TEGa and DMEAA are assumed, the growth rate of GaSb should be a linear function of the molar flow rate of TEGa into the growth chamber, no matter if DMEAA is present or not. If this assumption is valid, one can evaluate the periodicity of the superlattice on the basis of the known efficiency of GaSb and the superlattice's measured average aluminium concentration. The resulting superlattice

periodicity can then be compared to the measured value. This analysis will show that the above assumptions of a linear behaviour and the absence of pre-reactions do not hold for TEGa in (AlGa)Sb.

The growth rate of GaSb in a DMEAA-free environment has been measured by use of GaSb/Ga(AsSb)-superlattices (section 4.2.3). There, pre-reactions between TEGa and TMSb have not been observed. At a molar flow rate of 0.1197 mmol/min for TEGa a growth rate of 1.80 $\mu\text{m/h}$ was measured for GaSb. One can therefore assume the thickness of the GaSb in all GaSb/(AlGa)Sb-superlattices to be 21.6 nm according to the common GaSb-growth time of 43.2 seconds.

Neglecting the small difference (< 1%) in the lattice constants between AlSb and GaSb, the following definitions will be used in the calculations:

$$\begin{aligned} d[\text{GaSb}]_{(\text{AlGa})\text{Sb}} &:= d[(\text{AlGa})\text{Sb}] \cdot (1 - x_{\text{Al}}), \quad d[\text{AlSb}]_{(\text{AlGa})\text{Sb}} := d[(\text{AlGa})\text{Sb}] \cdot x_{\text{Al}} \\ \Rightarrow d[(\text{AlGa})\text{Sb}] &= d[\text{GaSb}]_{(\text{AlGa})\text{Sb}} + d[\text{AlSb}]_{(\text{AlGa})\text{Sb}} \end{aligned}$$

As a result the measured superlattice periodicity can be written as

$$d_{\text{SL}} = d[\text{GaSb}] + d[(\text{AlGa})\text{Sb}] = d[\text{GaSb}] + d[\text{GaSb}]_{(\text{AlGa})\text{Sb}} + d[\text{AlSb}]_{(\text{AlGa})\text{Sb}} \quad (1)$$

with $d[\text{GaSb}] = 21.6 \text{ nm}$ as shown above. Assuming that no pre-reactions occur, $d[\text{GaSb}]_{(\text{AlGa})\text{Sb}}$ can as well be calculated from the molar flow rate of TEGa into the reactor and therefore treated as known. A further equation can be now introduced for the average Al-concentration in the superlattice:

$$\bar{x}_{\text{SL}} = \frac{d[\text{AlSb}]_{(\text{AlGa})\text{Sb}}}{d[\text{AlSb}]_{(\text{AlGa})\text{Sb}} + d[\text{GaSb}]_{(\text{AlGa})\text{Sb}} + d[\text{GaSb}]} \quad (2)$$

Using equation (2) one can eliminate $d[\text{AlSb}]_{(\text{AlGa})\text{Sb}}$ in equation (1) and get the superlattice periodicity in the following form:

$$d_{\text{SL}} = d[\text{GaSb}] + d[\text{GaSb}]_{(\text{AlGa})\text{Sb}} + \frac{\bar{x}_{\text{SL}} (d[\text{GaSb}]_{(\text{AlGa})\text{Sb}} + d[\text{GaSb}])}{1 - \bar{x}_{\text{SL}}} \quad (3)$$

As a result, superlattice periodicities for the different samples can be calculated on the basis of the average aluminium concentration (#788: 0.26, #783: 0.24, #786: 0.20, #790: 0.11) and the known efficiency of TEGa. These calculated results are compared to the measured data in the following table:

Sample	#788	#783	#786	#790
measured $d_{\text{SL},m}$ [nm]	33	38	49	53
calculated $d_{\text{SL},c}$ [nm]	48	53	58	65
$d_{\text{SL},c} - d_{\text{SL},m}$	15	15	9	12

The discrepancy between the calculated and the measured values ($d_{\text{SL},c} - d_{\text{SL},m}$) shows directly that it is not justified to assume the absence of pre-reactions between TEGa and

DMEAA. All calculated periodicities are significantly higher than the measured values. This result clearly suggests that the efficiency of TEGa is very much reduced if DMEAA is present in the growth chamber, most likely due to pre-reactions between the two precursors.

Consequently, the growth rates of GaSb and AlSb in (AlGa)Sb must *both* be treated as unknown due to the unknown extent of the pre-reactions. The above calculations have to be modified correspondingly. However, one can still assume that in the Al-free part of the structure the TEGa-efficiency is known, i.e. $d[\text{GaSb}] = 21.6 \text{ nm}$. Equation (1) becomes

$$d_{SL} - 21.6 \text{ nm} = d[(\text{AlGa})\text{Sb}] = d[\text{GaSb}]_{(\text{AlGa})\text{Sb}} + d[\text{AlSb}]_{(\text{AlGa})\text{Sb}}$$

Now, the *measured* superlattice periodicity together with the *measured* average Al-concentration of the superlattice will be used to evaluate the growth rates of the binary constituents in (AlGa)Sb.

Equations (1) and (2) can be combined in order to get $d[\text{AlSb}]_{(\text{AlGa})\text{Sb}} = \bar{x}_{Sl} \cdot d_{Sl}$ and $d[\text{GaSb}]_{(\text{AlGa})\text{Sb}} = d_{SL} - 21.6 - d[\text{AlSb}]_{(\text{AlGa})\text{Sb}}$. As a result, $d[\text{AlSb}]_{(\text{AlGa})\text{Sb}}$ and $d[\text{GaSb}]_{(\text{AlGa})\text{Sb}}$ can now indeed be expressed in terms of the measured data \bar{x}_{Sl} and d_{SL} . This can now be used to analyse the decrease of the efficiency of TEGa as a function of x_{Al} : Knowing $d[\text{GaSb}]_{(\text{AlGa})\text{Sb}}$ and the corresponding molar flow rate of TEGa into the reactor, the efficiency of TEGa can be calculated as a function of the aluminium concentration in the (AlGa)Sb $x_{Al} = \frac{d[\text{AlSb}]_{(\text{AlGa})\text{Sb}}}{d[\text{AlSb}]_{(\text{AlGa})\text{Sb}} + d[\text{GaSb}]_{(\text{AlGa})\text{Sb}}}$. The results are

sample	788	783	786	790	(Al-free)
x_{Al}	0.75	0.55	0.37	0.18	0
efficiency TEGa [nm/mmol]	50	98	175	177	250

Figure 4.25 gives the efficiency of TEGa plotted against x_{Al} . It can be clearly seen that the efficiency of TEGa is reduced if the Al-concentration increases. This can be qualitatively understood by considering that the DMEAA molar flow rate was kept constant in all layers (0.1196 mmol/min): If in turn the amount of TEGa lost in pre-reactions with DMEAA is as well assumed to be approximately constant, then a larger fraction of the total TEGa flow is lost when less TEGa is introduced into the reactor at higher x_{Al} . Then, the overall result is that the efficiency of TEGa is effectively reduced when the molar flow rates of TEGa are reduced (see as well figure caption 4.25). In section 4.3.11 it will be shown that a certain carry-over of aluminium into the GaSb layers is highly likely. This effect is not included in the above model. Consequently, the Al concentrations in the (AlGa)Sb layers might be slightly smaller than the data calculated above.

As mentioned before, in all growth experiments the DMEAA molar flow rate into the

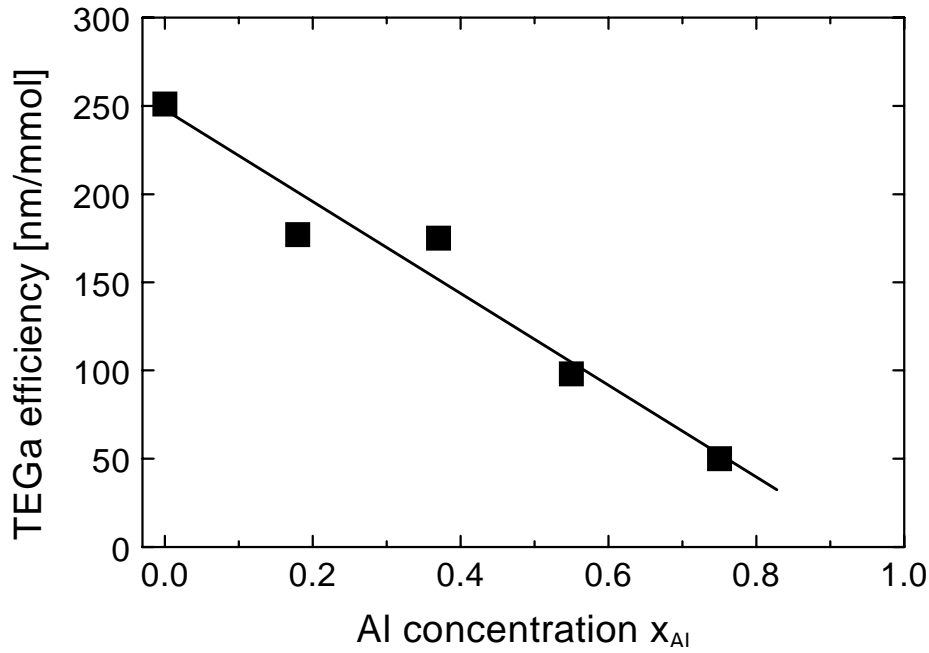


Figure 4.25: TEGa efficiency as a function of the Al-concentration x_{Al} in the solid. The behaviour suggests severe pre-reactions between TEGa and DMEAA. The molar flow rate of DMEAA into the reactor was held constant in all experiments, and the TEGa molar flow rate was varied in order to adjust x_{Al} . Assuming the amount of TEGa lost in pre-reactions with DMEAA to be more or less constant due to the constant flow rate of DMEAA, this constant amount of lost TEGa will naturally represent a bigger part of the total amount of TEGa at lower TEGa flow rates (i.e. higher x_{Al} 's). This model could serve as a qualitative explanation of the above behaviour.

reactor was held constant. In order to adjust x_{Al} the TEGa molar flow rate was adjusted correspondingly. Based on these constraints, the molar flow rate of both TEGa and DMEAA is known for a certain x_{Al} . It makes therefore sense to calculate an overall growth rate for (AlGa)Sb as a function of x_{Al} from the above data points: Using

$$v_{growth} [(AlGa)Sb] = v_{growth} [GaSb]_{(AlGa)Sb} + v_{growth} [AlSb]_{(AlGa)Sb}$$

and

$$v_{growth} [AlSb]_{(AlGa)Sb} = x_{Al} \cdot v_{growth} [(AlGa)Sb]$$

the result is:

$$v_{growth} [(AlGa)Sb] = \frac{v_{growth} [GaSb]_{(AlGa)Sb}}{(1 - x_{Al})}$$

The results are shown in figure 4.26. The dotted line is just a guide to the eye. Three different bulk samples with $x_{Al} \sim 0.18$ showed thickness fringes so that an independent determination of the (AlGa)Sb growth rate was possible. The resulting data agree within 5% with the values calculated above. As a result the above model for the growth rate of (AlGa)Sb and the related pre-reactions between DMEAA and TEGa are evidently supported. Consequently, all thicknesses of (AlGa)Sb layers mentioned later in this work will be based on the above model. It is interesting to note that thickness fringes of layers grown using TTBAI indicate the same tendency concerning a reduced TEGa efficiency. However, a systematic study of the pre-reactions between TTBAI and TEGa was not performed.

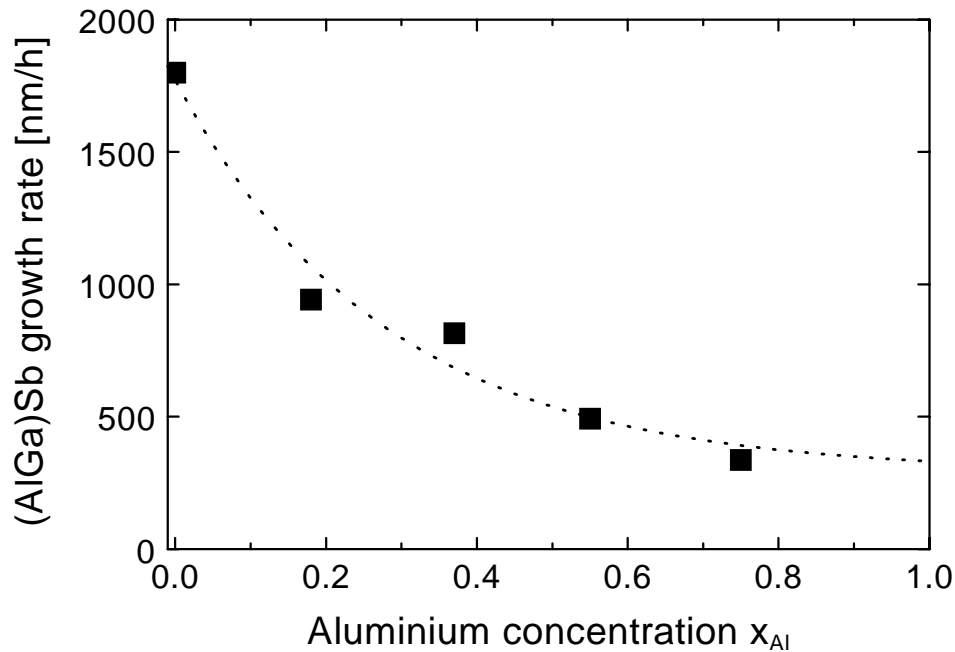


Figure 4.26: Calculated (AlGa)Sb growth rate as a function of the aluminium concentration x_{Al} in the solid. The data point for $x_{Al}=0.18$ could also be confirmed by measurements on corresponding bulk layers. The above representation is indeed meaningful because all (AlGa)Sb layers were grown with the same DMEAA molar flow rate.

4.3.7 Carbon contamination

Apart from the difficulties concerning the incorporation behaviour, carbon contamination will be a further major problem for (AlGa)Sb due to the reasons described in section 4.3.1. As carbon is usually incorporated as p-type impurity, a significant hole background concentration must be expected. Especially the standard precursor TMAl is known to lead to unacceptably high carbon concentrations in (AlGa)Sb. TTBAI and DMEAA should be preferable: As TTBAI is believed to decompose via a β -hydride elimination [116] and DMEAA has no direct Al-C bonds at all, both precursors are expected to decrease the carbon levels in (AlGa)Sb significantly. However, the extent of the pre-reactions observed above makes alkyl exchange reactions likely between the different metalorganic precursors, which might again increase the carbon incorporation into the layers. The carbon contamination in (AlGa)Sb was measured by SIMS as a function of the Al-concentration in the solid. The SIMS count rate was calibrated by ion implantation using an $(Al_{0.2}Ga_{0.8})Sb$ sample. The results are shown in figure 4.27. The figure contains four different sets of experiments:

Set A: The squares stand for experiments with TTBAI in which the aluminium concentration was adjusted by a variation of the ratio of the molar flow rates of TTBAI and TEGa. All other growth parameters were held constant, e. g. $T_{growth}=625^{\circ}C$.

Set B: The circles stand for experiments with TTBAI in which the aluminium concentration was varied by a variation of the growth temperature, i. e. by taking

advantage of the temperature dependent incorporation behaviour described in section 4.3.2. The gas phase composition was held constant in the experiments.

Set C: The experiments represented by up-triangles are equivalent to point a), except that DMEAA was employed instead of TTBAI and T_{growth} was 575°C.

Set D: The experiments represented by down-triangles are equivalent to point b), except that DMEAA was employed instead of TTBAI. However, it is important to note that these layers were grown using the DMEAA batch "B" which gave highly p-type and oxygen contaminated layers, while the up-triangle points are related to layers grown using a different batch of DMEAA (batch "A") that gave much better hole and oxygen data.

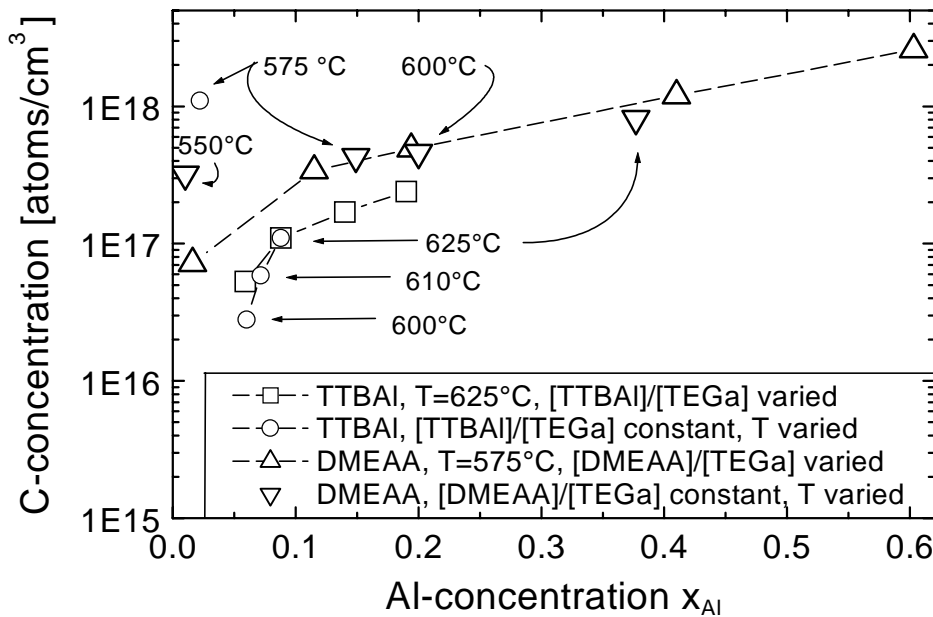


Figure 4.27: Carbon concentration in $(\text{AlGa})\text{Sb}$ as a function of the aluminium concentration in the solid x_{Al} . Both TTBAI and DMEAA were employed at different growth temperatures and $[\text{DMEAA}]/[\text{TEGa}]$ ratios.

Four main results can be derived from the figure:

1. As expected, the carbon concentration increases when more aluminium is added to the crystal.
2. There is no major difference between TTBAI and DMEAA. The values found for TTBAI are just slightly lower than the values found for DMEAA.
3. The growth temperature does not seem to have a significant influence on the carbon incorporation. (However, a data point for TTBAI at 575°C gave an extraordinarily high carbon concentration. Similarly, the DMEAA data point at 550°C (batch "B") is much higher than a comparable point representing a layer grown at 575°C (batch "A"). These results suggest that the carbon incorporation gets higher for both precursors if the growth temperature is below a certain minimum value.)
4. The two different DMEAA batches gave an equivalent carbon concentration for layers grown at temperatures $T_{\text{growth}} \geq 575^\circ\text{C}$.

On the one hand the pyrolysis routes for both TTBAI and DMEAA make a carbon incorporation unlikely. On the other hand both precursors show comparably high carbon concentrations in the crystal. These results taken together suggest that an alkyl exchange reaction in the gas phase or on the growth surface is responsible for the C-background. The observed behaviour proposes that activated aluminium species react with organic radicals arising from the TEGa and TMSb decomposition. This is confirmed by the findings of Wang et al. in [116] where TESb gave a carbon level in AlSb which was reduced by an order of magnitude compared to a corresponding layer grown using TMSb. As a consequence of the assumption of alkyl exchange reactions the problem of carbon contamination can not be solved by choosing a different novel aluminium precursor with more advantageous decomposition properties. It is very likely that this phenomenon can better be suppressed by kinetics than by thermodynamics: Changes in the gas flow pattern in the reactor should be introduced in order to minimise the contact time between the aluminium precursor and the other metalorganic sources.

4.3.8 Oxygen contamination

In section 4.3.1 it was shown that an increase of the V/III ratio can lead to a significant reduction of the oxygen concentration in (AlGa)As if arsine is employed as group V source. In contrast to the arsenides, the V/III ratio has to be adjusted in a very narrow range close to unity for the antimonides. Consequently, the oxygen level in (AlGa)Sb can not be significantly influenced by the group V overpressure. Therefore, all precursors for the MOVPE of (AlGa)Sb have to be employed in extremely high purity grades. In order to compare the oxygen incorporation with TTBAI and DMEAA, the four sets of layers A...D described in section 4.3.7 were analysed by SIMS with regard to the oxygen incorporation. The results are shown in figure 4.28.

While generally an increase of the oxygen level with increasing aluminium concentration x_{Al} was observed, the overall oxygen levels were very different for TTBAI and DMEAA. This is a major difference compared to the carbon contamination described in the preceding section where both precursors gave very similar results.

For TTBAI it was found that the higher the growth temperature for a given x_{Al} was, the more oxygen was found in the layers (sets A & B, squares and circles in figure 4.28). This behaviour suggests the presence of a thermally activated oxygen impurity in the precursor. In contrast to the layers grown with TTBAI, the oxygen incorporation was highly reduced when batch "A" of DMEAA was employed (set C, up-triangles).

A further batch of DMEAA (batch "B", set D, down-triangles) gave significantly higher oxygen levels compared to all other related experiments. This result suggests that an additional impurity was present in the DMEAA bubbler of batch "B". When the temperature was lowered at otherwise identical gas phase conditions, the aluminium concentration decreased correspondingly as expected (see section 4.3.2). However, the oxygen concentration remained constant at very high levels even for the lowest aluminium concentration. Obviously it was only the overall molar flow rate of the precursor into the reactor that determined the oxygen incorporation while the (thermally determined) efficiency of DMEAA played no important role.

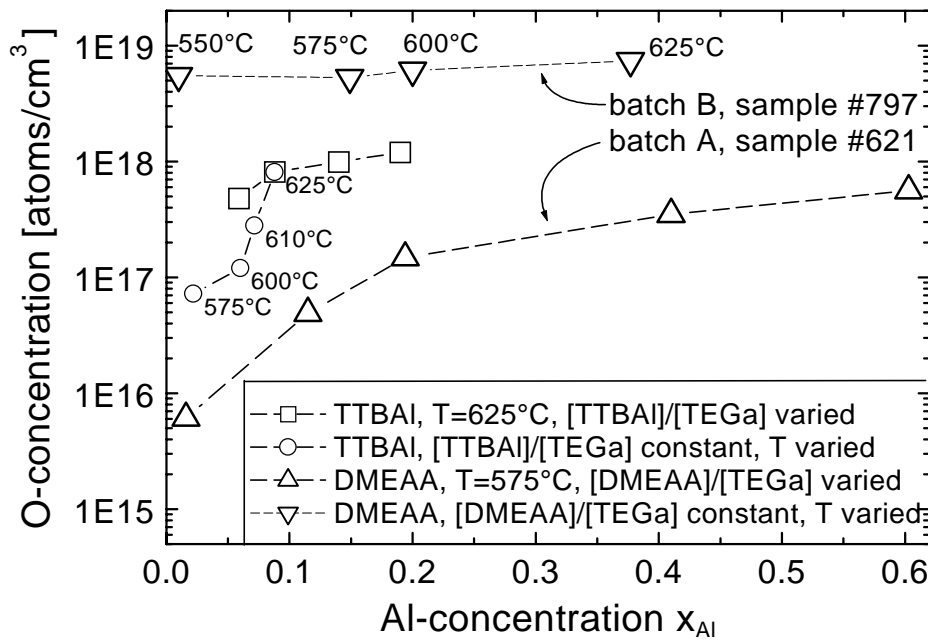


Figure 4.28: Oxygen concentration in (AlGa)Sb as a function of the aluminium concentration in the solid x_{Al} . The experiments were described in more detail in the preceding section 4.3.7.

It is interesting to note that there was as well a highly increased hole background in (AlGa)Sb grown with batch "B" of DMEAA, while the carbon contamination was not influenced by the suspected additional impurity. As oxygen is unlikely to form shallow acceptor states, an increase of the native acceptor concentration in the vicinity of oxygen impurities could possibly explain the increased hole concentrations. The hole concentrations of the material grown immediately after opening the new bubbler were so high that n-type doping was completely impossible. After many p-type layers had been grown with this precursor batch, the p-type background of the material decreased and n-type doping was again possible. This results suggests that the oxygen impurity had a higher vapour pressure than DMEAA and was gradually removed from the bubbler.

Finally, there were indications for a pressure increase in the bubbler after a long term storage. This can as well be interpreted as a decomposition process which was catalysed by the presence of an impurity.

In summary, DMEAA has given the lowest oxygen levels in the above experiments. However, a bad reproducibility of the purity was found. Therefore it is considered possible that a better TTBAI could as well produce (AlGa)Sb layers with comparably low oxygen levels. No final evaluation can be given concerning this point. Unfortunately, very little related data on O-contamination of (AlGa)Sb in the investigated composition range could be found in the literature [22, 109, 117]. The above oxygen concentrations in (AlGa)Sb grown with the first batch of DMEAA are among the best values published so far.

4.3.9 p-type background doping

Carbon is a p-type impurity in (AlGa)Sb. Consequently, the significant carbon incorporation described in section 4.3.7 will lead to a high background hole concentration. This hole conductivity is generally a major problem, and it was not until 1996 that n-type MOVPE-grown Al(As)Sb was first reported [22, 117]. However, according to figure 4.29 carbon can not be the only reason for the high hole concentrations in (AlGa)Sb: While for layers grown using batch "A"-DMEAA the hole concentrations as measured by Hall were clearly below the corresponding carbon levels, the hole concentrations were *higher* than the carbon background in the case of TTBAI. Similarly, batch "B" of DMEAA gave much higher hole concentrations than batch "A", whereas the carbon levels were comparable. However, both TTBAI and batch "B"-DMEAA had very high oxygen contaminations in common. A similar connection between O contamination and high p-type background was as well reported in [44]. As oxygen is unlikely to form shallow acceptor states, an increase of the native acceptor concentration in the vicinity of oxygen impurities could possibly explain the increased hole concentrations in the samples where the hole level was higher than the carbon level.

The overall hole concentrations as a function of the aluminium concentration are shown in figure 4.30. As expected, the hole background increases with increasing x_{Al} . While batch "A"-DMEAA gave the best (=lowest) hole concentrations, TTBAI and batch "B"-

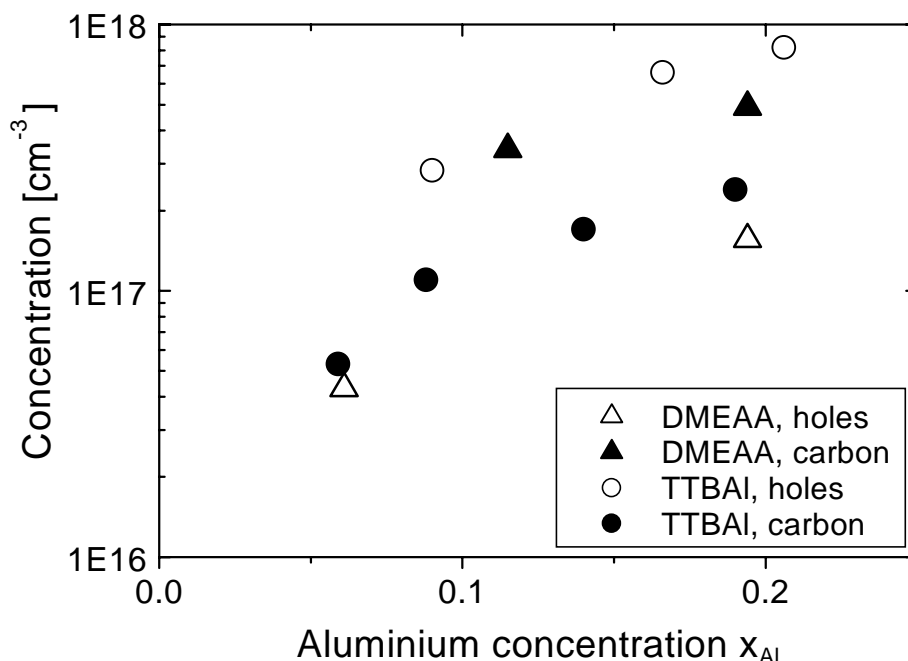


Figure 4.29: Carbon and hole concentration in $(Al_xGa_{1-x})Sb$ as a function of the aluminium concentration x_{Al} . While for DMEAA the hole concentration is lower than the carbon level, the opposite is found for TTBAI.

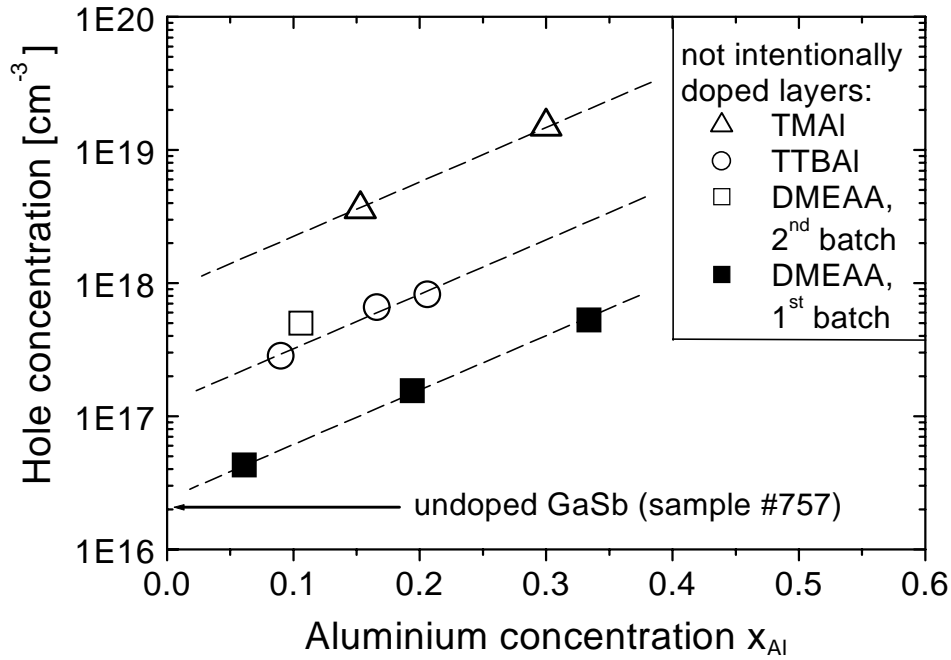


Figure 4.30: 300K-hole concentration of $(Al_xGa_{1-x})Sb$ as a function of the aluminium concentration x_{Al} . For comparison, the typical background of native acceptors in binary GaSb is shown as well.

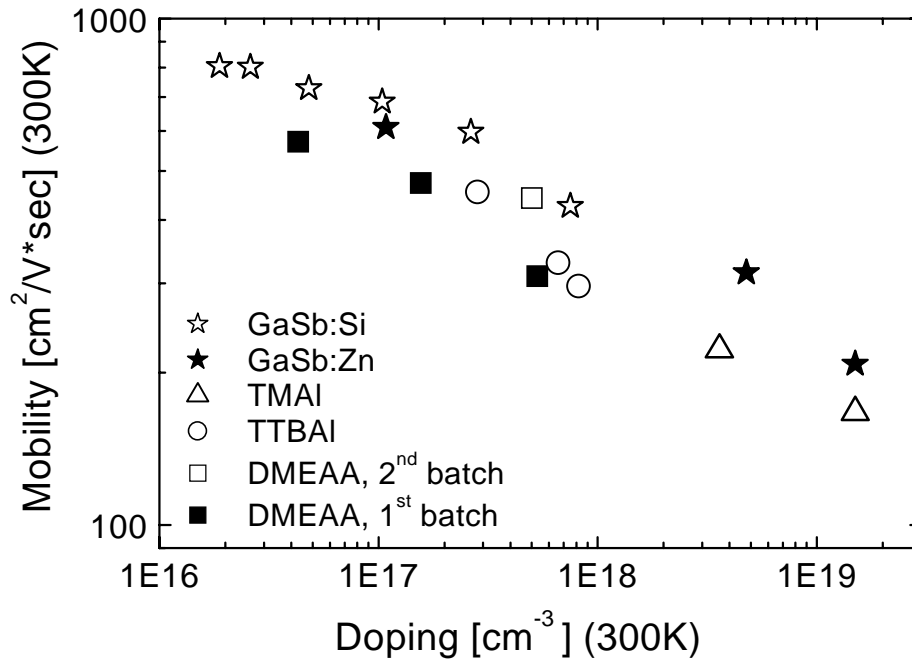


Figure 4.31: 300K-mobility of intentionally doped GaSb and nominally undoped $(AlGa)Sb$ as a function of the hole concentration. No significant difference between the aluminium precursors can be observed. The corresponding aluminium concentrations can be found in figure 4.30.

DMEAA showed much stronger p-type behaviour. Besides, the films grown in preliminary experiments with TMAI gave the highest hole contaminations of all samples. As already mentioned above, no final evaluation concerning the choice between TTBAI

and DMEAA as Al-precursor can be given: Due to the bad reproducibility of the precursor purity the comparability between the sources was limited.

The measured mobilities of the samples in figure 4.30 are presented as a function of the hole concentration in figure 4.31. For comparison, binary GaSb layers are as well included in the figure. No significant difference between (AlGa)Sb layers grown with different sources was observed. However, as expected the GaSb mobilities were systematically higher than the (AlGa)Sb values.

4.3.10 Tellurium as n-dopant

It is extremely difficult to achieve n-type conductivity for MOVPE-grown (AlGa)Sb. Two related problems have already been mentioned:

1. Due to the p-type nature of the group IV elements silicon and germanium in the MOVPE of antimonides it is difficult to find a suitable donor dopant. Successful n-doping of (AlGa)Sb has only been reported for tellurium [44, 109, 117] and tin [20, 22]. Here, the latter is somewhat surprising due to the contrary behaviour of silicon and germanium.
2. Nominally undoped (AlGa)Sb grown by MOVPE is usually highly p-type or not electrically active at all due to carbon and oxygen contaminations. Only novel Al-precursors such as TTBAI and DMEAA have been reported to give (AlGa)Sb layers with reduced hole concentrations that eventually allowed n-type doping.

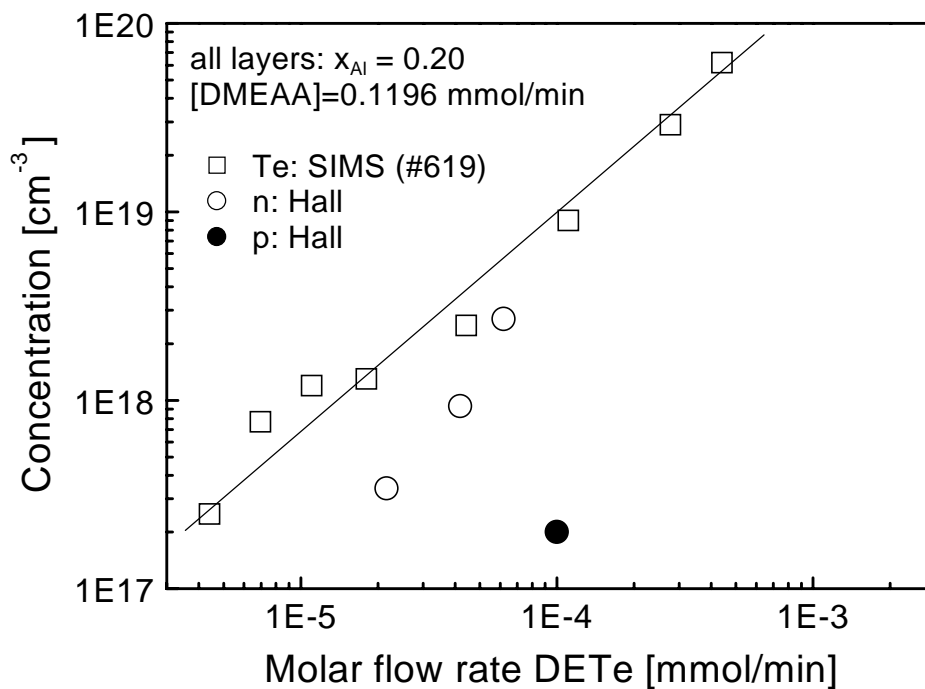


Figure 4.32: Concentrations of electrons/holes and tellurium atoms in $(Al_{0.2}Ga_{0.8})Sb$ as a function of the DETe molar flow rate. At $1 \cdot 10^{-4}$ mmol/min the n-type conductivity breaks down and the samples show p-type behaviour.

In this context the correct interpretation of Hall-measurements is quite complicated due to the Γ -L band crossing at $x_{\text{Al}}=0.2$ and the L-X band crossing at $x_{\text{Al}}=0.45$ [2]. SIMS measurements have shown that the concentration of tellurium atoms is usually much higher than the measured electron concentration [109]. This effect can probably not be fully explained by the presence of compensating carbon. Wang et al. [109] suggested deep electron traps related to tellurium to cause the reduced electron concentration. The Te-doped $(\text{Al}_{0.2}\text{Ga}_{0.8})\text{Sb}$ layers grown for this work showed another surprising property: Above a certain molar flow rate of DETe into the reactor, the n-type conductivity of $(\text{Al}_{0.2}\text{Ga}_{0.8})\text{Sb}$ broke down and the samples showed p-type behaviour. The result is illustrated in figure 4.32. This effect can maybe be attributed to an oxygen impurity in the DETe: It was already suggested in section 4.3.9 that the native acceptor concentration might increase in the vicinity of oxygen impurities. Hence, a p-type behaviour might well occur for high molar flow rates of an oxygen-contaminated DETe.

Figure 4.32 illustrates the main challenge when n-type $(\text{AlGa})\text{Sb}$ is to be grown by MOVPE: Only a very narrow range of atomic tellurium concentrations give n-type layers. When the tellurium concentration is too low, background carbon acceptors will dominate the resulting p-type layer. On the other hand, when the tellurium concentration gets too high, the layer will become p-type as well (presumably due to oxygen impurities). Consequently, one can never be sure if a Te-doped MOVPE-grown $(\text{AlGa})\text{Sb}$ -layer, which shows unwanted p-type conductivity, contains too little or too much tellurium. As the electron concentration in Te-doped $\text{Al}(\text{As}_{0.16}\text{Sb}_{0.84})$ lattice-matched to InAs has been reported to saturate in the 10^{16} -range [44] while up to $2.3 \cdot 10^{18} \text{ cm}^{-3}$ has been reported for Sn-doped $\text{Al}(\text{As}_{0.16}\text{Sb}_{0.84})$, tin might be a promising alternative that should be considered for future experiments.

4.3.11 DMEAA at interfaces: Stabilisation and carry-over

Many device applications depend on abrupt interfaces, for example emitting devices with quantum well active regions or tandem solar cells with Esaki tunnel diodes. The interface quality again depends mainly on three points:

1. *Can the precursors be switched on and off abruptly?*

On the one hand modern MOVPE equipment has very rapid gas switching valves so that the gas phase composition at the inlet nozzle can indeed be switched abruptly. However, an element can desorb from the reactor walls after the related precursor has been switched off, i. e. an unwanted carry-over into the subsequent layer can occur. Besides, some precursors condense at the stainless steel tubes between bubbler and reactor; consequently, when the source is switched into the reactor it will need some time to cover the tube insides until it reaches its maximum efficiency.

2. *Which exchange reactions occur during growth interruptions?*

When a sharp interface with well-defined properties is desired, the growth is usually interrupted for a few seconds by switching off the group III precursors. The crystal has to be stabilised during these growth interruptions under a group V atmosphere. Exchange reactions can occur if the stabilising precursor is changed during the growth interruption. This effect is widely used in order to adjust certain interface properties. For the antimonides the group V exchange reactions are of particular interest for InAs/GaSb -interfaces. Related MBE-experiments on the As/Sb -exchange are reported for example in [43, 123, 124].

3. Does diffusion occur during growth or processing?

At typical growth temperatures certain elements tend to diffuse readily through the crystal. A typical example is the dopant zinc which shows diffusion even at device processing temperatures. Consequently, the position of a pn-junction in a related device may change during processing. For this reason so-called “spacer-layers” are frequently incorporated into devices based on pn-junctions. As diffusion of substitutionally dissolved atoms in a crystalline solid involves point defects such as vacancies, diffusion may well be expected to be a significant effect for the antimonides due to generally accepted nature of the native acceptor defect. Therefore the substitution of zinc by silicon as acceptor dopant described in chapter 5 is considered an important step to stable sophisticated GaSb-based device structures.

Amongst the above points the switching behaviour of the aluminium precursor (point 1) is the most difficult problem for (AlGa)Sb. First indications of related problems had been reported in [103] where a carry-over of both Ga and Al was observed for AlSb/GaSb superlattices grown using TEGa, TEAl and TESb. Giesen et al. report a serious aluminium memory effect for TTBAI even between different growth runs [44]. Correspondingly, Wang et al. [116] report an accumulation of elementary aluminium on the final growth surface. As parasitic pre-reactions and pre-deposition have been shown to occur as well in this present work, the switching behaviour of DMEAA was analysed in detail. Figure 4.33 presents a SIMS measurement of the Al-concentration in an (AlGa)Sb-bulk layer with nominally constant aluminium concentration x_{Al} where growth interruptions were included in the growth sequence. The related interpretation of the measurement is given in the figure caption. When the group III precursors are switched on, DMEAA or related pre-reaction products condense at the tube insides or at cooler reactor parts. This parasitic process leads to a reduced DMEAA efficiency during the first nanometers of (AlGa)Sb, resulting in a lower value for x_{Al} . When the group III precursors are then switched off for a growth interruption, the condensed DMEAA or related pre-reaction products desorb and lead to a very slow growth of AlSb. The related material has been shown to be highly contaminated with oxygen and carbon. The presented interpretation is in line with the severe aluminium memory effects reported above for TTBAI [44, 116].

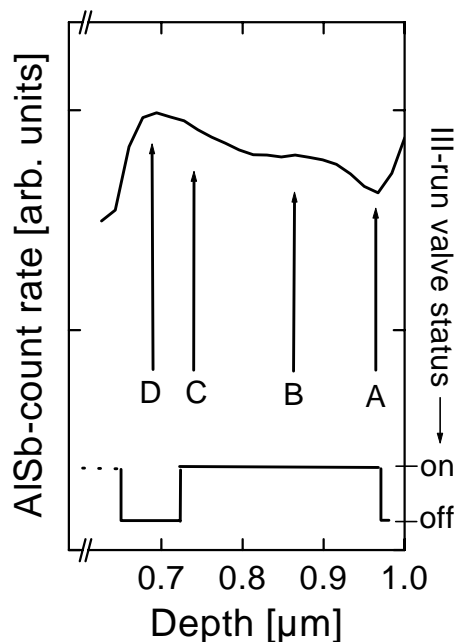


Figure 4.33:

AlSb count rate as measured by SIMS for an (AlGa)Sb-bulk layer with nominally constant Al-concentration where growth interruptions were included in the growth sequence. The results are interpreted as follows:

At “A” the preceding growth interruption ends and the group III precursors are switched on again. After a certain stabilisation time for the DMEAA, region “B” with a constant Al concentration is reached. In the subsequent growth interruption, aluminium desorbs from the reactor walls or tube insides, and a thin layer of AlSb is deposited (“D”). This layer is blurred by the SIMS (“C”). The presence of low-quality AlSb is confirmed by very high peaks of carbon and oxygen in region “D”. The corresponding switching status of the group III-run valves is as well shown in the figure.

A further experiment concerning aluminium memory effects was included in the superlattice structures described in section 4.3.6. Those (AlGa)Sb/GaSb-superlattices were capped with an (AlGa)Sb-bulk layer which nominally had the same Al-concentration as the (AlGa)Sb in the superlattice. While the aluminium concentration x_{Al} in the related layers of the superlattice was calculated in section 4.3.6, the value for x_{Al} in the (AlGa)Sb-bulk layer can be directly measured with HR-XRD. Due to the significant lattice mismatch between AlSb and GaSb relaxation effects were included in the analysis. Details on the HR-XRD measurements can be found in [49]. A comparison between the x_{Al} -data of bulk and superlattice can now provide further information on the switching behaviour of DMEAA.

Figure 4.34 shows the ratio $x_{Al}^{superlattice} / x_{Al}^{bulk}$ as a function of the aluminium concentration in the bulk material. It can be seen that for aluminium concentrations up to approximately 40 % the value x_{Al} of the (AlGa)Sb-layer in the superlattice is almost the same as in the bulk layer. For higher aluminium concentrations, a significant increase of the aluminium concentration in the superlattice compared to the bulk layer can be observed. This effect can only be due to the switching behaviour of the sources at the interfaces because the growth conditions of bulk-(AlGa)Sb and superlattice-(AlGa)Sb were identical in all other respects. The following explanation for the observed behaviour is suggested:

The above SIMS measurements had shown that DMEAA does not produce sharp interfaces: The reactor seems to take a certain time to reach a stable incorporation behaviour when DMEAA is switched on, leading to an overall "loss" of aluminium in an epitaxial structure. Similarly, Al-carry over is believed to happen when DMEAA is switched off, leading to an overall "gain" of aluminium in the layers. As the GaSb-layers were grown at identical conditions in all superlattice samples and the DMEAA molar

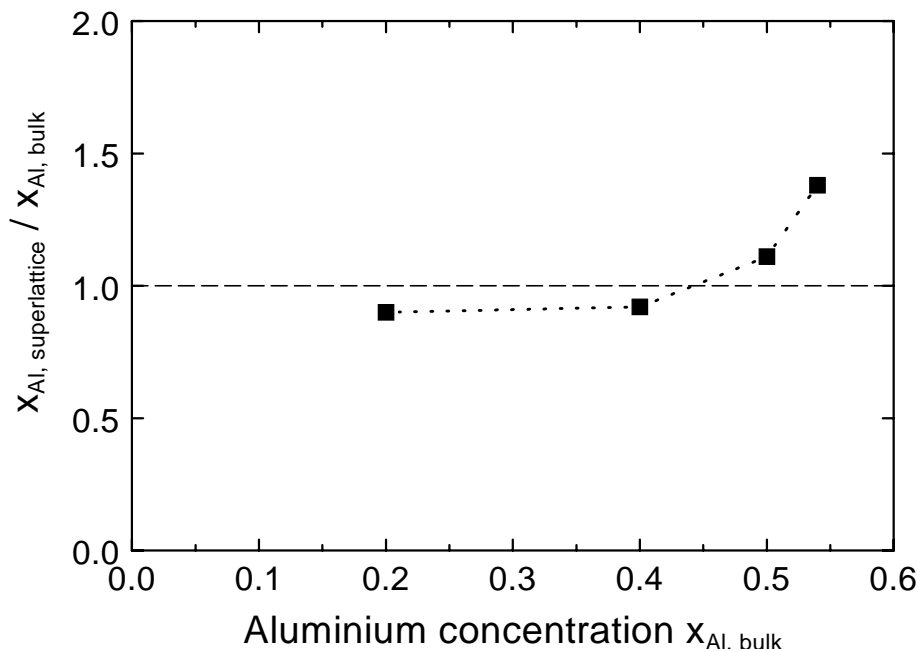


Figure 4.34: Ratio $x_{Al}^{superlattice} / x_{Al}^{bulk}$ as a function of the aluminium concentration in the bulk material. The observed behaviour is believed to be the overall result of a "loss"-process of aluminium at the interface GaSb \Rightarrow (AlGa)Sb and a "gain"-process of aluminium at the interface (AlGa)Sb \Rightarrow GaSb (see text).

flow rate was held constant for all (AlGa)Sb layers in this present work, a similar carry-over behaviour of Al into the GaSb can be expected at the interface (AlGa)Sb => GaSb for all samples. On the other hand, in the (AlGa)Sb layers of the superlattices the TEGa molar flow rate had to be varied in order to adjust the aluminium concentration. As a result, the switching behaviour of DMEAA has probably varied from one sample to the other at the interface GaSb => (AlGa)Sb. In this context, the lower growth rate and the lower TEGa molar flow rate is believed to lead to a quicker stabilisation of the DMEAA efficiency for higher x_{Al} 's.

Within this model it is believed that for *lower* Al-concentrations the "loss" of aluminium during the stabilisation period in (AlGa)Sb is approximately compensated by the "gain" of aluminium due to carry-over into GaSb. As a result, the ratio $x_{Al}^{superlattice} / x_{Al}^{bulk}$ is almost one. For *higher* Al-concentrations, the DMEAA efficiency is thought to stabilise quicker and the related "loss" might be reduced. As the carry-over "gain" at the interface (AlGa)Sb => GaSb is constant for all samples, at higher x_{Al} 's this gain can eventually become dominant over the "loss" associated with the stabilisation period at the other interface. The overall result is an increased average Al-concentration of the superlattice for higher Al-concentrations as observed in figure 4.34. It must be pointed out that this introduces a small additional error concerning the pre-reaction analysis in section 4.3.6 because stabilisation- and carry over-effects were excluded from those calculations.

The above findings have to be considered when devices are designed. As the AlSb-layers deposited during a growth interruption following an (AlGa)Sb film are highly contaminated with oxygen, the corresponding interface recombination velocity will be very high. Therefore, corresponding growth interruptions have to be strictly avoided in those regions of the photovoltaic devices (see section 6) where long minority carrier lifetimes are necessary.

4.4 Summary

Chapter 4 has given a summary of the lessons that had to be learned in order to deposit high-quality GaSb-based structures in a multiwafer MOVPE-reactor. The ranges for most GaSb-growth parameters are extremely narrow and the multiwafer geometry of the growth environment has proven to be an additional challenge. Various substrate issues have been discussed such as wet-chemical preparation, oxide desorption, and film morphology versus substrate miscut angle and V/III ratio. An activation energy for the oxide desorption was obtained, and in-situ etching of GaSb was demonstrated for the first time using TBCl. The growth rate of GaSb was examined as a function of the growth parameters. The electrical properties of undoped and n-type material were analysed. The PL-properties of undoped GaSb were shown as a function of the growth temperature and the V/III-ratio. The electrical and optical data of the material are well in line with the best values in the literature. Consequently, the employed precursor combination TEGa/TMSb/DETe can be recommended for the particular growth conditions in the multiwafer reactor. In addition to the aluminium-free material the successful growth of high-quality (AlGa)(AsSb) has as well been demonstrated for the first time in a multiwafer MOVPE-reactor. As the standard aluminium precursor TMAI is not suited for the growth of antimonides, two promising alternatives were compared to each other: DMEAA and TTBAI. (AlGa)(AsSb) with low oxygen and carbon levels could

be grown using DMEAA. However, this highly reactive precursor is subject to parasitic pre-reactions and pre-deposition. This becomes evident by considering the unusual non-linear incorporation behaviour, a white powder as pre-reaction product on the inlet nozzle, the temperature dependent efficiency even far above the corresponding decomposition temperature, reduced efficiencies that depend on the molar flow rates of other precursors, higher efficiencies at increased carrier gas flow rates, and finally a non-abrupt incorporation behaviour when the source is switched on or off. For the precursor combination TEGa/DMEAA/TMSb/TBAs n-type doping of (AlGa)(AsSb) with tellurium was shown to be possible but very difficult. Based on related literature reports, tin might be well suited as an alternative.

5 Results - Silicon as novel acceptor dopant in GaSb

Silicon is known as an amphoteric impurity in III-V compound semiconductors. It incorporates as n-type or p-type depending on the growth conditions, relative tetrahedral radii, and electronegativity. In As- and P-based III-V semiconductors the group V-rich growth conditions lead to an incorporation of Si preferentially on group III-sites under most growth conditions, making it a common n-type dopant [102]. As GaSb is grown at V/III-ratios close to unity, there is no significant group V-overpressure that could influence the incorporation behaviour of silicon. As a result, Si has been found to behave as acceptor in GaSb in MBE [84], LPE (ref. 18 in [3]), MOVPE [36, 37] and melt grown substrates ([84] and references therein). However, the level of understanding and experience concerning this acceptor in GaSb is still very limited. The following chapter presents novel results concerning the incorporation behaviour, the electrical properties and the optical properties of Si-acceptors in MOVPE-grown material. It is shown that Silicon can be employed as a well behaved acceptor dopant for GaSb grown by MOVPE. These results form the basis of the first ever reported Si-doped GaSb-based devices presented in chapter 6.

Besides, silicon can be expected to have three major advantages over zinc as the standard acceptor dopant in III-V semiconductors:

- Zinc is known to have a high diffusivity in III-V semiconductors at growth temperatures and even already at typical device processing temperatures. For this reason, so-called "spacer-layers" are frequently incorporated into devices based on pn-junctions. Silicon as group IV atom should not show this problem.
- Zinc has a high vapour pressure over a semiconductor surface during growth. Consequently it has to be employed in excess amounts which influence other mechanisms, e.g. lattice matching of (GaIn)P. Silicon does not show this problem.
- As the silicon acceptor incorporates on group V sites and the native acceptor in GaSb is always linked to an Sb vacancy, silicon doping can be expected to reduce the NA concentration. As zinc incorporates on gallium sites, this effect is unlikely for zinc.

5.1 Incorporation behaviour

In order to examine the incorporation of silicon into GaSb in the MOVPE process, Si-doped layers were analysed by SIMS- and Hall-measurements. The results are presented in the following figure 5.1. The concentration of atomic silicon as measured by SIMS is a linear function of the ratio of the molar flow rates $\frac{[SiH_4]}{[TEGa]}$ over a wide range of doping levels. On the other hand, the behaviour of the hole concentrations is slightly more complicated and will be analysed in detail in section 5.2.2. In addition, the doping levels for the lightly doped samples could as well be determined from CV-measurements on pn-junctions with heavily doped n-layers. A very good agreement with the above Hall data for lightly doped samples was obtained.

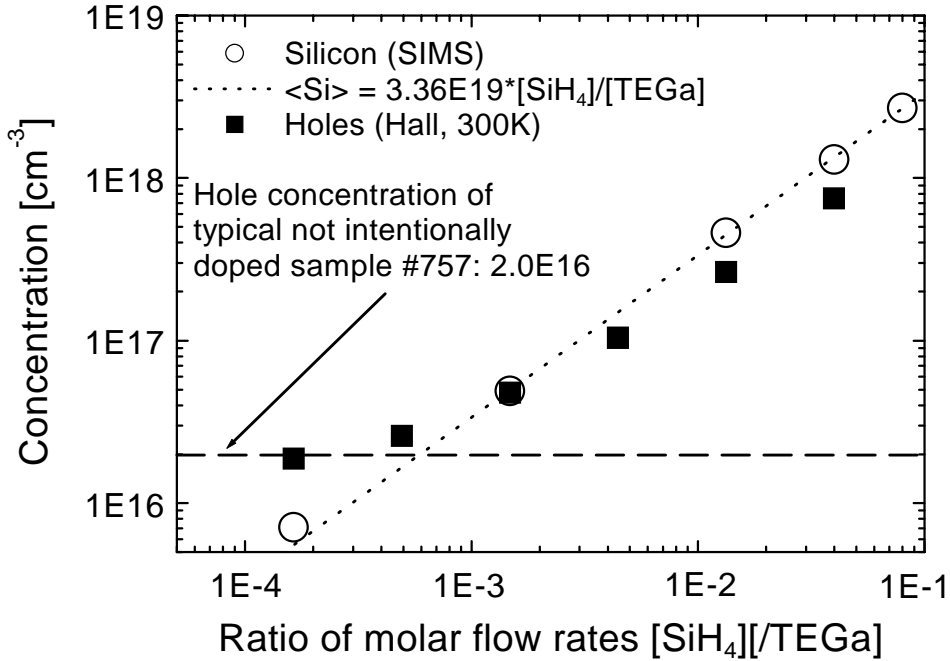


Figure 5.1: Incorporation behaviour of silicon into GaSb.

The silicon concentration as measured by SIMS is compared to the hole concentration at 300K.

5.2 Carrier mobility / compensation

5.2.1 Introduction

In a pure, intrinsic semiconductor the free electron and hole densities are equal. At $T=0K$ the Fermi energy lies midway between the valence and conduction band edges. With increasing temperature it moves slowly towards the band with the smaller density of states. This situation changes in a semiconductor doped with acceptors, donors or both. At very low temperatures $k_B T$ is less than the binding energy so that electrons (holes) are bound to donor (acceptor) impurities and make relatively little contribution to conduction. In this temperature region the mobile charge carriers are said to be „frozen out“. When kT is greater than the binding energy but still much less than the energy gap the impurities are ionised and the carrier concentration is almost independent of temperature (*exhaustion region*). If the temperature is increased further, eventually the equilibrium density of thermally generated electrons and holes will exceed the excess of electrons/holes due to impurities and the material will be an intrinsic semiconductor (*intrinsic region*).

The Fermi level in an n-type (p-type) semiconductor at low temperatures lies near and, if the impurity concentration is very high, within the conduction (valence) band. As the temperature increases and the intrinsic region is reached the Fermi level moves towards the centre of the energy gap. When the density of intrinsic carriers greatly exceeds the

impurity density the variation of the Fermi level with temperature follows that of a pure material.

In the description of the carrier densities in doped semiconductors the Fermi energy E_F can be eliminated by forming the product $np = n_i^2$. The intrinsic carrier concentration n_i can be calculated if the effective masses in all populated valleys of valence and conduction band are known. In GaSb the L minima in the conduction band lie energetically very near the Γ minimum, the complete expression is

$$n_i = 2 \cdot \left(\frac{2\pi \cdot k_B T}{h^2} \right)^{3/2} \cdot \sqrt{\left(m_L^{3/2} e^{-\Delta\Gamma_L/k_B T} + m_\Gamma^{3/2} \right) \cdot \left(m_{hh}^{3/2} + m_{lh}^{3/2} \right)} \cdot e^{-E_{gap}/2k_B T}$$

Accepting the effective masses given in [93], the resulting intrinsic carrier concentration at 300K is $n_i = 1.7 \cdot 10^{12} \text{ cm}^{-3}$. Using $np = n_i^2$ together with charge neutrality $n + N_A^- = p + N_D^+$ useful approximations can be given for each of the above mentioned temperature regions:

At very low temperatures kT is comparable to the major impurity's binding energy. Without proof, the electron density in this region can be approximated to be

$$n \sim N_D \cdot \exp\left(-\frac{E_D}{2kT}\right) \text{ where } E_D \text{ is the binding energy of the donor measured from the}$$

edge of the conduction band. Similar expressions apply to p-type material. At higher temperatures (*exhaustion region*) one can assume that all impurities are ionized, i.e. $N_A^- = N_A$ and $N_D^+ = N_D$. Substituting this together with $np = n_i^2$ into $n + N_A^- = p + N_D^+$ and thereby eliminating the minority carrier concentration, the result for a p-type semiconductor is the quadratic equation $p^2 + p(N_D - N_A) - n_i^2 = 0$. The solution is

$$p = \frac{N_A - N_D}{2} \pm \sqrt{\left(\frac{N_D - N_A}{2}\right)^2 + n_i^2}.$$

In the exhaustion region one can neglect n_i and get $p = N_A - N_D$ as the solution. (However, the assumptions $N_D^+ = N_D$ and especially $N_A^- = N_A$ are not strictly true.

Plotting $p \sim N_A \cdot \exp\left(-\frac{E_A}{2kT}\right)$ against T for different E_A shows that there can still be a

considerable concentration of neutral acceptors present at liquid nitrogen temperature.) As $np = n_i^2$ and n_i for GaSb is $n_i(300K) = 1.7 \cdot 10^{12} \text{ cm}^{-3}$, it follows that the minority carrier concentration n in p-type GaSb at liquid nitrogen temperature will be negligible compared to the majority carrier concentration p . In Hall-measurements the general

expression for the Hall-coefficient $R_H = \frac{p \cdot \mu_p^2 - n \cdot \mu_n^2}{e(p \cdot \mu_p + n \cdot \mu_n)^2}$ can therefore be simplified to

$$R_H = \frac{1}{e \cdot p} \text{ or } R_H = -\frac{1}{e \cdot n} \text{ for p- or n-type material, respectively.}$$

At higher temperatures one can approximate $n_i \gg |N_D - N_A|$ and

$$p = \frac{N_A - N_D}{2} \pm \sqrt{\left(\frac{N_D - N_A}{2}\right)^2 + n_i^2} \text{ gives } p = n_i (=n). \text{ In this temperature region both}$$

carrier types are present and the interpretation of Hall-measurements becomes difficult because the generalized formula for R_H must be used. However, several hundred °C are necessary to generate sufficiently high concentrations of intrinsic carriers in GaSb [16].

5.2.2 Results

Now the above considerations can be applied to Si-doped GaSb. As shown in 5.1 GaSb was doped with Silicon to various different doping levels and a related p-type conductivity was achieved. It is of particular interest to find out the degree of compensation of Silicon in GaSb as this impurity is usually incorporated as donor in GaAs and InP. In addition, the interpretation of PL spectra of Si-doped GaSb depends strongly on the background donor concentration. Two different methods have been used in order to estimate the degree of compensation in the samples:

1st approach: mobility versus hole concentration

In [127] hole-mobilities for GaSb are calculated as a function of the free hole concentration at 77K at various compensation ratios. However, some effects were excluded from the calculations, including scattering at dislocations (which must be expected for a >7% lattice mismatch between GaSb and GaAs) and hopping conductivity at low temperatures and high impurity concentrations. Neglecting these effects, the mobilities of silicon and zinc doped samples can now be compared to the calculated mobilities in [127] in order to obtain the compensation ratios. Figure 5.2

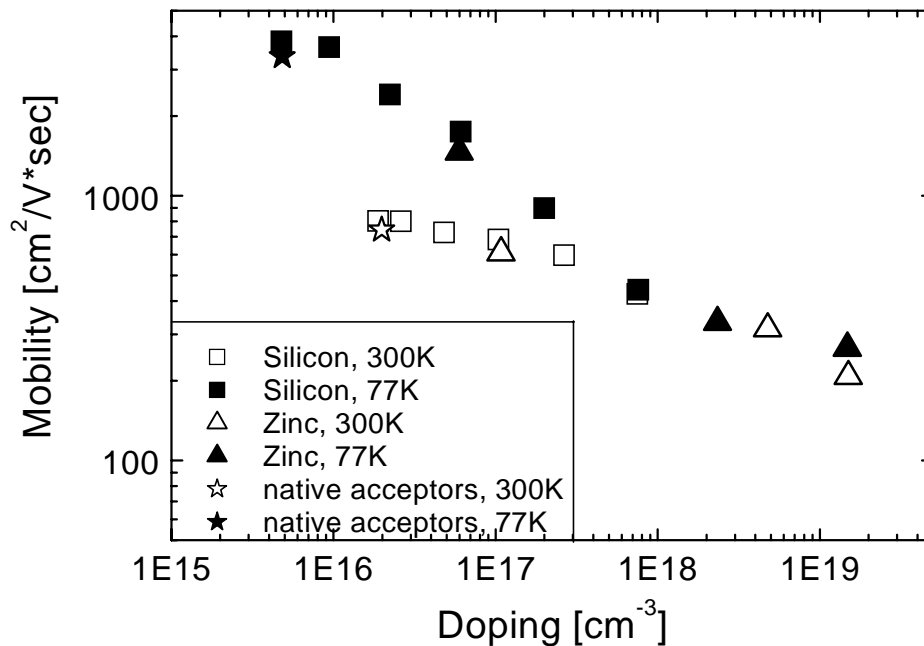


Figure 5.2: *Mobility versus hole concentration for silicon, zinc and the native acceptor.*

shows the hall mobilities of the samples as a function of the free hole concentration.

Comparing the measured Hall mobilities presented in the above figure to the calculated values taken from [127] (which unfortunately have only been calculated for rather low doping levels), the measured mobilities correspond to very high compensation ratios for samples with doping levels in the 10^{15} cm^{-3} -range, reaching approximately 0.7 for a not intentionally doped sample with $p_{77\text{K}} \sim 4.8 \text{ E}15 \text{ cm}^{-3}$. For higher Si-doping levels in the mid- 10^{16} cm^{-3} -range, a cautious extrapolation of the calculations given in [127] suggests a much lower compensation ratio of $N_D/N_A \sim 0.2 \dots 0.3$. This range of higher doping levels will be analysed in more detail by SIMS measurements described in the following text. The data will be summarized in figure 5.4.

Sample #552, which was chosen for a detailed analysis of the optical properties of moderately Si-doped GaSb in section 5.3, is not included in figure 5.2 because it was grown under slightly different growth conditions. It shows a free hole concentration of $1.7 \text{ e}16 \text{ cm}^{-3}$ and a corresponding compensation ratio of approximately $N_D/N_A \sim 0.45$.

Attention must be drawn to the fact that lattice mismatch and the resulting dislocation density might lead to a degradation of the hole mobility. This effect was not included in the calculations in [127]. It should have a greater impact on lighter doped samples because ionized impurity scattering will be more dominant at higher doping levels. It can therefore be suspected that the compensation ratio of approximately 0.7 for the NA-background doped sample is possibly over-estimated to a certain extent. This assumption is confirmed by comparing the results in [127] to the data given in [26]: The latter presents a thorough analysis of temperature dependent Hall-measurements on different not intentionally doped GaSb layers, thereby giving an independent determination of donor and acceptor concentrations. The authors' resulting compensation ratios are indeed somewhat lower compared to the values that their mobility-versus-concentration data would give in the model of [127]. Nevertheless, Bosacchi et al. still find a fairly constant compensating donor concentration of approximately $1 \dots 2 \text{ E}16 \text{ cm}^{-3}$ and get compensation ratios between 0.3 and 0.9 depending on the growth conditions. While on the one hand the above compensation ratio of 0.7 indeed appears to be slightly over-estimated, the minor deviation from the true value will not be significant with respect to the conclusions drawn in section 5.3.5. The nature of the compensating donor in the not intentionally doped samples has to remain unclear.

As a conclusion, the above findings suggest that not-intentionally doped and slightly silicon doped GaSb is highly compensated by an unknown donor. In contrast, silicon-doped GaSb at higher doping levels shows significantly lower compensation ratios. Here, the corresponding donor will be identified to be amphoteric silicon in the following text.

It should be noted that Si-doped samples with higher doping levels tend to show comparable free hole concentrations at 77K and 300K, while at lower doping concentrations the measurements at 77K give increasingly smaller hole concentrations than at 300K. This behaviour can be qualitatively understood by taking into account the two following points: Firstly, the material can be expected to show metallic conduction

at p-doping levels above approximately $1 \cdot 10^{18} \text{ cm}^{-3}$ [72]. Secondly, there are two acceptors involved which have different ionization energies: In the lower doped samples, which are dominated by the native acceptor with a high binding energy of approximately 34 meV [87], the ionization of the acceptors is far from complete at 77K. In contrast, the higher doped samples are dominated by silicon acceptors which have a much lower binding energy (see section 5.3). As a result their degree of thermal activation does not change significantly between 77K and 300K.

2nd approach: SIMS versus Hall

Assuming that Silicon is mainly incorporated substitutionally, the compensation ratio can as well be estimated by comparing SIMS-data to the free hole concentration. However, this is complicated because the hole conductivity in GaSb at low doping levels is significantly influenced by the background concentration of native acceptors. The experimental data were therefore analysed in the following way:

As shown in section 5.1, the silicon concentration $\langle Si \rangle$ in GaSb as measured by SIMS can be described as a linear function of the ratio of the molar flow rates $[SiH_4]$ and $[TEGa]$: $\langle Si \rangle = 3.36 \cdot 10^{19} \text{ cm}^{-3} \cdot \frac{[SiH_4]}{[TEGa]}$. The free hole concentration as measured

by Hall can now be described as a function of the silicon concentration $\langle Si \rangle$: Firstly it is assumed that the p-type conductivity at doping levels much higher than the NA concentration is dominated by Silicon acceptors. It follows that the percentage of Si atoms that are electrically active as acceptors is 56%: $N_{A,Si} = 0.56 \cdot \langle Si \rangle$. Assuming complete ionisation of the acceptors at 300K leads to $p_{Si} = 0.56 \cdot \langle Si \rangle$. Secondly it is assumed that Silicon acceptors and native acceptors both contribute equally to the total acceptor concentration at lower doping levels: $N_A = N_{A,Si} + N_{A,NA}$. Again, complete ionisation at 300K gives $p = p_{Si} + p_{NA}$. As a result one gets the following expression for the free hole concentration: $p = 0.56 \cdot \langle Si \rangle + p_{NA}$. This function is plotted in figure 5.3

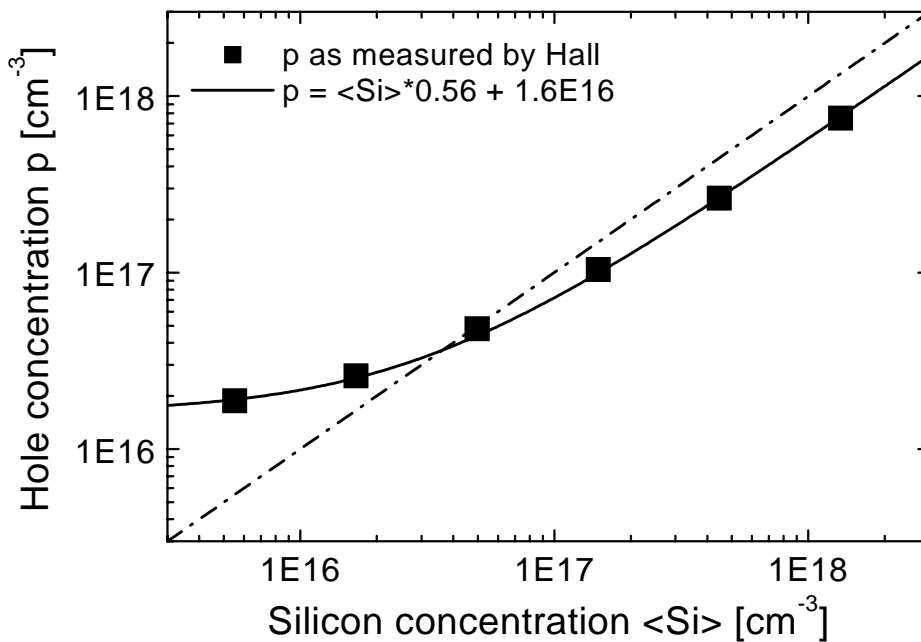


Figure 5.3: Hole concentration versus silicon concentration in GaSb. The given model can describe the hole concentrations over the entire doping range.

accepting $p_{NA} = 1.6 \cdot 10^{16} \text{ cm}^{-3}$ and $\langle Si \rangle = 3.36 \cdot 10^{19} \text{ cm}^{-3} \cdot \frac{[SiH_4]}{[TEGa]}$. The value of $p_{NA} = 1.6 \cdot 10^{16}$ in the function is in good agreement with the value of $p_{NA} = 2 \cdot 10^{16}$ which was measured for a typical not intentionally doped sample. In order to confirm that the silicon incorporation and activation into homoepitaxial and heteroepitaxial GaSb is indeed comparable, CV-measurements were performed on homoepitaxially grown pn-junctions. In well-suited samples (i. e. samples where the doping ratios were such that the corresponding depletion was almost entirely in the p-type material) the resulting hole concentrations were in very good agreement with the hole concentration determined in Hall measurements on heteroepitaxial samples. This result confirms the validity of the method.

The above results can now be used to determine the compensation ratio of silicon-doped GaSb at higher doping levels where $p = p_{Si}$: On the one hand the hole concentration in the exhaustion region corresponds to $p = p_{Si} = N_A - N_D$. On the other hand one can assume that silicon is mainly incorporated substitutionally and therefore $\langle Si \rangle = N_A + N_D$ (and $p = p_{Si} = 0.56 \cdot \langle Si \rangle$). Putting these results together one gets $p = p_{Si} = N_A - N_D = 0.56 \cdot (N_A + N_D)$, which gives a compensation ratio of $\frac{N_D}{N_A} \sim 0.28$. This value is in good agreement with the result obtained above using the theoretical hall mobilities: That approach suggested $\frac{N_D}{N_A} \sim 0.2 \dots 0.3$ for the samples in which the NA can be neglected (i.e. above $p_{300K} \sim 5 \cdot 10^{16} \text{ cm}^{-3}$). Moreover the result is in good agreement with [37] where compensation ratios of up to 25% were reported for Si-doped GaSb grown on semi-insulating GaAs.

5.2.3 Summary

Two different approaches have been used in order to find the degree of compensation for silicon doped p-type GaSb: For lightly doped samples the measured mobilities were compared to calculated ones, whereas for higher doping levels SIMS- and Hall-measurements were compared. In the transition region both approaches are in good agreement. In summary, they give the following picture: Not-intentionally doped and lightly silicon doped GaSb is highly compensated by an unknown donor. The corresponding Hall mobility suggests a compensation ratio of approximately 0.7 for a not intentionally doped sample. In contrast, silicon-doped GaSb at higher doping levels shows significantly lower compensation ratios in the range 0.2 ... 0.3. Here, SIMS measurements suggest that the amphoteric nature of silicon leads to a certain amount of Si-impurities incorporated on donor sites, resulting in a partly self-compensating behaviour. The results for layers grown under similar conditions are summarized in the following figure 5.4.

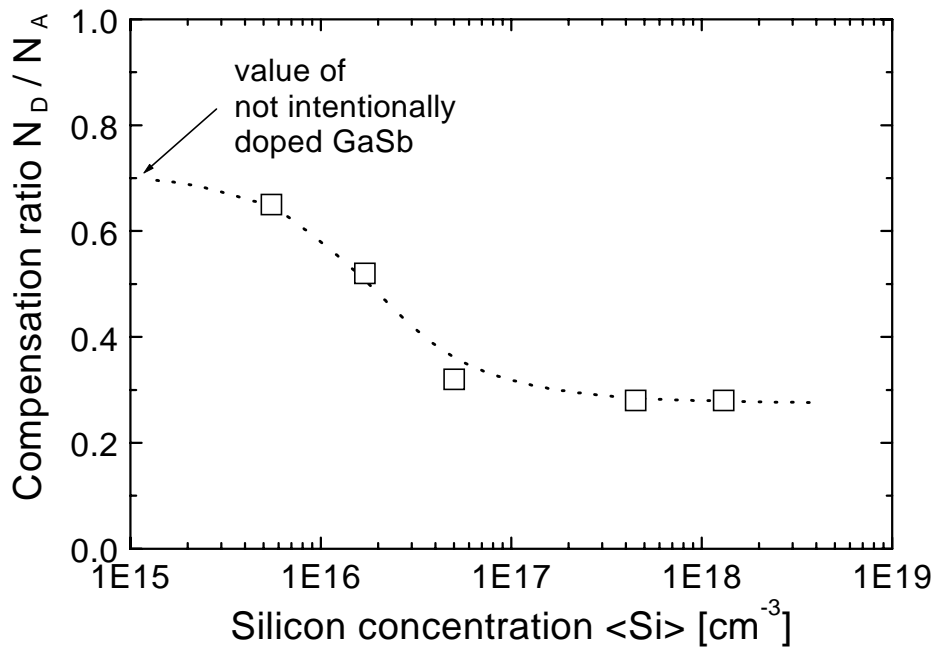


Figure 5.4: Compensation ratio of Si-doped GaSb as a function of the doping level. Only layers grown at otherwise identical growth conditions are included. The dotted line is a guide to the eye.

5.3 Optical properties

5.3.1 Introduction

The low temperature spectrum of undoped GaSb exhibits numerous PL lines in the range 700-810 meV. Not intentionally doped GaSb always exhibits p-type conductivity regardless of the applied method of crystal growth. The main method of reducing the concentration of these “native acceptors” has been to employ low-growth temperatures in epitaxial techniques. Additionally, transition metal doping has been reported as a promising possibility [48]. As already stated elsewhere, the native acceptors (NA’s) are based on a gallium vacancy-gallium antisite complex ($V_{\text{Ga}}, \text{Ga}_{\text{Sb}}$) which has been established to be a doubly ionizable acceptor with ionization energies of about 34 and 102 meV ([77], [76] and references therein). The PL-line corresponding to the neutral NA has been observed between 775 and 778 meV and is often denoted as A-line in the literature. Based on a significant shift to higher energies with increasing excitation density, it was suggested to be a donor acceptor pair transition (DAP) in [76] where a binding energy of 3.1 meV was estimated for the involved donor (as well [26] and references therein). However, other authors have suggested the A-line to be a conduction band-neutral native acceptor transition (e, NA^0) [30, 87].

At higher energies, several peaks have been observed which are commonly attributed to bound exciton transitions: Two PL lines with maxima at 805.4 and 803.4 have been denoted in the literature as BE1 and BE2, respectively [85]. The nature of these lines has been identified as excitons bound to the doubly ionizable neutral native acceptor. At that time, this result from Noack et al. [77] was the first observation of excitons bound to doubly ionisable acceptors. It is interesting to note that Haynes rule, which postulates

an increase in exciton binding energy with increasing binding energy of the involved acceptor [47], has been found *not* to hold for BE1 and BE2 [85].

A peak at 800.1 meV was shown to have the same decay mechanism as BE1 and BE2 using Zeeman splitting in magnetic fields. It was therefore as well identified as recombination of excitons bound to an unspecified acceptor in LPE-grown crystals and consequently denoted BE3 [85]. However, other authors have as well observed a line at approximately 800 meV in MOVPE- and MBE-grown material [30, 76]. These authors identify the line as (e, A^0) transition in MOVPE material [30] and as DAP transition or deep donor to band transition in MBE material [76], distinct from the BE3-line reported previously at the same energy. In this context, a detailed analysis of temperature dependent Hall-measurements in [125] for undoped MBE-GaSb suggests the presence of a donor and two kinds of acceptors, where one of the acceptors was shown to have the two ionisation levels ascribed to the NA. As will be discussed in section 5.3.6, a DAP- or (e, A^0) -like PL peak can indeed be expected in such material.

Bound exciton transitions typically show small half widths and disappear quickly with increasing temperature due to dissociation without a noticeable shift of energy. As a result, their behaviour is in clear contrast to that of donor-acceptor or free electron-acceptor recombination. The different mechanisms can therefore be reliably distinguished. In this context, the line in question at about 800 meV has as well been shown to be a characteristic feature of the Si-doped MOVPE-samples of the present work. As an excitonic character can be excluded from the following analysis below, the line will *not* be denoted as BE3 *but* as E-line throughout the following text.

A further PL line is commonly reported with a maximum at 796.1 meV, denoted as BE4 in e.g. [30, 76, 85]. The line is considered as PL recombination of an exciton bound to an unidentified neutral acceptor [85, 87]. While BE1 and BE2 seem to be the dominant excitonic transitions in material grown under stoichiometric or Ga-rich conditions, BE4 transitions are reported to be stronger in material grown under Sb-rich conditions ([30] and references therein). Chidley et al. [30] report as well that electrically higher quality material shows a smaller A/BE4-ratio.

An additional PL line at around 808 meV has been reported and is often denoted as D-line. It is ascribed to an exciton bound to a donor in [26], denoted as unidentified in [30, 86] and ascribed to a (D^0, h) transition in [24].

Finally, a free exciton (FE) transition in LPE-grown GaSb is reported at 809.9 meV [86] with a calculated binding energy of the free exciton stated as 2.1 meV in [76]. However, reports on FE peaks in MBE or MOVPE material are extremely rare. A corresponding FE peak in MBE grown material has been reported in [125], and only a related weak and hardly resolved shoulder has been seen in MOVPE material (ref. 12 in [125]).

Only one report on the PL of intentionally silicon doped MOVPE-grown GaSb could be found in the literature [37]. The PL spectrum reported therein shows two peaks. A peak at around 800 meV is suggested to represent an exciton bound to a neutral acceptor Si_{sb} , and the second peak at about 809 meV is suggested to be due to the free exciton recombination. However, no detailed analysis of the PL behaviour is reported and with regard to the following analysis the suggested nature of the two peaks in [37] is likely to be a misinterpretation.

The PL spectra of MBE-grown Si-doped GaSb reported in [84] represent a single PL line with maximum at about 796 meV and FWHM > 7 meV. By simply comparing the peak position to the known peak position of the BE4 line, the authors have ascribed the line to a recombination of excitons bound to neutral Si_{sb} -acceptors. However, a detailed analysis is not reported. The given linewidth and the absence of a detectable PL signal in the authors' related undoped MBE-GaSb add a serious degree of uncertainty to their interpretation.

GaSb layers grown by LPE, which were deliberately doped with Si or Ge, show doping related PL lines with maxima peaked at nearly equal energies of 801.2 meV (ref. 18 in [3]). The authors have ascribed the lines to donor acceptor pair transitions and estimate the binding energies of Si and Ge acceptors in GaSb as 9.4 ± 0.5 meV and 9.5 ± 0.5 meV, respectively. For comparison, an activation energy of the acceptor Si_{sb} in GaSb was reported as 11 meV in [35].

Obviously the data available on the PL characterisation of Si-doped epitaxial GaSb reveal a considerable uncertainty in the doping related PL peak positions and their assignments. In this context, especially the nature of the line at 800 meV in not intentionally doped and Si-doped GaSb (BE3- or E-line) remains controversial. The correlation between this line and Si-impurities needs a closer investigation which will be the prime motivation within the following analysis.

5.3.2 Experiment

Silicon-doped and nominally undoped GaSb was grown on Te-doped GaSb (100)-substrates, misoriented 2° toward (111)A. The following identical growth conditions were chosen in order to ensure the comparability between the samples: Triethylgallium (TEGa), tritertiarybutylaluminium (TTBAI), tertiarybutylarsine (TBAs) and trimethyl-antimony (TMSb) were used as metalorganic precursors. Silane (SiH_4) was used as source gas for Si-doping. The GaSb growth rate was $1 \mu\text{m}/\text{h}$ and the V/III ratio was 2 for all samples. Samples #550 and #552 were grown at 590°C without a buffer layer. In sample #511, the nominally undoped GaSb bulk layer was grown on a 200 nm $(\text{Al}_{0.06}\text{Ga}_{0.94})\text{Sb}$ -buffer layer at 600°C in order to prevent the diffusion of excited carriers into the substrate. As a result, sample #511 showed the highest integrated PL intensity compared to all other undoped samples. It was therefore selected as a reference sample for nominally undoped GaSb. The effect of the small growth temperature difference between #511 and #552/#550 can be neglected for the analysis of the PL properties. The following table summarizes the relevant data for the examined samples:

Sample	Dopant	Type	V/III-ratio	Thick-ness [μm]	ρ [cm^{-3}] at 300 K	ρ [cm^{-3}] at 77 K	μ [cm^2/Vsec] at 300 K	μ [cm^2/Vsec] at 77 K
#511	none	p	1.5	2	6.7e16	1.8e16	421	1840
#550	Si	p	1.5	2	5.3e17	-	470	-
#552	Si	p	1.5	2	4.8e16	1.7e16	514	2164

5.3.3 PL-results: Undoped GaSb

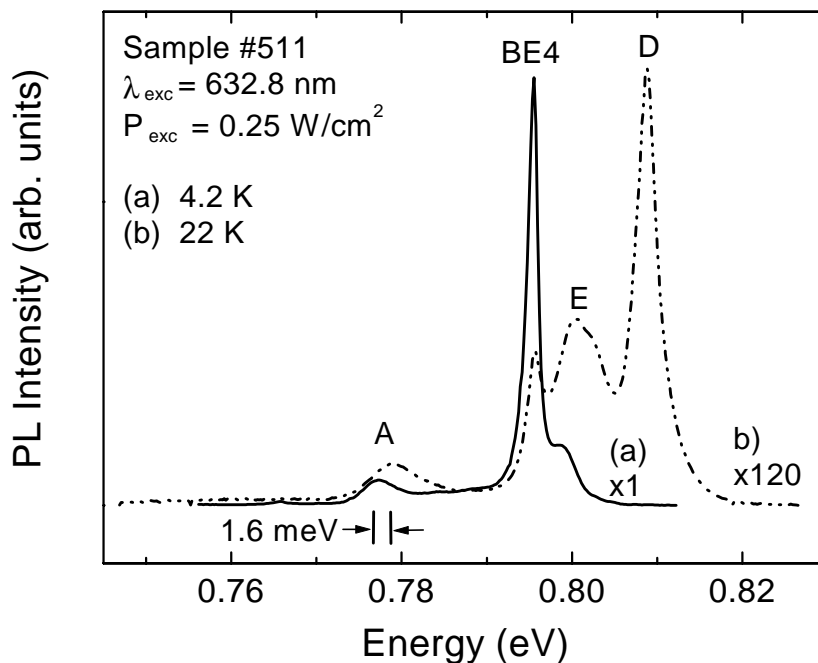


Figure 5.5: PL spectra of the not intentionally doped sample #511 recorded at a constant excitation density at two different temperatures.

The above figure 5.5 gives a survey of characteristic PL spectra of the not intentionally doped sample #511 in the range 745-830 meV. It shows two PL spectra recorded at 4.2 K and 22 K under constant excitation density of 0.25 W/cm^2 . PL spectra recorded at the two excitation densities of 0.1 W/cm^2 and 10 W/cm^2 at a constant temperature of 4.2 K and can be seen in the following figure 5.6.

In addition to the BE4 and A lines, the two figures show the temperature and excitation dependent evolution of two further lines, denoted as E and D, with maxima at around 0.800 eV and 0.808 eV, respectively. In common with the results reported by Chidley *et al.* [30] the E-line peak shifts to higher energies with increasing temperature (approximately 1.6 meV within the range 4.4-22 K). Similarly a less pronounced blue shift of this peak with increasing excitation density can be observed. In this context, it is important to emphasize the similar behaviour of the A-line peak, which also shows the same shift to shorter wavelengths on both temperature and excitation density rise.

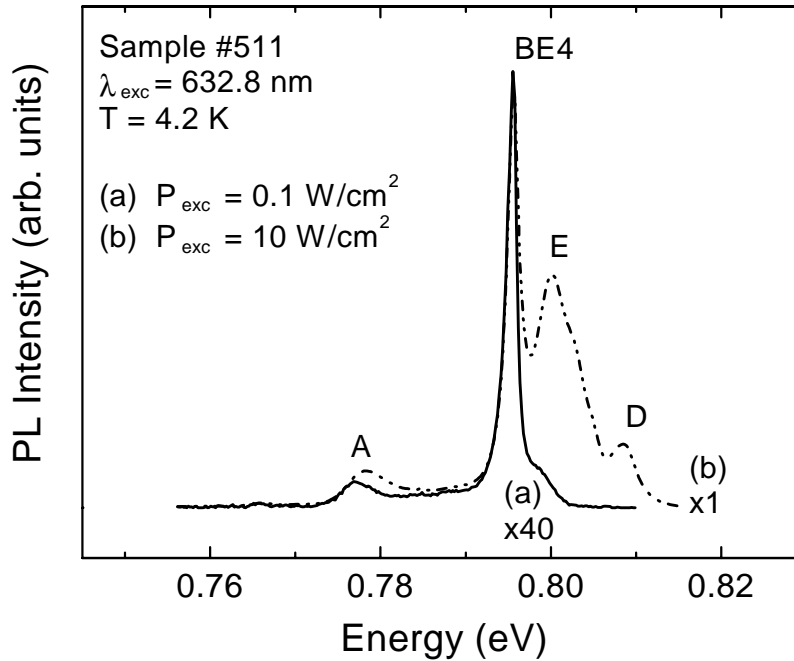


Figure 5.6: PL spectra of the not intentionally doped sample #511 recorded at a constant temperature at two different excitation densities.

5.3.4 PL-results: Si-doped GaSb

The following figure 5.7 shows a comparison of the PL spectra of the nominally undoped homostructure #511 and the intentionally Si-doped samples #550 and #552 recorded at equal experimental conditions.

The samples doped with Si show a strong increase in the integral PL compared to that of sample #511. The comparison between sample #511 and #552 is especially interesting because both samples show almost identical acceptor concentrations in Hall measurements.

While the PL spectrum of the Si-doped sample #552 reveals a multiline structure, the PL spectrum of sample #550 is a single broad band with a maximum at 796 meV and FWHM of 9.2 meV. The broad PL of sample #550 will be shown to be due to band-band luminescence in a highly doped and partially compensated semiconductor (see section 5.3.5). The further PL characterisation of Si-doped GaSb will therefore focus on the lightly doped sample #552.

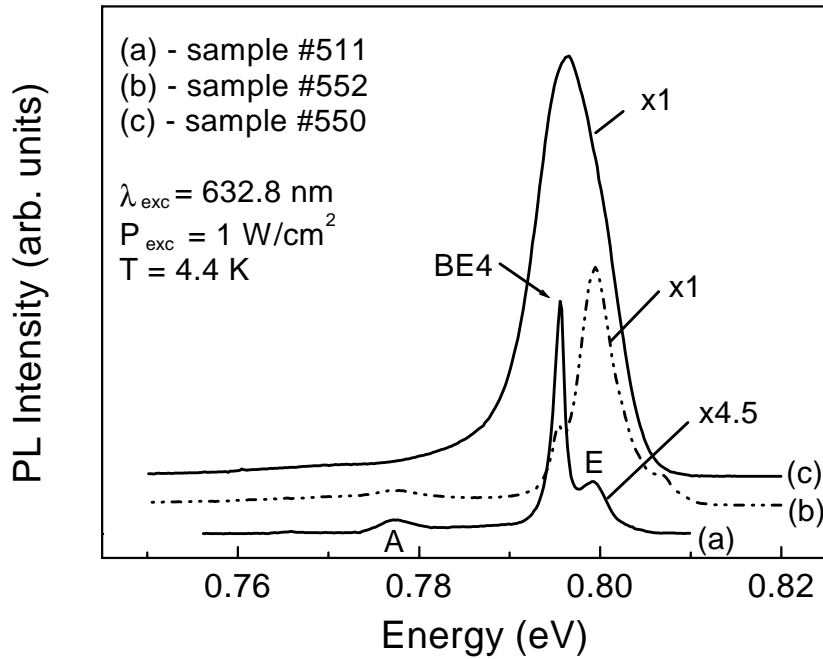


Figure 5.7: Comparison of the photoluminescence spectra of the not intentionally doped sample #511 and the silicon doped samples #550 and #552.

The following figure 5.8 shows the PL excitation density dependence for sample #552 in the range 790-815 meV at a constant temperature of 4.2 K.

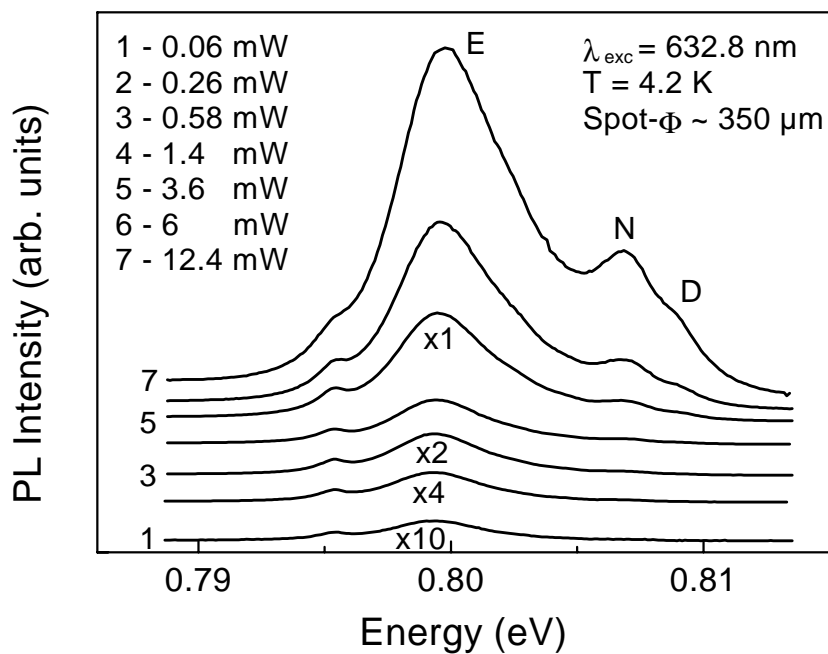


Figure 5.8: Photoluminescence excitation density dependence of the lightly silicon doped sample #552 at 4.2K. The spectra are displaced vertically for clarity.

The PL spectrum (figure 5.8) shows the same lines as the not intentionally doped sample #511 (BE4, E and D peaks; see previous section). However, the E-line is now dominant and shows a FWHM of ≈ 5 meV, while the BE4 line is strongly attenuated compared to the E-line. The E-line peak is shifted to higher energies when the excitation density is increased. A new peak at 0.807 eV, denoted as N, can be observed in the PL spectra. This peak apparently shows a constant position with increasing excitation density.

The temperature dependence of the #552 PL spectrum in the range 780-815 meV is depicted in figure 5.9 below. The BE4 line is thermally quenched rapidly and is hardly observable above 20 K. The E-line intensity declines with the temperature increase slower than BE4 and shows a shift to higher energies of about 0.8 meV in the range 4.4-36 K. The N-line is thermally quenched in the range 4.4-28 K without noticeable change in peak position. The D-line intensity increases with rising temperature and its peak position moves toward lower energies.

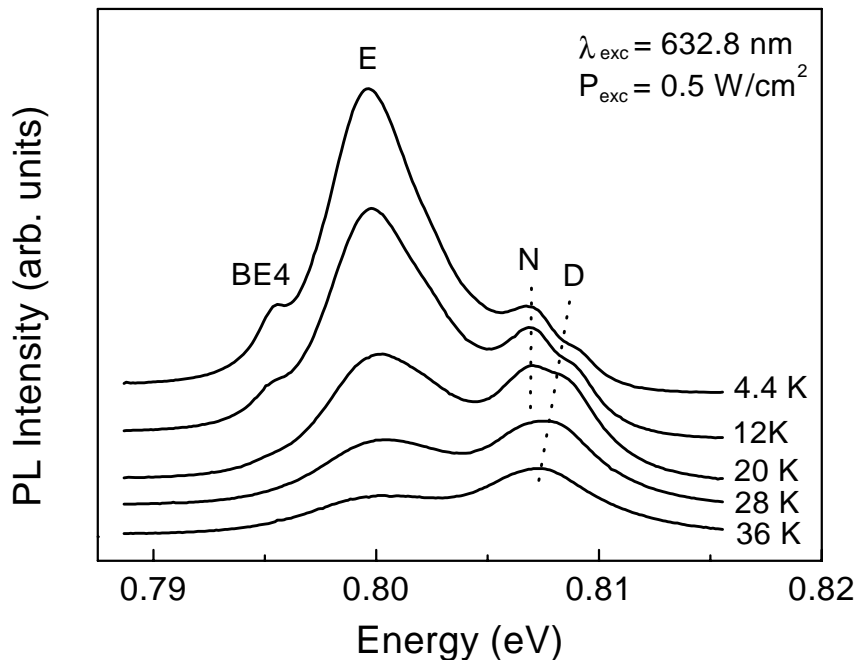


Figure 5.9: Photoluminescence temperature dependence of the lightly silicon doped sample #552 at 0.5 W/cm^2 . The spectra are displaced vertically for clarity.

5.3.5 Discussion of PL-results: Heavily doped GaSb

In the above collection of PL results the spectrum of sample #550 was shown to be a single broad band with a maximum at 796 meV and FWHM of 9.2 meV. In the following it will be shown that the broad PL of this sample can be considered as due to band-band luminescence in heavily doped material.

In a lightly n-doped (p-doped) semiconductor at low temperatures, electrons (holes) are localized at the donor (acceptor) impurities and low-temperature conduction is activated ([91], page 253). If the doping level is increased, impurity wavefunctions begin to

overlap and the related states can be delocalized on a scale of several impurity atoms. If the doping levels are increased even further, states in the centre of the impurity band become completely delocalised in real space and metallic conduction occurs. This transition between metallic and activated conduction is called an "Anderson-transition".

If charge carriers with a non-vanishing mobility are present, the Coulomb potential of a charged impurity in a doped semiconductor will be screened. In a linear approximation, the resulting overall potential can be written as $V = \frac{1}{4\pi} \cdot \frac{e}{\varepsilon \cdot r} \cdot \exp\left(-\frac{r}{r_0}\right)$ ([91], equ.

11.1.10). Here, r_0 is called the screening radius and ε stands for the permittivity of the material $\varepsilon = \varepsilon_0 \cdot \varepsilon_r$. In a highly doped and partially compensated semiconductor at low temperatures, the underlying transport mechanism will be hopping of uncompensated majority carriers (and mobile carriers in the bands at higher temperatures). In a linear approximation the corresponding screening radius can be described as (equ. 11.1.8 in [91] and equ. 2.1 in [70]):

$$r_0 = \frac{a_B}{2} \cdot \left(\frac{\pi}{3}\right)^{1/6} \cdot \left(\frac{1}{p \cdot a_B^3}\right)^{1/6}$$

Here, a_B stands for the Bohr radius of the majority impurity. Assuming that in partially compensated samples the underlying transport mechanism at low temperatures will be hopping of uncompensated majority carriers, p stands for $p = N_A - N_D$ ([91], p. 262).

It can be shown that bound states in a screened potential exist only if the screening radius r_0 is much greater than the related Bohr radius a_B ([53], p. 394). It can now be shown that bound states do not exist in sample #550, neither for acceptors nor for donors.

Firstly, the Bohr radii of acceptors and donors have to be calculated. In this context, one simple approach to describe shallow impurities is to the so-called *effective mass approximation*. Here it is assumed that the extra charge on a shallow impurity's nucleus is screened simply by the relative dielectric constant ε_r of the host crystal. It can be shown that the impurity can then be treated as a hydrogen atom with the additional factor $1/\varepsilon_r$ in the corresponding Coulomb potential $V = \frac{1}{4\pi\varepsilon_0} \cdot \frac{1}{\varepsilon_r} \cdot \frac{|e|}{r}$ and taking

effective masses m^* instead of the free space electron mass m_0 [126]. The extent of the bound-state wave function in real space can then be expressed in terms of a Bohr radius a_B^* which is related to the Bohr radius in the hydrogen atom $a_B = \hbar^2 / m_0 e^2 = 5.29177 \cdot 10^{-11} \text{ m}$ by $a_B^* = \left(\varepsilon_r \cdot m_0 / m^*\right) \cdot a_B$. In the following the effective masses and the static relative dielectric constant in GaSb are accepted from Stollwerk et al. [94] as $m_e^* = 0.047m_0$, $m_h^* = 0.32m_0$ and $\varepsilon_r = 15.69$. One can now estimate the Bohr-radii of the shallow donors and acceptors in GaSb as $a_B^e \sim 177 \text{ \AA}$ and $a_B^h \sim 26 \text{ \AA}$, respectively.

These Bohr radii must now be compared to the screening radius in sample #550. Accepting the free hole concentration as measured by Hall at room temperature as the concentration of uncompensated majority carriers $p_{\#550} = N_A - N_D = 5.3E17 \text{ cm}^{-3}$, one obtains a screening radius of $r_0 = 29 \text{ \AA}$.

As mentioned above, bound states in a screened potential exist only if the screening radius r_0 is much greater than the related Bohr radius a_B . The comparison between the calculated r_0 and the above Bohr radii shows that bound donor states can be excluded for sample #550 and bound acceptor states are highly unlikely. As a result, the broad PL of sample #550 is therefore considered as due to band-band luminescence in a highly doped and partially compensated semiconductor [23].

In p-type degenerate direct gap III-V semiconductors the optical band-gap shrinks with the concentration increase since the Burstein-Moss effect for holes is less effective than the bandgap narrowing. (For n-type GaSb the opposite is true and a corresponding blue-shift of the PL with increasing Te-doping has been observed. [24].) In ref. [Jain90] of [93] the band-gap narrowing of p-type GaSb at room-temperature as a function of the doping level is approximated as $\Delta E_{\text{gap}} = A * N^{1/3} + B * N^{1/4} + C * N^{1/2}$ with the following parameters for p-GaSb: $A = 8.07 \times 10^{-9} \text{ eV cm}$, $B = 2.8 \times 10^{-7} \text{ eV cm}^{3/4}$, $C = 4.12 \times 10^{-12} \text{ eV cm}^{3/2}$. This function is plotted in the following figure 5.10 (taken from [93]) together with experimental data obtained at 4K (ref. [Titkov81] in [93]).

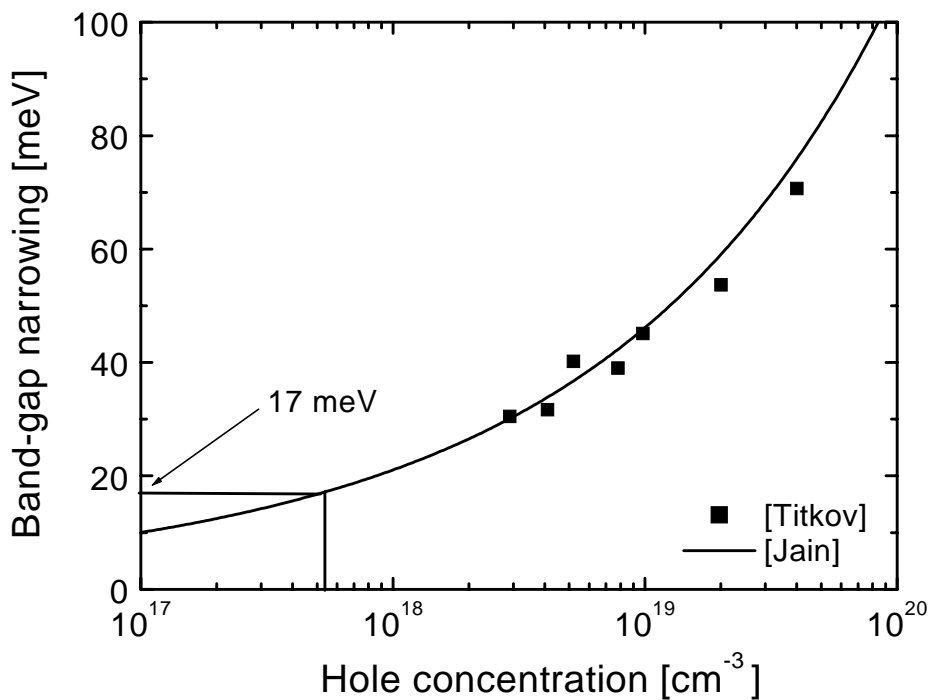


Figure 5.10: Band gap narrowing of p-type GaSb as a function of the hole concentration. Sample #550 is compared to the literature data given in the text.

A further confirmation of Jain's model is found in [52] for Zn-doped GaSb. At the doping level of sample #550 these data indicate a band gap narrowing of 17 meV. As a band gap of $E_G(2K)=812\text{meV}$ [76] is accepted for GaSb throughout this work, the 4.4K-PL peak position of 796 meV of sample #550 corresponds to a band gap narrowing of around 16 meV which is in reasonable agreement with the above approximation by Jain.

As an overall result, the broad line in the PL spectrum of sample #550 can be considered as due to band-band luminescence in highly doped and partially compensated GaSb with a band-gap reduced by about 16 meV.

5.3.6 Discussion of PL-results: Lightly doped GaSb

5.3.6.1 Introduction

In order to develop a detailed understanding of the PL of not intentionally doped and lightly silicon doped GaSb a thorough analysis of the peculiarities of this material must be carried out. In contrast to other III-V semiconductors, which can be deposited in very pure qualities nowadays, GaSb is always significantly p-type due to the native acceptor and notably compensated. Generally, in a lightly doped, partly compensated semiconductor at very low temperatures all minority impurities and an equal number of majority impurities will be charged ([91], p. 53). In spite of the presence of ionized impurities, no free carriers are present in the bands. Transport can only occur by carriers jumping from neutral majority impurities to charged ones without any excursion to the bands. This mechanism is called "hopping". Obviously, the presence of charged positions on majority impurities is a necessary condition for hopping transport. At low temperatures in lightly doped semiconductors this condition can only be fulfilled by compensation.

This situation results in charges which are randomly located in the semiconductor. The presence of these charges means an additional potential energy for mobile charge carriers in the crystal. A mobile charge carrier at the band edge will have a potential energy depending on the distribution of located charge clusters nearby. In other words, the band edge energy coincides with the carrier's potential energy and consequently the band edge itself will be subject to a modulation in real space ([80], chapter 6.1). This modulation is characterised by the related mean-square potential energy (equ. 11.2.7 in [91], SI-system; equ. 4 in [23]):

$$\gamma^2 = \frac{1}{4\pi} \cdot \frac{e^4}{\epsilon^2 \cdot r_0^2} \cdot (N \cdot r_0^3), \text{ or}$$

$$\gamma = \frac{1}{2\sqrt{\pi}} \cdot \frac{e^2}{\epsilon} \cdot \sqrt{N \cdot r_0}$$

In this expression, r_o stands for the screening radius which was already introduced for the Coulomb potential of a single charged impurity in section 5.3.2. In the related linear approximation the screening radius r_o does not depend on the magnitude of the potential to be screened ([91], chapter 11.1). Consequently, the expression from section 5.3.2 can as well be used in the above expression for γ and marks the characteristic size of a corresponding "potential well" [70]. N stands for the total concentration of charged centres in the partially compensated semiconductor. As all minority impurities and an equal number of majority impurities will be ionized at low temperatures, the total concentration of charged centres in a p-type sample is $N = N_A^- + N_D^+ = 2 \cdot N_D$. For a given majority impurity concentration it is evident that γ will increase with the compensation ratio.

According to the compensation ratios determined in section 5.2, the related data for the undoped sample #511 and the lightly silicon doped sample #552 are presented in the following table. The influence of a thin (AlGa)Sb-buffer layer in sample #511 was neglected. However, nominally undoped samples *without* a buffer layer confirmed the somewhat lower mobility of holes in undoped GaSb compared to the lightly silicon doped material #552.

	p [cm⁻³] at 300 K	p [cm⁻³] at 77 K	μ [cm²/ Vsec] at 77 K	Compen- sation ratio	N_A [cm⁻³]	N_D [cm⁻³]	γ [meV]	r_o [Å]
#511	6.7e16	1.8e16	1840	0.5	1.3E17	6.7E16	7.5	40
#552	4.8e16	1.7e16	2164	0.45	8.7E16	3.9E16	6.0	43

As a consequence of the fluctuations described by γ , a percolation level E_c for electrons is formed below the non-perturbed conduction band edge E_C^0 . Above this level electrons have a non-vanishing mobility and may be regarded as free [79]. The energetic distance γ_e between the non-perturbed band gap energy and the percolation level is $\gamma_e = E_C^0 - E_c < \gamma$. Similarly, a percolation level E_v for holes is formed with $\gamma_h = E_v^0 - E_v < \gamma_e < \gamma$.

Another very important conclusion can be drawn from the data in the above table: Considering that bound states in a screened potential exist only if the screening radius r_o is much greater than the related Bohr radius a_B ($a_B^e \sim 177 \text{ \AA}$, $a_B^h \sim 26 \text{ \AA}$, see section 5.3.5), the above screening radii in samples #552 and #511 imply that

- no bound states associated with isolated donors can be expected in the material, while
- well-defined bound states associated with isolated acceptors should be present.

As a consequence, two main kinds of optical transitions involving shallow impurities have to be discussed, namely tail-impurity (TI) transitions (i. e. a recombination of an electron captured in a localized state in the conduction band tail with a hole at one of the neighbouring acceptors) and band-impurity (BI) transitions (i. e. a recombination of a free electron with a hole captured by an acceptor). The situation is illustrated in the following figure 5.11:

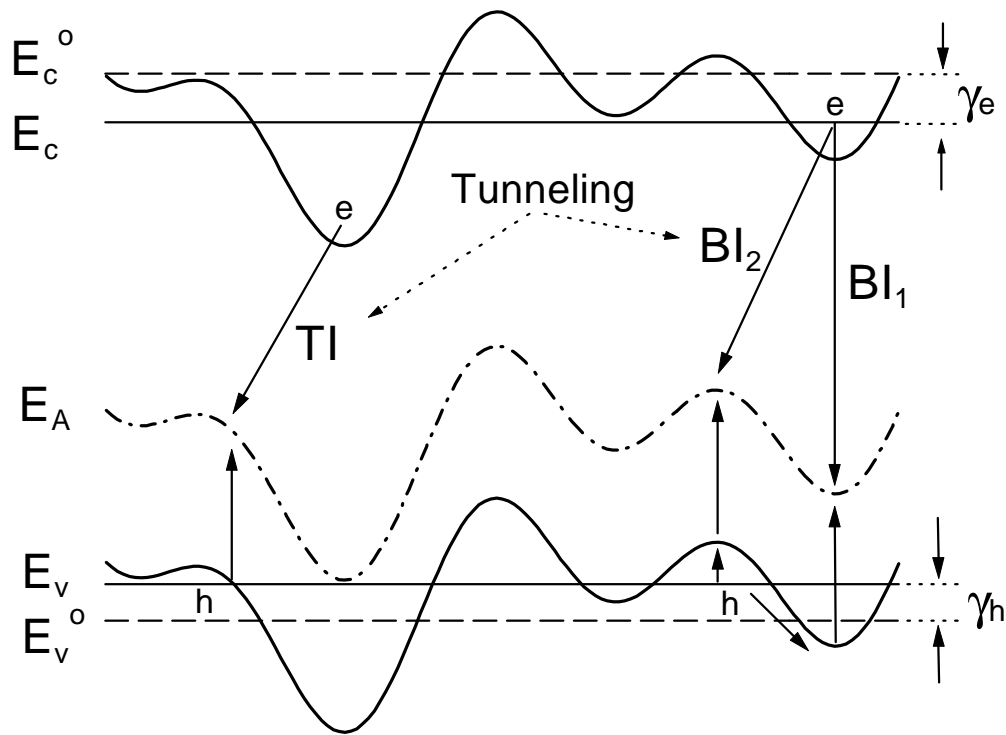


Figure 5.11: *Band structure in real space*

- local fluctuations of the band edges
- formation of percolation levels E_c and E_v that lower the band gap energy
- no bound states associated with isolated donors
- well-defined bound states associated with isolated acceptors at E_A

Electrons are not localised in a typical potential well of depth γ and size r_o in the conduction band because their effective masses are small and the typical well is rather shallow [79]. Consequently, most electrons will be free on their percolation level. Only point clusters of large numbers of donors will lead to localised states in the conduction band tail. On the other hand holes will usually be localised in the valence band tails because of their higher masses. Similarly, it is much easier for electrons than for holes to tunnel into the barriers. This will be considered in the discussion of the possible transitions below. A theoretical treatment and numerical simulation of the PL of this kind of material is given in [79]. Two important points shall be emphasized:

As a TI transition involves a localised electron, it can only occur in the vicinity of a deep potential well. At low temperatures, holes can not approach such a deep donor well and can therefore not be captured by an acceptor close to the well. As a result, a TI transition at low temperatures can not be vertical in real space and involves tunneling of the electron into the barrier. Due to the resulting small overlap of the wavefunctions the probability of a TI transition at low temperatures is low [79]. At elevated temperatures, TI transitions are quenched as well due to the thermal release of holes from the acceptor levels. As a result, the calculated intensity of the TI luminescence in figure 5 of reference [79] shows a maximum at a temperature of approximately 20 K and the line is quenched rapidly at higher or lower temperatures.

Apart from the TI transitions, two different kinds of BI transitions have to be considered (see figure 5.11): In addition to the usual BI1 channel it is as well possible that electrons tunnel notably into the conduction band humps, leading to the BI2 transitions in the above figure 5.11. As higher temperatures are needed to populate valence band states with holes that can neutralise BI1-acceptors, a shift of (tunneling-induced) BI2 to BI1 transitions occurs when the temperature is increased [79]. As BI1 transitions have higher energies than BI2 transitions, a temperature increase can cause a strong shift of the BI-related PL peak position to higher energies by several meV (figure 4 of [79]).

5.3.6.2 D-line

As stated in the introduction 5.3.1, in the region of the observed D-line energies a free exciton (FE) transition in GaSb is reported at 809.9 meV. At first sight one might therefore expect the D-line to represent free exciton recombination. However, the overall experience with MOVPE-grown GaSb makes the appearance of a well resolved FE unlikely. Besides, the D-line becomes dominant in the PL spectrum of not intentionally doped GaSb for temperatures above 28 K, it moves to lower energies with the temperature rise and to higher energies with increasing excitation density.

Therefore, a much more likely interpretation of the D-line is a recombination of a free electron from the electronic percolation level with a free hole from the valence band percolation level. Consequently the D-line peak position will reflect the band gap energy in the perturbed system: With increasing temperature the band gap decreases and a red-shift of the PL is observed, while at increasing excitation density the quasi-Fermi levels move to higher energies and cause a blue-shift of the PL line. As a result, the observed experimental behaviour can be well understood. Besides, taking the position of the D-line at 4.4 K to be 808.5 ± 0.4 meV (see figure 5.9) and accepting a band gap of 812 meV for non-perturbed GaSb at this temperature, the difference of 3.5 ± 0.4 meV can serve as a good estimate of the overall band gap reduction $\gamma_e + \gamma_h$ due to the perturbations.

5.3.6.3 BE4-line

As expected from the literature data on this line (see section 5.3.1), the BE4-line can be considered as PL recombination of an exciton bound to an unidentified neutral acceptor: The line is thermally quenched above 20K and keeps constant position with increasing temperature.

5.3.6.4 E- and A-lines

As reported in section 5.3.4, the E-line appears at approximately 800 meV and is the dominant line in the intentionally silicon doped sample #552. As described in the introduction, a line at 800 meV was previously identified as recombination of excitons bound to an unspecified acceptor in LPE-grown crystals and consequently denoted BE3 [85]. In contrast to this result, other authors as well observed a line at approximately 800

meV in MOVPE- and MBE-grown material [30, 76]. These authors identified the line as (e, A^0) transition in MOVPE material [30] and as DAP transition or deep donor to band transition in MBE material [76], distinct from the BE3-line reported previously at the same energy.

The E-line in sample #552 remains observable to temperatures above 40 K and shifts to higher energies with temperature rise (approx. 0.8 meV between 10 - 32 K). Comparing the thermal quenching of the E-line to the corresponding behaviour of the excitonic BE4-transition, an excitonic character of the E-line seems highly unlikely. Consequently, the coincidence between the E-line position in sample #552 and the BE3 line position reported in [85] must be considered accidental. Similarly, a DAP (donor acceptor pair) transition can be ruled out for the E-line because bound states associated with isolated donors can not exist in the material of sample #552 (see 5.3.6.1).

As an excitonic and a DAP character can now both be ruled out, TI and BI transitions are likely candidates for the E-line nature. The related impurity is almost certainly silicon because of the evident increase of the E-line intensity in the intentionally silicon-doped sample #552. In the not intentionally doped sample #511 a certain background of silicon is believed to be present due to impurities in the employed metalorganics. As no indication for silicon was found in GaAs layers grown with the same batch of TEGa, the TMSb is considered to be the source of background silicon in sample #511.

In order to estimate the binding energy of the silicon acceptor in GaSb, the exact nature of the silicon-related E-line must be identified. The relative E-line intensity shows a monotonous decrease with increasing temperature in the whole range between 4.4 and 36 K. No thermal quenching at low temperatures could be observed. As already stated at the end of section 5.3.6.1, this behaviour rules out a TI transition. On the other hand, both the E-line's strong blue shift with increasing temperature and its thermal quenching at elevated temperatures are well in line with the properties of BI transitions: While the shift from low-energy BI2 to high-energy BI1 transitions explains the observed blueshift of the E-line peak, the thermal release of holes from the acceptor levels explains the thermal quenching at elevated temperatures. In summary, a BI character of the E-line can be assumed.

It is important to emphasize the following point: The standard way to describe ($e A^0$)- (or "BI"-) transitions in non-perturbed band structures is the Eagles model [30]. This model predicts the thermal dependence of the peak position as $\hbar\omega = E_g(T) - E_A + \frac{k_B T}{2}$.

Here, E_A is the acceptor binding energy and $E_g(T) = E_g(0K) - \frac{a \cdot T^2}{b + T}$ with the Varshni coefficients $a=4.7E-4$ eV/K and $b=265$ K for GaSb [30]. This model predicts a maximum blue shift of 0.3 meV at 13K, whereas sample #552 shows a much more significant shift of approx. 0.8 meV between 10 - 32 K (see figure 5.12). Consequently, the Eagles model is not satisfactory with respect to sample #552 and it is essential to consider the influence of the fluctuating potential.

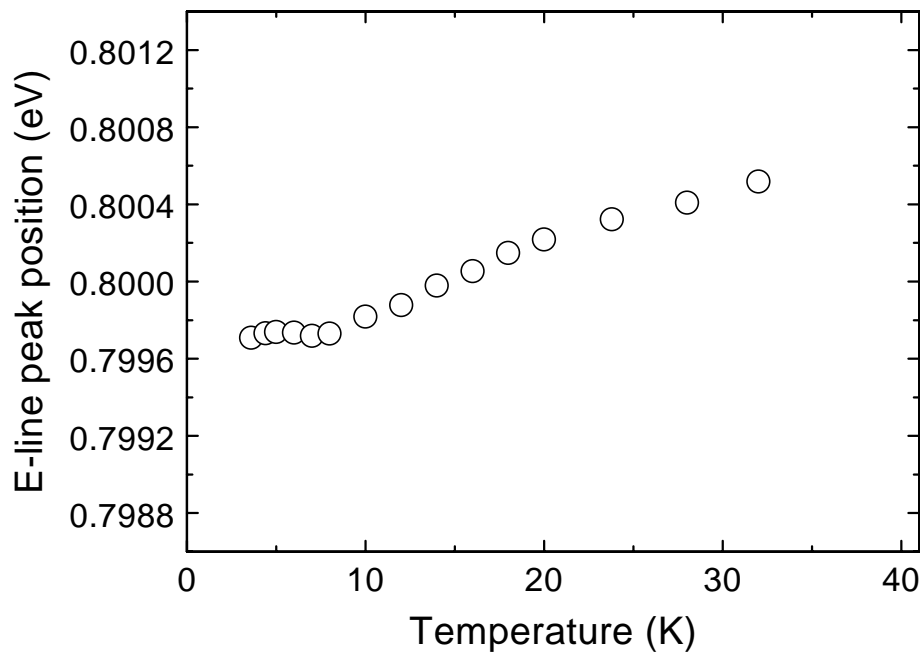


Figure 5.12: *E-line peak position versus temperature.*

The observed shift to higher energies cannot be explained by the Eagles model.

After having identified the nature of the E-line as BI transition, this result can now be used to evaluate the activation energy of the involved acceptor: As derived in [79], an extrapolation to 0K gives $\hbar\omega|_{E\text{-line}, 0K} = E_g(0K) - E_A - (\gamma_e + \gamma_h)$. From the D-line position at 4.4K (see section 5.3.6.2 & figure 5.9) a value of 3.5 ± 0.4 was derived for $\gamma_e + \gamma_h$. Accepting $E_g(0K) = 0.812$ eV and $\hbar\omega|_{E\text{-line}, 0K} \approx 799.7$ meV from the measurement at 4.4K, one gets an activation energy of $E_A = 8.8 \pm 0.4$ meV. For comparison, the literature data on the activation energy of the silicon acceptor are between 9 and 11 meV (see section 5.3.1) while the effective mass acceptor in GaSb has been suggested to have activation energies between 12.5 meV ([88] ch. 1, p. 25) and 16 meV [30].

After having shown that the E-line must be interpreted as band-impurity transition, the nature of the A-line needs some further comments too. As said in the introduction (section 5.3.1) the line has been suggested to be a donor acceptor pair transition (DAP) for example in [76] because of a significant shift to higher energies with increasing excitation density. Other authors have suggested the A-line to be a conduction band-neutral native acceptor transition (e, NA^0) [30, 87]. This obvious contradiction can be solved by accepting that the E-line and A-line are of the same nature, i.e. both are due to (e, A^0) - (or "BI"-) transitions with the participation of two different types of acceptors, namely silicon and the NA for E- and A-line, respectively:

While the A-line and the E-line in sample #511 both show a blue-shift of approximately 1.6 meV between 4.4 and 22K, the above blue shift in sample #552 is smaller. This can be understood by considering that the rms-fluctuations of the potential in sample #552 are smaller compared to sample #511 due to the reduced degree of compensation.

Consequently, the value of γ_h can be expected to be higher in sample #511, leading to a more pronounced blue shift of BI transitions with temperature.

Based on the comparable acceptor concentrations of the not intentionally doped sample #511 and the silicon doped sample #552, the dominance of the E-line in sample #552 suggests that the formation of native acceptors is suppressed by the silicon doping: As the silicon acceptor is incorporated on group V-sites in the crystal structure, a preferential incorporation of silicon on Sb-vacancies can be expected. Considering that the native acceptor (NA) always involves an Sb-vacancy, the NA concentration will be reduced by silicon doping. Taking into account the nearly equal acceptor concentrations of sample #511 and #552, the dramatic increase in the integral PL of sample #552 also indicates a substantial reduction of the non-radiative recombination rate in lightly silicon doped samples.

5.3.6.5 N-line

The line denoted with N is well pronounced in the intentionally Si-doped sample #552. On the other hand it is not observed in the PL spectra of GaSb background-doped with Si neither in this work nor in the literature [30]. The following specific features of the N-line suggest that the origin of this line is most probably a radiative recombination of excitons bound to Si_{Sb} :

- the line keeps constant position with the temperature rise as indicated in fig. 5.9,
- the line is thermally quenched similar to the excitonic BE4 line, and
- the line appears in the PL spectrum only when the dominant acceptor is Si_{Sb} .

5.3.6.6 Comments on the limitations of the model

A crucial feature of the above model is the estimate for the screening radius in the material. Based on the linear approximation given in Shklovskii et al. [91] and Levanyuk et al. [70] the following expression was used:

$$r_0 = \frac{a_B}{2} \cdot \left(\frac{\pi}{3}\right)^{1/6} \cdot \left(\frac{1}{p \cdot a_B^3}\right)^{1/6}$$

For partially compensated samples at low temperatures transport can only occur by carriers jumping from neutral majority impurities to charged ones without any excursion to the bands ("hopping"). In this case, p stands for $p = N_A - N_D$ ([91], p. 262). In the case of the above sample #552 the resulting screening radius was 43 Å. As hopping transport naturally depends on the presence of impurity states, a sphere with a radius of 43 Å might well be too small to contain an adequate number of acceptor (majority) states which can host screening charges. As a result, the true screening radius in the material might well be larger than in the above calculations and bound states associated with isolated donors might become possible from this point of view.

However, there is another strong argument against bound donor states: While on the one hand it is very difficult to predict mathematically when an electron wave function in the donor impurity band gets delocalised (i.e. extended over the entire system, "Anderson transition"), it is experimentally confirmed that the transition between metallic and activated conduction usually occurs at carrier concentrations N satisfying $N \cdot a_B^3 \approx 0.02$ ([91], p. 253). As this condition can be shown to be clearly fulfilled for the system of donors in the above samples, delocalised electron wave functions in the centre of the donor impurity band can be expected.

In summary, bound states associated with isolated donors (or clusters of donors) in the above samples appear very unlikely. Consequently, the interpretation of the E- and A-lines as ($e A^0$) transitions and of the D-line as ($e h$) transition is confirmed.

5.3.6.7 Summary

The PL properties of non-intentionally doped and lightly silicon doped GaSb have been studied. A formerly controversial PL line at approximately 800 meV could be ascribed to silicon acceptors in the material. By considering the potential fluctuations in doped and partially compensated semiconductors, the line could be identified as due to a transition of a free electron to neutral acceptor ($e Si_{sb}^0$). The coincidence of this so-called E-line with the BE3 line, which was previously reported at the same energy, must be considered accidental. Similarly, the nature of the A-line was shown to be due to a transition of a free electron to neutral *native* acceptor ($e NA^0$). All other PL peaks in the high-energy part of the spectrum could be explained within the concept of potential fluctuations due to the charged impurity distribution.

The activation energy of the silicon acceptor could be estimated as 8.8 meV. Generally, light doping with silicon resulted in a higher mobility, a reduced compensation ratio and an improved PL intensity compared to not intentionally doped samples. Silicon doping seems to result in a suppression of the native defect in GaSb and lead to a reduction of the non-radiative recombination rate in the material. These features make the silicon acceptor an interesting novel candidate for various GaSb-based device applications. In this context, the first ever reported Si-doped GaSb-based devices will be presented in the following section 6.

6 Results - Solar cells

6.1 Introduction

6.1.1 Band structure in real space

Several different kinds of photovoltaic devices will be presented in the following sections. They will be described by their nominal film structure and the related band structure in real space. Those band structures will be based on a “dark” situation without an applied voltage and without illumination. However, as it is very instructive the different modes of operation of a pn-junction will be shown in the following band structure diagrams 6.1, 6.2 and 6.3.

The figures want to illustrate general properties of the related situations and do not represent exact calculations. The underlying band gap was chosen as 0.72 eV, i. e. GaSb. The point of reference (0 volts) is the quasi-Fermi level for holes in the p-region.

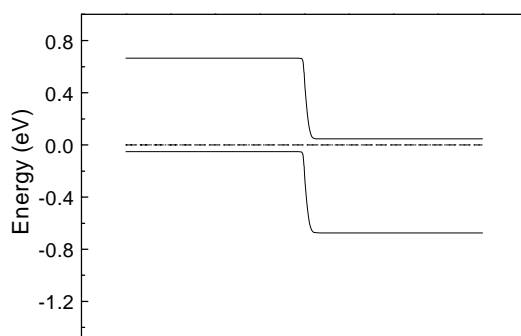


Figure 6.1:

Band structure of a pn-junction (band gap: 0.72 eV, GaSb) without an applied external voltage and without illumination. The Fermi level (dashed line) must be constant throughout the whole device. This representation of device structures will be used in the following sections of this chapter.

Figure 6.1 shows a pn-junction without an applied external voltage and without illumination. This representation will be used for all device structures in the subsequent sections of chapter 6. Figure 6.2 presents a pn-junction without illumination but with an external voltage applied. While the difference between the Fermi levels in the two quasi-neutral regions represents the external voltage, the splitting of the quasi-Fermi levels within / around the junction stands for the non-equilibrium situation linked primarily with a change of the diffusion currents. Figure 6.3 introduces a pn-junction with illumination in short-circuit- and open-circuit-condition. Note that the built-in potential over the open-circuit junction is effectively reduced due to the enhanced concentration of minority carriers in the quasi-neutral regions. This illustrates the fact that a diode can never give a voltage output corresponding to the band gap energy, i. e. $e \cdot V < E_g$ will always apply (see section 2.2.1).

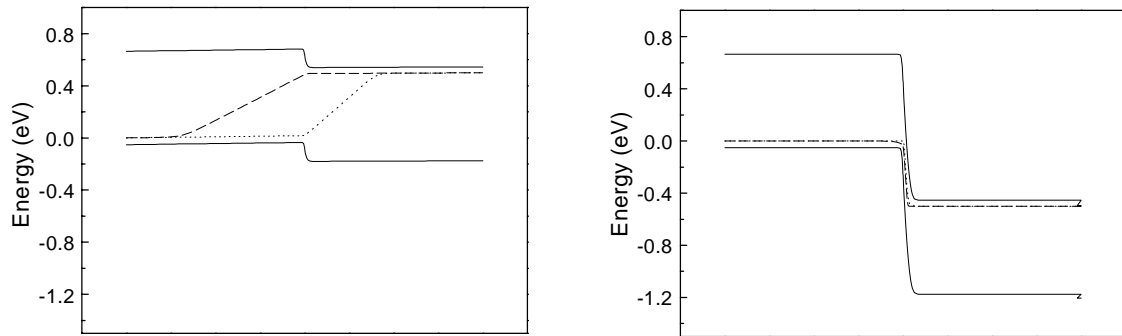


Figure 6.2: Band structure of a pn-junction (band gap: 0.72 eV, GaSb) without illumination but with an external voltage applied (left: forward bias, right: reverse bias). The quasi-Fermi levels for holes (dashed lines) and electrons (dotted lines) are also shown. The quasi-Fermi levels merge into one Fermi-level in the quasi-neutral regions. The related potential difference represents the applied voltage.

As the non-equilibrium situation is linked primarily with a change of the diffusion currents, the quasi-Fermi levels for electrons and holes are split within l around the junction.

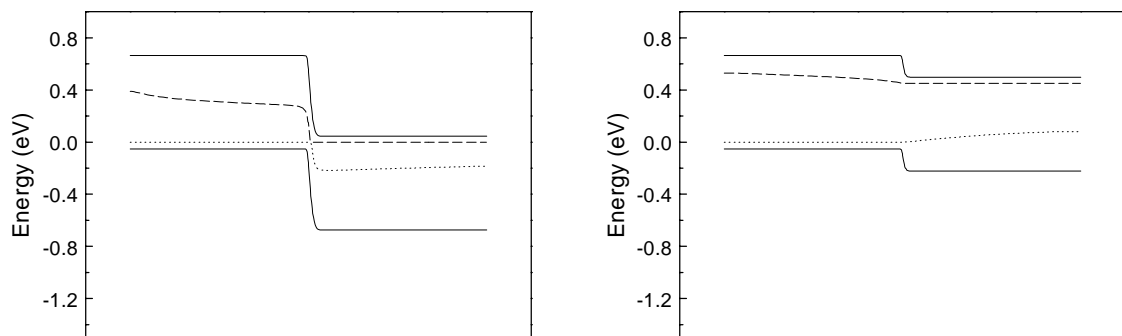


Figure 6.3: Band structure of a pn-junction (band gap: 0.72 eV, GaSb) with illumination in short-circuit- (I_{sc} , left) and open-circuit-condition (V_{oc} , right). At I_{sc} , there is no potential difference between the majority carrier quasi-Fermi levels on both sides of the junction. At V_{oc} , the potential difference between the majority carrier quasi-Fermi levels on the two sides of the junction represents the open-circuit voltage of the device. Besides, the built-in potential over the open-circuit junction is effectively reduced.

6.1.2 Fabrication technology

This section briefly describes the fabrication technology for the devices presented in chapter 6. The first step includes the photolithography for the contact grid fingers. After the deposition of the metal film sequence and a related lift-off process for non-developed photoresist, the gold-germanium backside contact is deposited. Subsequently, the contacts are thickened by gold-electroplating. A mesa is etched to define the device dimensions. The open mesa edges are covered with an anodic oxide for passivation purposes. Finally, bond wires are attached that connect the metal grid to larger contact pads. It must be noted that an antireflective coating was not employed.

The process is still under development with respect to the following problem: As shown in section 6.2.1, a high-band gap (AlGa)(AsSb) front surface passivation layer must be epitaxially grown as confinement for the minority carrier regions of the devices. This aluminium containing layer is expected to cause problems concerning the metal-/semiconductor- interface, i. e. series contact resistances. As a consequence, a highly doped GaSb contact layer is usually grown on top of the passivation layer and subsequently etched off inbetween the metal grid fingers. This etching step is a serious problem for the antimonides because a selective process that would etch GaSb and stop on (AlGa)(AsSb) is not known. For this purpose, an extremely slow etching process based on a developer was employed and the etch depth was determined merely by the time. Apart from the possible inaccuracy of the process with respect to depth and a possible surface roughening, this step had to be employed at the very end of the wet-chemical part of the technology. As a consequence, the passivating layer of anodic oxide on the mesa edge was removed again. This might cause problems such as leakage currents. As a result, the fabrication technology must be further improved in the future.

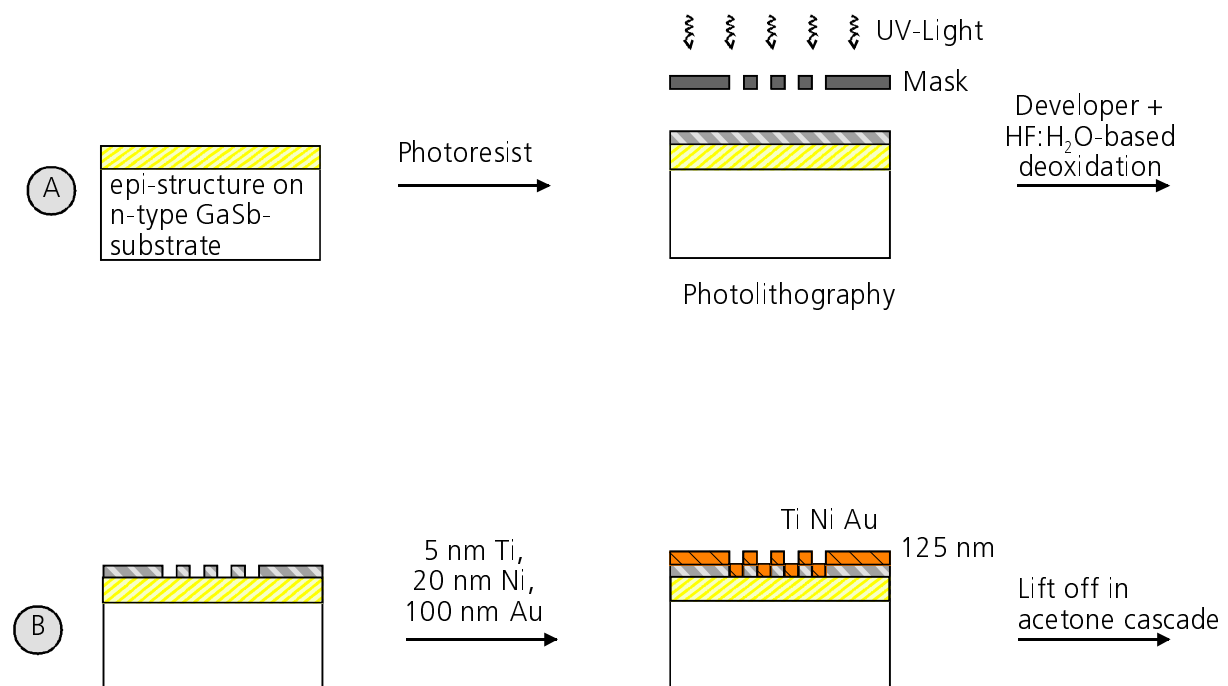


Figure 6.4a: Fabrication technology for epitaxially grown GaSb-based solar cells (I).

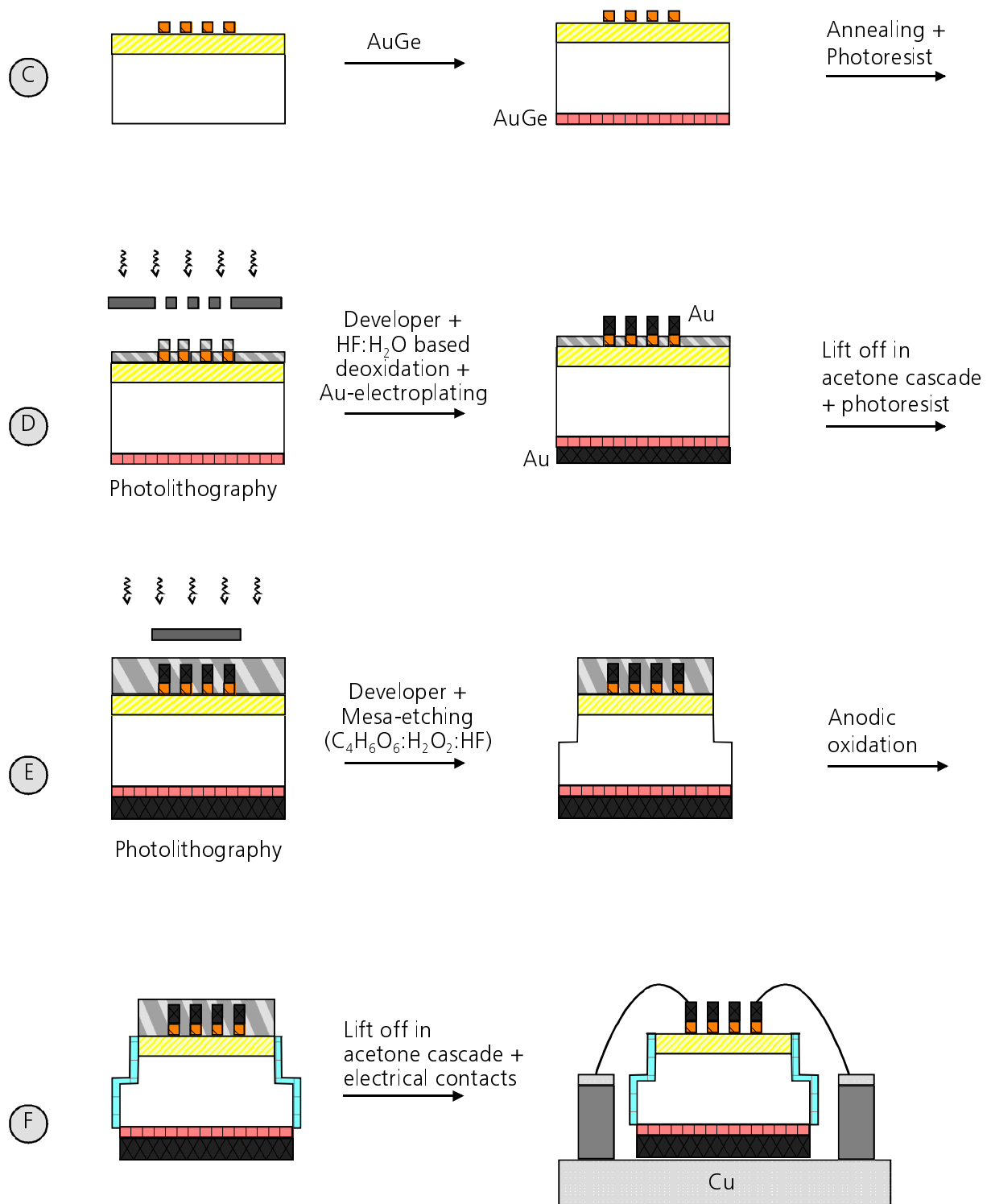


Figure 6.4b: Fabrication technology for epitaxially grown GaSb-based solar cells (II).

6.2 GaSb homojunction solar cells

6.2.1 Fundamental aspects of cell structure design

Several aspects must be considered when a photovoltaic device structure is designed. In the first place, the absorption of the incident spectrum must be as complete as possible in the active region of the device. Therefore, the incident spectrum and the spectral absorption coefficient of the material must be known. These data suggest that a solar spectrum is almost completely absorbed in 3 μm GaSb and a corresponding active thickness was chosen for the devices.

Furthermore, carriers should be photoexcited within a minority carrier diffusion length from the pn-junction in order to be able to contribute to the photocurrent. Therefore, the minority carrier lifetimes must be sufficiently high. In particular, the doping levels must not be chosen too high in order to minimise Auger- and radiative recombination. On the other hand, the doping levels must be chosen as high as possible in order to lead to a high built-in potential of the junction, i. e. a high voltage of the device, and reduce Ohmic losses. Therefore, the optimum device structure in terms of doping levels and position of the pn-junction can only be determined by a device modelling on the basis of accurate material parameters. As the corresponding data are usually not available with sufficient accuracy, qualitative considerations must guide the development.

GaSb contact layer $p=8\text{E}17\text{cm}^{-3}$, $d=5\text{nm}$
$(\text{Al}_{0.60}\text{Ga}_{0.40})(\text{As}_{0.05}\text{Sb}_{0.95})$ $p\sim 1\text{E}19\text{cm}^{-3}$, $d\sim 75\text{nm}$
GaSb emitter layer $p=1\text{E}17\text{cm}^{-3}$, $d=2.5\mu\text{m}$
GaSb base layer $n=5\text{E}17\text{cm}^{-3}$, $d=500\text{nm}$
GaSb BSF layer $n=7\text{E}17\text{cm}^{-3}$, $d=100\text{nm}$
$(\text{Al}_{0.2}\text{Ga}_{0.8})(\text{As}_{0.02}\text{Sb}_{0.98})$ $n\sim 1\text{E}18\text{cm}^{-3}$, $d\sim 80\text{nm}$
GaSb buffer layer $n=5\text{E}17\text{cm}^{-3}$, $d=360\text{nm}$

Moreover, the current in a solar cell is dominated by diffusion as there is no electric field present in the quasi-neutral regions (QNR's) around the pn-junction. Consequently, the carriers will not only reach the pn-junction but also the opposite interface, i. e. the front or backside of the device. The surfaces or interfaces usually have a high recombination velocity and photoexcited carriers are lost. Carriers must therefore either be driven away from these surfaces/interfaces by a built-in field, or the surfaces/interfaces must be of a nature that ensures a low recombination velocity. Both approaches will be used in the subsequent device structures.

Finally, the series resistance of the different layers must be considered. Especially for III-V cells in concentrating applications the current densities can become quite high. This is of particular importance with respect to the front contact grid because the metal coverage must be kept as small as possible.

Figure 6.5:

Layer sequence of solar cell structure 660. The related band diagram is shown in figure 6.6.

A corresponding cell structure is presented in figures 6.5 (layer sequence) and 6.6 (band

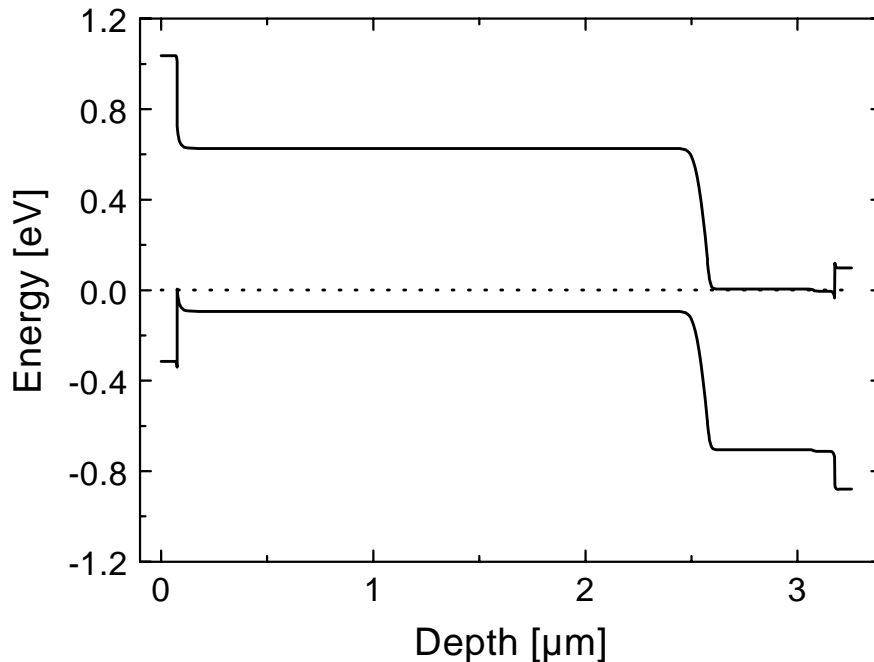


Figure 6.6: Band diagram of solar cell structure 660. The related layer sequence is shown in figure 6.5. The contact layer and the buffer layer were omitted in the band diagram. The band discontinuities are plausible estimates based on a valence band discontinuity of $\Delta E_v = 0.4$ eV for AlSb/GaSb.

diagram). The following points were considered when this particular design was developed:

- *Spatial arrangement of the pn-junction:*

The front-surface QNR of the pn-junction in a solar cell is usually called "emitter", while the other QNR is called "base". These terms are historically based on the development of the transistor. The first open question concerning cell design is now whether a "p-on-n" (i. e. a p-type emitter and an n-type base) or an "n-on-p" structure is advantageous. This question can be answered simply by considering material properties and device processing procedures for the antimonides: Good Ohmic metal contacts to p-GaSb can be easily made without any high temperature processing, while n-type material requires an annealing step. When an n-type layer is used as emitter, the annealing of the metal contact grid is likely to short-circuit the pn-junction by diffusion except when the n-type layer is very thick. However, a thick n-type emitter must be expected to be problematic because Hitchcock et al. [50, 51] report a small minority carrier diffusion length in MOVPE grown n-type GaSb believed to be due to deep level defects associated with tellurium, higher Auger recombination rates in n-type material and low hole mobility. Consequently, a p-type emitter should be used in the devices. This p-type emitter should be thick enough to ensure that most of the photons are absorbed in it so that the minority carrier properties of the n-type base are not very important (except for the saturation current density, see section 2.2.1). Furthermore, a thick p-type emitter will be beneficial with respect to excessive series resistance at low doping levels. Possible problems related to insufficient minority carrier diffusion lengths do not have to be expected because the mobilities (see section 4.2.4) and estimated lifetimes (according to [94]) suggest

electron diffusion lengths of several micrometers in p-doped GaSb. These considerations finally suggest a pn-junction profile as shown in figures 6.5 and 6.6. A similar design has also been reported in the literature with regard to (AlGa)(AsSb) thermophotovoltaic cells (e. g. [28, 114]). These points could also be confirmed in experiments: Solar cell structures were examined that were comparable to each other apart from the position of the pn-junction. Measurements confirmed a better quantum efficiency (fig. 7.19 in [14]) and ~50mV higher open-circuit voltage for a structure according to figures 6.5 and 6.6 compared to a structure with thin p-emitter and thick n-base (see also section 6.3). However, it must finally be mentioned that highly different GaSb-based structures are reported in the literature for devices produced on the basis of Zn-diffusion into bulk grown Te-doped substrates [99].

- *Back interface passivation:*

As already mentioned above, interfaces with critical recombination velocities will be present at the back side of the pn-junction. Particularly the substrate/epilayer interface can be expected to be a major problem due to a high impurity concentration. There are two possible ways to prevent the diffusion of photoexcited minority carriers to this interface: a field based on a homoepitaxial doping gradient (a so-called "back surface field" or "BSF") and a heteroepitaxial carrier confinement based on a wide band gap material. Both approaches are included in the device structure shown in figures 6.5. and 6.6. The wide band gap approach is complex because n-doped (AlGa)(AsSb) is difficult to achieve in MOVPE and the carry-over problem of aluminium (section 4.3.11) must also be considered. Moreover, a potential barrier for *majority* carriers also arises at the heterointerface except for very high doping concentrations. On the other hand, figure 6.6 immediately shows that the wide band gap material can be expected to be a much more effective minority carrier confinement than a mere doping gradient. A doping step must be significantly higher than the one included in figures 6.5 and 6.6 in order to achieve a comparable confinement. Unfortunately, this is prohibited by the low upper limit of the tellurium concentration for MOVPE-grown GaSb. As a consequence, an effective back interface passivation is difficult to design.

The above considerations were experimentally examined in related devices. The "combined-passivation-approach" (= doping-BSF plus (AlGa)(AsSb)-confinement) was included in a cell structure with a thin (~500 nm) Zn-diffused emitter and compared to a related structure without any back interface passivation. As these structures show a significant degree of photogeneration in the base due to the thin emitter, the back interface passivation can be predicted to influence the device performance. As expected, an improved quantum efficiency over almost the whole spectrum was found for the device *with* passivation, and consequently the combined-passivation-approach was confirmed to work fine (fig. 7.14 in [14]). The structure according to figures 6.5 and 6.6 has a thicker emitter (2.5 μm) and did not show a related long-wavelength decrease of the quantum efficiency when the n:(AlGa)(AsSb) confinement layer was omitted. This is probably caused by the reduced minority carrier generation in the base layers of these structures due to the thick emitters. As a consequence, the n:(AlGa)(AsSb) confinement layer could be omitted in all the device structures described in the following sections and a simpler single-layer doping-gradient passivation (BSF) was generally employed.

- *Front surface passivation:*

As already said above, a device with a thick p-type emitter is advantageous with respect to photoexcited minority carrier diffusion lengths, metal contact formation and series resistance. However, the success of this concept depends on a low front surface recombination velocity, i. e. a good surface passivation. Otherwise surface losses will dominate the performance of the solar cell. The passivation should *not* be based on a mere homoepitaxial doping gradient because in this case the absorption in the passivation layer would be too high. As an alternative, an oxide layer can be used for surface passivation purposes in silicon solar cells, but for III-V compound semiconductors the deposition of good oxides with low interface state density is problematic. Therefore, minority carrier confinement on the basis of a wide band gap heteroepitaxial "window" layer is the most promising alternative for the front surface passivation. Some related reports on the (AlGa)(AsSb)-passivation of (GaIn)(AsSb) emitters could be found in the literature [50, 51, 115], with [51] stating that a fitting procedure could no longer detect any significant front surface recombination loss in the related devices. The above considerations were experimentally examined with respect to MOVPE-grown GaSb-based devices in this thesis. A structure according to figure 6.5 was deposited in which the (AlGa)(AsSb) window layer was omitted (sample 658). The measured quantum efficiencies of the devices are compared in figure 6.7. The (AlGa)(AsSb)-window layer improves the quantum efficiency dramatically over almost the entire spectrum.

Figure 6.7 also contains the internal quantum efficiency of sample 769. This sample is equivalent to the structure 660 shown in figures 6.5 to 6.7, except that the (AlGa)(AsSb)-back interface passivation layer was omitted. This internal quantum efficiency was calculated on the basis of the reflection of a related wafer before the device fabrication, assuming a 10% contact grid metal coverage of the final device. This

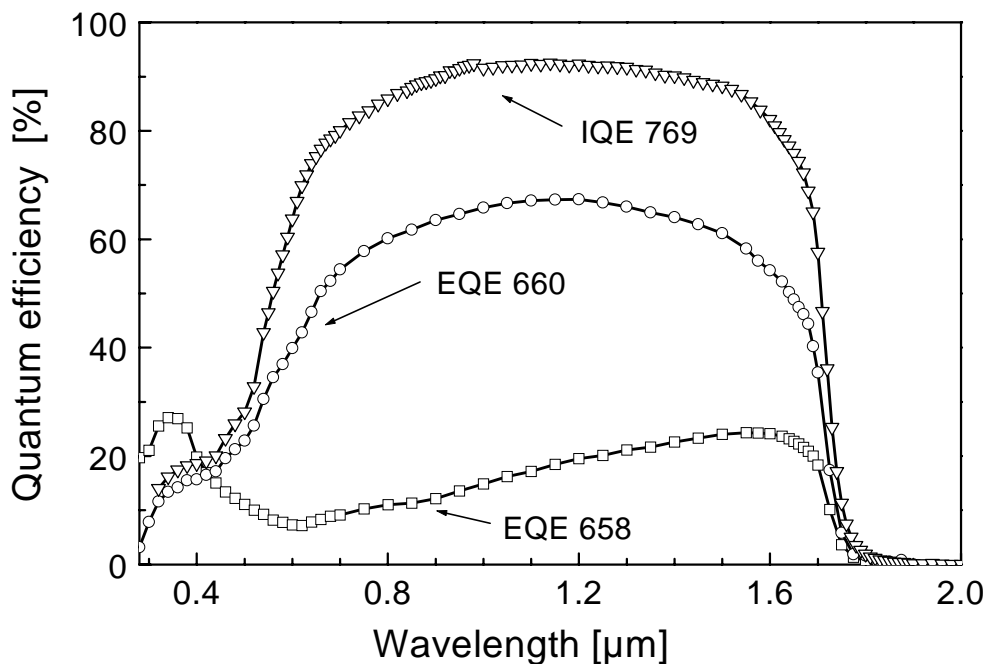


Figure 6.7: External quantum efficiencies of sample 660 (with (AlGa)(AsSb) window layer) and sample 658 (without any front surface passivation). The passivating effect of the window layer is clearly demonstrated. The estimated internal QE of sample 769 (= sample 660 without n:(AlGa)(AsSb)-BSF) is also shown.

value is a cautious estimate and probably too small due to the thicker contact grid fingers after electroplating. As the related EQE measurements were performed before the removal of the 5 nm GaSb contact layer, the related absorption loss leads to a further under-estimation of the real device performance. However, IQE-values above 90% are achieved for the spectral range 0.9 ... 1.4 μm which must be considered a very good value for these early stages of the device development. The best values are achieved in the range 1 .. 1.2 μm ; for shorter wavelengths the onset of the stronger absorption of the window and contact layers can be seen, while losses at longer wavelengths can probably be attributed to recombination in the base. The small peak at 400 nm corresponds to a local reflection minimum of GaSb. It must be noted that the quantum efficiency of the device in the intended application (see section 2.2.3) is only of interest for wavelengths above ~ 860 nm because photons with higher energies will be absorbed in the GaAs-based solar cell.

Further improvements of the device can be expected for window layers that show less absorption (reduced thicknesses, higher band gaps) and improved base layers. A direct metal contact to the (AlGa)(AsSb) window layer should also be examined in order to facilitate the device fabrication with respect to the removal of the GaSb contact layer.

6.2.2 Emitter doping level

A series of solar cell structures was deposited where the acceptor doping level in the emitter was varied while all other parameters were held constant. The reference structure is 769 (= 660 without (AlGa)(AsSb) back interface confinement). The devices

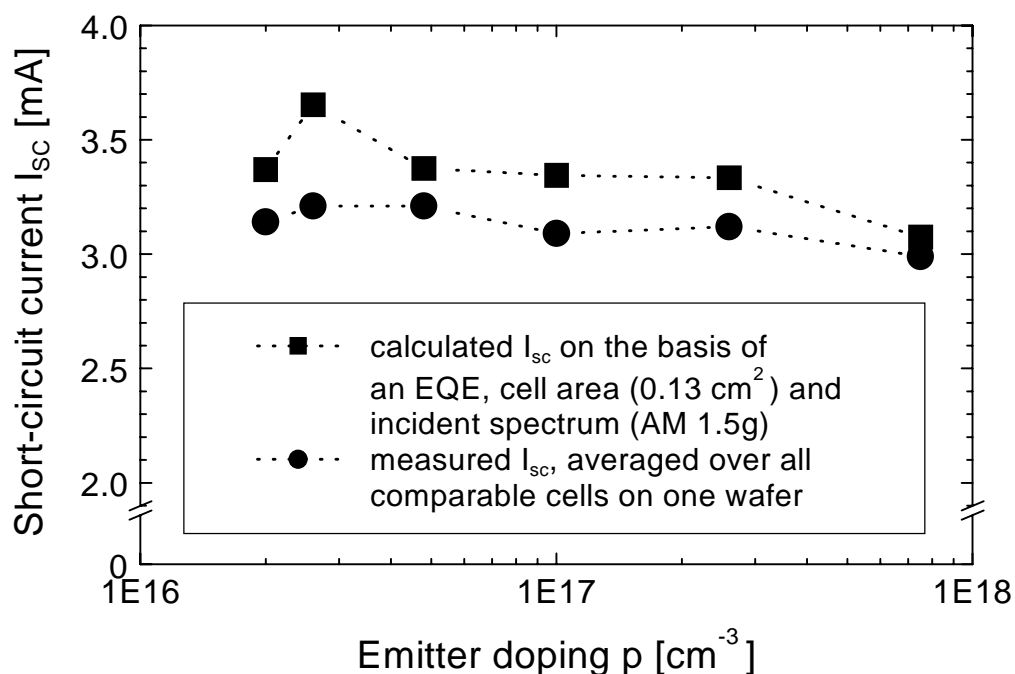


Figure 6.8: Short-circuit current of identical solar cells where only the acceptor doping level of the emitter was varied. The short-circuit current was calculated on the basis of the known cell area, an incident AM 1.5g spectrum and quantum efficiency measurements. In addition, measured values are shown that were averaged over all comparable cells on one wafer in a solar simulator.

were processed and the open-circuit voltages and the external quantum efficiencies measured. On the basis of an incident spectrum and a given cell area the quantum efficiency can be translated into a short-circuit current. The corresponding results are shown in figure 6.8 together with measured values that were averaged over all comparable cells on one wafer in a solar simulator. The lowest doping level corresponds to a nominally undoped emitter with a background concentration of native acceptors. Two prominent features of the data must be discussed: Firstly, a very low level of silicon acceptors seems to give the best short-circuit current of all structures. This result might represent an improved minority carrier lifetime due a reduced concentration of deep levels associated with native acceptors (see section 5.3). However, a related calibration mistake during the EQE measurement of the sample can not be ruled out as the direct measurement in a solar simulator does not give a similarly distinct result. The highest doping level gave a slightly reduced short-circuit current. This result is believed to represent the onset of a stronger loss of minority carriers due to a higher radiative recombination rate, while the lifetime at lower acceptor levels is probably dominated by doping-independent Shockley-Read-Hall recombination. The related behaviour of the open-circuit voltage is shown in figure 6.9.

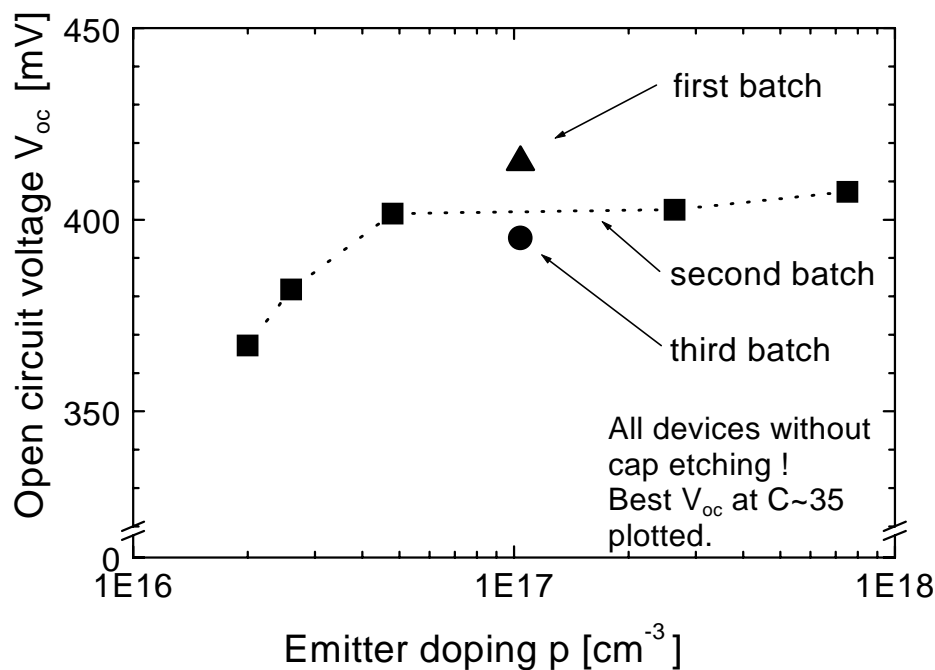


Figure 6.9: Open-circuit voltage of identical solar cells where only the acceptor doping level of the emitter was varied. 1st, 2nd and 3rd batch describe different sets of experiments.

As the minority carrier diffusion current is a linear function of the minority carrier concentration (equ. 12.73 in [54]), $p \cdot n = n_i^2$ means that the electron diffusion current in the emitter will follow $I_e^{diff} \propto 1/N_A$. As a result, the electronic saturation current density is reduced when the emitter doping level is increased. Furthermore, it was derived in section 2.2.2 that the open-circuit voltage increases when the saturation current decreases. Consequently, V_{oc} can be expected to rise with increasing N_A as long as the other material parameters such as carrier lifetimes and mobilities stay constant.

The open-circuit voltage was measured at a concentration ratio of approximately $C=35$ (defined by the corresponding short circuit current) because an operation of the device in a concentrating system is eventually intended. Moreover, shunt effects tend to lower V_{oc} at intensities around $C=1$. Each data point represents the best value of all cells on one wafer. In the experiments, an increase of the open-circuit voltage with increasing emitter doping can be observed for the lowest doping levels. However, between $5 \cdot 10^{16} \text{ cm}^{-3}$ and $8 \cdot 10^{17} \text{ cm}^{-3}$ a significant variation is no longer found. A related analysis of the saturation current density can be found in [49].

The batch numbers in the figure indicate different sets of experiments and show a certain irreproducibility. Whether this must be attributed to growth issues or the fabrication technology could not be clarified. For the given device structure, emitter doping levels around $1 \cdot 10^{17} \text{ cm}^{-3}$ appear most promising in this context.

6.2.3 Base doping level

In addition to the emitter doping level variation of the preceding section, a series of solar cell structures was deposited where the donor doping level in the emitter was varied while all other parameters were held constant. Again, the reference structure is 769. Open-circuit voltage and quantum efficiencies of the related devices were measured. The corresponding results are shown in figures 6.10 and 6.11. The external quantum efficiencies are very similar for all base doping levels. This can easily be explained because most of the absorption occurs in the emitter part of the structure and the minority carrier lifetime in the base does not significantly influence the device performance. The open-circuit voltage increases with increasing donor concentration. As

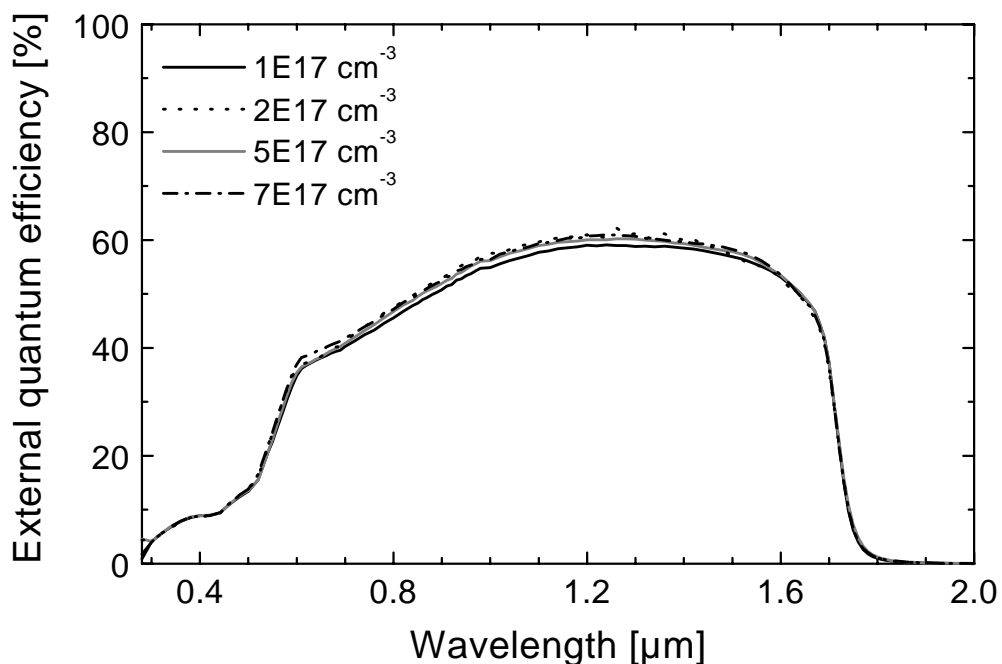


Figure 6.10: External quantum efficiencies of device structures based on the reference structure 769 (= figure 6.6 without (AlGa)(AsSb) back interface confinement). No variation of the quantum efficiencies with the base doping level is observed.

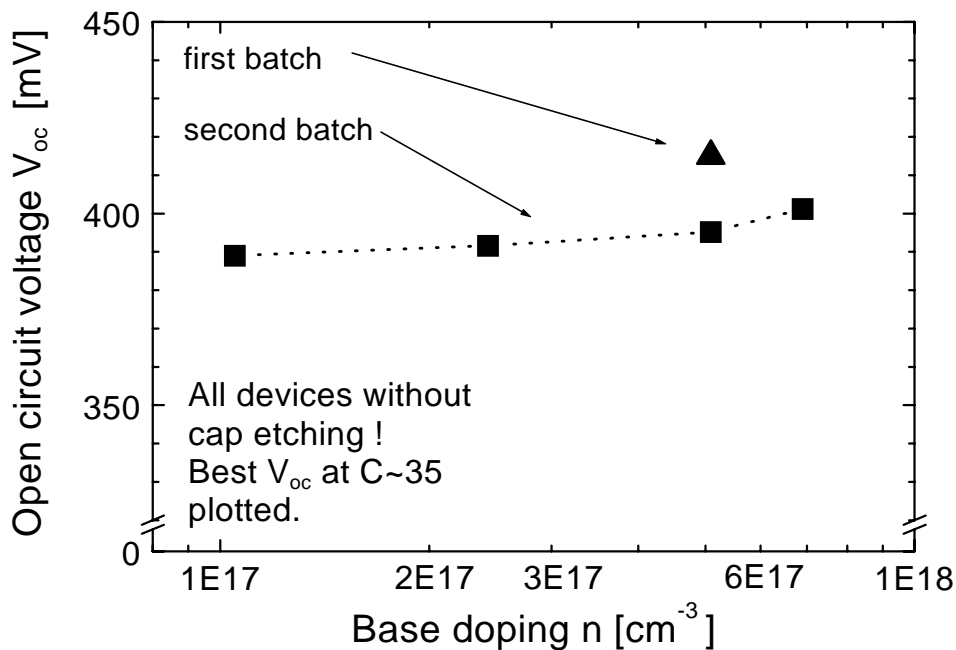


Figure 6.11: V_{oc} of identical solar cells where only the donor doping level of the base was varied. 1st and 2nd batch describe different sets of experiments.

a saturation has not been observed, even higher doping levels should be examined in the future. A significantly better voltage was achieved for a “first batch”-device (sample 714), indicating reproducibility problems concerning growth or fabrication technology.

6.3 (AlGa)(AsSb) homojunction solar cells

GaSb contact layer $p=8\text{E}17\text{cm}^{-3}$, $d=10\text{nm}$
$(\text{Al}_{0.60}\text{Ga}_{0.40})(\text{As}_{0.05}\text{Sb}_{0.95})$ $p\sim 1\text{E}19\text{cm}^{-3}$, $d\sim 75\text{nm}$
$(\text{Al}_{0.18}\text{Ga}_{0.82})(\text{As}_{0.02}\text{Sb}_{0.98})$ $p\sim 1\text{E}17\text{cm}^{-3}$, $d\sim 800\text{nm}$
$(\text{Al}_{0.18}\text{Ga}_{0.82})(\text{As}_{0.02}\text{Sb}_{0.98})$ $n\sim 1\text{E}18\text{cm}^{-3}$, $d\sim 180\text{nm}$
GaSb buffer layer $n=5\text{E}17\text{cm}^{-3}$, $d=360\text{nm}$

Figure 6.12:

Layer sequence of solar cell structure 772. The related band diagram is shown in figure 6.13.

In section 2.2.3 the multijunction approach for extremely high photovoltaic conversion efficiencies was described. It was shown that in a 4-junction system the third junction should be based on a band gap of approximately 1 eV, and (AlGa)(AsSb) was suggested as a promising material. However, the results presented in section 4.3 have shown that the MOVPE of high-quality (AlGa)(AsSb) is an extremely difficult challenge. Based on the results of section 4.3, a preliminary cell structure (sample 772) with a band gap around 0.9 eV could be deposited. The related layer sequence is presented in figure 6.12, and the band diagram in real space can be found in figure 6.13. As short minority carrier lifetimes and bad mobilities have to be expected in the material, the diffusion lengths are likely to be relatively limited, particularly in n-type material. Consequently, the layers in the active region of device 772 were chosen to be thinner than in the GaSb-cells. As n-type doping of (AlGa)(AsSb) with high Al-concentrations was prevented by a high background hole contamina-

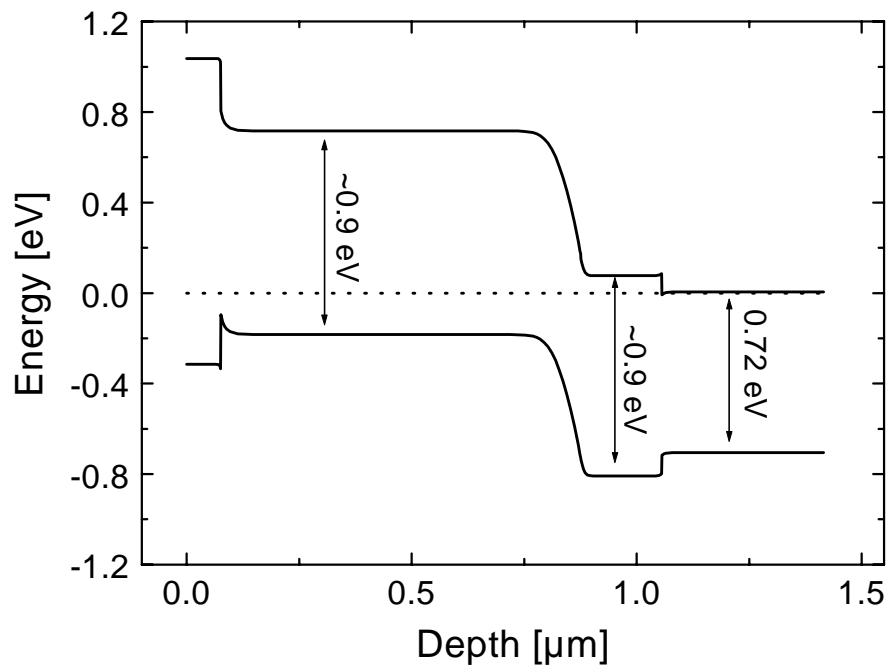


Figure 6.13: Band diagram of solar cell structure 772. The related layer sequence is shown in figure 6.12. The contact layer was omitted in the band diagram. The band discontinuities are plausible estimates based on a valence band discontinuity of $\Delta E_v = 0.4$ eV for AlSb/GaSb.

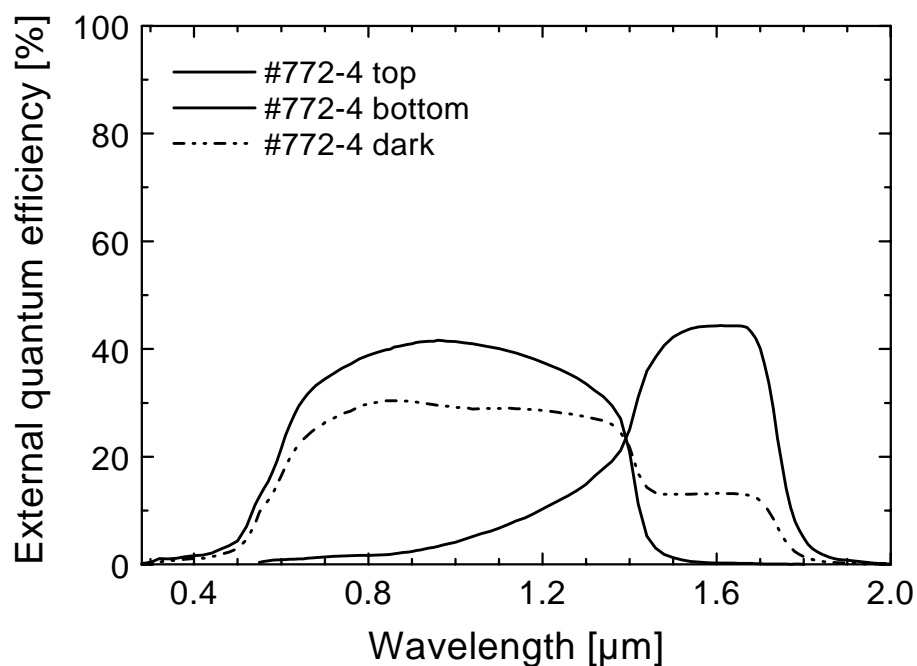


Figure 6.14: External quantum efficiency of the (AlGa)(AsSb) solar cell 772. The „dark“ measurement represents the standard technique without any bias light. The measurements termed „top“ and „bottom“ are related to more advanced methods which are usually employed for the analysis of tandem cells. A related reference can be found in the text on the following page.

tion, no wide band gap backside passivation of the active region could be incorporated into the structure.

The cell gave an open-circuit voltage of 472 mV at a concentration ratio of around 30. The measured quantum efficiency is shown in figure 6.14. Here, the „dark“ measurement represents the standard technique without any bias light. An EQE of around 30% was measured above the band gap of (AlGa)(AsSb) (~0.9 eV, i. e. ~1380 nm). Besides, a surprising and very interesting peculiarity was measured at wavelengths between 0.9 and 0.72 eV, i. e. between the band gaps of (AlGa)(AsSb) and GaSb: Here, the “dark” EQE of the device does not vanish but takes a finite value slightly above 10%. This can possibly be explained by absorption in the buffer layer: Due to their thermal distribution some of the photoexcited holes in the GaSb buffer might be able to overcome the barrier into the (AlGa)(AsSb) base. Here, they lead to a photocurrent and hence contribute to the quantum efficiency.

In order to examine this device in more detail, the cell was analysed with characterisation techniques that are usually employed for the analysis of monolithic tandem cells. The corresponding measurements can be found in [14]. However, an explanation for the related data with regard to the device structure can not yet be given.

6.4 Heterojunction solar cells

GaSb contact layer $p=8E17cm^{-3}$, $d=10nm$
$(Al_{0.60}Ga_{0.40})(As_{0.05}Sb_{0.95})$ $p\sim 1E19cm^{-3}$, $d\sim 75nm$
(AlGa)(AsSb) emitter x_{Al} and d : see below
GaSb base $n=1E17cm^{-3}$, $d=2.7\mu m$
GaSb BSF layer $n=7E17cm^{-3}$, $d=100nm$
GaSb buffer layer $n=5E17cm^{-3}$, $d=360nm$

sample	x_{Al}	$d_{emitter}$
763	0	270 nm
764	0.08	200 nm
742/762	0.15	190 nm
765	0.21	150 nm
766	0.33	140 nm

Figure 6.15: Layer sequence of pn-heterostructure cells.

A novel class of GaSb-based photovoltaic devices was developed: pn-heterojunction solar cells. Here, emitter and base consist of materials with different band gaps. The structure of the related samples is given in figure 6.15, the band diagram in figure 6.16. In addition to these p:(AlGa)(AsSb)/n:GaSb-structures a cell based on a p:GaSb/n:(AlGa)(AsSb)-structure will also be discussed below.

The pn-heterojunction needs a more complex description than the simple homojunction. As both the Fermi level *and* the band offsets must be correctly adjusted at the junction, an additional barrier is usually formed in one of the bands (see figure 6.16). A related extension of the Shockley diode model described in section 2.2.1 (“Solar cells - The ideal device”) is the Anderson-model, which considers the discontinuities of the band gap and dielectric function (12.7 in [54], 5.3.1 in [38]).

However, a major advantage of pn-heterojunctions with regard to solar cells can be illustrated within the expressions derived for Shockley homojunction diodes in section 2.2.1. There, the diffusion current (= saturation current or dark current) could be expressed in terms of material parameters:

$$I_0 = (I_n^{gen} + I_p^{gen}) = A \cdot e \cdot n_i^2 \left(\frac{D_e}{N_A L_e} + \frac{D_h}{N_D L_h} \right)$$

Furthermore, the open-circuit voltage was shown to depend on I_0 :

$$V_{oc} = \frac{kT}{e} \ln \left(\left| \frac{I_{sc}}{I_0} \right| + 1 \right)$$

As a higher band gap in emitter or base will reduce the related minority carrier diffusion current due to the lower value for n_i , the open-circuit voltage of the heterostructure device is likely to increase (as long as the material quality in terms of D and L is not influenced). The high barrier for minority carrier diffusion into the wide band gap material has the same consequence.

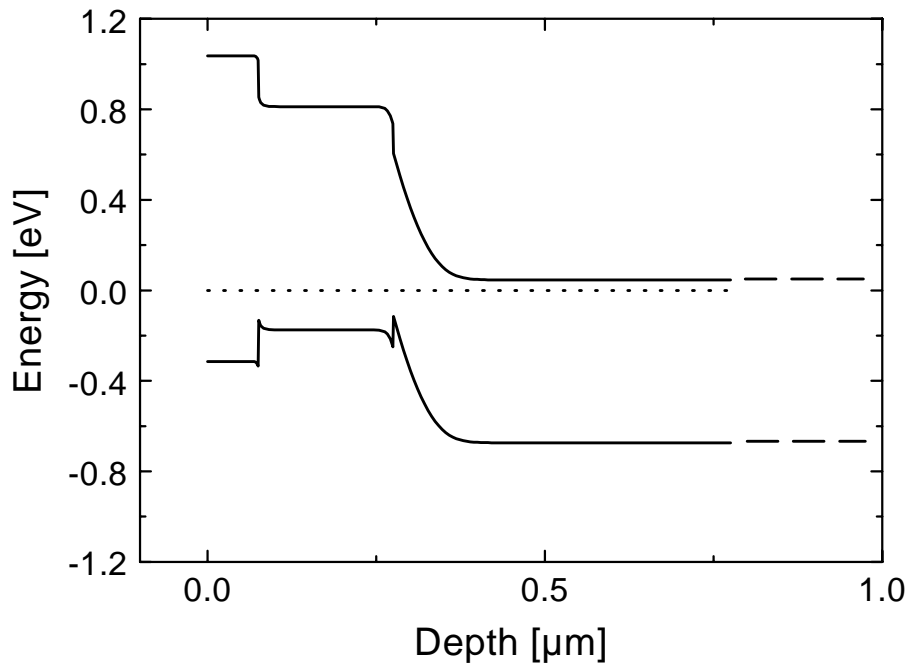


Figure 6.16: Band diagram of a heterojunction cell. The related layer sequence is shown in figure 6.15. The contact and BSF layers were omitted in the diagram. Emitter band gap and thickness were varied in the experiments.

However, this simple discussion neglects many important effects. The spike or notch in one of the bands tends to impede transport of photogenerated carriers and can even influence the dark I/V -curve. Tunneling through the barrier can occur in this context. The exact band alignment is hard to predict due to a severe uncertainty regarding band offsets (see for example [12] concerning (AlGa)(AsSb)/InAs). Charged interface states and dipoles can occur. Besides, the growth procedure might deposit extrinsic impurities at the heterointerface. The corresponding interface states provide a large density of non-radiative recombination centers that are particularly effective due to their position in the centre of the depletion region. A related modelling of devices based on the heterojunction (AlGa)(AsSb)/GaSb gets further complicated due to the lack of information on the optical data of (AlGa)(AsSb) [39]. Much experience concerning

heterojunction photovoltaic devices has been gained in the field of chalcopyrite solar cells: Related doping problems in some of the materials make heterointerfaces necessary for the realisation of pn-junctions. For example cells made of p-type CuInSe_2 -absorbers usually have n-type cadmiumselenide buffer layers below the n-type zincoxide window. The cadmiumselenide buffer moves part of the conduction band discontinuity away from the absorber surface. Even for a given high interface recombination velocity, recombination at the absorber interface is minimised when the Fermi level at the interface is close to one of the band edges. This is achieved by highly asymmetric doping in chalcopyrite solar cells [58]. In summary, it is difficult to predict the device performance of a particular heterojunction solar cell due to the wide parameter space. First reports [41] on enhanced open-circuit voltages of n:(AlGa)(AsSb)/p:(GaIn)(AsSb) photovoltaic cells grown by MBE are promising for the antimonides.

In order to examine the performance of p:(AlGa)(AsSb)/n:GaSb solar cells, a set of device structures was deposited according to figures 6.15 and 6.16. The aluminium concentration in the p-type emitter was varied between 33% and 0%. The emitter layers were nominally undoped, i. e. carbon background doped; their acceptor concentration varied between $2 \cdot 10^{16} \text{ cm}^{-3}$ and approximately $5 \cdot 10^{17} \text{ cm}^{-3}$ according to their Al-concentration (section 4.3.9). The open-circuit voltages of the devices are shown in figure 6.17.

In order to compare the open-circuit voltages of the above heterojunction cells to the data of homojunctions, it must be ensured that only devices from the same fabrication technology run are compared. Otherwise irreproducibilities during growth or fabrication would prohibit a fair comparison. In this context, the "2nd batch"-voltages in figure 6.17 must be compared to the homojunction cell voltages shown as "2nd batch" in figure 6.11. While the heterojunction cells with emitter Al-concentrations of 0%, 15%, and

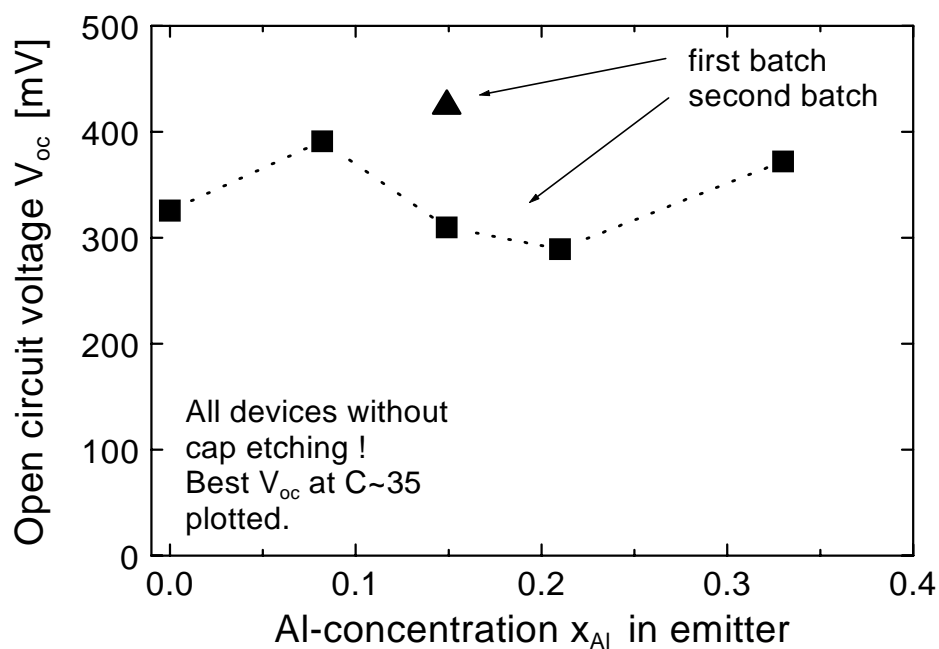


Figure 6.17: Open-circuit voltage of heterojunction solar cells based on the structure shown in figure 6.15 and 6.16. 1st and 2nd batch describe different sets of experiments.

21% are not as good as the homojunction cells, the structures with 8% and 33% show comparable voltages. Similarly, the "1st batch" heterojunction in figure 6.17 can be compared to the "2nd batch" homojunctions in figure 6.9. Here, the heterojunction ($x_{Al} = 0.15$) shows an approximately 20 mV higher V_{oc} compared to the homojunctions.

A final evaluation on whether heterojunction structures can give higher voltages than homojunctions can therefore not yet be given due to a general irreproducibility of the data. While it would be possible to try a qualitative discussion of the data in figure 6.17 in terms of the carrier concentrations and lifetimes (oxygen-related deep levels, direct-to-indirect transition of the material, intrinsic carrier concentration, ...), the scattering of the data must prohibit a convincing line of reasoning. As an overall result, heterojunctions devices have proven their potential to reach *at least the same* voltages as homojunctions cells based on GaSb. Further work concerning the optimum aluminium concentration is obviously necessary.

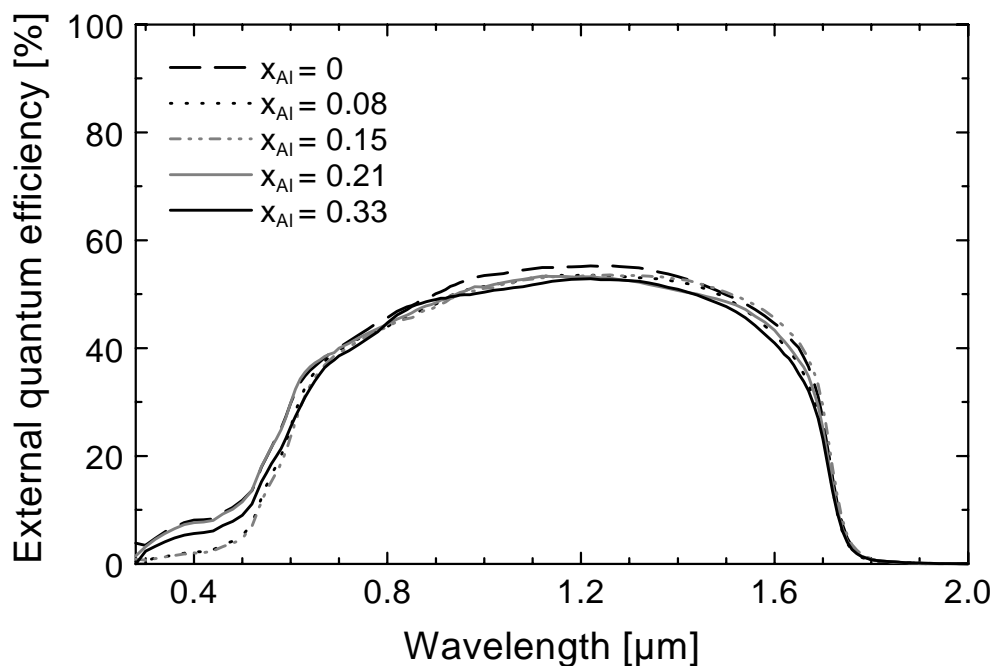


Figure 6.18: External quantum efficiencies of heterojunction solar cells for various aluminium concentrations of the emitter.

While it could be shown above that heterojunction cells have the potential to reach at least the same voltages as their homojunction counterparts, the corresponding short-circuit current density must not be neglected. The quantum efficiencies of the heterojunction devices are shown in figures 6.18 and 6.19. Firstly, it is obvious that the aluminium concentration in the emitter does not have a major effect on the quantum efficiency (figure 6.18). This result could be expected for wavelength that are absorbed in the GaSb base, but is to some extent surprising for the higher energies absorbed in the (AlGa)(AsSb) emitters: Here, the material quality has been shown to decrease rapidly with increasing aluminium concentration (section 4.3).

All the devices shown in figure 6.18 show peak values for the external quantum efficiency between 50 and 60%. This is slightly less than the homojunction devices presented in figures 6.7 and 6.10. However, as already said in section 6.2.1 MOVPE-grown tellurium doped GaSb can not be expected to be a very good absorbing material

with respect to minority carrier diffusion lengths. This is now further underlined by the fact that the "heterojunction" cell with $x_{Al}=0$ is actually a homojunction cell with a thin emitter and thick base; the EQE of the device (figure 6.18) compared to the EQE of the homojunctions with thick emitters and thin bases (figures 6.7 and 6.10) shows that the considerations concerning the fundamental aspects of cell design (section 6.2.1) were indeed correct: Absorption in p-type emitters gives better quantum efficiencies than absorption in n-type bases, and the open-circuit voltages show the same tendency.

These considerations can now be applied in order to improve the heterojunction cell structure: A reversed device structure (sample 773) was deposited, in which the junction is formed by a p-type GaSb emitter ($p=1\cdot 10^{17}\text{ cm}^{-3}$, $d=2.7\mu\text{m}$) and an n-type (AlGa)(AsSb) base ($n=1\cdot 10^{18}\text{ cm}^{-3}$, $d=180\text{nm}$). This device structure is very similar to the homojunction solar cells presented in section 6.1.2 with regard to the fact that most of the light is absorbed in a p-type GaSb emitter. Figure 6.19 shows the EQEs of a standard heterojunction cell (taken from figure 6.18), the reversed heterojunction 773 and a homojunction cell with the same emitter doping level as the reversed heterojunction. These cells were all grown and manufactured in the same run, so that their data are comparable. While the best standard heterojunction has approximately the same open-circuit voltage ($\sim 395\text{ mV}$) but a reduced EQE in comparison to the homojunction device, the reversed heterojunction has the same EQE as the homojunction but an improved V_{oc} (413 mV). As a result, the reversed heterojunction is likely to be the most promising device structure for solar cells with 0.72 eV absorber layers.

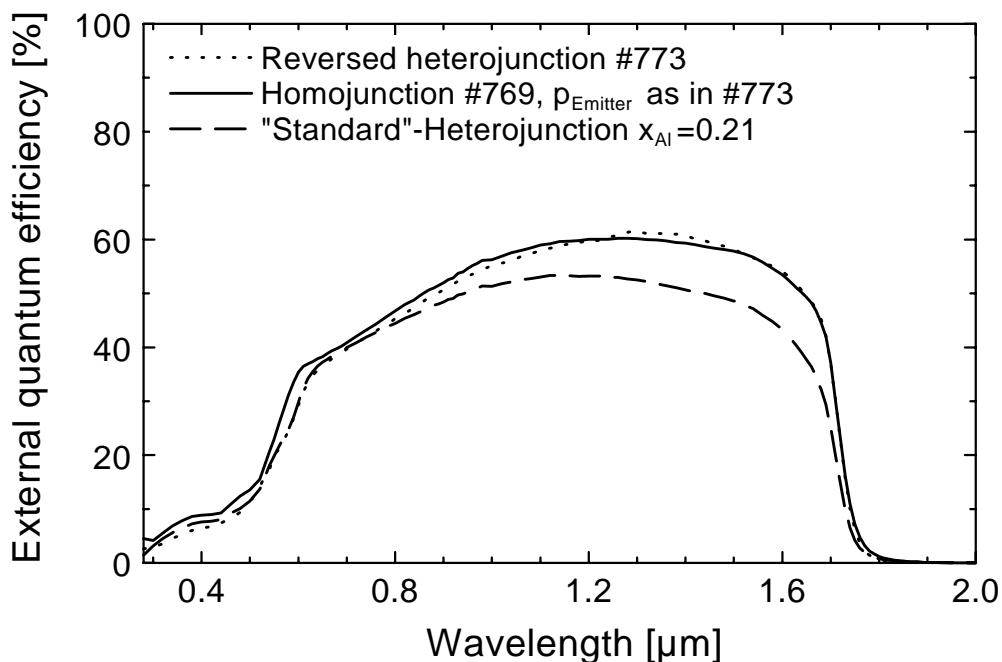


Figure 6.19: EQEs of the reversed heterojunction cell, a comparable homojunction and a standard heterojunction device. While the best standard heterojunction has approximately the same V_{oc} ($\sim 395\text{ mV}$) but a reduced EQE in comparison to the homojunction device, the reversed heterojunction has the same EQE as the homojunction cell but an improved V_{oc} (413 mV).

6.5 Tandem solar cells

In section 2.2.3 the concept of the monolithic tandem cell was introduced but the actual layer sequence and the band diagram remains to be shown. The device basically consists of two solar cells that are grown lattice-matched onto each other. The two cells are connected in series by an Esaki- (or „interband“-) tunnel diode which is a crucial feature of the device. The operating principle of the Esaki-diode is shown in figure 6.20.

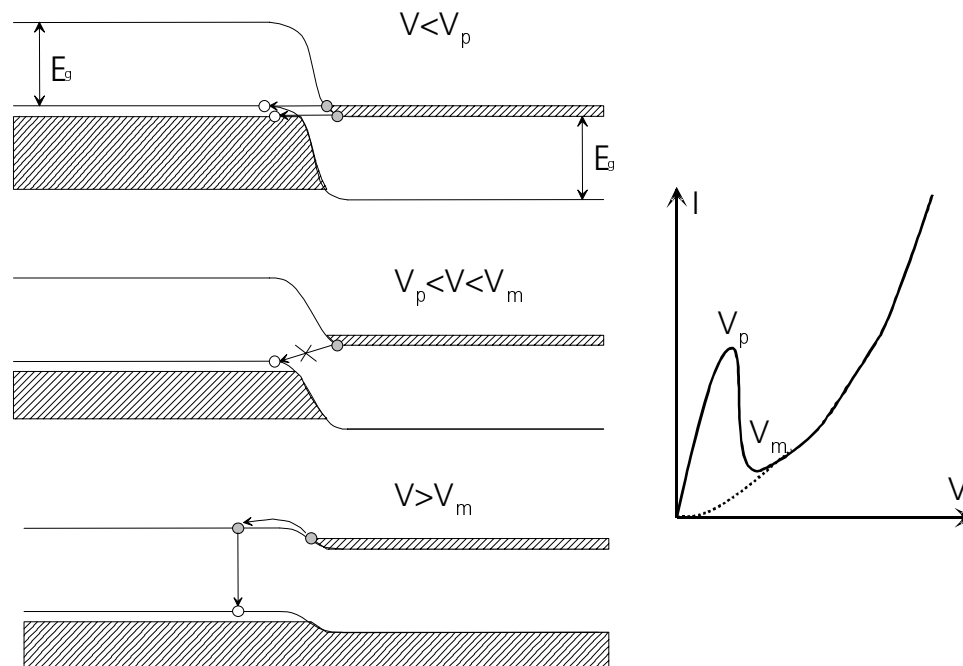


Figure 6.20: Band diagram (left) and I/V -curve (right) of an Esaki-tunnel diode [34].

In very heavily doped pn-junctions the depletion layer is very narrow and majority carriers can recombine via tunneling. Hence, a large tunneling current is observed at small forward bias ($V < V_p$). With increasing forward bias, the overlap decreases until tunneling can no longer occur ($V_p < V < V_m$). Based on the I/V -curve this behaviour is called „negative differential resistance“. At even higher bias, the current-voltage characteristic of a conventional diode is observed ($V > V_m$). An important property of the device is the peak tunneling current density at V_p which increases with increasing doping levels and decreasing band gap. The band diagram of a simple monolithic tandem cell is shown in figure 6.21. The tunnel junction polarity is reversed in comparison to the active pn-junctions of the two solar cells. This can be easily understood because the photocurrent flows in the reverse direction of the active junctions, but the majority carrier current through the tunnel diode must be a forward current. The photocurrents of the two cells will lead to a voltage across the tunnel junction so that majority carriers in regions D and E get annihilated and a tunneling current flows through the diode. As long as the photocurrent is small compared to the peak tunnel current, the voltage drop across the tunnel diode will be small. However, for bad tunnel junctions or very high photocurrents the tunneling eventually breaks down and the Esaki diode operates as a conventional diode, i. e. the current is based on diffusion instead of tunneling. The related voltage drop reduces V_{oc} of the whole tandem cell and hence the efficiency of the device.

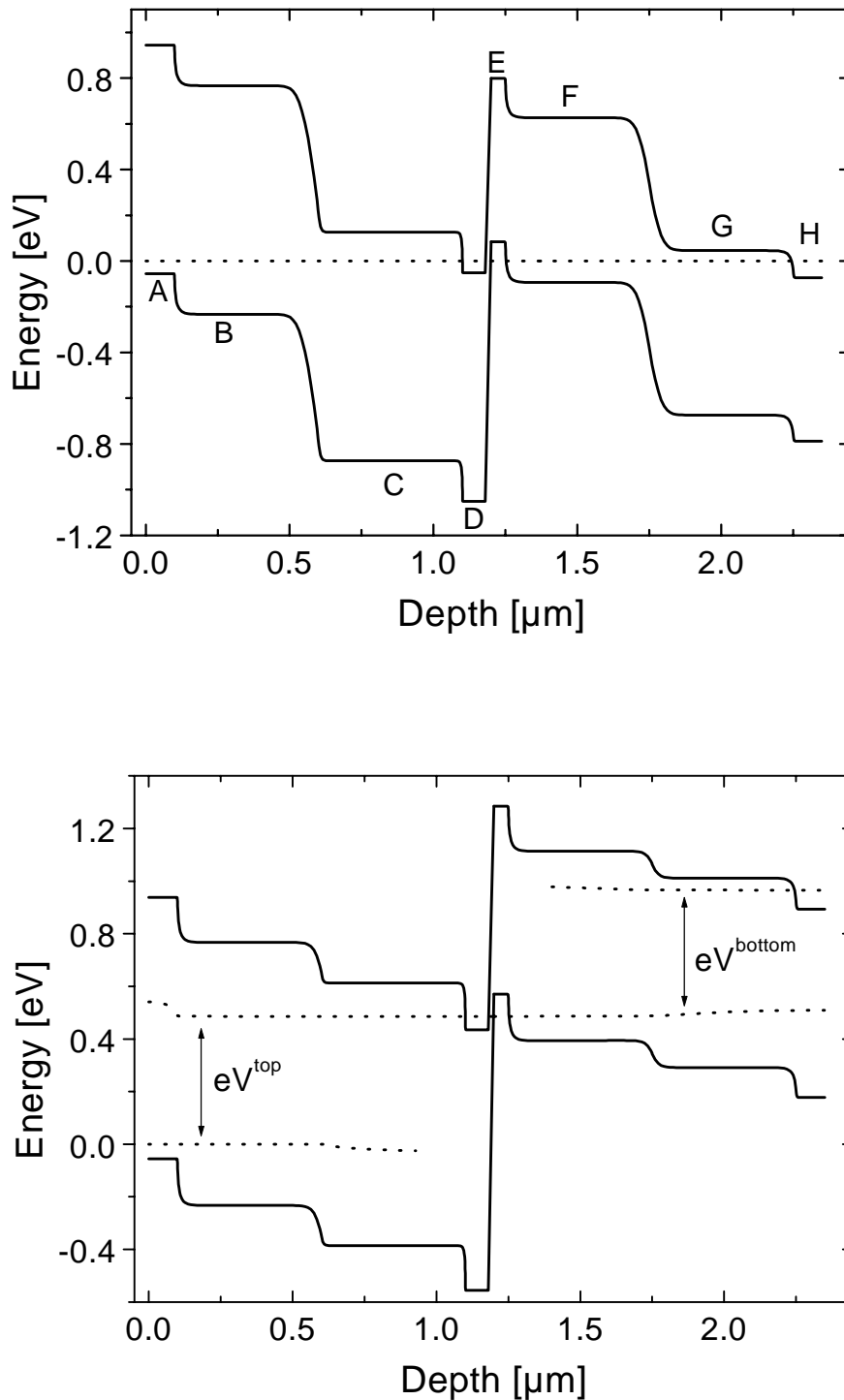


Figure 6.21: Band diagram of a simple monolithic tandem cell without light (above) and with light (below, V_{oc}). Energies and depth are arbitrarily chosen.

Layer legend: A: Front surface passivation field

B: Wide band gap emitter

C: Wide band gap base

D: Back interface passivation field / tunnel diode n-layer

E: Front interface passivation field / tunnel diode p-layer

F: Narrow band gap emitter

G: Narrow band gap base

H: Back interface passivation field

GaSb contact layer $p \sim 8E17 \text{cm}^{-3}$, $d \sim 10 \text{nm}$
$(\text{Al}_{0.60}\text{Ga}_{0.40})(\text{As}_{0.05}\text{Sb}_{0.95})$ $p \sim 1E19 \text{cm}^{-3}$, $d \sim 75 \text{nm}$
$(\text{Al}_{0.18}\text{Ga}_{0.82})(\text{As}_{0.02}\text{Sb}_{0.98})$ $p \sim 1E17 \text{cm}^{-3}$, $d \sim 800 \text{nm}$
$(\text{Al}_{0.18}\text{Ga}_{0.82})(\text{As}_{0.02}\text{Sb}_{0.98})$ $n \sim 1E18 \text{cm}^{-3}$, $d \sim 180 \text{nm}$
(GaIn)(AsSb) layer $n \sim 1E18 \text{cm}^{-3}$, $d \sim 20 \text{nm}$
$(\text{Al}_{0.60}\text{Ga}_{0.40})(\text{As}_{0.05}\text{Sb}_{0.95})$ $p \sim 1E19 \text{cm}^{-3}$, $d \sim 75 \text{nm}$
GaSb emitter layer $p \sim 1E17 \text{cm}^{-3}$, $d \sim 2.5 \mu\text{m}$
GaSb base layer $n \sim 5E17 \text{cm}^{-3}$, $d \sim 500 \text{nm}$
GaSb BSF layer $n \sim 7E17 \text{cm}^{-3}$, $d \sim 100 \text{nm}$
GaSb buffer layer $n \sim 5E17 \text{cm}^{-3}$, $d \sim 360 \text{nm}$

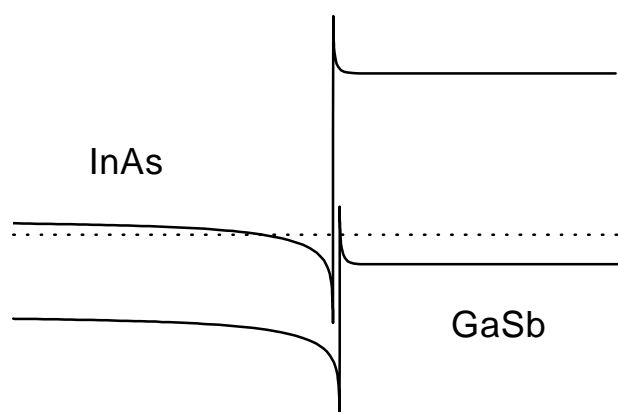
Figure 6.22:

Layer sequence of tandem cell structure 774.

concentrations were found in (AlGa)(AsSb). As a consequence, an n:(GaIn)(AsSb)/p⁺:(AlGa)(AsSb)-structure was tried as tunnel junction. However, related experiments with isolated mesa diodes based on similar junctions did not show an area of negative differential resistance. It must therefore be assumed that the upper doping limits in the antimonides are not sufficient to allow an adequately narrow junction. The "tunnel" junction will work as a conventional diode and a significant voltage drop will occur across the junction. Consequently, the open-circuit voltage of the device at a concentration ratio of around 25 was only 507 mV. However, there is a promising

It must be noted that the total current in the tandem cell is always limited by the cell with the lower photocurrent. On that basis, the quantum efficiencies of the two cells can be measured separately: When bias light with a suitable spectrum is used to "flood" one of the two cells, monochromatic probe light can be used to measure the QE of the other device. For maximum overall efficiencies, the photocurrent for a given spectrum must be the same in both cells due to the series connection. Preliminary results on antimony-containing tandem cells can be found in [15]. However, an MOVPE-grown monolithic (AlGa)(AsSb)/GaSb tandem cell still remains to be shown.

The 0.9 eV (AlGa)(AsSb)-solar cell (sample 772) presented in section 6.2 and a 0.72 eV GaSb-solar cell (section 6.1.2, emitter doping level: $1 \cdot 10^{17} \text{cm}^{-3}$) were combined in a preliminary tandem cell structure according to figure 6.22. As (AlGa)(AsSb) could not be doped much higher than $n \sim 10^{18} \text{cm}^{-3}$ no back surface passivation was included in the top cell structure. The design of the tunnel diode was based on the results of chapter 4: As the electron concentration in tellurium-doped antimonides seems to saturate at rather low values around $n \sim 10^{18} \text{cm}^{-3}$ the underlying material should have a small band gap to allow tunneling processes. On the other hand very high acceptor

**Figure 6.23:**

InAs/GaSb-band alignment.
A two-dimensional electron gas is formed in the InAs and a two-dimensional hole gas in the GaSb. A tunnel current will flow until the applied bias voltage will eventually prevent the corresponding overlap of the 2DEG and the 2DHG. Hence, a negative differential resistance can be observed.

alternative for a GaSb-based tunnel junction: In addition to the Esaki tunnel diode and the resonant intraband tunnel diode (RTD) (e. g. [126], 9.5), a further resonant tunneling device can be designed which is a hybrid of the Esaki and the RTD tunnel diode: the so-called resonant interband tunnel diode (RITD) which is based on the InAs/GaSb-band alignment (type IIB). Figure 6.23 shows the InAs/GaSb-heterojunction, at which a two-dimensional electron gas is formed in the InAs and a two-dimensional hole gas in the GaSb. A tunnel current will flow until the applied bias voltage will eventually prevent the corresponding overlap of 2DEG/2DHG and a negative differential resistance is observed [57]; the operating principle is basically the same as in corresponding RITD-InAs/AlSb/GaSb/AlSb/InAs-heterostructures (e. g. figure 8 in [89]). Due to the problems in achieving sufficiently high doping levels that would allow Esaki tunnel diodes in GaSb-based structures, the InAs/GaSb-heterojunction should therefore be considered in the further development of GaSb-based tandem cell structures.

Apart from the questions related to the tunnel diode and the open-circuit voltage, the quantum efficiency of the coupled devices is of interest. Therefore, the EQEs were measured using the bias-light techniques described above. Further details can be found in [14]. The results are shown in figure 6.24. The top cell has an EQE very similar to the corresponding single junction device shown in figure 6.14. The long-wavelength response is not observed because the responsible buffer layer was of course omitted in the tandem structure. The EQE of the bottom cell is limited by the absorption of the top cell for wavelengths below $\sim 1400\text{nm}$. At energies where the top cell is transparent the EQE of the bottom cell reaches values of approximately 55%. This is slightly less than the corresponding single junction device (figure 6.10, base doping $5 \cdot 10^{17} \text{cm}^{-3}$). This can be partly attributed to the optical interference patterns which are superimposed on the EQE; in addition, a significant absorption of the low band gap material in the tunnel diode must as well be expected. In summary, an MOVPE-grown GaSb-based monolithic (AlGa)(AsSb)/GaSb tandem cell has been demonstrated for the first time. Points for significant future improvements of the device have been identified.

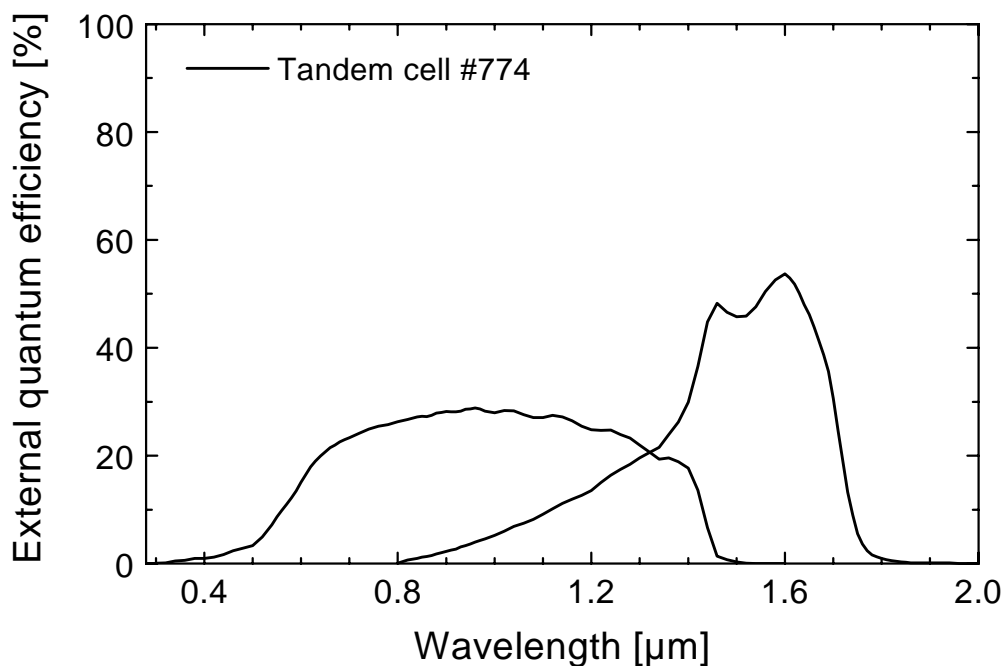


Figure 6.24: External quantum efficiency of a monolithic (AlGa)(AsSb)/GaSb tandem cell. The corresponding device structure is shown in figure 6.22.

6.6 Summary

GaSb homojunction solar cells have been developed. The starting point was a discussion of the fundamental aspects of cell structure design. Based on material data and literature reports, a structure was chosen which consists of a 2.5 μm p-type emitter and a 0.5 μm n-type base. The importance of a good front surface passivation was discussed. An (AlGa)(AsSb) window layer was shown to be very effective in this context. Internal quantum efficiencies above 90% have been achieved for the spectral range 0.9 ... 1.4 μm . This must be considered a very good value for these early stages of the device development. The effects of both the emitter and base doping levels on the EQE and V_{oc} could be determined.

Furthermore, an MOVPE-grown (AlGa)(AsSb) solar cell with a band gap of $E_{gap} \sim 0.9$ eV could be shown for the first time. Both the EQE and V_{oc} of this preliminary device need further improvement. The current device performance is mainly limited by the unsatisfactory purity of the novel metalorganic precursors which have been employed for the growth.

A GaSb and an (AlGa)(AsSb) cell were combined and an MOVPE-grown GaSb-based monolithic (AlGa)(AsSb)/GaSb tandem cell could be demonstrated for the first time. Apart from the above mentioned purity problems of the aluminium containing material, the device performance is also limited because of the low doping upper limits in the antimonides that prohibit the successful deposition of an Esaki tunnel diode in the structure. Here, further developments should either focus on novel dopants or on the type IIb-junction between InAs and GaSb in order to deposit successful tunnel junctions.

In addition, a novel class of GaSb-based photovoltaic devices was developed: pn-heterojunction solar cells. Here, emitter and base consist of materials with different band gaps. While the performance of p:(AlGa)(AsSb)/n:GaSb cells is believed to be limited by the minority carrier diffusion lengths in MOVPE-grown tellurium-doped GaSb base layers, a reversed p:GaSb/n:(AlGa)(AsSb) structure gave the same quantum efficiency as a corresponding GaSb homojunction device while the open-circuit voltage increased by approximately 20 mV. The increased voltage is believed to be due to a reduced dark current in the device. The reversed heterojunction approach can of course as well be included in future tandem cell concepts.

If a further improvement concerning the purity of the employed metalorganic precursors can be achieved, a thorough optimisation of the device structure and fabrication technology can eventually be expected to produce a highly efficient (AlGa)(AsSb)/GaSb tandem cell for a concentrating application.

7 Summary and outlook

The results presented in this work cover a wide range of both fundamental and applied aspects. These include the complex MOVPE growth of various III-antimonides as well as the electronic and optical properties of silicon-doped GaSb. The results of these detailed investigations made the development of novel photovoltaic device structures possible (e. g. monolithic (AlGa)(AsSb)/GaSb-tandem cells). The properties of the related solar cells were analysed with regard to the results on growth and material properties. A detailed summary is given in the following together with guidelines for future work.

The ranges for most GaSb-growth parameters are extremely narrow and the multiwafer geometry of the growth environment has proven to be an additional challenge. In this thesis, various substrate issues have been analysed such as oxide desorption and film morphology versus substrate miscut angle. An activation energy of 3 eV for the oxide desorption was obtained, and in-situ etching of GaSb was demonstrated for the first time using tertiarybutylchloride. The electrical and optical properties of GaSb grown in the multiwafer reactor have been shown to be well in line with the best values in the literature. Moreover, the successful growth of high-quality (AlGa)(AsSb) could be demonstrated for the first time in a multiwafer MOVPE-reactor. As the standard aluminium precursor trimethylaluminium is not suited for the growth of antimonides, two promising alternatives were compared to each other: dimethylethylamine alane and tritertiarybutylaluminium. The related results represent the first report of a *direct* comparison between the two sources. (AlGa)(AsSb) with low oxygen and carbon levels could be grown using the alane. However, this highly reactive precursor is subject to parasitic pre-reactions and pre-deposition. This became evident when the following points were observed: an unusual non-linear incorporation behaviour, a white powder as pre-reaction product on the inlet nozzle, a temperature dependent efficiency even far above the corresponding decomposition temperature, reduced efficiencies that depend on the molar flow rates of other precursors, higher efficiencies at increased carrier gas flow rates, and a non-abrupt incorporation behaviour when the source is switched on or off. However, further optimisation allowed the deposition of (AlGa)(AsSb) with sufficient quality for device applications. For the precursor combination TEGa/DMEAA/TMSb/TBAs n-type doping of (AlGa)(AsSb) with tellurium was shown to be possible but very difficult. Future work on this field must focus on two main points: Firstly, the purity of the novel precursors must be significantly improved by the manufacturers. Secondly, the growth conditions must still be improved in order to reduce the above-mentioned problems. For example, the temperature gradients and gas flow dynamics in the reactor should be further adapted to the particular properties of the antimonides. Tin should be tested as donor dopant for the material. With regard to a large number of possible applications, compositions should also be considered that are lattice-matched to InP.

Particular attention was drawn to silicon as novel acceptor dopant in the MOVPE of antimonides. This element is generally known as an amphoteric impurity in III-V semiconductors. However, in As- and P-based III-V compounds most growth conditions lead to an incorporation of Si preferentially on group III-sites, making it a common n-type dopant. On the other hand, Si has been found to behave as acceptor in many GaSb growth techniques, but the level of understanding and experience concerning this acceptor is still very limited. Therefore the incorporation behaviour and the electrical

properties of Si-acceptors in MOVPE-grown material were examined in chapter 5. The PL properties of not intentionally doped and lightly silicon doped GaSb were studied. A PL line at approximately 800meV, whose assignment had previously been controversial, has been identified as due to a transition of a free electron to neutral acceptor ($e \text{ Si}_{\text{Sb}}^0$). All other PL peaks in the high-energy part of the spectrum could also be explained within the concept of potential fluctuations due to the charged impurity distribution. The activation energy of the silicon acceptor could be estimated as $E_A = 8.8 \pm 0.4$ meV. Generally, light doping with silicon resulted in a higher mobility, a reduced compensation ratio and an improved PL intensity compared to not intentionally doped samples. Silicon doping might result in a suppression of the native defect in GaSb and is believed to lead to a reduction of the non-radiative recombination rate in the material. These features make the silicon acceptor an interesting novel candidate for various GaSb-based device applications. It was therefore used for the deposition of the device structures described in chapter 6. Further work concerning the silicon acceptor should consider the above mentioned assumption of a suppression of the native acceptor defect in GaSb. While the structural native defect can not be passivated by hydrogen implantation, a real extrinsic acceptor like silicon could offer this possibility and material with exceptionally low background acceptor concentrations can be expected. In addition, it will be very interesting to compare the Shockley-Read-Hall recombination rates in not-intentionally doped and lightly silicon doped GaSb; here, the drastically enhanced PL intensity in lightly silicon doped material is promising.

Based on the results concerning growth and doping, photovoltaic devices were developed. Firstly, the fundamental cell structure, the front surface passivation and the doping levels in GaSb pn-homojunction solar cells were analysed. Devices with internal quantum efficiencies above 90% have been achieved with silicon as p-type dopant in the active region. This must be considered a very good value for these early stages of the device development. Furthermore, an MOVPE-grown (AlGa)(AsSb) solar cell with a band gap of $E_{\text{gap}} \sim 0.9$ eV could be shown. This is the first report of a minority carrier device with MOVPE-grown (AlGa)(AsSb) in the active region. However, both the quantum efficiency and V_{oc} of this preliminary device need further improvement. The current device performance is mainly limited by the unsatisfactory purity of the novel metalorganic precursors which have been employed for the growth. In addition, an MOVPE-grown GaSb-based monolithic (AlGa)(AsSb)/GaSb tandem cell could be demonstrated for the first time. The device performance is partly limited because of the low doping upper limits in the antimonides that prohibit the successful deposition of an Esaki tunnel diode in the structure. In addition, a novel class of GaSb-based photovoltaic devices was developed: pn-heterojunction solar cells. Here, emitter and base consist of materials with different band gaps. A p:GaSb/n:(AlGa)(AsSb) structure gave the same quantum efficiency as a corresponding GaSb homojunction device while the open-circuit voltage increased by approximately 20 mV. The increased voltage is believed to be due to a reduced dark current in the device. The related heterojunction approach should be included in future tandem cell concepts. In addition, the further development could focus on the type IIB-junction between InAs and GaSb in order to deposit successful tunnel junctions. If a further improvement concerning the purity of the employed metalorganic precursors can be achieved, a thorough optimisation of the device structure and fabrication technology can eventually be expected to produce a highly efficient (AlGa)(AsSb)/GaSb-tandem cell for a concentrating application. Altogether, the results on fundamental aspects of growth and material properties have been successfully applied to the development of novel photovoltaic device structures based on GaSb.

Abbreviations

AFM	atomic force microscope
(AlGa)As	aluminium-gallium-arsenide
(AlGa)Sb	aluminium-gallium-antimonide
(AlGa)(AsSb)	aluminium-gallium-arsenide-antimonide
AM1.5d	terrestrial solar spectrum, direct light, air mass 1.5
ARC	antireflective coating
BSF	back surface field
CV	capacitance voltage
CVD	chemical vapour deposition
DAP	donor acceptor pair
DETe	diethyltellurium
DMEAA	dimethylethylamine alane adduct
EQE	external quantum efficiency
FWHM	full width at half maximum
GaAs	galliumarsenide
GaSb	galliumantimonide
Ge	germanium
HCl	hydrochloric acid
HR-XRD	high resolution X-ray diffraction
IQE	internal quantum efficiency
LPE	liquid phase epitaxy
MBE	molecular beam epitaxy
MOVPE	metalorganic vapour phase epitaxy
NDR	negative differential resistance
PL	photoluminescence
QNR	quasi-neutral region (of a pn-junction)
SIMS	secondary ion mass spectroscopy
TBAs	tertiarybutylarsine
TEGa	triethylgallium
TMAI	trimethylaluminium
TMSb	trimethylantimony
TTBAI	tritertiarybutylaluminium
V/III-ratio	ratio of the partial pressure of all group V and all group III sources in the gas phase of the MOVPE reactor

References

1. Aardvark, A., N.J. Mason, and P.J. Walker, *The growth of Antimonides*, Progress in Crystal Growth and Characterisation, 1998, 35(2-4), p. 207-241
2. Adachi, S., *Band gaps and refractive indices of AlGaAsSb, GaInAsSb, and InPAsSb: Key properties for a variety of the 2-4 μm optoelectronic device applications*, Journal of Applied Physics, 1987, 61(10), p. 4869 - 4876
3. Agert, C., P.S. Gladkov, and A.W. Bett, *Origin of the photoluminescence line at 0.8 eV in undoped and Si-doped GaSb grown by MOVPE*, submitted for publication in Semiconductor Science and Technology, 2001
4. Allerman, A.A., R.M. Biefeld, and S.R. Kurtz, *InAsSb-based mid-infrared lasers (3.8-3.9 μm) and light-emitting diodes with AlAsSb claddings and semimetal electron injection, grown by metalorganic chemical vapor deposition*, Applied Physics Letters, 1996, 69(4), p. 465 - 467
5. Allerman, A.A., S.R. Kurtz, R.M. Biefeld, and K.C. Baucom, *10-stage, 'cascaded' InAsSb quantum well laser at 3.9 μm* , Electronics Letters, 1998, 34(4)
6. Allwood, D.A., R.T. Carline, N.J. Mason, C. Pickering, B.K. Tanner, and P.J. Walker, *Characterisation of oxide layers on GaAs substrates*, Thin Solid Films, 2000, 364(1-2), p. 33 - 39
7. Allwood, D.A., I.R. Grant, N.J. Mason, R.A. Palmer, and P.J. Walker, *Reflections on a Semiconductor Crystal Surface*, Compound Semiconductor, 2000, 6(8)
8. Allwood, D.A., P.C. Klipstein, N.J. Mason, R.J. Nicholas, and P.J. Walker, *GaAs High Temperature Optical Constants and Application to Optical Monitoring within the MOVPE Environment*, Journal of Electronic Materials, 2000, 29(1), p. 99 - 105
9. Allwood, D.A., N.J. Mason, and P.J. Walker, *In situ characterisation of MOVPE by surface photoabsorption. I. Substrate oxide desorption*, Journal of Crystal Growth, 1998, 195, p. 163 - 167
10. Allwood, D.A., N.J. Mason, and P.J. Walker, *In situ characterisation of III-V substrate oxide desorption by surface photoabsorption in MOVPE*, Materials Science and Engineering, 1999(B66), p. 83 - 87
11. Almuneau, G., F. Genty, A. Wilk, P. Grech, A. Joullié, and L. Chusseau, *GaInSb/AlGaAsSb strained quantum well semiconductor lasers for 1.55 μm operation*, Semiconductor Science and Technology, 1999, 14, p. 89-92
12. Anwar, A.F.M. and R.T. Webster, *Energy bandgap of AlGaAsSb and conduction band discontinuity of AlGaAsSb/InAs and AlGaAsSb/InGaAs heterostructures*, Solid-State Electronics, 1998, 42(11), p. 2101 - 2104
13. Bauer, G. and W. Richter, *Optical Characterisation of Epitaxial Semiconductor Layers*. 1996: Springer, ISBN 3-540-59129-X
14. Beckert, R., *Dissertation: Charakterisierung von Infrarot empfindlichen Photovoltaikzellen*, 2001, Fraunhofer Institute for Solar Energy Systems, Freiburg, Germany & Albert-Ludwigs-Universität Freiburg, Germany
15. Bedair, S.M., M.L. Timmons, and J.P.C. Chiang, *Growth and Characterisation of AlGaAs/GaAs and AlGaAsSb/GaAsSb Cascade Solar Cells*, Inst. Phys. Conf. Ser., 1981, 56, chapter 6, p. 403 - 411
16. Beer, A.C. and R.K. Willardson, *Semiconductors and Semimetals*. Vol. 10 Transport Phenomena. 1975

17. Behet, M., P. Schneider, D. Moulin, K. Heime, J. Weitok, J. Tuemmler, J. Hermans, and J. Geurts, *Low pressure metalorganic vapor phase epitaxy and characterization of (Al,Ga)Sb/GaSb heterostructures*, Journal of Crystal Growth, 1996, 167(3-4), p. 415-20
18. Behet, M., B. Stoll, W. Brysch, and K. Heime, *Growth of GaSb and InSb by low-pressure plasma MOVPE*, Journal of Crystal Growth, 1992, 124, p. 377-382
19. Bell, G.R., N.S. Kaijaks, R.J. Dixon, and C.F. McConville, *Atomic hydrogen cleaning of polar III-V semiconductor surfaces*, Surface Science, 1998, 401(2), p. 125-37
20. Biefeld, R.M., A.A. Allerman, and S.R. Kurtz, *The growth of mid-infrared lasers and AlAsSb by MOCVD*, Journal of Crystal Growth, 1997, 174, p. 593-8
21. Biefeld, R.M., A.A. Allerman, S.R. Kurtz, and K.C. Baucom, *Progress in the growth of mid-infrared InAsSb emitters by metal-organic chemical vapor deposition*, Journal of Crystal Growth, 1998, 195, p. 356 - 362
22. Biefeld, R.M., A.A. Allermann, and M.W. Pelczynski, *Growth of n- and p-type Al(As)Sb by metalorganic chemical vapor deposition*, Applied Physics Letters, 1996, 68(7), p. 932-934
23. Bignazzi, A., A. Bosacchi, and R. Magnanini, *Photoluminescence study of heavy doping effects in Te-doped GaSb*, Journal of Applied Physics, 1997, 81(11), p. 7540-7
24. Bignazzi, A., E. Grilli, M. Guzzi, M. Radice, A. Bosacchi, S. Franchi, and R. Magnanini, *Low temperature photoluminescence of tellurium-doped GaSb grown by molecular beam epitaxy*, Journal of Crystal Growth, 1996, 169, p. 450 - 456
25. Blieske, U., *Dissertation: Konzentratorsolarzellen aus Galliumarsenid: Modul- und Tandem-Anwendungen*, 1995, Fraunhofer Institute for Solar Energy Systems, Freiburg, Germany & University of Konstanz, Germany
26. Bosacchi, A., S. Franchi, P. Allegri, V. Avanzini, A. Baraldi, C. Ghezzi, R. Magnanini, A. Parisini, and L. Tarricone, *Electrical and photoluminescence properties of undoped GaSb prepared by molecular beam epitaxy and atomic layer molecular beam epitaxy*, Journal of Crystal Growth, 1995, 150, p. 844 - 848
27. Cao, D.S., Z.M. Fang, and G.B. Stringfellow, *Organometallic vapor-phase epitaxial growth of AlGaSb and AlGaAsSb*, Journal of Crystal Growth, 1991, 113, p. 441-448
28. Charache, G.W., P.F. Baldasaro, L.R. Danielson, D.M. DePoy, M.J. Freeman, C.A. Wang, H.K. Choi, D.Z. Garbuzov, R.U. Martinelli, V. Khalfin, *et al.*, *InGaAsSb thermophotovoltaic diode: Physics evaluation*, Journal of Applied Physics, 1999, 85(4), p. 2247-2252
29. Chen, W.-K. and J. Ou, *Influence of As/Al and Sb/Al Gas Flow Ratios on Growth of AlAsSb Alloys*, Japanese Journal of Applied Physics, 1995, 34, p. L1581 - L1583
30. Chidley, E.T.R., S.K. Haywood, A.B. Henriques, N.J. Mason, R.J. Nicholas, and P.J. Walker, *Photoluminescence of GaSb grown by metal-organic vapour phase epitaxy*, Semiconductor Science and Technology, 1991, 6(1), p. 45-53
31. Chin, V.W.L., *Electron mobility in GaSb*, Solid-State Electronics, 1995, 38(1), p. 59 - 67
32. Da Silva, F.W.O., C. Raisin, M. Silga, M. Nouaoura, and L. Lassabatere, *Chemical Preparation of GaSb (001) substrates prior to MBE*, Semiconductor Science and Technology, 1989, 4, p. 565-569

33. Da-Cheng, L., L. Xianglin, W. Du, and L. Lanying, *Growth of GaSb and GaAsSb in the single phase region by MOVPE*, Journal of Crystal Growth, 1992, 124, p. 383-388
34. Dimroth, F., *Dissertation: Metallorganische Gasphasenepitaxie zur Herstellung von hocheffizienten Solarzellen aus III-V Halbleitern*, 2000, Fraunhofer Institute for Solar Energy Systems, Freiburg, Germany & University of Konstanz, Germany
35. Dutta, P.S., H.L. Bhat, and V. Kumar, *The physics and technology of gallium antimonide: an emerging optoelectronic material*, Journal of Applied Physics, 1997, 81(9), p. 5821-70
36. Ehsani, H., I. Bhat, R. Gutmann, and G. Charache, *p-type GaSb and GaInSb layers grown by metalorganic vapor phase epitaxy using silane as the dopant source*, Applied Physics Letters, 1996, 69(25), p. 3863 - 3865
37. Ehsani, H., I. Bhat, C. Hitchcock, R.J. Gutmann, G. Charache, and M. Freeman, *p-Type and n-type doping in GaSb and GaInSb layers grown by metalorganic vapor phase epitaxy*, Journal of Crystal Growth, 1998, 195, p. 385 - 390
38. Fahrenbruch, A.L. and R.H. Bube, *Fundamentals of Solar Cells*. 1983: Academic Press, ISBN 0-12-247680-8
39. Ferrini, R., M. Patrini, and S. Franchi, *Optical functions from 0.02 to 6 eV of AlGaSb/GaSb epitaxial layers*, Journal of Applied Physics, 1998, 84(8), p. 4517 - 4524
40. Fuhs, W., *Festkörperphysikalische Grundlagen. Solarzellen*, ed. D. Meissner. 1993, ISBN 3-528-06518-4
41. Garbuzov, D.Z., R.U. Martinelli, V. Khalfin, H. Lee, N.A. Morris, G.C. Taylor, J.C. Connolly, G.W. Charache, and D.M. DePoy, *A Novel Approach for the Improvement of Open Circuit Voltage and Fill Factor of InGaAsSb/GaSb Thermophotovoltaic Cells*, AIP Conf. Proc. 420, 1998, p. 1400 ff
42. Genty, F., G. Almuneau, L. Chusseau, A. Wilk, S. Gaillard, G. Boissier, P. Grech, and J. Jacquet, *Growth and characterization of vertical cavity structures on InP with GaAsSb/AlAsSb Bragg mirrors for 1.55 μm emission*, Journal of Crystal Growth, 1999, 201/202, p. 1024 - 1027
43. Georgiev, N. and T. Mozume, *Effect of group-V species exchange at the interfaces of InGaAs/AlAsSb superlattice*, Journal of Crystal Growth, 2000, 209, p. 247 - 251
44. Giesen, C., M.M. Beerbom, X.G. Xu, and K. Heime, *MOVPE of AlAsSb using tritertiarybutylaluminium*, Journal of Crystal Growth, 1998, 195, p. 85 - 90
45. Graham, R.M., A.C. Jones, N.J. Mason, S. Rushworth, A. Salesse, T.Y. Seong, G. Booker, L. Smith, and P.J. Walker, *Improved materials for MOVPE growth of GaSb and InSb*, Semiconductor Science and Technology, 1993, 8(10), p. 1797-802
46. Green, M.A., *Solar Cells*. 1982: Prentice-Hall, ISBN 0-13-82270
47. Haynes, J.R., *Experimental proof of the existence of a new electronic complex in silicon*, Physical Review Letters, 1960, 4(7), p. 361 - 363
48. Hidalgo, P., B. Méndez, P.S. Dutta, J. Piqueras, and E. Dieguez, *Luminescence properties of transition-metal-doped GaSb*, Physical Review B, 1998, 57(11), p. 6479 - 6484
49. Hinkov, V., *Diplomarbeit: Untersuchungen an GaSb-basierenden MOVPE-Strukturen und Solarzellen*, 2001, Fraunhofer Institute for Solar Energy Systems, Freiburg, Germany & Albert-Ludwigs-Universität Freiburg, Germany

50. Hitchcock, C.W., R.J. Gutmann, J.M. Borrego, I.B. Bhat, and G.W. Charache, *Antimonide-Based Devices for Thermophotovoltaic Applications*, IEEE Transactions on Electron Devices, 1999, 46(10), p. 2154 - 2161
51. Hitchcock, C.W., R.J. Gutmann, H. Ehsani, I.B. Bhat, C.A. Wang, M.J. Freeman, and G.W. Charache, *Ternary and quaternary antimonide devices for thermophotovoltaic applications*, Journal of Crystal Growth, 1998, 195, p. 363 - 372
52. Hjelt, K. and T. Tuomi, *Photoluminescence and electrical properties of MOVPE-grown zinc-doped gallium antimonide on gallium arsenide*, Journal of Crystal Growth, 1997, 170, p. 794-798
53. Hook, J.R. and H.E. Hall, *Solid State Physics*. 2 ed. 1991: John Wiley & Sons Ltd., ISBN 0 471 92805 4
54. Ibach, H. and H. Lüth, *Festkörperphysik*. 4 ed. 1995: Springer-Verlag, ISBN 3-540-58575-3
55. Juang, F.S. and Y.K. Su, *Growth and properties of GaSb, GaInSb and GaAlSb epilayers by MOCVD*, Prog. Crystal Growth and Charact., 1990, 20, p. 285 - 312
56. Khan-Cheema, U.M., P.C. Klipstein, D.G. Austing, J.M. Smith, N.J. Mason, P.J. Walker, and G. Hill, *Interface effects, band overlap and the semimetal to semiconductor transition in InAs/GaSb interband resonant tunneling diodes*, Solid-State Electronics, 1994, 37(4-6), p. 977 - 979
57. Khan-Cheema, U.M., N.J. Mason, P.J. Walker, P.C. Klipstein, and G. Hill, *High pressure studies of negative differential resistance in InAs/GaSb resonant conduction heterostructures*, J. Phys. Chem. Solids, 1995, 56(3/4), p. 463 - 467
58. Klenk, R., *Characterisation and Modelling of Chalcopyrite Solar Cells*, to be published in Thin Solid Films, 2001
59. Kodama, M., *Oxide Removal from the GaSb Surface and Fabrication of MBE GaSb Photodiodes and Au-GaSb Schottky Diodes*, Advanced Materials for Optics and Electronics, 1994, 4, p. 319 - 325
60. Kodama, M., J. Hasegawa, and M. Kimata, *Influence of Substrate Preparation on the Morphology of GaSb Films Grown by Molecular Beam Epitaxy*, J. Electrochem. Soc.: Solid-State Science and Technology, 1985, 132(3), p. 659-662
61. Koeth, J., T. Bleuel, R. Werner, and A. Forchel, *1.5 μm Ga(Al)Sb laser grown on GaAs substrate by MBE*, Journal of Crystal Growth, 1999, 201/202, p. 841 - 843
62. Koeth, J., R. Dietrich, and A. Forchel, *GaSb vertical-cavity surface-emitting lasers for the 1.5 μm range*, Applied Physics Letters, 1998, 72(13), p. 1638 - 1640
63. Koljonen, T., M. Sopanen, H. Lipsanen, and T. Tuomi, *Metalorganic vapor phase epitaxial growth of AlGaSb and AlGaAsSb using all-organometallic sources*, Journal of Crystal Growth, 1996, 169(3), p. 417-23
64. Kondow, M., B. Shi, and C.W. Tu, *In situ etching using a novel precursor of tertiarybutylchloride (TBCl)*, Journal of Crystal Growth, 2000, 209, p. 263 - 266
65. Kurtz, S.R., A.A. Allerman, R.M. Biefeld, and K.C. Baucom, *High slope efficiency, "cascaded" midinfrared lasers with type I InAsSb quantum wells*, Applied Physics Letters, 1998, 72(17), p. 2093 - 2095
66. Landolt-Börnstein, *Numerical Data and Functional Relationships in Science and Technology*, , 22, "Semiconductors", Subvolume a, p. 102
67. Lepkowski, T.R., R.Y. DeJule, N.C. Tien, M.H. Kim, and G.E. Stillman, *Depletion corrections in variable temperature Hall measurements*, Journal of Applied Physics, 1987, 61(10), p. 4808 - 4811

68. Létay, G. and A. Bett, *Thermodynamic limit and optimum bandgap structure for multibandgap solar cells and TPV cells*, to be published in proceedings of 17th European Photovoltaic Solar Energy Conference and Exhibition, Munich, 22-26 Oct. 2001, 2001
69. Leu, S., F. Höhnsdorf, W. Stolz, R. Becker, A. Salzmann, and A. Greiling, *C- and O-incorporation in (AlGa)As epitaxial layers grown by MOVPE using TBAs*, Journal of Crystal Growth, 1998, 195, p. 98-104
70. Levanyuk, A.P. and V.V. Osipov, *Edge luminescence of direct-gap semiconductors*, Sov. Phys. Usp., 1981, 24(3), p. 187 - 215
71. Lewerenz, H.-J. and H. Jungblut, *Photovoltaik*. 1995: Springer, ISBN 3-540-58539-7
72. Mathur, P.C. and S. Jain, *Hole transport properties in gallium antimonide from 77 to 300°K*, Physical Review B, 1979, 19(6), p. 3152 - 3158
73. Milnes, A.G. and A.Y. Polyakov, *Review - Gallium Antimonide Device Related Properties*, Solid-State Electronics, 1993, 36(6), p. 803 - 818
74. Moto, A., S. Tanaka, T. Tanabe, and S. Takagishi, *GaInP/GaAs and mechanically stacked GaInAs solar cells grown by MOCVD using TBAs and TBP as V-precursors*, Solar Energy Materials & Solar cells, 2001, 66, p. 585- 592
75. Nakamura, F., K. Taira, K. Funato, and H. Kawai, *Se and Te doping in LP-MOCVD-grown GaSb using H₂Se and DETe*, Journal of Crystal Growth, 1991, 115, p. 474-478
76. Nicholas, D.J., M. Lee, B. Hamilton, and K.E. Singer, *Spectroscopic Studies of Shallow Defects in MBE GaSb*, Journal of Crystal Growth, 1987, 81, p. 298 - 303
77. Noack, R.A., W. Rühle, and T.N. Morgan, *Bound excitons at doubly ionizable acceptors in GaSb*, Physical Review B, 1978, 18(12), p. 6944
78. Novak, J., S. Hasenoehrl, M. Kucera, K. Hjelt, and T. Tuomi, *Sulphur doping of GaSb grown by atmospheric pressure MOVPE*, Journal of Crystal Growth, 1998, 183(1-2), p. 69-74
79. Osipov, V.V., T.I. Soboleva, and M.G. Foigel, *Interimpurity radiative recombination in heavily doped semiconductors*, Sov. Phys. Semicond., 1977, 11(7), p. 752 - 759
80. Overhof, H. and P. Thomas, *Electronic Transport in Hydrogenated Amorphous Semiconductors*. Springer Tracts in Modern Physics. Vol. 114. 1989, Berlin, Heidelberg, New York: Springer
81. Pascal, F., F. Delannoy, J. Bougnot, L. Gouskov, G. Bougnot, P. Grosse, and J. Kaoukab, *Growth and characterization of undoped and N-type (Te) doped MOVPE grown gallium antimonide*, Journal of Electronic Materials, 1990, 19(2), p. 187- 95
82. Peter, M., *Dissertation: Herstellung und Charakterisierung von antimonidischen III-V Halbleiterheterostrukturen für IR-Diodenlaser*, 1999, Fraunhofer Institute for Applied Solid State Physics, Freiburg, Germany & Albert-Ludwigs-Universität Freiburg, Germany
83. Rode, D.L., *Semiconductors and Semimetals: Transport Phenomena*, ed. R.K. Willardson and A.C. Beer. Vol. 10. 1975, New York, San Francisco, London: Academic Press, ISBN 0-12-752110-0
84. Rossi, T.M., D.A. Collins, D.H. Chow, and T.C. McGill, *p-type doping of gallium antimonide grown by molecular beam epitaxy using silicon*, Applied Physics Letters, 1990, 57(21), p. 2256 - 2258
85. Rühle, W. and D. Bimberg, *Linear and quadratic Zeeman effect of excitons bound to neutral acceptors in GaSb*, Physical Review B, 1975, 12(6), p. 2382 - 2390

86. Rühle, W., W. Jakowetz, C. Wölk, R. Linnebach, and M. Pilkuhn, *Optical Studies of Free and Bound Excitonic States in GaSb*, Phys. Stat. Sol. (b), 1976, 73, p. 255
87. Salesse, A., R. Alabedra, Y. Chen, M. Lakrimi, R.J. Nicholas, N.J. Mason, and P.J. Walker, *Improved photoluminescence from electrochemically passivated GaSb*, Semiconductor Science and Technology, 1997, 12(4), p. 413-18
88. Schubert, E.F., *Doping in III/IV Semiconductors*. 1993: Cambridge
89. Seabaugh, A. and R. Lake, *Tunnel Diodes*. Encyclopedia of Applied Physics. Vol. 22. 1998. 335 - 359, ISBN 3-527-29475-9
90. Shin, J., Y. Hsu, T.C. Hsu, and G.B. Stringfellow, *InSb, GaSb and GaInSb Grown using Trisdimethylaminoantimony*, Journal of Electronic Materials, 1995, 24(11), p. 1563 - 1569
91. Shlovskii, B.I. and A.L. Efros, *Electronic Properties of Doped Semiconductors*, ed. M. Cardona, P. Fulde, and H.J. Queisser. 1984: Springer, ISBN 3-540-12995-2
92. Singh, J., *Semiconductor Optoelectronics*. 1995: McGraw-Hill, ISBN 0-07-113577-4
93. Stollwerk, G., *Dissertation: Entwicklung eines hocheffizienten GaAs/GaSb Tandem Konzentration Solarzellen Moduls*, 1998, Fraunhofer Institute for Solar Energy Systems, Freiburg, Germany & Albert-Ludwigs-Universität Freiburg, Germany
94. Stollwerk, G., O.V. Sulima, and A.W. Bett, *Characterization and simulation of GaSb device-related properties*, IEEE Transactions on Electron Devices, 2000, 47(2), p. 448 - 457
95. Stolz, W. and T. Whitaker, *TBAs and TBP - Improved Group V Sources for MOVPE*, Compound Semiconductor, 1999, 5(7), p. 29 - 35
96. Stringfellow, G.B., *Organometallic Vapor-Phase Epitaxy: Theory and Practice*. 1989: Academic Press, ISBN 0-12-673840-8
97. Stringfellow, G.B., *Organometallic Vapor-Phase Epitaxy: Theory and Practice*. 2 ed. 1999: Academic Press, ISBN 0-12-673842-4
98. Su, Y.K., H. Kuan, and P.H. Chang, *Investigation of Se-doped GaSb epilayers grown by low pressure metal-organic chemical vapor deposition*, Solid-State Electronics, 1993, 36(12), p. 1773-8
99. Sulima, O.V. and A.W. Bett, *Fabrication and simulation of GaSb thermophotovoltaic cells*, Solar Energy Materials & Solar Cells, 2001, 66, p. 533 - 540
100. Takamasu, T., N. Miura, K. Taira, K. Funato, and H. Kawai, *Study of negative differential conductivity in an InAs/GaSb/InAs diode under pulsed high magnetic fields*, Physica B, 1993, 184, p. 259 - 262
101. Tanaka, A., J. Shintani, M. Kimura, and T. Sukegawa, *Multi-step pulling of GaInSb bulk crystal from ternary solution*, Journal of Crystal Growth, 2000, 209, p. 625 - 629
102. Tao, M., *A kinetic model for metalorganic chemical vapor deposition from trimethylgallium and arsine*, Journal of Applied Physics, 2000, 87(7), p. 3554 - 3562
103. Tümmler, J., J. Woitok, J. Hermans, J. Geurts, P. Schneider, D. Moulin, M. Behet, and K. Heime, *Growth and characterization of Sb-based heterostructures grown by LP-MOVPE*, Journal of Crystal Growth, 1997, 170, p. 772-6
104. Tuttle, G., J. Kavanaugh, and S. McCalmont, *(Al,Ga)Sb Long-Wavelength Distributed Bragg Reflectors*, IEEE Photonics Technology Letters, 1993, 5(12), p. 1376 - 1379

105. Vineis, C.J., C.A. Wang, and K.F. Jensen, *In-situ reflectance monitoring of GaSb substrate oxide desorption*, Journal of Crystal Growth, 2001, 225, p. 420 - 425
106. von Eichel-Streiber, C., M. Behet, M. Heuken, and K. Heime, *Doping of InAs, GaSb and InPSb by low pressure MOVPE*, Journal of Crystal Growth, 1997, 170, p. 783 - 787
107. Vurgaftman, W.W. Bewley, C.L. Felix, and J.R. Meyer, *Midwave-Infrared Semiconductor Lasers*, Compound Semiconductor, 2000, 6(3), p. 60 - 63
108. Wang, C., *personal communication*
109. Wang, C.A., *Organometallic vapor phase epitaxial growth of AlSb-based alloys*, Journal of Crystal Growth, 1996, 170(1-4), p. 725-31
110. Wang, C.A., *OMVPE growth of GaInAsSb in the 2-2.4 μm range*, Journal of Crystal Growth, 1998, 187
111. Wang, C.A. and H.K. Choi, *Lattice-matched GaSb/AlGaAsSb double-heterostructure diode lasers grown by MOVPE*, Electronics Letters, 1996, 32(19), p. 1779-81
112. Wang, C.A. and H.K. Choi, *GaInAsSb/AlGaAsSb multiple-quantum-well diode lasers grown by organometallic vapor phase epitaxy*, Applied Physics Letters, 1997, 70(7), p. 802 - 804
113. Wang, C.A. and H.K. Choi, *OMVPE Growth of GaInAsSb/AlGaSb for Quantum-Well Diode Lasers*, Journal of Electronic Materials, 1997, 26(10), p. 1231 - 1236
114. Wang, C.A., H.K. Choi, D.C. Oakley, and G.W. Charache, *Recent progress in GaInAsSb thermophotovoltaics grown by organometallic vapor-phase epitaxy*, Journal of Crystal Growth, 1998, 195, p. 346-355
115. Wang, C.A., H.K. Choi, G.W. Turner, D.L. Spears, M.J. Manfra, and G.W. Charache, *Lattice-Matched Epitaxial GaInAsSb/GaSb Thermophotovoltaic Devices*, Proceedings of *Thermophotovoltaic Generation of Electricity: Third NREL Conference*, 1997, p. 75 - 87, NREL: The American Institute of Physics
116. Wang, C.A., M.C. Finn, S. Salim, K.F. Jensen, and A.C. Jones, *Tertiarybutylaluminum as an organometallic source for epitaxial growth of AlGaSb*, Applied Physics Letters, 1995, 67(10), p. 1384-1386
117. Wang, C.A., K.F. Jensen, A.C. Jones, and H.K. Choi, *n-AlGaSb and GaSb/AlGaSb double-heterostructure lasers grown by organometallic vapor phase epitaxy*, Applied Physics Letters, 1996, 68(3), p. 400 - 402
118. Wang, C.A., S. Salim, K.F. Jensen, and A.C. Jones, *Characteristics of GaSb growth using various gallium and antimony precursors*, Journal of Crystal Growth, 1997, 170, p. 55-60
119. Whitaker, T., *Magnetic Sensors - Indium Antimonide in Pole Position*, Compound Semiconductor Spring II, 1998, p. 29 - 32
120. Wiley, J.D., *Semiconductors and Semimetals: Transport Phenomena*, ed. R.K. Willardson and A.C. Beer. Vol. 10. 1975, New York, San Francisco, London: Academic Press, ISBN 0-12-752110-0
121. Woelk, E., H. Jurgensen, R. Rolph, and T. Zielinski, *Large scale production of indium antimonide film for position sensors in automobile engines*, Journal of Electronic Materials, 1995, 24(11), p. 1715-18
122. Wolfram, P., W. Ebert, J. Kreissl, and N. Grote, *MOVPE-based in-situ etching of In(GaAs)P/InP using tertiarybutylchloride*, Journal of Crystal Growth, 2000, 221, p. 177 - 182
123. Xie, Q. and J.E. Van Nostrand, *Line-of-sight mass spectrometric study of As/Sb exchange on Sb-terminated and Ga-terminated GaSb (001) during molecular*

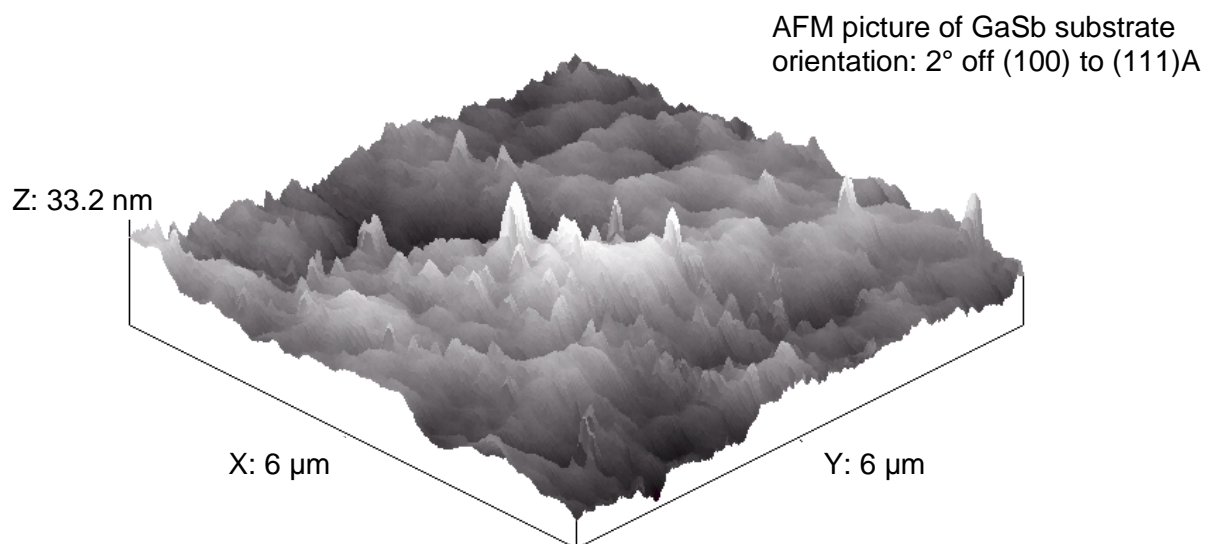
- beam epitaxy*, Journal of Vacuum Science Technology A, 1999, 17(2), p. 342 - 346
124. Xie, Q., J.E. Van Nostrand, J.L. Brown, and C.E. Stutz, *Arsenic for antimony exchange on GaSb, its impact on surface morphology, and interface structure*, Journal of Applied Physics, 1999, 86(1), p. 329 - 337
 125. Xie, Q., J.E. Van Nostrand, R.L. Jones, J. Szelove, and D.C. Look, *Electrical and optical properties of undoped GaSb grown by molecular beam epitaxy using cracked Sb1 and Sb2*, Journal of Crystal Growth, 1999, 207, p. 255 - 265
 126. Yu, Y.P. and M. Cardona, *Fundamentals of Semiconductors*. 2 ed. 1999: Springer, ISBN 3-540-65352-X
 127. Zhao, G.Y., H. Ebisu, T. Soga, T. Egawa, T. Jimbo, and M. Umeno, *Electrical Transport Properties of GaSb Grown by Molecular Beam Epitaxy*, Japanese Journal of Applied Physics, 1998, 37(part 1, No. 4A), p. 1704 - 1708
 128. Zimmermann, G., Z. Spika, T. Marschner, B. Spill, W. Stolz, E.O. Göbel, P. Gimmnich, J. Lorberth, A. Greiling, and A. Salzmänn, *GaAs substrate pretreatment and metalorganic vapour phase epitaxy of GaAs, AlAs and (AlGa)As using beta-eliminating trialkyl-As precursors*, Journal of Crystal Growth, 1994, 145, p. 512 - 519

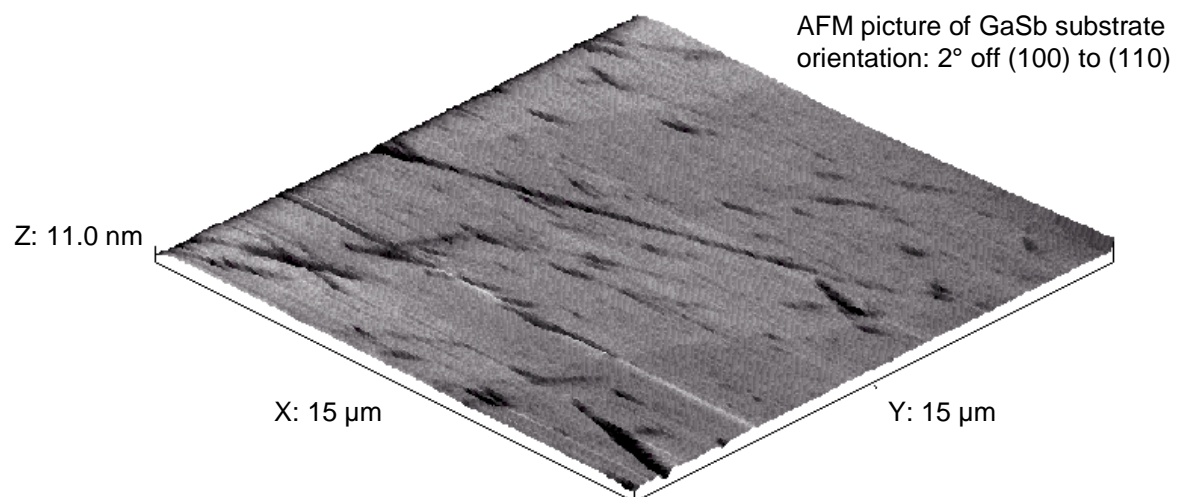
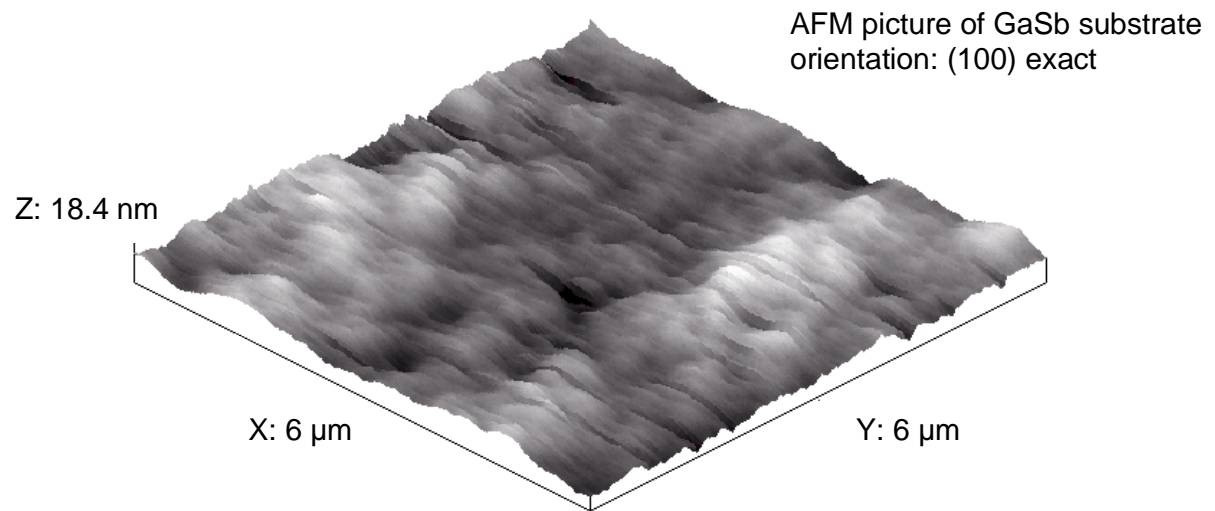
The band diagrams in chapter 6 were created by making use of the PC1D simulation software (Copyright 1998, University of New South Wales, Version 5.3). A related basis concerning the material data was accepted from [94].

Appendix: Substrates

Substrate morphology

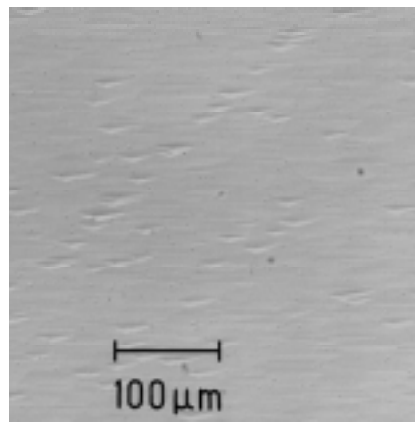
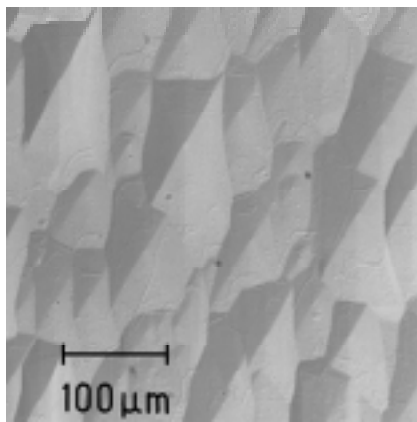
The following figures show AFM's of the different substrates that were used for the growth experiments. While the (100) exact oriented substrates were only employed for very early growth experiments, the 2° off to (111)A substrates were used for the majority of growth experiments. Most of the device structures were grown on the 2° off (100) to (110) substrates as these were available with a 2" diameter.





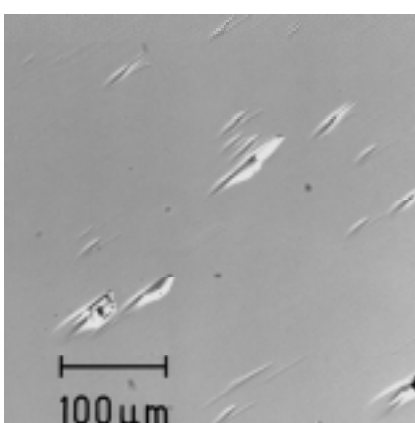
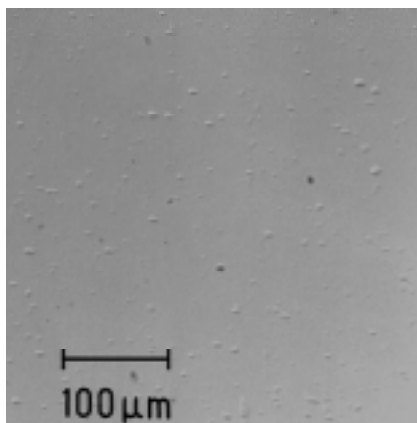
Epi-layer morphology versus substrate miscut angle

The following figures show Normarski contrast optical micrographs of a solar cell epitaxial structure grown on different substrates in the same run. It can easily be seen that the morphology of the layer is strongly dependent on the substrate miscut angle: While (100) exact substrates gave very rough morphologies with a high density of faceted defects, much better morphologies were obtained for the 2° to (111)A miscut. Even better morphologies resulted on 2° to (110) substrates. Here, one batch of substrates gave nearly perfect morphologies, while a second batch showed some defects. Obviously, the choice of the right substrate is a crucial point for the growth of antimonides. A detailed microscopic study into the nucleation behaviour as a function of the substrate miscut angle and the substrate preparation would be of high interest.



Normarski contrast optical micrographs of solar cell epi-structure #732, grown on the above substrate-orientations

left: (100) exact
right: 2° off (100) to (111)A



Normarski contrast optical micrographs of solar cell epi-structure #732, grown on GaSb, 2° off (100) to (110)

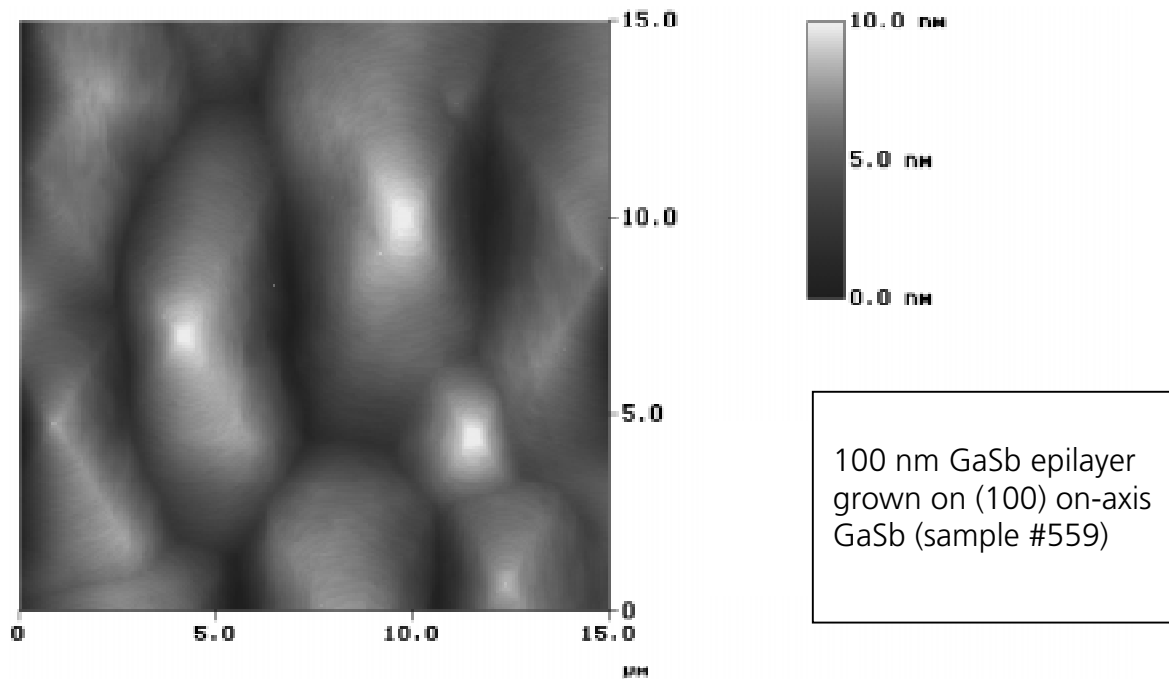
left: first batch
right: second batch

The following figure shows an AFM picture of an epitaxial GaSb layer of 100 nm thickness. The layer was deposited on a (100) exact substrate in order to examine the shape and size of the faceted defects at small film thicknesses. The comparison between this layer and the above solar cell structure on a (100) exact substrate shows that

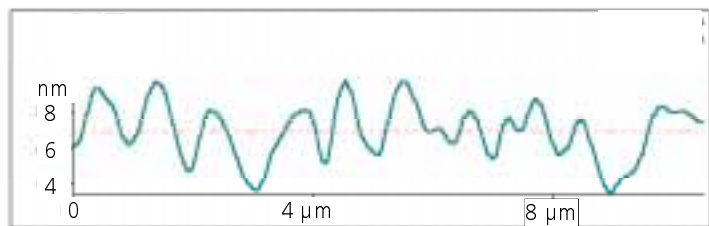
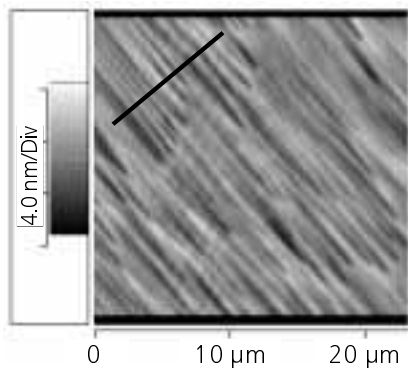
- the defects form in the early stages of the growth, and
- the thicker the layer gets, the bigger the defects become.

These findings could be interpreted in the following way:

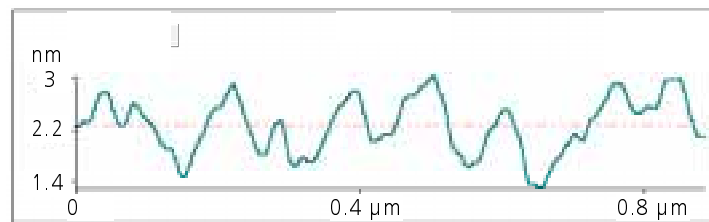
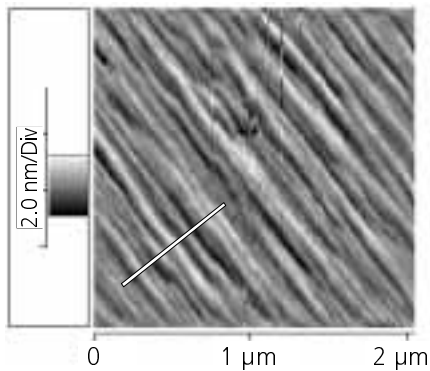
If structural defects originate from an imperfect nucleation process, the defects will grow and the crystal planes with the lowest growth rate will remain. These planes form the surfaces of the faceted defects in the figures. The defects coalesce when the deposition process proceeds, so the thick solar cell structure above shows less but bigger defects than the thin epitaxial layer below. As already said above, a detailed microscopic study into the homoepitaxial nucleation behaviour of GaSb would be of high value.



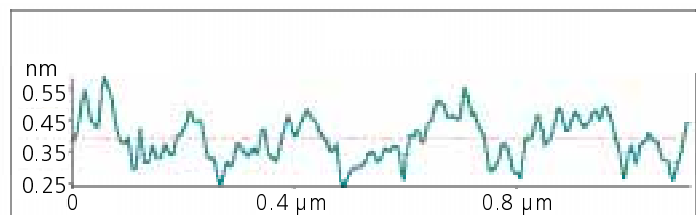
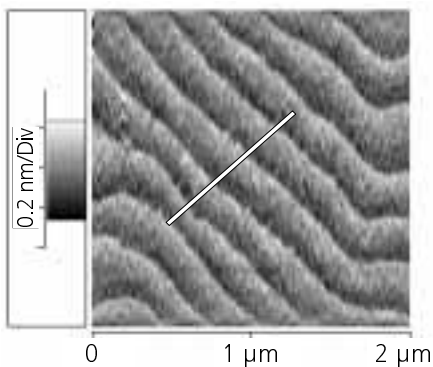
While misoriented GaSb substrates gave the best results in the growth process at Fraunhofer ISE, the process in the Clarendon laboratory was optimised for exact (100) substrates. The following figure compares a layer grown at Fraunhofer ISE in Freiburg on a 2° to (111)A-substrate to a layer grown at the Clarendon laboratory in Oxford on an exact (100) and a 2° to (110)-substrate. While the atomic terraces on the exact (100) sample indicate a step flow growth mode, the morphologies of both layers grown on misoriented substrates suggest a step bunching mode.



Sample #793: GaSb, substrate: 2° off to (111)A
(grown at Fraunhofer ISE)



Sample #4093: GaSb, substrate: 2° off to (110)
(grown at University of Oxford)



Sample #4093: GaSb, substrate: (100) exact
(grown at University of Oxford)

Publications

- 1.: F. Höhnsdorf, J. Koch, C. Agert, W. Stolz, *Investigations of (Galn)(NAs) bulk layers and (Galn)(NAs)/GaAs multiple quantum well structures grown using tertiarybutylarsine (TBAs) and 1,1-dimethylhydrazine (UDMHy)*, Journal Of Crystal Growth (195) 1-4 (1998) p. 391-396
- 2.: C. Ellmers, F. Höhnsdorf, J. Koch, C. Agert, S. Leu, D. Karaiskaj, M. Hofmann, W. Stolz, and W. W. Rühle, *Ultrafast (Galn)(NAs)/GaAs vertical-cavity surface-emitting laser for the 1.3 μm wavelength regime*, Applied Physics Letters, Vol. 74, No. 16, p. 2271 - 2273, 19 April 1999
- 3.: H.J. Kolbe, C. Agert, W. Stolz, G. Weiser, *Confinement effects in bulk samples derived from the Franz-Keldysh effect*, Physical Review B, Volume 59, Issue 23, June 15 1999, p. 14896 - 14898
- 4.: H.J. Kolbe, C. Agert, W. Stolz, G. Weiser, *Coherence in real space: the transition range from bulk to confined states studied by the Franz-Keldysh effect*, Physica E 6 (2000) 173-176
- 5.: A. Wagner, C. Ellmers, F. Höhnsdorf, J. Koch, C. Agert, S. Leu, M. Hofmann, W. Stolz, W. W. Rühle, *(Galn)(NAs)/GaAs vertical-cavity surface-emitting laser with ultrabroad temperature operation range*, Applied Physics Letters, Vol. 76, No. 3, p. 271f (2000)
- 6.: L. M. Smith, S. A. Rushworth, M. S. Ravetz, R. Odedra, R. Kanjolia, C. Agert, F. Dimroth, U. Schubert, A. W. Bett, *Low oxygen content trimethylaluminum and trimethylindium for MOVPE of light emitting devices*, Journal of Crystal Growth, 221 (2000), p. 86 - 90
- ^x7.: C. Agert, P. Lanyi, O.V. Sulima, W. Stolz, A. W. Bett, *Growth of antimony-based materials in a multi-wafer planetary MOVPE-reactor*, IEE Proceedings – Optoelectronics, Vol. 147, No 3, June 2000, p. 188 - 192
- ^x8.: A.W. Bett, R. Adelhelm, C. Agert, R. Beckert, F. Dimroth, U. Schubert, *Advanced III-V Solar Cell Structures Grown by MOVPE*, Solar Energy Materials & Solar Cells, 66 (1-4) 2001, p. 541 - 550
- 9.: C. Agert, F. Dimroth, U. Schubert, A. W. Bett, S. Leu, W. Stolz, *High-efficiency (AlGa)As/GaAs solar cells grown by MOVPE using TBAs at low temperatures and low V/III-ratios*, Solar Energy Materials & Solar Cells, 66 (1-4) 2001, p. 637 - 644
- ^x10.: C. Agert, P. Lanyi, A. W. Bett, *MOVPE of GaSb, (AlGa)Sb and (AlGa)(AsSb) in a multiwafer planetary reactor*, Journal Of Crystal Growth 225 (2001) p. 426-430

- ^x11.: C. Agert, P. S. Gladkov, A. W. Bett, *Origin of the photoluminescence line at 0.8 eV in undoped and Si-doped GaSb grown by MOVPE*, to be published in *Semiconductor, Science and Technology*
- ^x12.: C. Agert, R. Beckert, V. Hinkov, O. V. Sulima, A. W. Bett, *Novel device structures for infrared solar cells based on GaSb: pn-homojunctions, pn-heterojunctions, and tandem cells*, to be published in *Proceedings of 17th European Photovoltaic Solar Energy Conference, Munich, Germany, 2001*

The above list contains only publications in scientific journals and conference proceedings. Posters and talks are not included. Publications that contain parts of this work are marked as “^x”.

Curriculum Vitae

- 03/2001 – 06/2001 Research project with Dr. N. Mason, University of Oxford, UK
- 10/1998 - 11/2001 PhD in Physics at the Fraunhofer Institute for Solar Energy Systems ISE, Freiburg, Germany
Scholarship from the Studienstiftung des deutschen Volkes
- 04/1998 - 07/1998 Research project on semiconductor lasers for fibre-based telecommunication applications, University of Marburg
- 03/1998 Physik-Diplom (Master's degree in Physics)
overall mark: *sehr gut mit Auszeichnung* ($\approx 1^{\text{st}}$ with distinction)
- 06/1996 - 12/1997 Research project (*Alternative nitrogen precursors in the MOVPE of III-nitrides*) and Diplomarbeit (\approx MSc project) (*MOVPE of (GaN)(PAs) with the precursors TBAs and TBP*) with Dr. W. Stolz, Materials Sciences Centre, Philipps-University, Marburg
- 08/1995 - 09/1995 *Test of components of a photovoltaic hybrid system for applications in rural areas of developing countries*
Siemens Solar GmbH, Munich, Germany
- 02/1995 - 03/1995 *Study on social structures and related electricity needs in developing countries with regard to photovoltaic applications*
RWE Energie AG, Essen, Germany
- 10/1994 - 03/1998 Physics studies (continued), Philipps-University, Marburg
- 10/1993 - 06/1994 3rd year Physics studies at the University of Kent, UK
University diploma with merit in Physics
- 10/1991 - 06/1993 Physics studies, Philipps-University, Marburg, Germany
Vordiplom (intermediate examination)
overall mark: *sehr gut* ($\approx 1^{\text{st}}$ class)
- 07/1990 - 06/1991 Military service, working in photo processing laboratory
- 1990 Secondary School: Schwalmgymnasium Treysa
final exam: Abitur (A'Level equivalent), overall mark: 1.0
- 19/12/1970 born in Ziegenhain, Germany

Acknowledgements

I am very grateful to the following people and organisations who have contributed to the success of this work:

- Dr. Andreas Bett
- Dr. Wolfgang Stolz
- Professor Wolfgang Rühle
- Professor Peter Thomas
- Professor Wolfram Wettling
- Dr. Peter Gladkov
- Dr. Nigel Mason
- Dr. Oleg Sulima
- Ute Schubert and Dr. Frank Dimroth
- Dr. Peter Lanyi, Keith Belcher, Rolf Beckert, and Gerald Siefer
- Vladimir Hinkov
- the whole GaAs-group at Fraunhofer ISE
- the Studienstiftung des deutschen Volkes

Special thanks are due to my parents, to Bianca and to the Counting Crows.